A Novel Approach to Monitor Tissue Oxygen Saturation with Broadband Near-Infrared Spectroscopy

Zuzana Kovácsová

A thesis submitted in partial fulfillment

of the requirements for the degree of

Doctor of Philosophy

of

UCL

Department of Medical Physics & Biomedical Engineering

UCL

November 16, 2020

I, Zuzana Kovácsová, confirm that the work presented in this thesis is my own. Where information has been derived from other sources, I confirm that this has been indicated in the work.

Abstract

Cerebral oximetry is the measurement of tissue oxygen saturation, StO_2, with near-infrared spectroscopy (NIRS). The technique offers a non-invasive assessment of cerebral oxygenation and has potential to be used as a biomarker in neonatal critical care, particularly hypoxic-ischaemic encephalopathy (HIE). HIE is a major cause of neonatal mortality and affected neonates need continuous cerebral monitoring to guide treatment and improve patient outcome.

While multiple algorithms to recover StO_2 have been published, issues with low measurement accuracy or extracranial tissue signal contamination remain. This thesis is focused on the exploration of recovering StO_2 from continuous-wave broadband NIRS measurements with the aim to develop a novel algorithm to recover StO_2 with increased dynamic range and depth resolution. The novel algorithm, broadband multidistance oximetry (BRUNO), recovers StO_2 from a broadband multidistance measurement of the attenuation slope against distance. BRUNO combines and expands two other StO_2 algorithms, spatially resolved spectroscopy (SRS) and broadband fitting (BF).

The evaluation of algorithm performance was done in data obtained in computational simulations and phantoms. The median error of brain StO_2 recovered in simulations of brain and extracerebral tissue oxygenation changes was 1.1% with BRUNO, 2.3% with BF and 3.8% with SRS. Measurements during full oxygenation-deoxygenation cycles in a homogeneous blood phantom showed differences in the dynamic range of the algorithms; BRUNO recovered StO_2 over 0–100%, BF over 0–90% and SRS over 40–80%. These results show higher accuracy of BRUNO StO_2, higher sensitivity to brain oxygenation and wider dynamic range. Measurements of StO_2 in one neonate with HIE showed that the StO_2 algorithms led to different baseline values. Including an automated data assessment step in BRUNO to evaluate the suitability of collected spectra for analysis ensured BRUNO reliability. These findings highlight the effect of StO_2 algorithm selection on oxygenation recovery; applying BRUNO in the clinical care setting could reveal further insight into complex oxygenation processes occurring during neonatal brain injury.

Impact statement

The work described in this thesis contributes knowledge to research within academia, the clinical environment and the commercial sector.

The project is focused on the development of a novel algorithm to recover oxygenation with broadband near-infrared spectroscopy (NIRS). The motivation comes from the often inconsistent study results in the field of oximetry; inspiring an investigation of currently used algorithms, leading to a new algorithm, BRUNO. The step-by-step description of algorithm development, based on an evidence-driven approach, identified areas for potential improvement of oximetry; with a higher focus on data analysis. Measurements in optical phantoms have shown that the practical application of algorithms often leads to different results than predicted in simulations and highlight the need for instrument validation. Given the current efforts in the field to introduce standardised instrument validation protocols, this thesis further proves the urgency. Another academic benefit of this work lies in the fact that BRUNO is currently the first broadband and multi-distance oximetry algorithm used in continuous-wave NIRS, showing that it is possible to recover oxygenation quickly, with high accuracy and at a low cost. The algorithm will be further used in the research group; and as BRUNO is available for free online, it will hopefully inspire other research groups to pursue broadband multi-distance NIRS and implement it in their own systems, further testing the capabilities of the algorithm.

Achieving a reliable measurement of oxygenation with BRUNO will have significant impact in the field of neonatal brain injury monitoring and beyond. Hypoxic-ischaemic encephalopathy treatment is in need of a reliable biomarker of brain health. With the use of an accurate and reliable method for tissue oxygenation assessment, neonates could benefit from earlier diagnosis than with currently used methods (such magnetic resonance spectroscopy), improving patient outcome. Other clinical applications which could benefit from BRUNO oxygenation measurements include monitoring of stroke patients, during cardiac surgery or muscle oxygenation assessment. Having a real-time and low-cost biomarker of tissue oxygenation can guide treatment and prevent negative

outcome, save lives and decrease the significant financial cost to the NHS.

There are many commercially available oximetry systems used in the intensive care for application ranging from paediatric monitoring to management of cardiac surgery. Issues with inter-instrument comparison are well known in the field and hinder the uniform setting of intervention ranges, preventing oximetry from becoming a standard clinical tool. Increasing the interest in instrument validation and algorithm development can help improve the standard of oximetry in clinical care and gain the trust of healthcare professionals, providing them with a reliable and simple biomarker of cerebral health.

Acknowledgements

Firstly, I would like to thank my supervisors: Professor Ilias Tachtsidis, for giving me this unique opportunity, for his genuine encouragement and being always ready to share his vast knowledge; and Dr Gemma Bale, who has not only been an inspiring researcher, but also an understanding, generous and kind friend.

I am grateful to have been part of BitMap, a unique environment fostering excellence in research. I would like to thank Professor Hamid Dehghani, for his management of the consortium, and also his genuine support of all of us, early stage researchers. His and Joshua Deepak Veesa's input was also crucial for the use of NIRFAST in this work, and I thank them for their enthusiasm and availability to answer any of my questions.

My special thanks goes to Dr Subhabrata Mitra, who has been incredibly understanding and keen to help at any time during my research in the hospital. Thank you for your neverending patience and wisdom. I would also like to thank the BORL group at the University of Zurich, particularly Dr Helene Isler, for lending me their phantom and teaching me how to use it.

I have been fortunate to work alongside a motivating team of researchers in the Multimodal Spectroscopy group at UCL. This work would not have been possible without Fred, who has never rejected any of my endless requests for more data or more phantom studies. I would also like to thank Paola, Josh, Nico, Izzy, and Phong, and a special shout-out goes to Luca, who has been my favourite person to spend time with at airports waiting for various delayed flights. I am so happy to have met many lovely friends in the UCL Biomedical Optics Laboratory, the fantastic BORL Buddies, who made every day at work fun, I will always miss our tea breaks.

I must also thank my amazing and beautiful friends from home: Markéta, Michaela and Kristýna, you have yet failed to stop me.

This journey would have been impossible without the unconditional support and love of my parents and my sister Gabriela, who's extraordinary success has always been an inspiration to me. I am so lucky and grateful to have you all. Finally, thank you, Alex, for always being there for me.

Publications resulting from this work

Literature reviews

Kovacsova, Z., Bale, G., & Tachtsidis, I. (2018). Medical Use of NIR monitoring. In Encyclopedia of Biomedical Engineering. Elsevier Inc.

Peer-reviewed journal papers

Under review: **Kovacsova, Z.**, Bale, G., Mitra, S., Lange, F., Tachtsidis, I. (2020) Algorithm for absolute quantification of neonatal cerebral saturation with multi-distance broadband NIRS. Biomedical Optics Express.

Conference proceedings

Kovacsova, Z., Bale, G., Mitra, S., de Roever, I., Meek, J., Robertson, N., & Tachtsidis, I. (2018). Investigation of Confounding Factors in Measuring Tissue Saturation with NIRS Spatially Resolved Spectroscopy. Oxygen Transport to Tissue XL, Advances in Experimental Medicine and Biology, 1072.

Lanka, P., Yang, L., Orive-Miguel, D., Veesa, J. D., Tagliabue, S., Sudakou, A., ... **Kovacsova, Z.**, Tachtsidis, I., ... Pifferi, A. (2019). The BITMAP exercise: a multi-laboratory performance assessment campaign of diffuse optical instrumentation. Proc. SPIE 11074, Diffuse Optical Spectroscopy and Imaging VII, 110741A.

Orive-Miguel, D., Lanka, P., Yang, L., Tagliabue, S., Sudakou, A., Samaei, S., ... **Kovacsova, Z.**, Tachtsidis, I., ... Pifferi, A. (2019). The BitMap dataset: an open dataset on performance assessment of diffuse optics instruments. Proc. SPIE 11074, Diffuse Optical Spectroscopy and Imaging VII, 110741B.

Conference presentations

Oral presentation: Investigation of confounding factors in measuring tissue saturation with NIRS spatially resolved spectroscopy. In 43rd Annual Meeting of the International Society on Oxygen Transport to Tissue (ISOTT 2017). Halle an der Saale, Germany.

Poster: The development of a novel algorithm to measure brain tissue oxygen saturation with broadband NIRS. In 159. seminar of the International Center of Biocybernetics: Optics in Neuromonitoring 2018. Warsaw, Poland.

Poster: A multi-distance broadband approach to measure brain tissue oxygen saturation with NIRS. In 5th biennial meeting of the Society for functional near-infrared spectroscopy (fNIRS 2018). Tokyo, Japan.

Poster: A multi-distance broadband approach to measure brain tissue oxygen saturation with NIRS. In 18th Symposium on Neuromonitoring and Treatment of Neurocritical Patients (PIC 2018). Barcelona, Spain.

Oral presentation: A broadband multi-distance approach to measure tissue oxygen saturation with continuous wave near-infrared spectroscopy. In European Conference on Biomedical Optics (ECBO 2019). Munich, Germany.

Poster: A broadband multi-distance approach to measure brain tissue oxygen saturation with NIRS. In 2nd biennial meeting of the UK Society for functional near-infrared spectroscopy (fNIRS UK 2019). Birmingham, United Kingdom

Prizes

ISOTT **Duane F Bruley Award**, August 2017

fNIRS UK **Best Poster Award runner-up**, September 2019

Contents

List of figures **19**

List of tables **25**

Abbreviations **27**

Nomenclature **29**

1 Introduction **31**

1.1 Introduction to brain oximetry 31

1.2 Introduction to the clinical background 32

1.3 Motivation and aims 34

1.4 Thesis outline 36

1.5 Personal statement 37

2 Oxygen metabolism and neonatal brain injury **39**

2.1 Oxygen metabolism 39

2.1.1 Cellular respiration 39

2.1.2 The respiratory system 40

2.1.3 Gas exchange and transport 41

2.1.4 Oxygen delivery and consumption 44

2.1.5 Oxygen metabolism: summary 46

2.2 The neonatal brain 46

2.2.1 Anatomy of the brain 46

2.2.2 Cerebral circulation 50

2.2.3 Brain development 51

2.3 Hypoxic-ischaemic encephalopathy 54

2.3.1 Progression . . . 55
2.3.2 Diagnosis and treatment . . . 57
2.3.3 Clinical monitoring and imaging of infants with HIE . . . 58
2.3.4 The neonatal brain and HIE: summary . . . 63

3 Cerebral oximetry: optical techniques 65
3.1 Light transport in tissue . . . 65
3.1.1 Absorption . . . 65
3.1.2 Scattering . . . 67
3.1.3 Beer-Lambert law . . . 69
3.2 Differential spectroscopy with CW NIRS . . . 70
3.2.1 Broadband CW NIRS . . . 72
3.3 NIRS instrumentation . . . 72
3.4 Absolute measurements with continuous-wave NIRS . . . 75
3.4.1 Radiative transfer equation and the diffusion equation . . . 75
3.4.2 Broadband spectral analysis with CW NIRS . . . 80
3.4.3 Tissue oxygen saturation measurements . . . 82
3.4.4 Spatially resolved spectroscopy . . . 84
3.4.5 Broadband fitting . . . 85
3.5 Summary . . . 87

4 Cerebral oximetry: application in neonatal care 91
4.1 Cerebral oximetry in the intensive care . . . 91
4.1.1 Establishing cerebral oximetry in the neonatal care . . . 92
4.1.2 Challenges . . . 92
4.2 Cerebral oximetry in hypoxic-ischaemic encephalopathy . . . 102
4.2.1 StO_2 in healthy newborns . . . 102
4.2.2 StO_2 in newborns with HIE . . . 103
4.2.3 Summary . . . 108

5 Instrumentation and data acquisition 115
5.1 Instrumentation . . . 115
5.1.1 CYRIL 1 . . . 115
5.1.2 CYRIL 2 . . . 121

5.1.3 TR NIRS MAESTROS . . . 138
5.2 NIRFAST simulations . . . 138
5.2.1 Mesh . . . 140
5.2.2 Simulated models . . . 142
5.3 Phantom measurements . . . 144
5.3.1 Homogeneous phantom . . . 145
5.3.2 Two-layer phantom . . . 147
5.4 Neonatal studies . . . 148
5.4.1 Monitoring neonates with HIE: session 1 . . . 149
5.4.2 Monitoring neonates with HIE: session 2 . . . 150
5.5 Summary . . . 150

6 Application of spatially resolved spectroscopy in broadband NIRS 153
6.1 Motivation . . . 153
6.2 Confounding factors in SRS . . . 154
6.3 Method . . . 156
6.3.1 Patients . . . 156
6.3.2 Data selection . . . 157
6.3.3 Data analysis . . . 157
6.3.4 Data classification . . . 159
6.3.5 Relationship between HIE severity and StO_2 . . . 159
6.3.6 Statistical analysis . . . 159
6.4 Results . . . 161
6.4.1 StO_2 in neonates with HIE . . . 166
6.5 Discussion . . . 169
6.6 Conclusion . . . 175

7 Measuring tissue saturation with single-distance broadband NIRS 179
7.1 Motivation . . . 179
7.2 Implementation of broadband fitting . . . 180
7.2.1 Coupling of μ_a and μ_s' . . . 182
7.2.2 Wavelength selection . . . 185
7.2.3 Absorption by water . . . 189

7.3 Discussion . . . 192
7.4 Conclusion . . . 194

8 Development of a novel brain oximetry algorithm 195
8.1 Requirements . . . 195
8.2 Proposed algorithm . . . 197
8.3 Data preparation . . . 198
8.3.1 Homogeneous phantom data preparation . . . 198
8.3.2 Two-layer phantom data preparation . . . 203
8.4 Model selection . . . 207
8.4.1 ZBC model . . . 207
8.4.2 EBC model . . . 208
8.4.3 Impact of light source-detector separation . . . 209
8.4.4 Scattering & absorption crosstalk . . . 211
8.4.5 Model performance . . . 213
8.4.6 Model selection: conclusion . . . 218
8.5 Additional algorithm considerations . . . 219
8.5.1 Wavelength selection . . . 220
8.5.2 Chromophore selection . . . 223
8.5.3 Source-detector separation . . . 224
8.6 BRUNO summary . . . 226
8.7 The performance of BRUNO . . . 228
8.7.1 NIRFAST simulations . . . 228
8.7.2 Phantoms . . . 234
8.8 Discussion . . . 239
8.8.1 Model selection . . . 240
8.8.2 Wavelength selection . . . 240
8.8.3 Boundary conditions . . . 241
8.8.4 Fitting process . . . 242
8.8.5 Noise and smoothing . . . 242
8.8.6 Recovery of absorption and scattering . . . 243
8.8.7 Algorithm performance . . . 244
8.9 Conclusion . . . 253

9 Measuring cerebral oxygenation in neonates with HIE 255

9.1 Introduction . . . 255

9.2 Methods . . . 256

9.2.1 Ethical approval . . . 256

9.2.2 Recruited infants . . . 257

9.2.3 Measurement protocol . . . 257

9.2.4 Data analysis . . . 260

9.3 Results . . . 266

9.3.1 StO_2 in baby C . . . 266

9.3.2 Relationship between StO_2 and SpO_2 . . . 274

9.3.3 Repeatability . . . 274

9.3.4 Excluded data . . . 276

9.4 Discussion . . . 279

9.4.1 Data quality . . . 279

9.4.2 Calculating StO_2 with different algorithms . . . 281

9.4.3 StO_2 as a measure of physiology in HIE . . . 283

9.4.4 Repeatability . . . 284

9.5 Conclusion . . . 285

10 Conclusion 287

10.1 Summary . . . 287

10.1.1 Recovering StO_2 with SRS and BF . . . 287

10.1.2 Broadband multidistance oximetry development and performance . . . 288

10.1.3 Measurement of StO_2 in a neonate with HIE . . . 290

10.2 Further work . . . 291

10.2.1 BRUNO performance . . . 291

10.2.2 Validation . . . 292

10.2.3 Real-time measurements . . . 293

10.2.4 Application of BRUNO in adult and muscle measurements . . . 294

10.2.5 Spatially resolved spectroscopy and broadband fitting . . . 295

10.2.6 StO_2 in HIE . . . 295

10.3 Conclusion . . . 296

Bibliography **297**

A Baby Brain Study consent form **323**

List of figures

2.1 Schematic diagram of the gas exchange between pulmonary and systemic blood flow. . . . 41
2.2 The O_2 - haemoglobin dissociation curve. . . . 43
2.3 Relationship between oxygen delivery and oxygen consumption. . . . 45
2.4 Neuron structure 48
2.5 Cerebral cortex lobes. . . . 49
2.6 The cerebral autoregulation curve. . . . 50
2.7 The progression of HIE 56
2.8 Example of EEG recordings in neonates with HIE. . . . 59
2.9 MRI of HIE infants. . . . 61
2.10 Lac/NAA measurement in neonates with normal and poor outcome. . . . 61

3.1 Absorption spectra of main tissue chromophores. . . . 67
3.2 The comparison of a linear and exponential model of scattering. . . . 69
3.3 Schematic of TR, FD and CW NIRS. . . . 74
3.4 Source and image configuration for ZBC and EBC. . . . 79
3.5 Differentiated extinction spectra. . . . 81
3.6 Diagram of a multidistance NIRS approach. . . . 83

4.1 Axial cross-section diagram of a multidistance oximetry measurement. . . . 98
4.2 Published StO_2 measurements in neonates with HIE 106

5.1 Patient end of CYRIL 1. . . . 117
5.2 Input ferrule of the detector fibres. . . . 117
5.3 Patient end fibre arrangement. . . . 118
5.4 3D design of the probe holder. . . . 118
5.5 CYRIL 1 in the NICU. . . . 119

5.6 Setting CCD binning on CYRIL 1 120
5.7 Measurement of reference spectra in a customised poster tube. 121
5.8 CYRIL 2 probe holder. 123
5.9 The CYRIL 2 setup. 123
5.10 Spectral lines of argon. 125
5.11 Argon spectrum measured with CYRIL. 125
5.12 CCD background noise collected in pixel (250, 250) over 1000 acquisitions. . . . 128
5.13 The pixel-wise SNR across the whole CYRIL CCD. 129
5.14 Spectra collected with Detector 4 at 30 mm separation with one individual pixel strip and when 20 strips are binned. 130
5.15 Spectra collected with the CYRIL 1 and CYRIL 2 setups at binning width = 16 with detector 1. 130
5.16 The data collection window of the CYRIL 2 VI. 132
5.17 CYRIL 2 VI spectra display. 132
5.18 CYRIL 2 VI concentration changes display. 133
5.19 Example intensity data collected with CYRIL retrospectively viewed in the CYRIL 2 VI. 133
5.20 Detected counts against y-axis pixels for all 8 detectors when each detector illuminated individually. 134
5.21 Flowchart summarising the process of CYRIL 2 data collection with the new VI. 135
5.22 Reference spectra collected in a dark room and a customised poster tube. 137
5.23 The MAESTROS system 139
5.24 Example of neonatal head meshes used in computational simulations. 141
5.25 Detector and light source setup on a 40-week neonatal head mesh. 142
5.26 Spectra simulated with NIRFAST in models A, B, C, D. 143
5.27 Schematic of the homogeneous phantom measurement setup. 146
5.28 Two-layer phantom with sensors and NIRS optodes attached. 148

6.1 The increase of attenuation over distance. 156
6.2 Data selection for the SRS investigation. 157
6.3 Steps in SRS data analysis. 160
6.4 StO_2 acquired using 7 different approaches in a measurement which had "positive" and "regular" attenuation slopes. 161

6.5 Correlation map of different SRS approaches. 163
6.6 Measurement with a "regular", "positive" slope. 165
6.7 Measurement with a "irregular", "positive" slope. 165
6.8 Measurement with a "irregular", "negative" slope. 165
6.9 StO_2 recovered in severe and moderate HIE with different SRS approaches. . . . 168
6.10 Change of StO_2 in HIE neonates during the first days of life. 169
6.11 Change of StO_2 in HIE neonates during the first days of life grouped by HIE severity. 169

7.1 BF applied to a reflectance measurement in a liquid phantom. 180
7.2 Flowchart describing the process of recovering StO_2 with BF. 181
7.3 Examples of μ_s' used when generating models of reflectance used for the recovery of μ_a with BF. 183
7.4 c_{HHb}, c_{HbO_2} and StO_2 recovered with BF while a and b were fixed at constant values. 184
7.5 Sum of residuals when recovering StO_2 with BF when μ_s' is fixed. 185
7.6 Spectral derivatives of HHb, HbO_2 and H_2O extinction spectra. 186
7.7 The 1st and 2nd spectral derivatives of $\frac{\partial R}{\partial param}$. 187
7.8 Scattering and absorption recovered with BF by fitting in 1 or 3 steps compared to the truth. 190
7.9 The effect of WF set to a specific value on the recovery of c_{HHb}, c_{HbO_2}, a, b and StO_2 with BF. 190
7.10 The recovered μ_a and μ_s' retrieved with BF when WF was set to different values. 191
7.11 The recovered μ_{eff} retrieved with BF when WF was set to different values. . . . 191

8.1 The effect of CCD bin width on the quality of a spectrum collected at 30 mm separation, exposure 1 s. 199
8.2 The change of absorption throughout the oxygenation-deoxygenation cycles in a homogeneous phantom. 200
8.3 Reflectance and attenuation collected at 20 mm SDS during complete oxygenation and deoxygenation of the homogeneous phantom. 201
8.4 The oxygenation of the homogeneous phantom measured with the TR system MAESTROS compared to CYRIL counts. 202
8.5 The first and second spectral derivatives of reflectance in the homogeneous phantom. 202

8.6 The attenuation slope and the derivative of the attenuation slope with respect to wavelength in the homogeneous phantom. 203
8.7 Spectra collected in a two-layer phantom at 15 and 30 mm SDS during phantom oxygenation and deoxygenation. 204
8.8 Attenuation collected at 15 and 30 mm SDS during complete oxygenation and deoxygenation of the two-layer phantom. 204
8.9 Reflectance collected at 15 and 30 mm SDS during complete oxygenation and deoxygenation of the two-layer phantom. 205
8.10 The oxygenation of the two-layer phantom measured with the TR system MAESTROS compared to CYRIL counts. 205
8.11 The attenuation slope and the derivative of the attenuation slope with respect to wavelength in the two-layer phantom. 206
8.12 The first and second spectral derivatives of reflectance in the two-layer phantom. 206
8.13 Comparison of the slope of attenuation obtained with models utilising EBC or ZBC. 210
8.14 StO_2 recovered with BRUNO using $\frac{\partial A_{ZBC}}{\partial \rho}$ or $\frac{\partial A_{EBC,F}}{\partial \rho}$ while a and b were fixed at constant values. 212
8.15 The comparison of different light transport models when applied in BRUNO to $\frac{\partial A}{\partial \rho}$ collected the homogeneous phantom. 215
8.16 StO_2 in the homogeneous phantom measured with MAESTROS compared to BRUNO analysis with 3 different $\frac{\partial A}{\partial \rho}$ models. 216
8.17 StO_2 in the two-layer phantom measured with MAESTROS compared to BRUNO analysis with 3 different $\frac{\partial A}{\partial \rho}$ models. 217
8.18 The comparison of μ_a and μ_s' recovered with $\frac{\partial A_{ZBC}}{\partial \rho}$ and $\frac{\partial A_{EBC,F}}{\partial \rho}$ at the same point. 218
8.19 BRUNO with $\frac{\partial A_{ZBC}}{\partial \rho}$ and $\frac{\partial A_{EBC,F}}{\partial \rho}$ before and during a measurement artefact. 219
8.20 Differentiating $\frac{\partial^2 A}{\partial \rho \partial \lambda}$ with respect to each parameter. 221
8.21 The comparison of fitting BRUNO in one or two steps to StO_2 measured with MAESTROS. 223
8.22 The effect of adding 5 μM oxCCO to $\frac{\partial A^2}{\partial \rho \lambda}$. 225
8.23 Attenuation slope $\frac{\partial A}{\partial \rho}$ measured across 4, 3, or 2 detectors in the phantoms. 225
8.24 The process of calculating StO_2 with BRUNO. 227
8.25 StO_2 recovered in 5 different models, n = 50. 230
8.26 Recovering StO_2 from model E, homogeneous, during a GM deoxygenation. . . 231

8.27 Recovering StO_2 from model E, two-layer, during a GM deoxygenation. 231
8.28 The absolute error of the recovered StO_2 with 4 different algorithms in model E. . 232
8.29 Recovering StO_2 from model F during Gm and ECT oxygenation changes. 233
8.30 Scatter plot of the true StO_2 in brain in model F compared to measured with CYRIL and analysed with BRUNO, BF, SRS and BB SRS. 234
8.31 Recovering StO_2 collected in phantom measurements with BRUNO, BF, SRS and BB SRS compared to MAESTROS. 235
8.32 Scatter plot of StO_2 in the homogeneous phantom measured with MAESTROS compared to measured with CYRIL and analysed with BRUNO, BF, SRS and BB SRS. 236
8.33 Scatter plot of StO_2 in the two-layer phantom measured with MAESTROS compared to measured with CYRIL and analysed with BRUNO, BF, SRS and BB SRS. 237
8.34 Recovering StO_2 in the range 40–90 % collected in phantom measurements with BRUNO, BF, SRS and BB SRS. 238
8.35 The error of recovering StO_2 in a homogeneous and two-layer phantom with different StO_2 recovery algorithms. 239
8.36 The comparison of $\frac{\partial A^2}{\partial \rho \lambda}$ collected in a CYRIL 1 and CYRIL 2 setup. 243
8.37 The absolute error when recovering StO_2 in model F with different scattering constant h. 246
8.38 StO_2 in phantom measurements recovered with MAESTROS, BRUNO and BF at two different SDS, 15 and 30 mm. 249
8.39 StO_2 recovered with BF in the two-layer phantom and the corresponding c_{HHb} and c_{HbO_2}. 250
8.40 StO_2 (normalised) measured in the two-layer phantom with MAESTROS, BRUNO and SRS. 251

9.1 Example of a good BRUNO fit on a high-quality spectrum collected during a deoxygenation of the homogeneous phantom. 260
9.2 Example of a good and a bad BRUNO fit on data collected in baby C and the corresponding residuals of the normalised BRUNO fit. 262
9.3 Example of a normalised BRUNO fit with small residuals but poor data quality. Data were collected in baby C with detectors 7–8. 263

9.4 Flowchart describing the process of assessing the quality of a BRUNO fit through the calculation of a score. 264
9.5 Score calculated for a measurement in baby C with the corresponding StO_2. . . . 265
9.6 StO_2 during two deoxygenation events in baby C on day 2 and day 3 of life. . . . 268
9.7 StO_2 in baby C on day 2 and day 3 of life. 269
9.8 The correlation between StO_2 measured with BRUNO vs. with BF/SRS/BB SRS on day 2 and day 3 collected in baby C 270
9.9 Bland-Altman analysis of StO_2 measured with BRUNO vs. with BF/SRS/BB SRS on day 2 and day 3 collected in baby C 271
9.10 The distribution of StO_2 grouped by day of life for the 4 different algorithms. . . 272
9.11 SpO_2 measured with pulse oximetry and StO_2 measured with BRUNO on days 2 and 3. 273
9.12 StO_2 measured with 4 different algorithms during 5 measurements during the precision study in baby C. 275
9.13 Examples of intensity spectra, $\frac{\partial A}{\partial \rho}$ and $\frac{\partial^2 A}{\partial \rho \partial \lambda}$ with good or poor coupling. 277
9.14 $\frac{\partial A}{\partial \rho}$ and $\frac{\partial^2 A}{\partial \rho \partial \lambda}$ collected on day 3 on the RS in baby C. 278
9.15 $\frac{\partial^2 R}{\partial \lambda^2}$ collected on day 3 on in baby C with detectors 1, 4, 5 and 8. 279

List of tables

3.1 Methods for the measurement of StO_2 with CW NIRS 88

4.1 Studies measuring StO_2 in brain injured neonates. 109

5.1 CYRIL 2 wavelength resolution 126
5.2 Differences between the original VI used in CYRIL 1 and a new version developed for the use in CYRIL 2. 136
5.3 The optical properties set in five different models of the neonatal head used for the generation of broadband spectra in NIRFAST. 143
5.4 The optical properties used in models E and F, simulating layer desaturations. . . 144
5.5 Liquid phantom measurement protocol. 146

6.1 h calculated from published μ_s' measurements. 156
6.2 StO_2 values obtained for each approach and sub-approach. 162
6.3 The regularity and positivity of the slope calculated across different separations. . 166
6.4 Validity of StO_2 and slope regularity/positivity. 167
6.5 Mean StO_2 in HIE grouped by severity. 167
6.6 Mean StO_2 in HIE grouped by day of life. 168

7.1 Boundary conditions for the analysis of model B with BF. 189
7.2 Fitting spectra from model B with BF either across the whole spectrum at once or with first fitting for WF, then c_{HHb} and other parameters. 189

8.1 Comparison of SRS and BF 196
8.2 Boundary conditions for analysing phantom data with BRUNO. 207
8.3 Mean StO_2 recovered from spectra acquired in model E with $\frac{\partial A_{ZBC}}{\partial \rho}$ and $\frac{\partial A_{EBC}}{\partial \rho}$. . . 214
8.4 Fitting spectra from model B with BRUNO either across the whole spectrum at once or with first fitting for WF. 223

8.5 Boundary conditions for NIRFAST spectra analysis with BRUNO and BF. 229
8.6 The duration of recovering StO_2 collected in phantom measurements with BRUNO, BF, SRS and BB SRS. 236
8.7 Comparison of SRS, BF and BRUNO 252

9.1 Clinical details of subjects monitored during the second session of the Baby Brain Study at UCLH. 257
9.2 Boundary conditions for analysing baby data with BRUNO. 265
9.3 The mean scores of long measurements in all subjects. 266
9.4 Spearman's rho ρ_s measuring the correlation of StO_2 recovered with 4 different algorithms. 267
9.5 Mean StO_2 on day 2 and day 3 measured with all algorithms. 272
9.6 Spearman's correlation coefficients ρ_s for SpO_2 vs. StO_2 measured with all 4 algorithms on day 2 and 3 in baby C, LS, 15–30 mm SDS. 274
9.7 The mean StO_2 for each block, the within-measurement standard deviation σ_{block} and between-measurement standard deviation σ_{intra} in the repeatability measurement in baby C. 275

Abbreviations

aEEG	amplitude integrated electroencephalography
ATP	adenosine triphosphate
BB SRS	broadband spatially resolved spectroscopy
BF	broadband fitting
bNIRS	broadband near-infrared spectroscopy
BRUNO	broadband multidistance oximetry
CBF	cerebral blood flow
CCD	charge-coupled device
CCO	cytochrome c oxidase
CO_2	carbon dioxide
CSF	cerebrospinal fluid
CT	computed tomography
CW	continuous wave
DCS	diffuse correlation spectroscopy
EBC	extrapolated boundary conditions
ECT	extracerebral tissue
EEG	electroencephalography
EPO	erythropoietin
$FADH_2$	reduced flavine adenine dinucleotide
FD	frequency domain
FEM	finite element method
FWHM	full width at half maximum
GA	gestational age

GM	grey matter
GW	gestational week
H_2O	water
HbO_2	oxyhaemoglobin
HHb	deoxyhaemoglobin
HIE	hypoxic-ischaemic encephalopathy
ICG	indocyanine green
Lac/NNA	lactate and N-acetylaspartate ratio
LED	light-emitting diode
LS	left side
MBBL	modified Beer-Lambert law
MMC	Monte Carlo
MRS	magnetic resonance spectroscopy
NADH	reduced nicotinamide adenine dinucleotide
NE	neonatal encephalopathy
NICU	neonatal intensive care unit
NIR	near-infrared
NIRS	near-infrared spectroscopy
O_2	oxygen
oxCCO	oxidised cytochrome c oxidase
RS	right side
RTE	radiative transfer equation
SDS	light source-detector separation
SNR	signal-to-noise ratio
SRS	spatially resolved spectroscopy
TH	therapeutic hypothermia
THb	total haemoglobin
TOI	tissue oxygenation index
TR	time resolved
VI	virtual instrument
WM	white matter
ZBC	zero boundary conditions

Nomenclature

a	scattering amplitude
A	attenuation
b	scattering power
c	concentration
$CMRO_2$	cerebral metabolic rate of oxygen
d	distance
D	diffusion coefficient
DO_2	oxygen delivery
DPF	differential pathlength factor
$FTOE$	fractional tissue oxygen extraction
g	anisotropy factor
h	normalised slope of μ_s' against wavelength
I	intensity
$\vec{J}$	current density
k	extinction coefficient
k_{SRS}	unknown scaling factor
k_{Hb}	oxygen binding capacity of haemoglobin
L	radiance
n	refractive index
O_a^{art}	arterial oxygen content
OER	oxygen extraction ratio
P	partial pressure
R	reflectance

R^2	coefficient of determination
SaO_2	arterial oxygen saturation
SjO_2	jugular bulb oxygen saturation
SO_2	oxygen saturation
SpO_2	pulse oximetry measure of arterial oxygen saturation
StO_2	tissue oxygen saturation
SvO_2	venous oxygen saturation
t	time
VO_2	oxygen consumption
WF	water fraction
α	specific absorption coefficient
ε	specific extinction coefficient
λ	wavelength
μ_{eff}	effective attenuation coefficient
μ_a	absorption coefficient
μ_s	scattering coefficient
μ_s'	transport scattering coefficient
μ_t	total scattering coefficient
Φ	fluence rate
ρ	detector spacing
ρ_s	Spearman's Rho
σ	standard deviation

Chapter 1

Introduction

The first chapter of this thesis introduces the motivation to this PhD project. A brief summary to the technical and clinical background is followed by the individual aims and objectives of the work. The last sections of this chapter outline the subsequent chapters of the thesis and my contribution to the project.

1.1 Introduction to brain oximetry

In 1977, inspired by the transparency of biological tissue in the near-infrared (NIR) region, Frans Jöbsis developed a novel optical monitoring technique based on the interaction of light with haemoglobin, the oxygen-carrier in blood. While light is absorbed strongly by haemoglobin and other chromophores in the visible wavelength range; the interaction weakens in the NIR, letting light travel up to a few centimeters deep in tissue. Additionally, the absorption spectrum of haemoglobin changes depending on whether the molecule is bound to oxygen or not. Using near-infrared spectroscopy (NIRS), Jöbsis could quantify the difference in absorption properties of oxygenated haemoglobin HbO_2 and deoxygenated haemoglobin HHb and link it to the concentration changes of these substances in tissue, obtaining a non-invasive measure of the tissue oxygenation state [1].

Oxygenation monitoring with NIRS is a relatively simple and non-expensive technique. In a continuous-wave setting, a light source continuously illuminates the tissue underneath and a detector placed on the surface measures the light that travelled through the tissue. The optical properties of the tissue are quantified from the recovered spectrum and its changes over time. Most NIRS systems operate on a few wavelengths selected from the NIR range; broadband NIRS (bNIRS) utilises a whole broadband spectrum (several tens to hundreds nm of wavelengths) to get a more thorough assessment of the optical properties of a medium.

The main advantage of NIRS lies in its ability to detect local tissue hypoxia non-invasively

and in real time. The clinical potential of tissue oxygenation monitoring with NIRS in the neonatal intensive care unit was demonstrated in 1985 by Jane Brazy and collegues, who measured cerebral oxygenation in preterm infants [2]. This was followed by a collaboration between University College London (UCL) and University College London Hospital (UCLH) in 1988, demonstrating the use of NIRS to derive blood flow in preterm infants [3]. Since then, the field has grown and NIRS is becoming a valuable tool in the adult and neonatal clinical care; being used for monitoring during cardiovascular surgery or during the treatment of traumatic brain injury patients [4].

One NIRS measured parameter with a notable clinical interest is tissue oxygen saturation StO_2. Defined as the ratio of the concentration of HbO_2 (c_{HbO_2}) over the sum of total haemoglobin concentration, the sum of the concentrations of HbO_2 and HHb (c_{HHb}), $c_{THb} = c_{HbO_2} + c_{HHb}$, Eq. (1.1), the measurement of StO_2, oximetry, reflects the relationship between cerebral oxygen supply and demand.

$$StO_2 = \frac{c_{HbO_2}}{c_{THb}} \times 100\%. \tag{1.1}$$

A significant advantage of StO_2 measurements is the opportunity to quantify absolute oxygenation levels, in contrast to standard NIRS measurements tracking only oxygenation changes. Driven by the desire for a real-time, user-friendly and non-invasive tool to measure oxygenation levels in tissue and hence obtaining an immediate assessment of tissue haemodynamics, many research and commercial NIRS systems to measure cerebral StO_2 have been developed.

While the clinical relevance of measuring StO_2 in the clinic has been demonstrated in various settings, such as preterm cerebral hypoxia management [5] or traumatic brain injury [6], a lack of consistent study results and proven clinical advantages is hindering brain oximetry from becoming a standard tool in the intensive care unit [7]. This lack of clinical evidence is caused by various issues which are still waiting to be solved, such as the difficulty in comparing readings from different NIRS instruments [8], extracranial signal contamination [9], lack of validation protocols [10], insufficient sensitivity or precision [11, 12]. Improving the measurement of StO_2 and highlighting its clinical potential requires improvements in the engineering of instruments, data collection and analysis, as well as performing further clinical studies evaluating the prognostic value of the parameter.

1.2 Introduction to the clinical background

Adequate oxygen supply to tissue cells is crucial for sustaining aerobic respiration; a series of chemical reactions responsible for the maintenance of cellular metabolic processes. Oxygen

reaches tissue from the blood stream, where it is carried bound to haemoglobin, a molecule found in red blood cells. While the supply of oxygen to tissue exceeds oxygen consumption in normal conditions; inadequate oxygen supply can lead to hypoxia, tissue oxygen deprivation. Although processes which can sustain cellular metabolism during hypoxia to a certain degree are present, such as anaerobic metabolism, prolonged hypoxia can cause tissue damage. The brain is susceptible to hypoxic damage as it has very high metabolic demands.

The neonatal brain is especially vulnerable during transition, when a lack of oxygen supply can occur. Severe hypoxia during delivery can lead to hypoxic-ischaemic encephalopathy (HIE); a neurological disorder occurring in about 1.5 per 1000 live births [13]. The progression of the injury depends on the severity of the hypoxic insult, mildly injured patients can recover without any complications; more severe cases of injury can result in disability or death. Injury assessment and treatment at the neonatal intensive care unit (NICU) relies on brain monitoring. Currently, the most reliable injury biomarker in infants with HIE is measured with magnetic resonance spectroscopy (MRS). However, it can only be used after several days following injury. To fill the information gap within the first few days, electroencephalography (EEG) is used as a predictor of outcome during the first hours of life, with current research focused on improving its prediction ability during later days of life [14]. A disadvantage of EEG is the need for trained personnel to apply probes and interpret results. There is hence an urgent need to establish additional biomarkers which would help with injury management. These should be measured non-invasively on the cotside, operated by non-specialist personnel and provide real-time information on brain health with a prognostic value.

There is an effort to fill this need for a new monitor with NIRS. HIE is caused by insufficient oxygen delivery and can be accompanied by hyperoxygenation, increased perfusion and a lack of cerebral autoregulation [15]. NIRS could shine light into HIE treatment by detecting such pathophysiologies, whether by identifying differences in StO_2 between injured and healthy infants, severe or moderate cases, or helping clinicians understand which part of the brain has been injured. In fact, it has been shown that monitoring metabolism with NIRS during treatment can help assess injury severity earlier than with MRS [16], and many other studies have measured tissue oxygenation StO_2 in infants with HIE. It is, however, impossible to draw firm conclusions on the benefits of oximetry in HIE treatment due to the different results. While some studies report increased oxygenation during HIE [17], others report a decrease [18] or no difference between HIE injury and the healthy control group [19]. Improving the reliability of StO_2 measurements

could help unify these results and enable the clinicians a deeper understanding of the underlying physiology of HIE.

1.3 Motivation and aims

The Baby Brain Study is a research collaboration between the Institute of Women's Health at UCLH and UCL, aimed at evaluating the relationship between magnetic resonance measured biomarkers and outcome of neonates with acute brain injury. Additionally, it is also focused on assessing the use of NIRS monitoring in neonatal brain injury, particularly on monitoring cytochrome c oxidase (CCO), a metabolic enzyme participating in aerobic respiration, and its predictive value. The measurement of CCO concentrations with NIRS has been performed by the Multimodal Spectroscopy group from the Biomedical Optics Research Laboratory based at UCL. Led by Professor Ilias Tachtsidis, the group's aim is to develop optical biomarkers of physiology to improve our understanding of brain health. The potential use of CCO as an indicator of brain health has been demonstrated by Dr Gemma Bale, who linked neonatal brain injury severity to CCO concentration changes measured with CYRIL, an in-house developed continuous-wave broadband NIRS system designed specifically for the use in the NICU [16, 20]. To further investigate NIRS measured brain injury biomarkers, the focus moved to tissue oxygen saturation StO_2 for its ability to assess brain physiology immediately. The question was whether the disparity found in publications reporting StO_2 measured in neonates with HIE was caused by the complex physiological background of HIE varying between subjects, or by the measurement of StO_2 itself, influenced by different engineering setups and data analysis algorithms.

The opportunity to start the investigation of the application of tissue oximetry in HIE arose through participation in the "Brain injury and trauma monitoring using advanced photonics" (BitMap) project, a Marie Skłodowska-Curie Innovative Training Network [21]. Comprising of a collaboration between 10 European research institutions, the aim of the project was to develop a suite of standardised non-invasive devices for brain monitoring in neurocritical care, with a focus on traumatic brain injury and neonatal hypoxia. Working as an Early Stage Researcher, my task in BitMap was to implement an accurate measurement of StO_2 in CYRIL through the development of a novel StO_2 measurement algorithm and to investigate the application of tissue oximetry in the detection of hypoxia in neonates with HIE. The use of an in-house developed broadband NIRS system in this application was beneficial as it not only gave the opportunity to use a broadband NIRS system and recover additional information about the optical properties of the tissue but also ensured transparency of data collection without any instrument calibration assumptions, as present

in commercial NIRS systems [22], and update the hardware as needed.

The work described in this thesis is focused on investigating the hypothesis that it is possible to improve the accuracy of continuous-wave NIRS StO_2 measurements through the combination of recent engineering solutions with innovative data analysis algorithms, the key focus is on bNIRS and the application in neonatal care. The main aims of this PhD are:

- To develop a novel algorithm to calculate StO_2 from continuous-wave, multidistance bNIRS measurements. The objective is to obtain a measure of StO_2 sensitive to cerebral tissue, track oxygenation with high accuracy, dynamic range and precision.

- To evaluate the performance of the algorithm with the use of data obtained in computational simulations and phantom measurements; and to compare it to other, currently used StO_2 calculation algorithms.

- To demonstrate the application of the algorithm to data collected in infants diagnosed with HIE and assess the relationship between StO_2 and HIE severity.

These aims were achieved through the completion of the following objectives:

- The CYRIL system was updated to ensure the collection of high quality data. These updates included the change of the way the computer collects data from CYRIL's light detector, the creation of a new user interface and hardware updates.

- NIRS broadband data for StO_2 algorithm performance assessment was collected through two means; computational simulations of NIRS spectra using NIRFAST (a software toolbox for multimodal optical imaging [23, 24]) and performing measurements on tissue simulating optical phantoms.

- Currently used methods of measuring StO_2 were used to obtain StO_2 from broadband NIRS data. Two different data analysis algorithms, spatially resolved spectroscopy (SRS) [25] and broadband fitting (BF) [26], were investigated and the influence of algorithm on the recovered StO_2 was evaluated.

- The strengths of SRS and BF were used as a basis for the development of the new data analysis algorithm, broadband multidistance oximetry (BRUNO). The performance of the novel algorithm was compared to SRS and BF.

- CYRIL was used in a clinical setting at the NICU. Infants with HIE were monitored on the cotside with CYRIL and StO_2 was obtained with different calculation algorithms. The influence of data analysis algorithms on the prognostic value of in oximetry in HIE was explored.

1.4 Thesis outline

The work in this thesis is divided into ten chapters. The next three chapters cover the background to this work. Chapter 2 is focused on respiration, the anatomy of the brain, neonatal brain development and the causes, progression and management of HIE.

Chapter 3 introduces the field of NIRS. The means of describing optical properties of tissue are listed, with a summary of light transport in tissue. These are followed by a short section on NIRS instrumentation and an outline of the most important data analysis algorithms, including those for absolute measurements.

Chapter 4 provides a deeper understanding of the application of absolute measurements, specifically oximetry, with continuous-wave NIRS. The need for a measure of cerebral oxygenation is described, but also the issues surrounding the measurement of cerebral oxygenation. The second half of the chapter is a review of cerebral oximetry measurements in neonates with HIE.

The next 5 chapters describe the experimental part of this PhD project. Chapter 5 reports the methods; the instrumentation and the collection of the majority of data used in this work, from optical phantom measurements and computational simulations, to monitoring in the NICU.

Chapters 6 and 7 are each an investigation of the application of already known oximetry algorithms, spatially resolved spectroscopy and broadband fitting, respectively. The exploration of their application points out aspects which are desirable in the measurement of oxygenation.

The key findings of the previous two chapters led to the development of a hybrid oximetry algorithm in Chapter 8. The first sections describe the design of the algorithm; its performance is compared to other oximetry algorithms in the second half of the chapter.

The application of BRUNO to data collected in neonates diagnosed with HIE is in Chapter 9; outlining the methods of the data collection, the data processing and the results.

Chapter 10 is the final chapter, providing a summary of the work done and the key findings. Suggestions for further work on BRUNO are also outlined.

1.5 Personal statement

The presented work is a multidisciplinary project covering different areas from the theoretical development and investigation of data analysis to measurements in the NICU. It can be divided into multiple parts:

1. Theoretical work on the investigation of current StO_2 measurement algorithms and the development of a novel method.

2. NIRFAST simulations and collection of dynamic optical phantom data.

3. Collection and analysis of NIRS data in the NICU.

The first, theoretical, part of the work was done by myself, with the helpful guidance of my supervisors Professor Ilias Tachtsidis and Dr Gemma Bale, and other colleagues from the Multimodal Spectroscopy group.

The second part comprising of data collection was done mostly by me. I created a new LabVIEW environment for CYRIL for data collection and storage; I was responsible for the upkeep and maintenance of the system. I used NIRFAST to simulate broadband NIRS spectral data and used CYRIL to collect NIRS data in optical phantoms. Dr Frédéric Lange developed the homogeneous optical phantom and helped with all phantom measurements; setting up the phantom and operating the time-resolved system MAESTROS. Dr Lange also provided me with analysed data from MAESTROS. The two-layer phantom was designed at and borrowed from the Biomedical Optics Laboratory at the University of Zurich. The measurements with the two-layer phantom were performed in UCL with the help of Dr Lange, who was operating the MAESTROS system and analysing MAESTROS data. The CYRIL system operation and data analysis was performed by me.

The collection of all NICU data was in collaboration with the team at the NICU at UCLH. Some of the data used in this work was collected by Dr Gemma Bale during her work on CCO measurements. The measurements on neonates treated in the NICU were conducted with Dr Subhabrata Mitra, a consultant neonatologist at the NICU. He had experience with using CYRIL in the NICU environment and assisted me with the preparation the system and protocols, approached the parents of potential study subjects and collected consent, and helped me set up the measurements afterwards. I was responsible for the quality of the collected optical data, data analysis and data storage. Dr Mitra placed the optodes on the patients and also removed them at the end of the

measurement. If he was not present, another member of the clinical team (nurses working with the patient) removed the optodes.

Chapter 2

Oxygen metabolism and neonatal brain injury

The clinical motivation of this work is to monitor oxygenation in the injured neonatal brain. The beginning of this chapter is focused on explaining the role of oxygen in the healthy brain, covering respiration, brain anatomy and neonatal brain development. Once the role of oxygen in the functioning of the brain is outlined, the next sections move on to pathological conditions, focusing on neonatal brain injury caused by a lack of oxygen. In the later sections, the clinical management of neonatal brain injury is described.

2.1 Oxygen metabolism

Oxygen (O_2) is crucial for the function of aerobic organisms; cells in biological tissue require it to synthesise useable energy, adenosine triphosphate (ATP). ATP stores energy in the form of bonds between phosphate groups, which can be broken up to release energy; it is the main fuel of cellular metabolic processes. ATP synthesis from oxygen is called aerobic respiration, taking place within tissue cells. The net turnover of ATP is measured by metabolic rate, which determines overall oxygen consumption - a person at rest consumes about 250 ml of O_2 per minute [27].

2.1.1 Cellular respiration

Cellular respiration is a metabolic pathway in which cells produce ATP by breaking down biochemical energy from nutrients. There are two types of respiration, aerobic in the presence of oxygen, and anaerobic, which does not require oxygen. In normal conditions, cells in the human body use aerobic respiration. Some cells, such as in skeletal muscle, can utilise anaerobic respiration during high-intensity exercise when oxygen delivery is not sufficient [28]. Other cells can switch to anaerobic metabolism if there is not enough oxygen present.

Aerobic respiration breaks down glucose into carbon dioxide (CO_2) and water (H_2O) and produces ATP. The whole metabolic process consists of 4 main pathways. The first step occurs in

the cellular cytosol and is called glycolysis, during which glucose breaks down into pyruvate and generates ATP. Another byproduct of this process is reduced nicotinamide adenine dinucleotide, NADH. The second stage takes place within the mitochondrial matrix where pyruvate oxidation turns pyruvate into acetyl-CoA, which is oxidised in the third stage of the process, the Krebs cycle. Reduced flavine adenine dinucleotide ($FADH_2$) and more ATP is generated in this process. The last stage, oxidative phoshorylation, is the most ATP efficient. Occuring in the cristae of mitochondria, electrons released from NADH and $FADH_2$ join the electron transport chain. Electrons are carried across the mitochondrial inner membrane from electron donors to electron acceptors via redox reactions. Coupled to a transfer of protons, a proton gradient is created across the boundary. The enzyme ATP synthase transports the protons back into the matrix, generating ATP. The whole process of aerobic respiration yields 30–32 ATP molecules.

Anaerobic respiration occurs when there is not enough oxygen present. Oxygen cannot accept electrons in the mitochondrial electron transport chain and NADH instead uses its electrons and reoxidises by reducing pyruvate to lactate. The ATP yield of this metabolic pathway is much less than in aerobic respiration, only 2 ATP molecules are produced, and is followed by a build up of lactate in tissue.

2.1.2 The respiratory system

The respiratory system is responsible for the exchange of O_2 and CO_2, the waste product of cellular respiration, between the body and the environment during the breathing cycle. The system consists of the conducting zone, which connects the lungs to the external environment, and the respiratory zone, where gas exchange occurs in alveoli.

The conducting zone includes the nose, nasophagus, larynx, trachea, bronchi, bronchioles and terminal bronchioles. These are responsible for the conduction of air into the lungs and also humidify, filter and warm it. The walls of the airways consist of smooth muscle and can change their diameter in response to the autonomic nervous system; these dilations/relaxations result in airflow fluctuations. The respiratory zone comprises of respiratory bronchioles, alveolar ducts and alveolal sacs lined with alveoli. These pouchlike evaginations of the walls of these structures are responsible for exchanging O_2 for CO_2 between the air and blood. It is a rapid process, the alveolic walls are very thin and lined with capillaries. Gases are transferred between capillary blood and alveolar gas via diffusion. Each lung has approximately 300 million alveoli with a diameter of approximately 200 μm [27].

2.1.3 Gas exchange and transport

Gas exchange refers to the diffusion of O_2 and CO_2 between the lungs and other tissue. Once oxygen enters blood in the pulmonary capillaries, the oxygenated blood becomes systemic blood. It flows to the left ventricle via pulmonary veins and exits the heart via the aorta, from where it eventually reaches systemic capillaries. Systemic capillaries provide other tissue with O_2 from the bloodstream. O_2 diffuses through the capillary wall to the cells; at the same time, CO_2 enters the blood flow. Deoxygenated venous blood is carried through the superior and inferior venae cavae to the right side of the heart, where it is pumped into pulmonary arteries which divide into arterioles and the pulmonary capillaries.

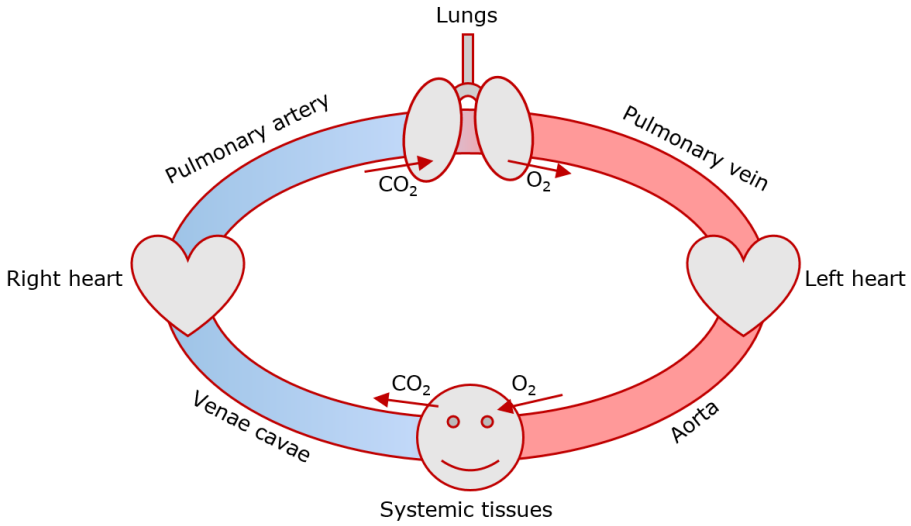

Figure 2.1: Schematic diagram of the gas exchange between pulmonary and systemic blood flow. Right heart = right atrium and ventricle, left heart = left atrium and ventricle.

The diffusion processes between the blood stream and the surrounding environment obey fundamental gas laws:

- Dalton's law of partial pressure helps understand the frequently used term partial pressure of a gas. The partial pressure of a gas in a mixture of gases is the pressure that gas would exert if it occupied the total volume of the mixture at the same temperature; Dalton's law states that the sum of partial pressures of all gases in a mixture equals the total pressure [27]. The partial pressure of oxygen P_{O_2} inside the lungs is hence related to atmospheric pressure P_{atm}, the partial pressure of water P_{H_2O} and carbon dioxide P_{CO_2} and the fraction of inspired oxygen and the respiratory quotient (the ratio of eliminated CO_2 and consumed O_2). P_{O_2} is around 100 mmHg in the alveoli [29, 30].

- Henry's law for concentrations of dissolved gases relates the partial pressure of a gas in equilibrium with a liquid phase (e.g. blood) to the concentration of the gas in the liquid phase. At equilibrium, the partial pressure of a gas in the liquid phase is equal to the partial pressure in gas phase. Consequently, the higher the solubility of a gas, the higher its concentration in a solution. The difference in partial pressures of oxygen P_{O_2} drives the diffusion from the alveoli to the capillaries based on Henry's law.

- Fick's law on the diffusion of gases states that the volume of gas transferred per unit time is directly proportional to the driving force, the diffusion coefficient of the gas, the surface area and inversely proportional to the membrane barrier thickness. The driving force is the partial pressure difference of the gas across the membrane, not the difference in concentrations.

O_2 and CO_2 are carried in blood in a dissolved, bound or chemically modified form; the total gas concentration in it is the sum of all these forms. The majority of O_2 in blood is bound to haemoglobin, most CO_2 is carried in a chemically modified version, as bicarbonate [27].

Only dissolved gas molecules contribute to the partial pressure, not bound or chemically modified (e.g. oxygen bound to haemoglobin). Only 2% of O_2 is found in the diffused state and is not sufficient to meet the metabolic needs of the body. The other 98% of O_2 is reversibly bound to haemoglobin inside red blood cells. This molecule is a globular protein whose four haem sites can each bind one oxygen molecule; each gram of haemoglobin can bind up to 1.34 ml of O_2 [31]. Oxygenated haemoglobin is called oxyhaemoglobin (HbO_2), its deoxygenated form is deoxyhaemoglobin (HHb). The amount of bound oxygen in blood is quantified by oxygen saturation SO_2, the amount of O_2 bound to haemoglobin relative to the maximal amount of O_2 that can be bound by haemoglobin. SO_2 is equal to the bound O_2 content in the blood (excluding the 2% of dissolved O_2) divided by the O_2 carrying capacity of haemoglobin multiplied by 100%. Blood saturation can be divided into arterial blood saturation SaO_2 and venous blood saturation SvO_2. Normal SaO_2 values measured by pulse oximetry range from 95 to 100%; SvO_2 is lower, with normal values between 65 and 75% [32, 33].

Oxygen delivery to tissue depends not only on the O_2 content but also on blood flow. Therefore, the properties of blood vessels and pressure affect oxygenation; blood flow is directly proportional to the pressure difference between the two ends of a vessel and inversely proportional to the resistance of a blood vessel. Resistance is determined by the viscosity of blood and by the length and radius of the blood vessel; changing resistance is the main mechanism of changing blood flood, either by vasodilation (decreased resistance) or vasoconstriction (increased resistance).

The relationship between haemoglobin saturation and the partial pressure of oxygen P_{O_2} is described by the O_2 - haemoglobin dissociation curve (Figure 2.2). The saturation of haem sites does not increase linearly with P_{O_2}. Saturation increases steeply as P_{O_2} changes from 0 to about 40 mmHg and levels off between 50 and 100 mmHg. The cause of this shape is the change of affinity of the haem groups for O_2 as each oxygen molecule binds; binding of one molecule increases the affinity for the second molecule and so forth. Affinity for the last, fourth molecule is the highest and occurs at values of about 60–100 mmHg. The relatively low threshold for affinity shows that decreases in alveolar P_{O_2} (e.g. due to atmospheric pressure) do not compromise the ability of haemoglobin to bind oxygen to some degree [27]. Once haemoglobin becomes fully saturated, oxygenation is no longer influenced by P_{O2} and breathing oxygen at high partial pressures (hyperoxia) increases the risk of oxygen toxicity [34].

A partial pressure gradient needs to be constantly maintained from blood to tissue to enable O_2 diffusion. It is maintained by tissue consuming oxygen and decreasing P_{O_2}, keeping haemoglobin affinity to oxygen low, which then ensures that O_2 will be unloaded, increasing P_{O_2}.

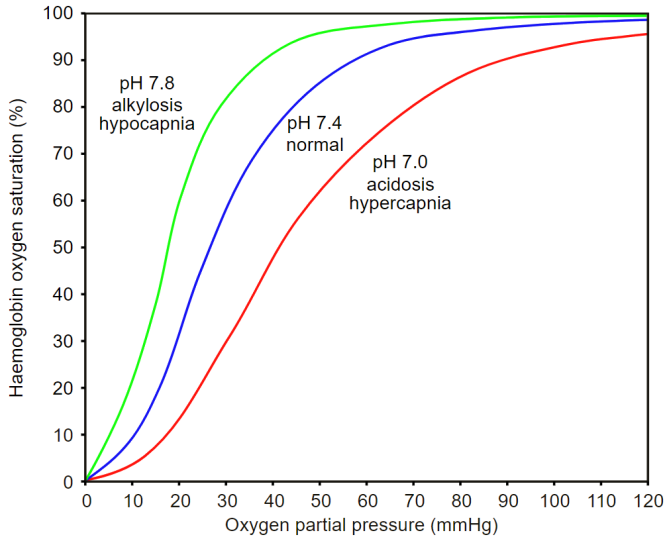

Figure 2.2: The O_2 - haemoglobin dissociation curve and its shifts during pH and P_{CO_2} changes. An increase in P_{CO_2} (hypercapnia), temperature, 2,3-diphosphoglycerate (2,3-DPG) and decrease in pH (alkylosis) cause a shift to the right. A decrease in P_{CO_2} (hypocapnia), temperature, 2,3-DPG and increase in pH (acidosis) cause a shift to the left. Taken from [35].

The dissociation curve shows how oxygen can be loaded and unloaded from haemoglobin in different parts of the body. The high P_{O2} in alveoli corresponds to almost 100% saturation and high affinity, haemoglobin is tightly bound - as much as possible oxygen should be loaded in the lungs. P_{O_2} decreases in tissue and oxygen is unloaded in tissue and oxygen saturation decreases.

A P_{O2} above 35 mmHg in the brain is considered enough to maintain normal oxygenation [30].

Changes in the environmental conditions can cause fluctuations of the affinity of haemoglobin to oxygen, hence shift the dissociation curve to the left or the right.

- Shift to the right: haemoglobin affinity is decreased (red line in Figure 2.2), caused by an increase of metabolic activity; which also increases P_{CO_2} and decreases pH. This decreases the affinity of haemoglobin and unloads oxygen to meet metabolic demand. The increase of temperature has the same effect, as heat produced by metabolism signals the need for more oxygen. The increases of 2,3-diphosphoglycerate can also cause a shift to the right as it reduces affinity. This substance is a product of glycolysis in red blood cells, its production increases under hypoxic conditions and boosts the unloading of O_2 [27].

- Shift to the left: the affinity of haemoglobin increases (green line in Figure 2.2), in a decrease of metabolism (P_{CO_2} and temperature decrease, pH increases) or a decrease of the concentration of 2,3-diphosphoglycerate [27].

2.1.4 Oxygen delivery and consumption

The main aim of blood flow is to deliver nutrients and O_2 to cells depending on their metabolic demand and to remove waste products and CO_2. The metabolic demands of cells depend on their function; while the brain, heart, adrenal glands and renal cortex have persistently high oxygen demands, the spleen or skin have lower requirements. Blood flow towards vital organs is prioritised, and local vascular mechanisms, such as vasodilation and vasoconstriction, can redistribute blood flow. Failure of such compensatory mechanisms leads to hypotension, the diminishing of organ blood flow, causing hypoxia and potential cell death.

Oxygen delivery, DO_2, is the total amount of oxygen delivered to tissue per minute irrespective of blood flow distribution. In normal conditions, it meets the oxygen requirements of tissue, the oxygen consumption, VO_2, and maintains aerobic metabolism. DO_2 is calculated from the oxygen content of arterial blood and the cardiac output. In a healthy adult, DO_2 is around 900 ml/min [1]. In comparison, a patient with anaemia, a low SaO_2 of 75% and a reduced cardiac output has a DO_2 of 288 ml/min [36], highlighting the influence of anemia, oxygen desaturation and a low cardiac output on DO_2.

Oxygen consumption VO_2 is derived from the cardiac output and the difference between arterial and venous oxygen content. The oxygen extraction ratio, OER, defined as $OER = \frac{VO_2}{DO_2}$,

[1] Normal 75 kg subject at rest with an oxygen content of arterial blood of 170 ml/l and an cardiac output of 5.3 l/min, SaO_2 = 96% [36].

which is about 25% in a healthy normal adult [36] and increases with higher oxygen extraction. The oxygen not extracted returns to the lungs and is accounted for in venous oxygen saturation SvO_2. VO_2 is determined by the cellular metabolic rate related to the net turnover of ATP; a higher metabolic rate increases VO_2.

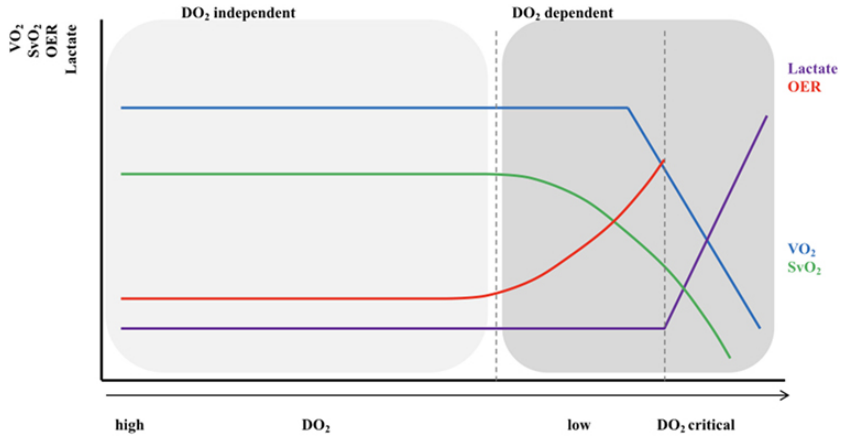

Figure 2.3: Relationship between oxygen delivery and oxygen consumption. X-axis shows the gradual decrease in DO_2 with the lowest DO_2 on the right side of the figure. Light grey area: VO_2 is DO_2 independent; dark grey area: VO_2 is DO_2 dependent. Taken from [37].

Figure 2.3 shows the relationship between DO_2 and VO_2, OER, SvO_2 and lactate, a byproduct of glycolysis. During normal DO_2 levels, VO_2 remains independent. When DO_2 decreases, OER increases, decreasing SvO_2. A critical DO_2 is reached when OER is maximal, an increase in lactate is seen from the rise of anaerobic metabolism and a cellular lack of oxygen to metabolise pyruvate from lactate. A further decline of DO_2 leads to tissue hypoxia.

Hypoxia occurs when oxygen delivery does not meet the demands of cells to maintain adequate aerobic metabolism. Causing a failure of metabolic cellular processes, it potentially leads to tissue damage. Four major types of hypoxia occur via different mechanisms [31]:

- The most common type is hypoxic hypoxia, when there is not enough oxygen present in the lungs, e.g. during an airway blockage or lung diseases causing a decrease in P_{O_2} with a subsequent decrease of O_2 delivery to tissue.
- Anemic hypoxia occurs when blood is unable to carry O_2 due to low haemoglobin levels (anemia) or carbon monoxide poisoning, when carbon monoxide binds to haemoglobin.
- Circulatory hypoxia is caused by diminished blood flow to an organ due to an obstruction.
- Histologic hypoxia is a result of a block in the electron transport chain preventing the utilisation of O_2. This can occur in respiratory chain poisoning with cyanide or sodium azide.

Tissue is tolerant to hypoxia in a certain degree, these strategies include the reduction of metabolic rate, increased oxygen extraction, enzyme adaptation to low oxygen pressures or anaerobic energy production [38]. The length of tissue tolerance to hypoxia varies. The most sensitive organ is the brain, brain cell survival time in hypoxic conditions is below 3 minutes, whereas skeletal muscle can survive up to 1.5 hours and vascular smooth muscle up to 3 days [38]. This signifies the urgent need to reestablish oxygen delivery to brain tissue during hypoxia.

2.1.5 Oxygen metabolism: summary

The maintenance of adequate oxygen supply to tissue is crucial as it is necessary for aerobic respiration and hence energy production. The respiratory system is responsible for the exchange of oxygen and carbon dioxide between the environment (air in the lungs) and the body; this exchange occurs in pulmonary capillaries wrapped around alveoli and the rate of diffusion is driven by the difference in the partial pressures of the gas across the membrane. The majority of oxygen in the blood flow is bound to haemoglobin, only a small part of it is dissolved and accounts for P_{O_2}. The binding ability of haemoglobin to oxygen depends on P_{O_2}; this relationship is described by the O_2 - haemoglobin dissociation curve. The oxygen requirements of tissue are given by the metabolic demand; in normal conditions, oxygen delivery exceeds oxygen consumption.

Failure of sufficient oxygen supply can lead to tissue damage due to the inability to meet its metabolic requirements. Brain cells survive only about 3 minutes in hypoxic conditions. This is clinically important as it shows the need for real-time monitoring of oxygen supply to the brain during interventions which can cause hypoxia, such as cardiac surgery, or during brain injury.

2.2 The neonatal brain

The normal function of the brain depends on a continous supply of oxygen through the vascular system, as it metabolises rapidly. Due to its high oxygen dependency, it is an especially fragile environment during hypoxic conditions, which can lead to brain injury. This section provides a description of brain anatomy, its development, the progression of HIE and how it is treated in the NICU.

2.2.1 Anatomy of the brain

The nervous system is the most complicated structure in the human body; the brain is considered outstanding among mammalian brains and is still a subject of extensive research. It has very high energy requirements; the brain itself uses about 20% of oxygen and 25% of the glucose consumed by the human body, yet accounts for only about 2% of body mass. The majority of

the O_2 consumption of the brain is used for energy metabolism and only a small fraction is used for other purposes, such as the synthesis and metabolism of neurotransmitters. The brain has little energy reserve and is highly dependent upon energy supply, a failure of this soon leads to perturbation of neurological functions, loss of consciousness and coma [39].

Most energy is used up by neurons, the basic structural and functional unit of the nervous system. It is currently assumed that the human brain contains around 86 billion neurons [40]. The function of neurons is to receive, process and transmit stimuli to other neurons or effector organs through synapses. Neurons vary within the peripheral nervous system and the central nervous system and are split between three main types:

- Sensory neurons respond to stimuli from receptors in sensory organs and send information to the brain.
- Motor neurons receive signals from the brain and the spinal cord and send them to effectors, which are responsible for muscle contraction and glandular outputs.
- Interneurons serve as connections between other neurons in neural networks. They remain in the central nervous system and have no contact to receptors and effectors.

The basic structure is the same for all three types and consists of a cell body with the nucleus, dendrites responsible for the receiving of signals and the axon, which conducts the signal to other neurons. A neuronal axon can be up to one metre long. The signals from axons to dendrites are transmitted through synaptic terminals and are thus the primary mean of intercommunication in the nervous system; dendrites and axons can develop side branches to increase the surface area of the neuron. Figure 2.4 shows the structure of a neuron.

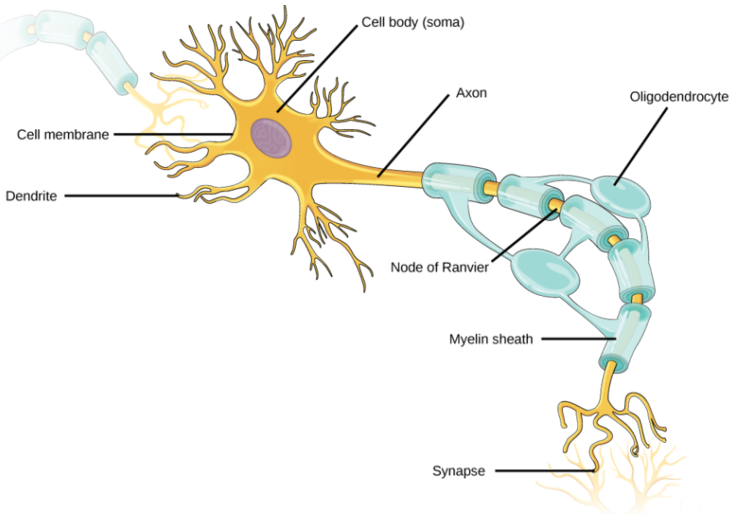

Figure 2.4: The structure of a neuron. Taken from [41].

The neuron has a resting potential of about -70 mV from inside the membrane to the outside. Signals are transmitted through an action potential, a reversal of polarity in response to stimuli. When the impulse reaches presynaptic terminals, calcium channels are opened and calcium ions enter the terminal, boosting the release of neurotransmitters into the synaptic cleft. The free neurotransmitters interact with the receptor molecules of the postsynaptic membrane, open ion-specific channels and allow the flow of an electric current carried by charged ions through the membrane. The pumping of ions across the membrane requires the addition of energy, which is supplied in the form of ATP. Hence, neurons require a steady supply of O_2 for ATP synthesis to maintain normal function.

Several other types of cell are necessary to maintain and support the functions of neurons. These are called neuroglia and they regulate the concentration of ions and participate in the blood-brain barrier; they cannot transmit electrical impulses.

- Astrocytes are the most common type of neuroglia and also the most numerous cell type within the central nervous system [42]. They have several functions including synaptic support, axon guidance, blood-brain barrier and blood flow control.
- Oligodendrocytes create the myelin sheath (Figure 2.4) around the axon and provide support and insulation.
- Microglia are the resident macrophage cells, respond to injury and are the main form of central nervous system immune defense.

The two main types of central nervous system tissue type are grey matter (GM) and white matter (WM), GM consists of cell bodies and all synapses, WM is made out of axons and provides the connections between neurons.

The brain is the centre of the nervous system and is responsible for the centralised control of the whole body. Its three main parts are the cerebrum, the brainstem and the cerebellum. The largest part, the cerebrum, is divided into the left and right cerebral hemispheres and the diencephalon. Each hemisphere is divided into four main lobes (Figure 2.5); the frontal lobe is placed at the front and is responsible for several functions including planning, prediction, speech and discrete motor movement. The temporal lobe is found on the sides of the brain. Among other functions, it processes hearing and memory. The parietal lobe is behind the frontal lobe and is the centre of pain, temperature, touch, taste and pressure. The occipital lobe is at the back and processes visual information [43].

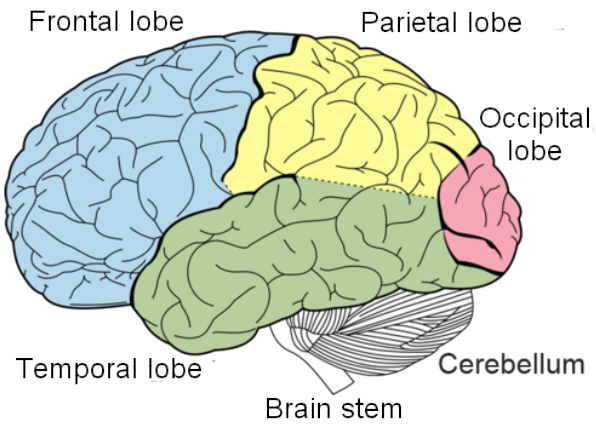

Figure 2.5: Cerebral cortex lobes. Adapted from [44].

The cerebellum, placed below the occipital lobe, is responsible for muscle coordination and balance. Below the surface of the hemispheres are the basal ganglia, which control the execution of movement. The brain stem consists of several parts, the midbrain, medulla and pons. The midbrain is a control center for visual, auditory, motor system information and autonomic functions including heart and breathing rate. It sends motor and sensory signals to the cerebral cortex via the thalamus, a small structure just above the brain stem. The pons regulates breathing and also transmits signals between other brain structures. The medulla is responsible for reflexes and involuntarily controls; it is connected to the spinal cord.

The surface of the hemispheres consists of GM; WM forms the deep part of the brain. The brain is suspended in cerebrospinal fluid (CSF) and protected by the skull. Three layers of mem-

branes, the meninges, separate the brain from the skull; dura matter, arachnoid matter and pia matter, closest to the brain. CSF, which has a similar composition to blood plasma, circulates between arachnoid and pia matter. As a cushioning, it protects the brain from damage by sudden movement and its own weight. The blood-brain barrier, a semipermeable membrane on the surface of capillaries, is responsible for separating the brain and CSF from the blood stream and regulates which substances can enter and exit the brain. Water, some gases and lipid-soluble molecules pass it by diffusion, glucose and amino acids are transferred by selective transport. The barrier also allows for the exit of metabolism waste products from the brain.

2.2.2 Cerebral circulation

The brain requires about 750 ml of blood per minute to maintain its oxygen needs at normal activity. As neurons have a high rate of metabolism, they are more sensitive to oxygen deprivation than other kinds of cells; 5 to 10 seconds of blood supply interruption are enough to cause changes in the neuronal activity, a few minutes can cause irreversible neuronal damage [43, 45].

Two main arteries carry blood from the aorta to the brain; the internal carotid arteries and the vertebral arteries. The internal carotid arteries enter the skull through the temporal bone, the vertebral arteries through the occipital bone. They are connected in the brain via the Circle of Willis, a vascular loop on the surface of the upper brain stem. The circle branches into arteries which provide blood supply. A circular structure is beneficial in the case of the blockage of a major vessel as it could be compensated by the blood supply from another vessel [45]. Blood from the hemispheres drains through capillaries into the cerebral veins; superficial, located at the surface of the cerebrum, and deep, which drain the interior. Blood exits the skull via the internal jugular veins.

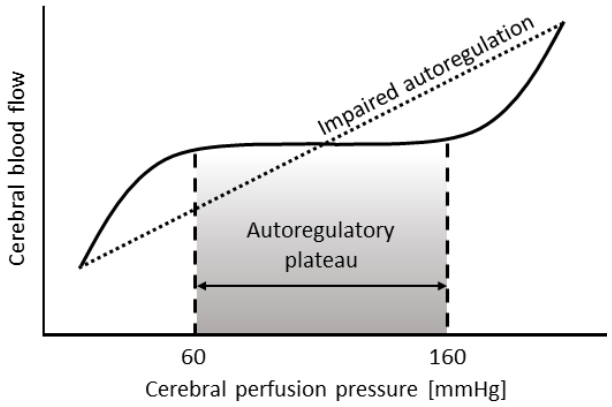

Figure 2.6: The cerebral autoregulation curve. The solid line plots CBF as a function of the cerebral perfusion pressure in a normal state. The dotted line shows the cerebral perfusion pressure to CBF relationship with impaired autoregulation during situations such as acute stroke.

Normal functioning of the brain relies on a tight regulation of blood flow and oxygen delivery, total blood flow to the brain is remarkably constant in a normal physiological state. Autoregulation is the ability to maintain cerebral blood flow despite changes in perfusion pressure; CBF stays constant with changing pressure in the region of the autoregulatory plateau, Figure 2.6. It is present in many vascular beds but especially well-functioning in the brain. Autoregulation is maintained within normal limits, when CBF is at approximately 50 ml per 100 g of brain tissue per minute at a cerebral perfusion pressure in the range of approximately 60–160 mmHg with considerable individual variation. Autoregulation is lost outside these limits and CBF becomes linearly dependent on the mean arterial pressure. Ischaemia occurs when cerebral perfusion pressure falls below the autoregulation limits; an increase of oxygen extraction from the blood compensates for the reduction of CBF. The maintenance of autoregulation is crucial for the normal function of the brain as the loss of autoregulation mechanisms causes significant brain injury [46].

The oxygen needs of the brain are often described in terms of the cerebral metabolic rate of oxygen, $CMRO_2$, related to OER, cerebral blood flow CBF and the arterial oxygen content O_2^{art}.

$$CMRO_2 = CBF \times OER \times O_2^{art}. \tag{2.1}$$

CBF and $CMRO_2$ can provide an important assessment of brain health and have significant implications in brain development and neonatal pathological conditions, including HIE, hydrocephalus or congenital heart disease [47].

2.2.3 Brain development

The age of a foetus is described in terms of gestational age, which is counted from the first day of the last menstrual period of the mother. The length of an average singleton pregnancy is 40 weeks. Deliveries from 37 weeks onwards are considered term, deliveries before gestational week (GW) 37 are preterm; infants born before GW 28 are extremely preterm.

The brain starts developing in GW 3, when neural progenitor cells differentiate. Brain development lasts until the early twenties, even though small developmental changes occur throughout the whole lifespan. The brain is a complex and dynamic structure; its development is an adaptive process during which new neural structures and functions emerge and differentiate. It is affected both by genes and environment; they support the increasingly complex functions and structures of the brain - neither is descriptive and determines the outcome. Gene expression is particularly important in the embryonic period, when interactive cell-cell processes alter the development of

other cells but the external environment still plays an essential role. The influence of the external factors rises during the foetal and postnatal period [48].

The basic structures of the brain and the central nervous system are established by the end of the embryonic period (end of GW 8). The main compartments of the nervous systems are defined; most cortical neurons are in their position in the neocortex and begin to form essential brain networks [48]. The brain undergoes striking changes in the foetal period (GW 9 until end of gestation); the brain begins as a smooth structure and gradually develops the gyral and sulcal folding pattern. The first sulci form between the cerebral hemispheres, from GW 8 up to 22, other primary sulci follow up to GW 26. The secondary sulci start forming in GW 30 until GW 35 and the formation of tertiary sulci extends into the postnatal period. This development occurs simultaneously with dramatic cellular changes; which centre around neuron production, migration and differentiation. Neuron production starts around GW 5 with primary neural tube formation; neurons migrate and form different grey matter structures in the brain until midgestation [49]. Neurotransmitters, dendrites and axonal processes form pathways in neural networks, which make up WM [48]. The number of glial progenitor cells (cells producing neurons and connective tissue) increases for a long postnatal period, they migrate, differentiate and mature throughout childhood. The full temporal extent of these processes in humans is still unknown; in vivo brain imaging gives important information about these age-related alterations and helps link them to behaviour [48].

2.2.3.1 From the neonatal to the adult brain

The work in this thesis is focused on neonates. There are significant differences between the adult and the neonatal brain, among them skull thickness and the different metabolic requirements.

The human brain is a continuously changing environment; while significant changes develop during childhood and adolescence, the brain continuously evolves throughout adulthood [50]. The rapid growth of the brain in early age indicates differences in physiology and anatomy of infant and adult human heads; the neonatal brain is about 25% of the adult brain size at birth, although the neonatal body weight is only around 5% of adult body weight [51]. The small neonatal skull has open sutures and fontanels allowing some buffering of intracranial pressure, which is lower than in adults [51]. Fontanels are closed by the age of 12–18 months. In the neonate the skull is much thinner than in the adult; around 1.5–2.5 mm thick [52], compared to 6–8 mm [53]. In total, the extracerebral layer of adults, consisting of skin, skull and cerebrospinal fluid is 10–30 mm thick [54].

The cerebral metabolic rate of oxygen $CMRO_2$, the rate of oxygen consumption by the brain,

is much lower in the healthy neonatal brain than in adults: 38.3 $\pm$ 17.7 μmol/l00 g/min in neonates vs. 150–200 μmol/l00 g/min in adults [55]. Cerebral blood flow is also lower in neonates, around 13 ml/100 g/min [55] compared to 60 ml/100 g/min in the adult grey matter [56]. These differences are likely due to the lower metabolic demands of the neonatal brain. While it has been shown that the nerve cell density is much higher in the neonate than in the adult, the neonatal brain has less neuronal processes, synapses, myelination, neurotransmitters and receptors, which leads to fewer neuronal activities and lower oxygen consumption [55].

2.2.3.2 Foeto-neonatal cardiovascular transition

Foetal gas exchange occurs in the placenta, which receives oxygen rich blood from the mother. The umbilical cord connects the foetus to the placenta and carries oxygenated, nutrient-rich blood in the umbilical vein. The most highly oxygenated blood supplies the myocardium and the brain, only a small portion of blood perfuses the lungs. Deoxygenated blood returns from the foetus to the placenta via umbilical arteries. The foetal circulation differs from the adult circulation by function in two parallel circuits with equal left and right ventricle pressures. Most oxygenated blood travels from the right atrium to the left atrium and ventricle through the foramen ovale, a small hole between the two heart atria.

Significant cardiovascular changes follow cord clamping at delivery. These changes take seconds to hours, and it takes weeks for the last transition to finalise. Initially after losing pulmonary blood supply, systemic vascular resistance rises and affects cardiac output. The onset of breathing leads to the closure of the foramen ovale and completes the transition from a parallel to a serial circulation.

Intrinsic and external factors can influence the transition process, and difficulties with adaptation to the transition process and oxygen delivery can arise particularly in preterm infants, but also in term infants. A major cause of early neonatal mortality is perinatal asphyxia, defined as "*a lack of blood flow or gas exchange to or from the foetus in the period immediately before, during, or after the birth process*" [57]. Many processes can lead to perinatal asphyxia, including insufficient oxygen supply from the mother before and during birth, long and difficult delivery, infections and problems with the airways of the infant, impaired development or blockage. In order to decrease mortality and improve patient outcome, cardiovascular monitoring is of critical importance in infants with impaired oxygen delivery during and after transition.

2.2.3.3 Cardiovascular monitoring in the neonatal intensive care

Monitoring in the intensive care is focused on the optimisation of haemodynamics and temperature to maintain adequate organ tissue oxygenation and combat hypoxia, shock, and multiorgan failure. In the NICU, cardiovascular monitoring is applied in all infants and the aim is to answer three key questions; whether there is evidence of cardiac dysfunction, whether the tissue perfusion is adequate and whether there is any indication of tissue hypoxia [58].

Multimodal monitoring is standard in intensive care; the use of multiple tools to measure different physiological parameters and obtaining a global assessment of the patient's health. The main observations of the infant's wellbeing include heart rate, capillary refill time and measurements of markers of end-organ perfusion, such as skin colour/temperature or urine output. Cardiac output is one of the major determinants of oxygen delivery and should be regularly/continously measured. The most used non-invasive technique of measuring cardiac output is neonatologist performed echocardiography, a non-invasive absolute assessment of the cardiac output and end-organ perfusion. Transcutaneous doppler technique is used for a rapid measurement of the cardiac output by measuring blood flow velocity across the aortic and pulmonary valve but is used only as a trend monitor [37].

Organ perfusion and oxygen delivery are monitored to early detect changes in regional blood flow, oxygen consumption and extraction. Pulse oximetry non-invasively measures the arterial oxygen saturation and hence the adequacy of oxygen supply in capillaries [58]. Cerebral monitoring with near-infrared spectroscopy to measure regional tissue oxygenation and fractional tissue extraction is also spreading among intensive care units [7].

Other invasive monitoring tools are used, such as mixed venous saturation as a measure of balance between oxygen delivery and tissue oxygen demand, and arterial blood gas analysis, which measures pH, SaO_2, P_{CO_2}, P_{O_2} and other parameters, such as lactate or glucose levels to quantify metabolism [58]. However, non-invasive monitoring methods are preferred at the cotside.

2.3 Hypoxic-ischaemic encephalopathy

The immature brain is a very fragile environment; growing and developing quickly. Damage can arise from various neurodevelopmental disorders which include a broad range of pathologies: motor disorders, genetic disorders, damage due to neurotoxicants, and others. The following section is focused on neonatal brain injury caused by metabolic events.

Neonatal encephalopathy (NE) is a disturbance of neurological function apparent in the early days of a term neonate's life associated with multi organ dysfunction manifested by abnormal

levels of alertness, seizures, often respiratory difficulties and depressed tone [59]. The definition excludes neonates under 35 GW because specific behavioural reactions and reflexes observed for NE diagnosis can be impossible to test in a premature brain due to brain development [60]. The incidence of NE is estimated at 3 per 1000 live births [13]. There are various causes of NE, including hypoxic-ischaemic encephalopathy, perinatal infections, placental abnormalities, metabolic disorders, coagulopathy and neonatal vascular stroke, but the cause is often unidentified [59].

The focus of this work is on infants with HIE. The terms NE and HIE are often used interchangeably [61]; the use of NE versus HIE can be considered controversial, as it is often difficult to diagnose hypoxia-ischaemia and to prove that HIE was indeed the cause of NE [62]. However, the discussion on the suitability of which term to use is outside of the scope of this work and in the following chapters, HIE is considered a subset of NE caused by ischaemia (insufficient blood supply to the brain) and hypoxia (deprivation of oxygen).

HIE is the neurological pathology following severe perinatal asphyxia and has an incidence of 1.5 per 1000 live births, the occurrence is higher in developing countries [13, 59, 63]. Up to 60% of infants with HIE will die or will have severe disabilities including intellectual disability, epilepsy and cerebral palsy; HIE has a significant psychological and economical impact on families and society [64].

During perinatal asphyxia, the foetus can survive with insufficient oxygen delivery by reducing oxygen demand and increasing blood flow to vital organs, such as the heart and the brain, to maintain oxygen delivery. However, this response diverges depending on the severity of asphyxia; severe cases lead to apnoea and the neonate will require resuscitation [65]. This prolonged lack of oxygen supply to the brain leads to HIE, followed by events including acidosis, release of inflammatory mediators and the formation of free radicals; which impair the autoregulatory function and lead to cell death. The most common symptoms are respiratory and feeding difficulties, depression of tone and reflexes and a low level of consciousness; seizures usually develop within first 24 h of life [66].

2.3.1 Progression

The underlying events of HIE are the result of impaired cerebral blood flow and oxygen delivery. The effects are complex and evolve over time; the pathology progresses over multiple stages: primary insult, latent phase, secondary energy failure and tertiary phase (Figure 2.7).

The primary insult is caused by the initial reduction of cerebral blood flow, followed by abnormal control of cerebral haemodynamics with a combination of vasodilatation and vasoparalysis [68].

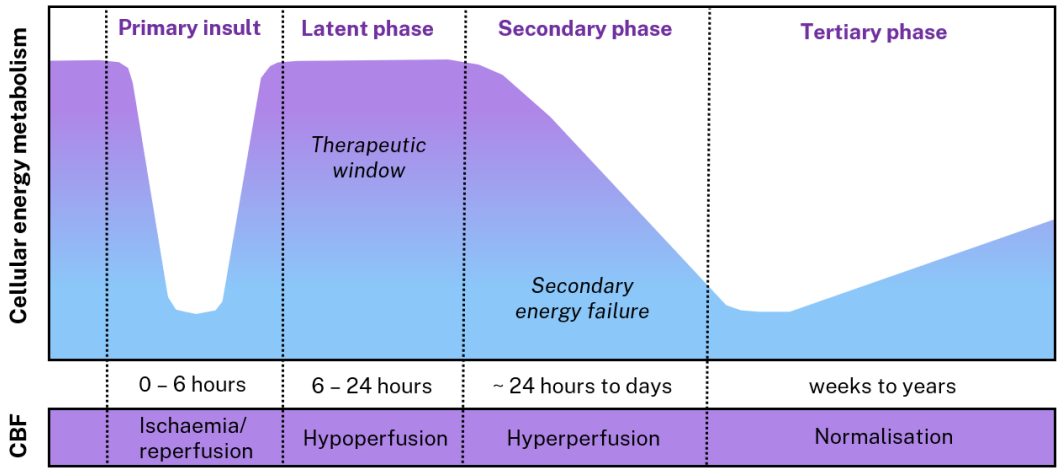

Figure 2.7: The progression of HIE over time and its effects on cellular energy metabolism and cerebral blood flow (CBF). The primary insult, a period of ischaemia, is followed by a latent phase, which is the time to treat. In the secondary phase, a secondary energy failure occurs despite adequate oxygenation, during which mitochondrial failure leads to delayed cell death. CBF and metabolism is restored in the tertiary phase, but pathological processes can occur for years after the insult [67].

The ischaemic insult leads to a reduction of oxygen and glucose and hence a decrease in ATP production. This causes a failure of many mechanisms maintaining cell integrity, triggering a cascade of events leading to cerebral edema, ischemia and microvascular damage with resultant necrosis or apoptosis. The level of damage and cell death depends on the severity of the hypoxic-ischaemic insult [64].

The initial injury is followed by a latent phase, in which blood flow is restored and the brain is recovering, cerebral metabolism returns to normal levels. It has been found that the haemodynamics in term infants with acute HIE are abnormal with an increase in cerebral blood volume and its response to changes in arterial carbon dioxide tension [68]. The level of cerebral blood volume abnormality is related to outcome [68] and also the length of the recovery period depends on the severity of the primary injury; it is shorter for severe injury. It is however difficult to establish when exactly this latent stage ends and the secondary insult starts. It is mostly 6 to 48 hours following the initial injury; the secondary energy failure is related to oxidative stress, excitotoxicity and inflammation and leads to further damage to neuronal tissue during a state of hyperperfusion and impaired autoregulation in severe cases [64, 69]. The severity and length of the secondary insult varies; it has been shown that clinical neurodevelopmental outcomes at 1 and 4 years of age are correlated with the severity of the secondary insult at 15 hours [70]. After the secondary energy failure, the tertiary phase is a stage of persisting pathological processes occurring for weeks, months and years after the insult [67].

2.3.2 Diagnosis and treatment

Early diagnosis of HIE is crucial for effective treatment, as the latent phase is considered the optimal timing for therapeutic intervention and can be quite short. HIE diagnosis is based on symptoms including abnormal heart rate tracings, low Apgar scores or the need for respiratory support. A detailed examination of the infant includes: neurological assessment, which may have to be repeated as the signs change quickly; blood count and clotting, liver function tests, blood glucose and lactate measurements and other signs of metabolic disorders. Additional investigation may follow if a diagnosis is not confirmed. The severity of the injury is assessed based on the Sarnat staging criteria, which divide the injury into mild (stage I), moderate (stage II) and severe (stage III). Mildly injured infants have normal EEG patterns and muscle tone but are hyperalert and their sucking reflex is weak/absent [64]. The majority of mildly injured infants have a good long term outcome without the need for HIE treatment [71].

Moderately injured neonates are lethargic, hypotonic and often suffer from seizure. Severely injured patients are stuporous, muscle tone is flaccid and autonomous function is absent. The presence of moderate or severe HIE has a strong association with an adverse neurological outcome [72]. It is also necessary to keep in mind that the level of severity of the injury may change over the first few days after birth [73]. Predictors of outcome in HIE include heart rate, Apgar score, need and duration for resuscitation and the severity of acidaemia, and have a high specificity and negative predictive value if assessed soon after birth (5 min for Apgar score) [73].

Moderate and severe HIE neonates are treated with therapeutic hypothermia (TH), which is currently the most common treatment method. The infant is cooled down to a temperature below homeostasis, providing neuroprotection following an ischaemic neuronal insult [74]. Timing is crucial for TH, as it is most effective during the latent phase of the injury, also called the "therapeutic window". The therapy has to last until the end of the secondary phase of the injury to be effective, suggesting that repair occurs over a long period of time [70]. TH is delivered either through head or whole body cooling of the infant to a temperature between 33°C and 36.5°C for 48 to 72 hours followed by a period of rewarming. Longer or deeper cooling has been shown to be harmful. Clinical trials compared TH initiated 6 to 24 hours after birth to not cooling, TH reduced death or disability with a 76% probability [75]. Overall, TH helps some neonates but additional treatments are needed to improve infant survival with normal developmental outcomes. Additionally, as the outcome depends on detecting the accurate aetiology of HIE and assessing the severity of the injury, accurate imaging and diagnosis could help with developing a more patient-specific

treatment system [59, 64].

Other types of treatment are currently being investigated in clinical trials; among them is the use of erythropoietin (EPO), a glycoprotein hormone which acts as a neuroprotective agent. It has been shown that the administration of EPO to moderate and severe HIE neonates reduced the risk of cerebral palsy and cognitive impairment. EPO was also used in conjunction with TH, which reduced the risk of death. More clinical trials are needed to investigate the effectiveness of the combination of EPO and TH [76]. The transplantation of stem cells is an emerging, promising HIE therapy. It has been shown that the combination of this therapy with TH improved outcome, but this treatment is rather new and requires extensive research and more understanding of the underlying mechanisms [77]. Current research is also looking at the use of xenon to reduce excitotoxicity, or melatonin, which could inhibit apoptosis [64, 78].

Additionally to TH, infants with HIE may receive supportive care individually tailored to the needs of the infants, which aid with the management of potential multiorgan dysfunction. This includes ventilation or the administration of parenteral fluids [78]. Creating an individual treatment plan for the infant requires the use of reliable monitoring and injury biomarkers.

2.3.3 Clinical monitoring and imaging of infants with HIE

Infants with HIE are treated and monitored at the NICU. Apart from using monitoring techniques to help with the diagnosis of HIE or injury severity, it helps with ensuring that oxygen supply is adequate after the HIE insult and infants are monitored before, throughout and after TH. Commonly used for non-invasive, real-time oxygenation monitoring in the intensive care unit is pulse oximetry. Pulse oximeters work on the basis of light absorption in haemoglobin and as the absorption properties of oxygenated and deoxygenated blood are different (more in the next chapter), it is possible to measure oxygenation of the arterial blood, the pulsating component of blood. Oxygenation measured with pulse oximetry SpO_2 is a measure of arterial oxygen saturation SaO_2, which reflects the global oxygenation. Pulse oximeters have an accuracy of 3% [34]. An SpO_2 of 95% may represent SaO_2 between 92% and 98% in 68% of measurements and even an SaO_2 of 100% in 16% of cases. This is important because high SpO_2 values can occur during oxygen therapy and as seen on the oxygen dissociation curve in Figure 2.2, a high SaO_2 corresponds to high P_{O2} values which can lead to oxygen toxicity. Additional measurements of tissue oxygenation are desirable; one alternative is the direct measurement of SaO_2 with co-oximetry which requires samples of blood and is hence invasive. Nevertheless, monitoring SaO_2 is a measure of the global oxygenation of tissue and is not an indicator of local oxygenation which is desirable for

the management of hypoxic brain injury (the relationship between SaO_2 and StO_2 is discussed in section 4.1.2.1).

Other monitoring techniques can be combined with pulse oximetry to obtain additional information about perfusion, including measurements of CO_2 levels by means of capnography or transcutaneous monitoring [34]. Arterial blood pressure and blood glucose levels, temperature and heart rate are also monitored. Imaging is used to assess the adequacy of treatment and to help with diagnosis; several imaging tools are available in clinical care to aid with diagnosis.

2.3.3.1 EEG & aEEG

Multichannel EEG is a measure of neuronal electrical activity. Spontaneous electrical activity of the brain can be affected by conditions such as oedema, inflammation, lesions or metabolic imbalance [79] and abnormalities in signal indicate the presence of a pathology. EEG signal characteristics such as amplitude, presence of discontinuity, length of inter-burst interval, absence of sleep-wave cycling and presence of seizures are related to HIE severity and can help predict outcome [79]. EEG monitoring is standard in HIE care; abnormalities in the reading are part of the NHS criteria for the enrolment of neonates in TH treatment and is used for diagnosis of severe HIE [80].

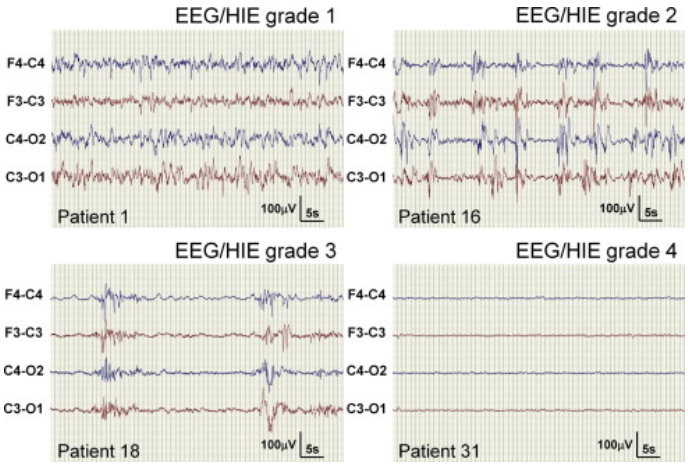

Figure 2.8: Ideal examples of graded EEG recordings taken in during the first day of life in neonates with HIE. Each grade corresponds to a level of abnormality in the signal, this grading correlates with the Sarnat score of HIE and outcome (grade 1 = good outcome, grade 4 = worst outcome). Taken from [81], reproduced with permission of Elsevier.

An example of different EEG patterns during HIE is in Figure 2.8. The grading of the signal quality corresponds to the level of abnormality, with 1 being only mildly abnormal and 4 inactive; this grading correlates with Sarnat grading and the outcome [81]. Amplitude integrated EEG (aEEG) can help detect seizures, unless they are short (< 30 s), but is still superior to other detection

methods of seizures. The optimal time to assess aEEG for prognosis is 48 hours. Return to normal voltage is associated with good outcome [82]. The disadvantage of EEG and aEEG is the need for experienced staff to perform and interpret the measurements, decreased prognostic values in the early hours of life [80] and lack of standardised EEG signal classification methods for HIE assessment [81]. EEG measurements would also benefit by measures of cerebral haemodynamics $CMRO_2$ changes, which precede or accompany the secondary energy failure during HIE [83, 84].

2.3.3.2 Magnetic resonance imaging and spectroscopy

Magnetic resonance imaging (MRI) is the leading modality for assessing injury severity. It can be used to measure the cerebral metabolic rate of oxygen or blood flow and it detects the pattern of injury. HIE affects various regions of the brain. The visualisation of the brain injury depends on the severity, the timing and the abruptness of the initial events. There are two main patterns observed in MRI; watershed and basal ganglia/thalamic. The watershed patterns affect areas between the main arterial supplies and deep in the sulci, leading to oedema, cerebral cortex necrosis and infarction. The second pattern, basal ganglia/thalamic, occurs more often in acute, profound injury. Deep grey matter and active regions of the cerebral cortex are damaged first. Both injury patterns are predictors of outcome; watershed patterns lead to cognitive impairment, basal ganglia/thalamic lesions are associated with severe motor and cognitive disability [85]. Examples of both types of injury patterns are in Figure 2.9. Brain changes consistent with HIE take time to evolve and the extend of the injury can be underestimated if imaged too early. It is thus recommended to perform MRI between 5 and 14 days of age. T1 and T2 imaging has high specificity and sensitivity as a predictor of long-term outcome, diffusion weighted MRI can detect findings earlier but has a lower prognostic value [78]. The disadvantages of MRI are its limited access, need for sedation, price, need for specialist staff and having to wait several days for the injury to develop.

MRS is increasingly used for the diagnosis and prediction of outcome through the measurement of the ratio of lactate and n acetyl aspartate (Lac/NAA). Increased lactate levels in the injured brain are caused by impaired mitochondrial function and oxidative phosphorylation and can persist for months in brains of infants with adverse outcome [86]. Recent work has shown that a ratio of 0.39 as a threshold had a high specificity and sensitivity to motor, cognitive and language outcome [86]. Figure 2.10 shows Lac/NAA for neonates with normal and poor outcome. A weakness of this measurement is that the value is taken from a single voxel and might not correspond to the location of the biggest damage, so combining MRS with MRI can increase specificity while maintaining sensitivity [87].

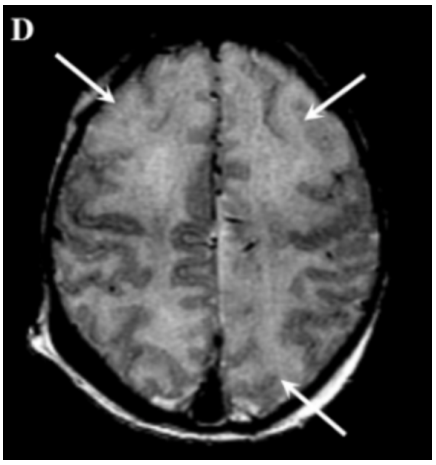

(a) T2 image of HIE injury with a watershed pattern with loss of grey white differentiation (arrows). Taken from [88], reproduced with permission of Elsevier.

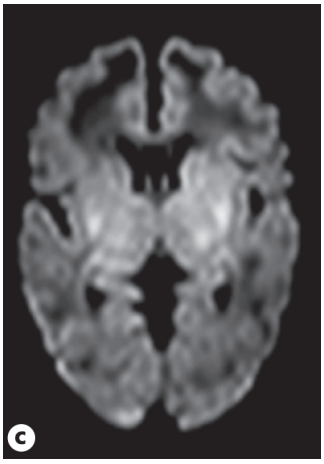

(b) Diffusion-weighted image of HIE injury with a basal ganglia and thalamus pattern. Taken from [89].

Figure 2.9: Examples of MRI from neonates with HIE.

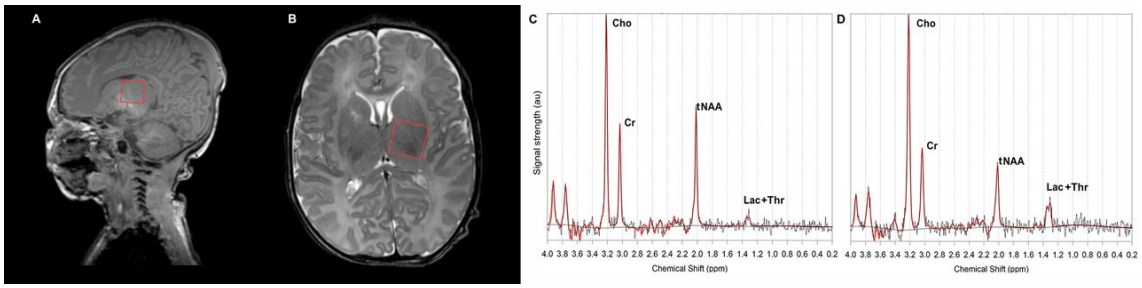

Figure 2.10: A,B: position of the voxel for spectral acquisition (A: saggital, B: axial). C: neonate with normal outcome, Lac/NAA = 0.19. D: neonate with poor outcome, Lac/NAA = 0.62. Taken from [86], reproduced with permission of BMJ Publishing Group Ltd.

2.3.3.3 Ultrasonography

Transcranial ultrasound can detect intracerebral lesions and oedema and the benefits of the technique include wide availability, ease of repetition and no need for sedation. As HIE progresses, ultrasound can be used for assessment of the evolution of the injury and for prognosis [90]. However, drawbacks of the technique include operator dependency or low sensitivity for detecting cortical lesions [66].

Transcranial Doppler ultrasound measures the velocity of blood flow; changes in blood flow are related to the occurrence of asphyxia. Analysis of blood flow curves during systole and diastole allows calculation of the resistive index, which is a measurement of cerebral vascular dynamics and the integrity of cerebral autoregulation. Abnormalities in the resistive index are correlated with HIE prognosis but its prognostic value is decreased during TH [90].

2.3.3.4 Computed tomography

Computed tomography is useful for screening intracranial haemorrhage in very sick infants without the need for sedation, however, its sensitivity and specificity is lower than MRI. CT underestimates the severity of white matter and cerebral cortex injury, another major disadvantage of CT is the radiation exposure [66, 85].

2.3.3.5 Near-infrared spectroscopy

The use of NIRS in the management of HIE is becoming increasingly popular as it is a real-time assessment of cerebral haemodynamics, and, in contrast to pulse oximetry, measures regional trends. It has several advantages in comparison to the other monitoring methods: it can be used within the first minutes of life, it does not require specialist staff, is non-invasive and can provide information in real time. While some devices are trend monitors, absolute oxygenation measurements would let the clinician obtain an immediate assessment of tissue oxygenation, informing on brain health. The potential of NIRS in HIE treatment is for use in diagnosis and injury progression monitoring, but also on assessing the HIE injury pattern, e.g. if StO_2 readings differ in infants with a watershed pattern or basal ganglia/thalamic pattern of injury.

Several different parameters can be measured with NIRS, such as changes in the concentration of haemoglobin and CCO or StO_2 (defined in (Eq. 1.1)), and others. Measurements of haemoglobin concentration changes can detect regional hypoxia, and combining the measurement with CCO monitoring can help with diagnosing moderate and severe brain injury within the first days of life [16]. The potential of monitoring StO_2 non-invasively during HIE as a means of immediate oxygenation assessment is a subject of research and will be further discussed in Chapter 3.

Cerebral blood flow can be measured with NIRS by measuring the concentration of a tracer, indocyanine green (ICG) [91]. When combined with a measure of arterial oxygen saturation (e.g. pulse oximetry), NIRS can also be used to obtain an estimate of cerebral metabolic rate of oxygen, $CMRO_2$ [91, 92].

The combination of NIRS with diffuse correlation spectroscopy is used in research to measure cerebral blood flood and oxidative metabolism simultaneously [16, 93, 94, 95]. Diffuse correlation spectroscopy is an optical technique to measure blood flow by injecting light into tissue and quantifying the temporal change of the light reflected back, these changes are due to scattering on moving red blood cells, which relates to the speed of the moving cells [96].

Commercial systems are also used to measure tissue oxygenation StO_2 and fractional tissue

oxygen extraction $FTOE$ [97],

$$FTOE = \frac{SpO_2 - StO_2}{SpO_2}. \tag{2.2}$$

An increase in $FTOE$ shows an increase of oxygen extraction by brain tissue and hence higher oxygen consumption in relation to oxygen delivery [84].

The application of NIRS in the neonatal care is still subject to extensive research and not yet widely available [98], driven by the need for non-invasive and simple measurements of cerebral haemodynamics.

2.3.4 The neonatal brain and HIE: summary

The brain is a complex system evolving throughout the whole life. It is particularly vulnerable to hypoxic damage during prenatal development and in the neonatal period. Hypoxic-ischaemic encephalopathy is brain injury caused by hypoxic and ischaemic events in term infants leading to metabolic energy failure and cell death. Severe cases of the injury can lead to irreversible damage (e.g. cerebral palsy) or neonatal death. Infants with moderate or severe HIE are treated with TH, which provides neuroprotection by cooling to a temperature below homeostasis. Early diagnosis is crucial for effective treatment of the injury. Currently, several imaging modalities are used in the clinic, among them MRI or EEG. However, as these modalities require specialist staff and can be often unavailable, NIRS could fill the gap for a low-cost, non-invasive and easy to use monitor of oxygen delivery and metabolism in the neonatal intensive care.

Chapter 3

Cerebral oximetry: optical techniques

Oxygenation monitoring with NIRS is of clinical importance as it can detect local tissue hypoxia in real time and non-invasively. The following chapter describes how NIRS is based on the absorption of light by biological tissue and what makes oxygenation measurable. Further sections provide a deeper look into different quantities we can measure with NIRS, in particular tissue oxygen saturation, StO_2, an absolute measurement of tissue oxygenation. The description of this quantity is accompanied by an introduction to theory of light transport in tissue and a summary of different algorithms applied to measure this clinically desirable measure of tissue oxygenation.

3.1 Light transport in tissue

The use of visible and near-infrared light has huge potential for use in medical care for both imaging and treatment, as it has several advantages: it is non-ionising, most methods are non-invasive, light can yield biochemical information and can be controlled easily. The measurement of arterial oxygenation SpO_2 with pulse oximetry has proven that optical modalities can play an important role in treatment. Nevertheless, one drawback of using light in imaging and therapy is the limited transparency of biological tissue in the visible range of wavelengths, caused by the strong attenuation of light by tissue. Two interactions contribute to this process: absorption and scattering. The level of attenuation depends on the light wavelength, the size of the scattering particle, present chromophores and the structure of the medium. The attenuation of light in biological tissue is a complex process comprising of multiple scattering events and the absorption by various types of molecules.

3.1.1 Absorption

In light absorption, light energy is absorbed by matter and converted into another type of energy (heat). This only occurs if the frequency of the light matches the absorption frequency of the

matter. Absorption properties of a medium are quantified with the absorption coefficient μ_a (with the unit reciprocal centimetre [cm^{-1}]) which describes the probability of a photon being absorbed over an infinitesimal path. The absorption cross section for a single absorber indicates the absorbing capability; the absorption coefficient is the total cross-sectional area for absorption per unit volume. In the case of multiple absorbing compounds, the total absorption coefficient is the sum of the individual absorption coefficients.

Absorption properties are often expressed in terms of the concentration of the absorber c and the specific absorption coefficient α:

$$\mu_a = c\alpha. \tag{3.1}$$

The specific absorption coefficient α describes the probability of absorption for a unit concentration of a compound over unit length. Absorption can be also measured in log base 10, using the extinction coefficient k:

$$\mu_a = \ln(10)k, \tag{3.2}$$

or using the log base 10 of the specific absorption coefficient, obtaining the specific extinction coefficient ε:

$$\varepsilon = \frac{\alpha}{\ln(10)} = \frac{\mu_a}{\ln(10)c} = \frac{k}{c}. \tag{3.3}$$

Each absorbing molecule, a chromophore, has a distinct absorption spectrum which illustrates the wavelength-specificity of absorption. The main absorbers of light in tissue include melanin, water, lipid and haemoglobin. Due to their absorption properties in the range of visible wavelengths, visible light does not penetrate skin deeper than a few mm [99].

Figure 3.1 shows the absorption spectra of main tissue chromophores. Water is a strong absorber in wavelengths below 200 nm and beyond 900 nm. This low, but not negligible, absorption makes tissue relatively transparent in the visible/near-infrared wavelength range. The most important chromophore for NIRS is haemoglobin, whose four haem sites can bind to oxygen. The presence of oxygen changes its optical properties - the difference in the absorption properties of these two states, oxygenated and deoxygenated haemoglobin is significant in the "optical window" ($\approx$ the near-infrared range 650–1000 nm); the point of equal absorption at 798 nm is known as the isosbestic point. Tissue is the most transparent in this range and it has been shown that light of these wavelengths can travel as far as 8 cm deep in tissue [101]. NIRS uses the optical window to achieve maximal depth of light penetration. The absorption by other chromophores, such as fat, collagen etc. can be assumed negligible for most NIRS applications, as their concentration does

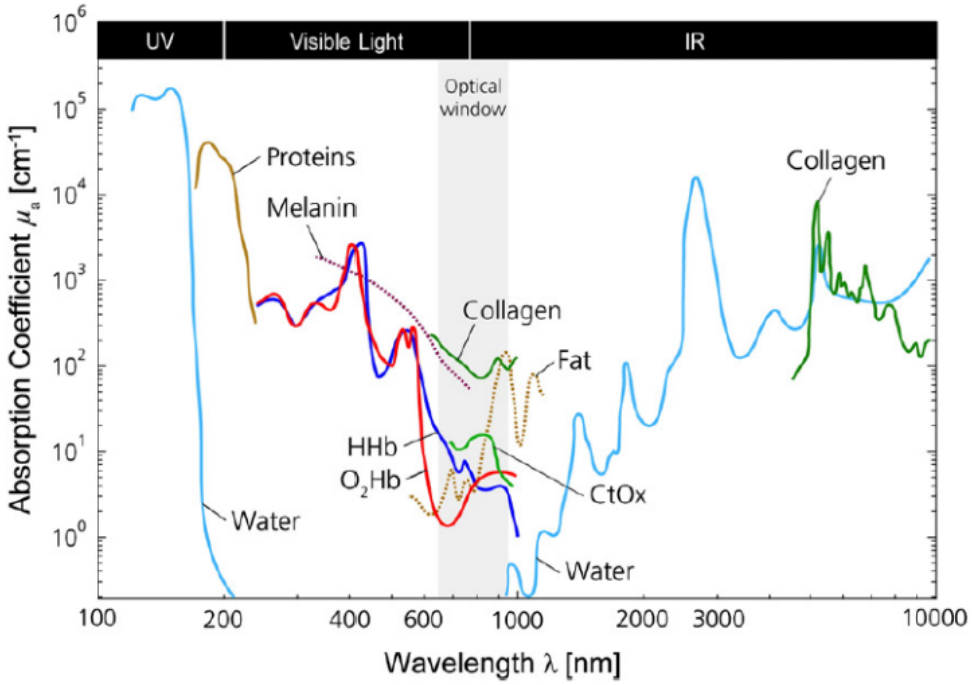

Figure 3.1: Absorption spectra of main tissue chromophores. Taken from [100], reproduced with permission of Elsevier.

not change rapidly during the measurement period or the absorption is very weak.

NIRS can also be used to track the concentration of other chromophores with lower concentrations, such as CCO, which participates in the electron transport chain during ATP production in the mitochondria. Through the measurement of this enzyme, is it possible to quantify cell metabolism [102]. Optical contrast agents can be also used in NIRS - ICG can be injected into the bloodstream to study cerebral perfusion [103]. While the absorption of light by water in the NIR region is quite weak compared to haemoglobin, as it is present in high concentrations, it can be also a chromophore of interest, especially when NIRS is used for absolute concentration measurements [104]. As this work is focused on haemoglobin concentration measurements, haemoglobin is the main chromophore of interest in the methods further described, unless stated otherwise.

3.1.2 Scattering

Scattering is caused by medium inhomogeneities and is the main source of attenuation in tissue. For example, in brain tissue, scattering is approximately 50 times more likely than absorption [105]. Such a medium is called a diffuse medium. Photons are mostly scattered by structures whose size matches the wavelength and with a different refractive index from the surrounding medium. The volume-averaged refractive index in most biological tissue n is around 1.34–1.62, and 1.33 for water [106]. The scattering properties of a medium are described by the scattering

coefficient μ_s [cm^{-1}]; the probability of a photon being scattered over an infinitesimal path. Similarly to the absorption coefficient μ_a, the scattering coefficient is the total cross-sectional area for scattering per unit volume.

When light is scattered in tissue with multiple scattering events and random orientations of scattering structures, the individual scattering angles θ are ignored and the direction of scattering is described using the anisotropy factor g, $g = \langle cos\theta \rangle$, which characterises scattering in terms of the relative forward versus backward direction of scatter [104]. For most tissue, g is high, as the majority of light is scattered forward.

Light travelling through a diffuse medium loses all of its original directionality after a certain distance due to multiple scattering events; the scatter can be assumed to be isotropic. A reduced scattering coefficient is used to describe isotropic scattering; the transport scattering coefficient μ_s', which describes the average pathlength between isotropic scattering events given by $1/\mu_s'$,

$$\mu_s' = \mu_s(1-g). \tag{3.4}$$

In biological tissue, light is mostly scattered on cells and their membranes. Scattering on a sphere of any size is described by Mie theory, and Rayleigh scattering is used for Mie scattering on particles much smaller than the wavelength of light. In tissue, both Mie and Rayleigh theory are used to describe scattering; the dependence of scattering on wavelength is summarised by a combination of both:

$$\mu_s'(\lambda) = a'\Big[f_{Ray}\Big(\frac{\lambda}{500(nm)}\Big)^{-4} + (1-f_{Ray})\Big(\frac{\lambda}{500(nm)}\Big)^{-b_{Mie}}\Big]. \tag{3.5}$$

Equation (3.5) describes the wavelength dependence of scattering in terms of the separate contributions of each type of scattering at the reference wavelength 500 nm. a' is just a scaling factor, $a' = \mu_s'$ (500 nm). The first part of the equation, $a' f_{Ray}(\lambda/500\text{ nm})^{-4}$ accounts for Rayleigh scattering and the second part, $a'(1-f_{Ray})(\lambda/500\text{ nm})^{-b_{Mie}}$ accounts for Mie scattering, b_{Mie} is scattering power describing the wavelength dependence of the process. f_{Ray}, a' and b_{Mie} can be experimentally measured and vary for different tissue types [104].

The wavelength dependence of scattering can be described by a simpler exponential relationship:

$$\mu_s'(\lambda) = a\Big(\frac{\lambda}{500(nm)}\Big)^{-b} \tag{3.6}$$

where a is a scaling factor and is equal to μ_s' at the normalising reference wavelength, which is

500 nm, but can be arbitrary. b, the scattering power, describes the wavelength dependence. As both Eq. (3.5) & (3.6) are equally good for routine prediction of tissue scattering for use in predicting light diffusion behaviour withing 400–1300 nm, either can be used [104]. Additionally, as the relationship between λ and μ_s' visually appears linear in the NIR [107], a linear approximation can be used as an alternative to Eq. (3.6):

$$\mu_s'(\lambda) = a'\lambda + b'. \tag{3.7}$$

Figure 3.2 shows the comparison of the linear and exponential models of the wavelength dependence of scattering based on measurements of μ_s' at 690 nm and 820 nm. Both models give a similar estimate and start diverging at longer wavelengths past 850 nm.

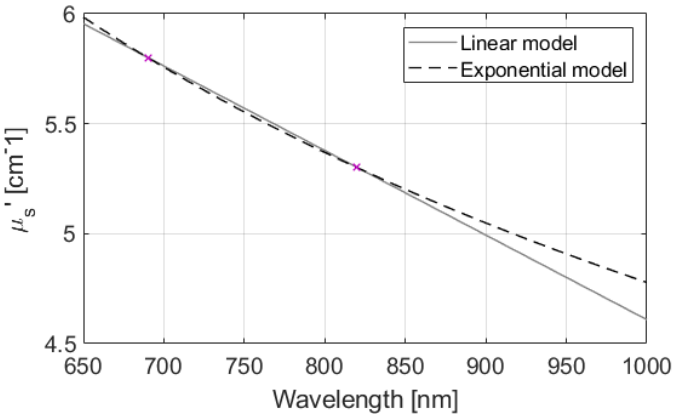

Figure 3.2: The comparison of a linear, Eq. (3.7), and exponential model, Eq. (3.6), of scattering. The two pink data points are μ_s' measured in a neonate [108].

3.1.3 Beer-Lambert law

NIRS is based on quantifying the intensity change of light travelling through tissue which is caused both by absorption and scattering. Attenuation is defined as the ratio of the incident I_0 to transmitted I intensity of a light beam travelling a distance d through an attenuating medium:

$$A = \log_{10}\left(\frac{I_0}{I}\right), \tag{3.8}$$

where $I_0 = I(d = 0)$. Reflectance R is used to describe the fraction of the incident light that has been reflected :

$$R = \frac{I}{I_0}. \tag{3.9}$$

If the beam travels through a purely scattering medium, the intensity loss is described by an exponential decrease:

$$I = I_0 \exp(-\mu_s d). \tag{3.10}$$

In the case of absorption, a similar relationship to Eq. (3.10) is used to describe the attenuation due to absorption of light with intensity I_0 travelling through a purely absorbing medium, the Lambert-Bouguer law:

$$I = I_0 \exp(-\mu_a d). \tag{3.11}$$

The Lambert-Bouguer law can be also expressed in terms of k, Eq. (3.2) as:

$$I = I_0 10^{-kd}. \tag{3.12}$$

For a non-scattering medium, the combination of attenuation, Eq. (3.8), with Eq. (3.12) and (3.3) gives the Beer-Lambert law:

$$A = \log_{10}\left(\frac{I_0}{I}\right) = kd = \varepsilon cd. \tag{3.13}$$

This law states that attenuation is directly proportional to chromophore concentration in the medium. It can be applied to a non-scattering medium containing several different chromophores, their contributions can be summed:

$$A = \sum_n \varepsilon_n c_n d, \tag{3.14}$$

where ε_n and c_n are the specific extinction coefficient and the chromophore concentration of the nth chromophore [109].

3.2 Differential spectroscopy with CW NIRS

The aim of NIRS is to measure concentrations, or concentration changes over time, of HbO_2 and HHb as a way of assessing tissue oxygenation through illumination of the tissue with near-infrared light. The work described in this thesis is focused on measurements in which light with a non-changing intensity constantly illuminates tissue and light that travels through the tissue is detector on the surface. These measurements are called continuous-wave, CW NIRS. Other modes of illumination and detection will be described in later sections.

CW systems use a modified version of the Beer-Lambert law, Eq. (3.14), to link light intensity to chromophore concentration. In contrast to the Beer-Lambert law, which does not account for scattering, the modified Beer-Lambert law (MBLL) (Eq. 3.15) includes two extra terms: G, an

unknown wavelength-dependent term representing light losses due to scattering, and *DPF*, the dimensionless differential pathlength factor that accounts for pathlength increases due to multiple scattering in a diffuse medium. *DPF* has been measured for many different tissue types [110].

$$A = \sum_n \varepsilon_n c_n dDPF + G \tag{3.15}$$

The MBLL assumes homogeneous tissue and no time variations in the scattering properties of the medium and concentrations of other chromophores so that detected light intensity fluctuations can be attributed solely to haemoglobin concentration changes.

The unknown term G prevents calculating absolute chromophore concentrations from light attenuation using MBLL. Therefore, most CW systems measure only temporal concentration changes Δc from attenuation changes ΔA during the measurement period and assume that G at all wavelengths stays constant : $G_{\lambda_j}(t_1) = G_{\lambda_j}(t_2)$ [109].

In order to resolve for absorption by HbO_2 and HHb, measurements at at least two wavelengths λ_j are necessary. The wavelengths to recover haemoglobin are in the NIR range and typically chosen either side of the isosbestic point (Figure 3.1). The aim is to solve Eq. 3.16:

$$A_{\lambda_j} = \log_{10}\left(\frac{I_{0\lambda_j}}{I_{\lambda_j}}\right) = \varepsilon_{HHb,\lambda_j} c_{HHb,\lambda_j} dDPF + \varepsilon_{HbO_2,\lambda_j} c_{HbO_2,\lambda_j} dDPF + G_{\lambda_j}. \tag{3.16}$$

Measurements at two times t_1 and t_2; $\Delta A_{\lambda_j} = A_{\lambda\, j}(t_2)$ - $A_{\lambda\, j}(t_1)$ give:

$$\Delta A_{\lambda_j} = \varepsilon_{HHb,\lambda_j} \Delta c_{HHb,\lambda_j} dDPF + \varepsilon_{HbO_2,\lambda_j} \Delta c_{HbO_2,\lambda_j} dDPF + G_{\lambda_j}(t_2) - G_{\lambda_j}(t_1). \tag{3.17}$$

Looking at only the change of concentrations allows to not account for other tissue chromophores, as their concentrations are assumed constant. In the case of two wavelengths and assuming no change in scattering losses over time ($G_{\lambda_j}(t_1) = G_{\lambda_j}(t_2)$) yields:

$$\begin{bmatrix} \Delta A_{\lambda_1} \\ \Delta A_{\lambda_2} \end{bmatrix} = dDPF \begin{bmatrix} \varepsilon_{HHb,\lambda_1} & \varepsilon_{HbO_2,\lambda_1} \\ \varepsilon_{HHb,\lambda_2} & \varepsilon_{HbO_2,\lambda_2} \end{bmatrix} \begin{bmatrix} \Delta c_{HHb} \\ \Delta c_{HbO_2} \end{bmatrix}, \tag{3.18}$$

with the solution

$$\begin{bmatrix} \Delta c_{HHb} \\ \Delta c_{HbO_2} \end{bmatrix} = \frac{1}{dDPF} \begin{bmatrix} \varepsilon_{HHb,\lambda_1} & \varepsilon_{HbO_2,\lambda_1} \\ \varepsilon_{HHb,\lambda_2} & \varepsilon_{HbO_2,\lambda_2} \end{bmatrix}^{-1} \begin{bmatrix} \Delta A_{\lambda_1} \\ \Delta A_{\lambda_2} \end{bmatrix}, \tag{3.19}$$

which gives the concentration changes of oxyhaemoglobin c_{HbO_2} and deoxyhaemoglobin c_{HHb} between t_1 and t_2.

3.2.1 Broadband CW NIRS

The use of only two wavelengths is sufficient to resolve changes in HbO_2 and HHb, as their absorption spectra are distinct and the concentrations of these chromophores are high in tissue. In theory, adding a third wavelength would enable monitoring of a third chromophore, denoted as X. However, some chromophores of interest are present at much lower concentrations than haemoglobin and can lack distinct spectral features, which makes them difficult to detect. Examples are ICG or CCO, tracking its oxidised state (oxCCO) is used as a marker of cell metabolism. The absorption spectrum features a broad peak and it is difficult to resolve for its concentration changes using only a small number of wavelengths; however, if a broadband spectrum is used in NIRS, the spectral changes due to this third, less concentrated chromophore can be accurately resolved [20, 111, 112]. The matrix representation of bNIRS applying n wavelengths to measure chromophores HbO_2, HHb and X is a variation of Eq. 3.19 :

$$\begin{bmatrix} \Delta c_{HHb} \\ \Delta c_{HbO_2} \\ \Delta c_X \end{bmatrix} = \frac{1}{dB} \begin{bmatrix} \varepsilon_{HHb,\lambda_1} & \varepsilon_{HbO_2,\lambda_1} & \varepsilon_{X,\lambda_1} \\ \varepsilon_{HHb,\lambda_2} & \varepsilon_{HbO_2,\lambda_2} & \varepsilon_{X,\lambda_2} \\ \vdots & \vdots & \vdots \\ \varepsilon_{HHb,\lambda_n} & \varepsilon_{HbO_2,\lambda_n} & \varepsilon_{X,\lambda_n} \end{bmatrix}^{-1} \begin{bmatrix} \Delta A_{\lambda_1} \\ \Delta A_{\lambda_2} \\ \vdots \\ \Delta A_{\lambda_n} \end{bmatrix} \tag{3.20}$$

bNIRS is not only used for the measurement of chromophore concentration changes through the MBLL. The main advantage of bNIRS is that the collection of broadband spectra yields more information about tissue as one can observe absorption peaks of individual chromophores, giving the option to measure additional quantities. Absolute measurements with bNIRS will be further discussed later in this chapter.

3.3 NIRS instrumentation

The main components of a basic NIRS system are a light source and a detector; the system can have several source-detector pairs to cover multiple brain regions at once. The light source and detector can be either small and be placed directly on the skin or can be connected to the skin using optical fibers. The systems usually operate in reflectance mode; with the probes holding light sources and detectors placed on the examined tissue. Monitoring of the frontal lobe through the forehead is a popular solution as it avoids signal loss due to hair in the way. Systems with

many measurement channels (light source-detector pairs) are also available for the imaging of the whole head. The distance between the source and detector is related to the depth of light penetration; the light that reaches the detector travels an elliptical path, increasing source-detector distances enables deeper light penetration but bigger intensity losses. It is key to find a compromise between required detected intensity, preventing tissue damage from optical power and sufficient depth penetration. For adults, commonly used source-detector distances are around 3 cm, which enable imaging up to a depth of 2 cm and can provide information about the oxygenation of grey matter [102]. The light source of choice depends on the applied wavelengths; some instruments use only a few wavelengths, other use broadband sources with tens to hundreds of wavelengths. The sources can be laser diodes, lasers, light-emitting diodes (LEDs) or white light sources, such as halogen lamps. The emitted light is delivered to the tissue, travels through the skull and is collected by the detector or detector fibres. It is then measured by a charge-coupled device (CCD) camera or photodiode [111].

The attenuation of the light travelling through tissue depends on the optical properties of the illuminated tissue. The Beer-Lambert law, Eq. (3.14), presents a way of quantifying chromophore concentration changes by measuring the attenuation of light over time. However, as it holds only in a non-scattering medium, it cannot be directly used in NIRS; more complex techniques have been developed to measure optical properties of a diffuse medium. NIRS systems are divided into three main categories based on the length of illumination of the monitored tissue, detection mode and the data analysis.

Time resolved (TR) NIRS (Figure 3.3a) is a complex method able to measure optical properties of a medium and use these to obtain absolute values of chromophore concentrations, generally HbO_2 and HHb. An ultrashort ($\approx$ 100 ps) pulse of light is emitted into tissue and is attenuated by absorption and broadened by scattering. The distribution of the photon arrival times (the time point spread function of the light passed through the tissue) is measured and saved in the form of a histogram of number of photons and their arrival time [113]. The optical properties of the medium (the transport scattering coefficient μ_s', the absorption coefficient μ_a and also the length of the photon path) are calculated from the time response function. It is also possible to selectively target different depths of tissue by time gating the signal, only collecting photons arriving after a certain time, as photons travelling through deeper tissue take longer to arrive [114]. TR NIRS is the most informative NIRS technology but also the most complex one [115], its commercial availability is limited.

Frequency domain (FD) (Figure 3.3b) NIRS, also called phase modulation/intensity modulated spectroscopy is a Fourier domain equivalent of TR measurements. An intensity modulated (50 MHz to 1 GHz) light wave passes through tissue and emerges with a phase shift caused by light attenuation in tissue. The phase shift contains information about the time of flight. Scanning through all frequencies is required to obtain the same information as from TR NIRS. If a system measures at only one frequency, the use of a multidistance setup with two or more light source-detector separations (SDS) can yield information about the tissue oxygenation [114, 115].

CW (Figure 3.3c) systems emit light at a constant intensity and measure only the intensity change of the light emerging from tissue. The systems are thus simpler than FD and TR systems and do not generally measure absolute optical properties of tissue, most applications measure only changes of chromophore concentrations using the MBLL. The simplicity of CW systems makes them desirable for commercial application and several data analysis techniques have been developed to allow absolute quantification of optical properties. These will be discussed in the next section.

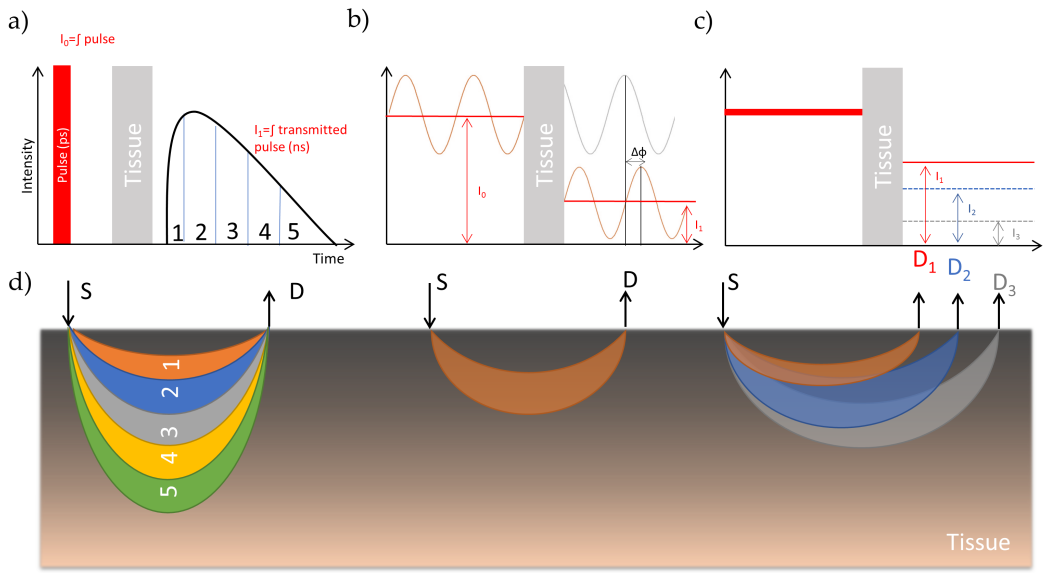

Figure 3.3: Schematic of the three NIRS detection modes. (a) TD NIRS mode, an ultra-short light impulse is shined onto the tissue and the broadened and attenuated re-emitted pulse is measured after passing through the tissue. (b) FD NIRS, a modulated continuous light source is shined onto the tissues and phase shift $\Delta\phi$ of the emerging attenuated light is measured. (c) CW NIRS, a continuous light is shined onto the tissues and the attenuated re-emitted light is measured. (d) Representation of the photon path in tissues for each technique. S: source, D: detector. Taken from [114].

3.4 Absolute measurements with continuous-wave NIRS

The primary application of CW NIRS is the measurement of chromophore concentration changes with differential spectroscopy; these starts from an arbitrary zero baseline and are used for trend monitoring. Absolute NIRS measurements allow a quantification of absolute optical properties and an immediate assessment of the monitored tissue haemodynamics.

Absolute optical measurements are more complicated requiring complex NIRS setups. Two main problems need to be taken into account when designing instrumentation for absolute measurements [112]:

- Multiple scattering events in biological tissue makes estimation of μ_a more difficult than similar measurements in a non-scattering medium in a standard analytical spectroscopy setting.
- Tissue contains other chromophores than just haemoglobin and those contribute to the overall absorption. While their concentrations are assumed constant during NIRS trend measurements, this is no longer relevant when quantifying absolute absorption.

The means of dealing with these problems differ among systems. FD and TR NIRS apply advanced engineering solutions to separate scattering and absorption directly and often account for additional chromophores, mostly water [104]. In CW NIRS, separation of scattering and absorption is challenging and many different algorithms have been developed to obtain an absolute assessment of tissue optical properties.

Data analysis algorithms are based on diffusion theory, which models the propagation of light in biological tissue. The next section of this chapter provides a brief introduction to diffusion theory followed by an overview of methods of absolute CW NIRS measurements.

3.4.1 Radiative transfer equation and the diffusion equation

The radiative transfer equation, RTE, is an analytical model of the propagation of electromagnetic waves in an attenuating medium. It is essentially an expression of the conservation of energy, describing the changes of radiance $L(\vec{r},\hat{s},t)$ due to attenuation, and its simplified versions are used to model light propagation in tissue in NIRS.

Spectral radiance L_v is the energy flow per unit normal area per unit solid angle per unit time per unit temporal frequency bandwidth, where the normal area is perpendicular to the direction of the flow. Radiance $L(\vec{r},\hat{s},t)$ is the spectral radiance integrated over a narrow frequency range

$(\nu, \nu+\Delta\nu)$, where $\vec{r}$ is the position, $\hat{s}$ is the unit direction vector, t is time;

$$L(\vec{r},\hat{s},t) = L_v(\vec{r},\hat{s},t)\Delta\nu. \tag{3.21}$$

Fluence rate Φ is the energy flow per unit area per unit time regardless of the direction of the flow:

$$\Phi(\vec{r},t) = \int_{4\pi} L(\vec{r},\hat{s},t)d\Omega, \tag{3.22}$$

where $d\Omega$ is a differential solid angle element. Current density $\vec{J}$ is the net energy flow per unit area per unit time:

$$\vec{J}(\vec{r},t) = \int_{4\pi} \hat{s}L(\vec{r},\hat{s},t)d\Omega. \tag{3.23}$$

Based on these quantities, the RTE for $L(\vec{r},\hat{s},t)$ travelling through an infinitesimal volume at the speed of light c is:

$$\frac{1}{c}\frac{\partial L(\vec{r},\hat{s},t)}{\partial t} = -\hat{s}\cdot\nabla L(\vec{r},\hat{s},t) - \mu_t L(\vec{r},\hat{s},t) + S(\vec{r},\hat{s},t) + \mu_s \int_{4\pi} L(\vec{r},\hat{s}',t)P(\hat{s}'\cdot\hat{s})d\Omega'. \tag{3.24}$$

P is a phase function describing the probability of light travelling with direction $\hat{s}'$ being scattered in the direction $\hat{s}$. S is additional power injected into the volume and μ_t is the total attenuation coefficient equal to the sum of the absorption coefficient μ_a and the scattering coefficient μ_s [116]. The RTE consists of 5 main terms:

- $\frac{1}{c}\frac{\partial L(\vec{r},\hat{s},t)}{\partial t}$ is the change in radiance in a short time t caused by the following events:
- $-\hat{s}\cdot\nabla L(\vec{r})$ is the net inflow of light entering or leaving the volume.
- $-\mu_t L(\vec{r},\hat{s},t)$ is the intensity loss due to attenuation.
- $S(\vec{r},\hat{s},t)$ is additional light being injected into the volume.
- $\mu_s \int_{4\pi} L(\vec{r},\hat{s}',t)P(\hat{s}'\cdot\hat{s})d\Omega'$ is light scattered into direction $\hat{s}$ from direction $\hat{s}'$.

Solving the RTE analytically is complicated; it can be simplified by applying the diffusion approximation, which assumes that the radiance in a medium with much stronger scattering than absorption, $\mu_s' \gg \mu_a$, is nearly isotropic after sufficient scattering [106]. The probability of scattering in biological tissue is much higher than absorption and diffusion theory is used to model light propagation.

3.4.1.1 Derivation of the diffusion equation

Functions defined over the sphere can be represented on the basis of spherical harmonics, an infinite set of harmonic functions [117]. Expanding radiance through first order spherical harmonics $Y_{n,m}$, Eq. (3.25), leads to the diffusion equation.

$$L(\vec{r},\hat{s},t) \approx \sum_{n=0}^{1} \sum_{m=-n}^{n} L_{n,m}(\vec{r},t) Y_{n,m}(\hat{s}), \tag{3.25}$$

where $L_{n,m}$ are the expansion coefficients and the term for $n = 0$ and $m = 0$ represents the isotropic component of radiance, the term for $n = 1$ and $m = 0,\pm 1$ represent the anisotropic component [106]. Approximating radiance as almost isotropic with one isotropic and one first-order anisotropic term yields

$$L(\vec{r},\hat{s},t) = \frac{1}{4\pi}\Phi(\vec{r},t) + \frac{3}{4\pi}\vec{J}(\vec{r},t)\hat{s}. \tag{3.26}$$

Substituting Eq. (3.26) into the RTE, Eq. (3.24), assuming an isotropic light source and integrating over the full 4π gives

$$\frac{\partial\Phi(\vec{r},t)}{c\partial t} + \mu_a\Phi(\vec{r},t) + \nabla\vec{J}(\vec{r},t) = S(\vec{r},t). \tag{3.27}$$

Fluence rate can be regarded as a measure of concentration and the diffusion of photons in a scattering medium as the movement of photons down concentration gradients [118]. Fick's law, Eq. (3.28) states that the current density $\vec{J}(\vec{r},t)$ down a concentration gradient is:

$$\vec{J}(\vec{r},t) = -D\nabla\Phi(\vec{r},t). \tag{3.28}$$

The constant D is the diffusion coefficient,

$$D = \frac{1}{3(\mu_a + \mu_s')}. \tag{3.29}$$

Applying Fick's law; substituting Eq.(3.28) in Eq. (3.27) yields the diffusion equation

$$\frac{\partial\Phi(\vec{r},t)}{c\partial t} + \mu_a\Phi(\vec{r},t) - \nabla[D\nabla\Phi(\vec{r},t)] = S(\vec{r},t). \tag{3.30}$$

Two approximations were made: radiance was approximated only in first order harmonics and that the fractional change in current density in one transport mean free path is small. Both can be translated into a single condition $\mu_s' \gg \mu_a$ to achieve a diffuse medium.

When light enters a medium, the fluence rate does not peak on the surface, but at a distance

slightly beneath it, due to photons being backscattered at the boundary and contributing to the fluence rate. This region is of the order of about two to three transport mean free paths ($\sim$ 3 mm in biological tissue with $\mu_s' \approx 1$ mm^{-1}) and the diffusion equation does not apply in this region [119].

3.4.1.2 Solutions to the diffusion equation

The solution to the diffusion equations depends on the type of medium the light is travelling through. For the majority of applications in NIRS, biological tissue is considered a homogeneous, semi-infinite slab. Taking the layered structure of the human head into account, with tissue, skull, cerebrospinal fluid and then the layers of the brain itself, this assumption could lead to inaccuracies. Tissue inhomogenities become particularly important when they occur on a greater spatial scale than the distance over which the photon direction is randomised (given by the transport mean free path, around 1 mm in most tissue). Measurements at SDS of 15–40 mm have shown that if the shallow layer is thin, $\sim$ 4 mm, the optical properties recovered with homogeneous models are representative of the deeper layer, whereas they are representative of the shallow layer if it is thicker than $\sim$ 13 mm [120]. As the extracerebral layers in neonates are thin (the skull thickness is 1.5–2.5 mm [52]), the use of a homogeneous model is sufficient. However, the thickness of adult extracerebral layers often exceeds 1 cm [121], heterogenenous models can be considered for a more precise measurement. The use of models applying two- [122, 123, 124, 125, 126] or three-layer [127] geometries has been demonstrated but the practical application remains challenging, as some a-priori information about the layers is required. The work described in this thesis is focused on neonatal application, the model applied is the semi-infinite homogeneous medium slab model.

While the layered structure can be simplified, the homogeneous slab model introduces a different type of error in neonatal NIRS measurements - the curvature of the neonatal skull is the dominant source of errors when recovering absorption [121]. Fortunately, the effect of the head curvature have been found to be minimal when recovering tissue oxygenation StO_2 [128].

Solving the diffusion equation requires a selection of boundary conditions, which constrain the possible distribution of photons in the medium. The aim is to obtain a solution to the diffusion equation that is equal to the solution to the RTE in the asymptotic region. While different types of boundary conditions with varying complexity can be used [129, 130], two particular types are used most commonly in NIRS: the zero boundary (ZBC) and extrapolated boundary conditions (EBC).

Zero boundary conditions

ZBC are the most simple and approximate conditions, used in many NIRS applications [25]. The

average fluence rate is set equal to zero at the physical boundary, $\phi(\rho, z = 0) = 0$ [130, 131]. While not physically correct as this situation does not account for the reflection of photons at the boundary, it is a simple expression that can be rapidly evaluated. Zero fluence rate at the boundary is achieved by placing the light source inside the medium, at a distance $z_0 = (\mu_a + \mu_s')^{-1}$ and by placing a negative image source at $-z_0$, Figure 3.4. Solving the diffusion equation for a semi-infinite homogeneous medium with these boundary conditions illuminated by a continuous-wave light source leads to a reflectance R_{ZB} at a distance from the light source ρ [109, 132]:

$$R_{ZBC}(\rho) = \frac{z_0}{2\pi r_1^2}\left(\frac{1}{r_1} + \mu_{eff}\right) exp\left(-\mu_{eff} r_1\right), \tag{3.31}$$

where $r_1^2 = z_0^2 + \rho^2$ and μ_{eff} is the effective attenuation coefficient; $\mu_{eff} = \sqrt{3\mu_a(\mu_a + \mu_s')}$.

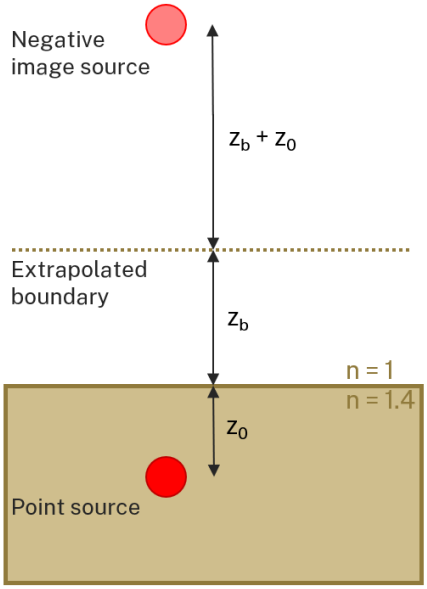

Figure 3.4: Source and image configuration for two types of boundary conditions, ZBC and EBC. In the case of ZBC, the negative image source is placed at a distance -z_0, z_b is zero. For EBC, z_b is given by Eq. (3.32).

Extrapolated boundary conditions

EBC state that the fluence rate equals zero at a point outside of the medium, the extrapolated boundary, placed at $-z_b$. This provides much more accurate estimates of the fluence in the medium near a boundary than ZBC [130]. A point source is placed at z_0 and a negative source at $-z_0 - 2z_b$, where z_b is:

$$z_b = \frac{1 + R_{eff}}{1 - R_{eff}} 2D, \tag{3.32}$$

where R_{eff} is the fraction of photons that is diffusely reflected at the boundary. It was calculated that for the refractive index of biological tissue $n = 1.4$, $R_{eff} = 0.493$ [116, 133]. D is the diffusion coefficient; $D = 1/[3(\mu_a + \mu_s')]$. Solving the diffusion equation for a semi-infinite, homogeneous medium yields reflectance R_{EB} from a continuous-wave light source:

$$R_{EBC}(\rho) = \frac{1}{4\pi}\Big[z_0\big(\mu_{eff} + \frac{1}{r_1}\big)\frac{exp(-\mu_{eff}r_1)}{r_1^2} + (z_0 + 2z_b)\big(\mu_{eff} + \frac{1}{r_2}\big)\frac{exp(-\mu_{eff}r_2)}{r_2^2}\Big], \quad (3.33)$$

where $r_1^2 = z_0^2 + \rho^2$ and $r_2^2 = (z_0 + 2z_b)^2 + \rho^2$ [134].

For most applications, using ZBC is sufficiently precise; it introduces large errors close to the light source but is a sufficiently good approximation for biological tissues. Using EBC improves the model of light transport for a more precise measurement [116, 131, 134].

3.4.2 Broadband spectral analysis with CW NIRS

One of the earliest absolute measurements obtained with CW NIRS was the measurement of *DPF* with the use of broadband spectra and evaluating the features corresponding to tissue chromophores.

Water is an important tissue chromophore, its absorption is much weaker than haemoglobin within 650–900 nm but it does contribute to the overall attenuation as it is present at high concentrations. Water lacks any significant spectral features in the optical window, but it is possible to emphasise them through obtaining a second spectral derivative of the spectrum. Figure 3.5 shows how features in the absorption spectra of the chromophores become much more apparent through differentiation.

The use of the water absorption spectrum to quantify the differential pathlength factor *DPF*, defined in Eq. (3.15), was introduced by Matcher and colleagues [135]. The method is based on measuring the amplitude of water spectral absorption features and relating them to *DPF*: as *DPF* exceeds d (the distance travelled through a absorbing medium) by a factor of three to six, also the amplitudes of the spectral features of absorbers increase by the same factor [135]. It is hence possible to relate the amplitude of water features to *DPF* thanks to the concentrations of water in tissue being generally stable and known [136]. An issue in measuring the amplitude of spectral features is that an *in vivo* spectrum has an arbitrary baseline offset caused by scattering losses and also system photometry. It can be overcome by performing a differential analysis; the use of spectral derivatives removes optode surface-tissue contact artifacts and baseline offsets [135, 137, 138].

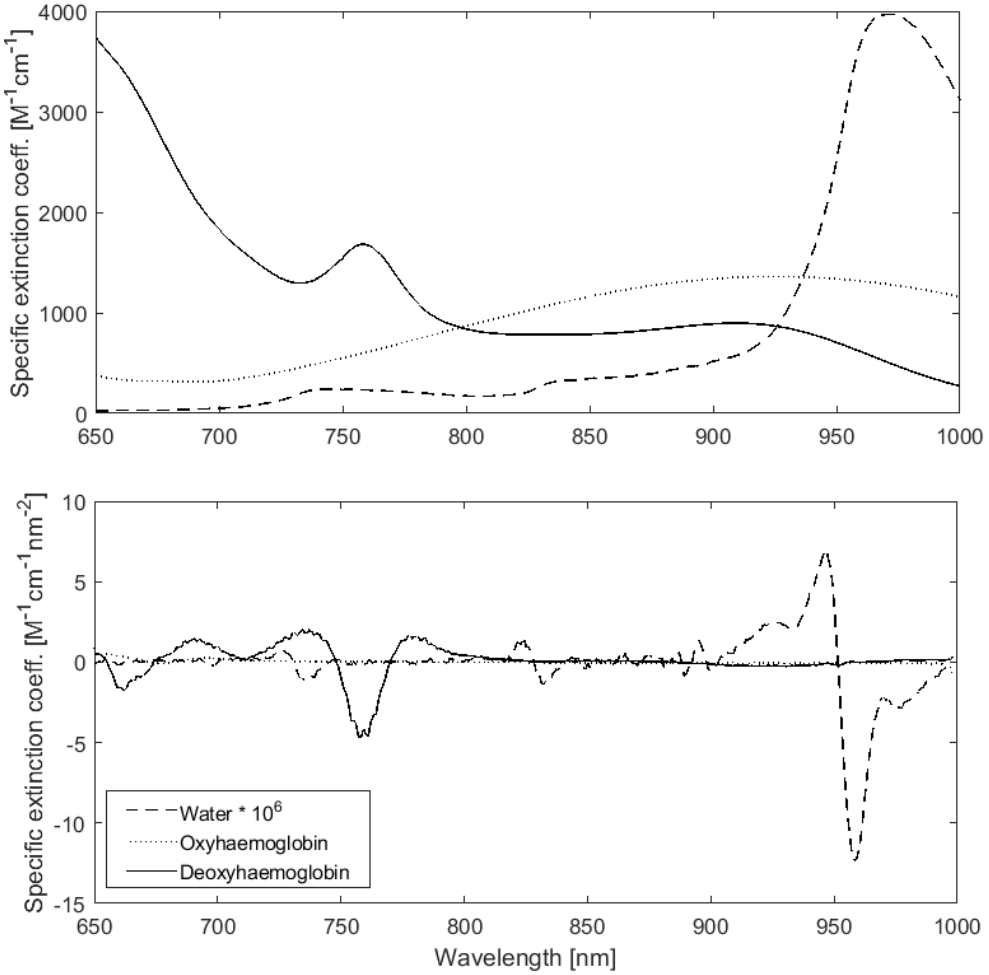

Figure 3.5: The extinction spectra of haemoglobin and water and their second spectral derivative. The specific extinction coefficient of water was multiplied by 10^6 to make its features more apparent. Extinction spectra measured by Wray et al. (1998) [136].

As seen in Figure 3.5, the second derivative water spectrum for water has three distinctive features which can be used for the estimation of *DPF*: a large 950 nm feature and smaller, yet for high *DPF* visible, features at 730 nm and 820 nm. The 820 nm H_2O feature is most suitable for analysis, as the 730 nm feature is hidden by the larger HHb features in that region and the 950 nm feature does not show water concentration accurately as absorption is higher and scattering lower at this wavelength. To obtain the *DPF*, the height of the water peak at 820 nm is measured and compared to the size of the water peak in a non-scattering medium. Combining the ratio of these amplitudes with the concentration of water in the solutions gives the *DPF* [135].

The method was further developed to also calculate the absolute concentrations on HHb [137]. Next to the amplitude of the water feature, the amplitude of the 760 nm Hb feature is also measured. As the concentration of water is known, one can calculate the concentration

of HHb from the amplitude ratio. HbO_2 is not included in the analysis as the second spectral differential spectrum has no significant features (Figure 3.5). Additionally, if the method is combined with another measurement of blood volume (total haemoglobin HbT concentration), one can calculate oxyhaemoglobin concentrations. The main drawback of this method is that it is based on a homogeneous medium, the accuracy relies on the knowledge of water concentration and wavelength-dependent effects of scattering are not accounted for.

3.4.3 Tissue oxygen saturation measurements

Measurements of chromophore concentration changes in a clinical setting is used for regional oxygenation trend monitoring. A desirable improvement of NIRS monitoring is the addition of an absolute measurement of the oxygenation of tissue.

NIRS systems to measure absolute c_{HHb} and c_{HbO_2} require advanced engineering solutions to account for scattering and absorption. Therefore, an index which does not require knowledge of absolute μ_a and μ_s' is used, StO_2, defined as the ratio of c_{HbO_2} and c_{THb}.

$$StO_2 = \frac{c_{HbO_2}}{c_{HHb} + c_{HbO_2}} \times 100\% = \frac{c_{HbO_2}}{c_{THb}} \times 100\%, \tag{3.34}$$

where c_{THb} is total haemoglobin concentration. StO_2 is a measurement of oxygen saturation SO_2, the amount of O_2 bound to haemoglobin relative to the maximal amount of O_2 that can be bound to haemoglobin. It is of great clinical interest, as it can inform on the balance between oxygen supply and demand.

Several different methods to measure StO_2 have been developed. Two different engineering setups are mostly used for the measurement:

- Single-distance measurements: these methods apply one light source-detector pair (as in a standard MBLL setup) to obtain a measure of StO_2. They can benefit from a broadband approach, similarly to the absolute measurements of DPF and c_{HHb} described previously, the individual features of chromophores visible in a broadband spectrum can be identified. The measured spectra can be directly compared to a theoretical model of the spectrum from diffusion theory, leading to the quantification of StO_2.

- Multidistance measurement: instead of using just one detector, at least two light source-detector pairs are used. The detectors are placed at different SDS from the light source. Attenuation or reflectance is measured at each distance; the multidistance setup allows for the quantification of the change of the quantity over distance; the slope. The benefit of this

approach is that it decreases the contamination of the signal from extracerebral layer contributions [100]. As light travels through tissue from the light source towards the detectors at multiple distances ρ, it shines through the superficial (extracerebral) layers and the deeper tissue layers (brain), before emerging at the surface and being detected. The depth of penetration increases with ρ, the contribution of the extracerebral tissue signal is considered equal at all separations. The contribution of the extracerebral layers can be cancelled out, leaving a measurement of the attenuation slope with signal from the deep tissue, Figure 3.6. This slope is then used to calculate StO_2.

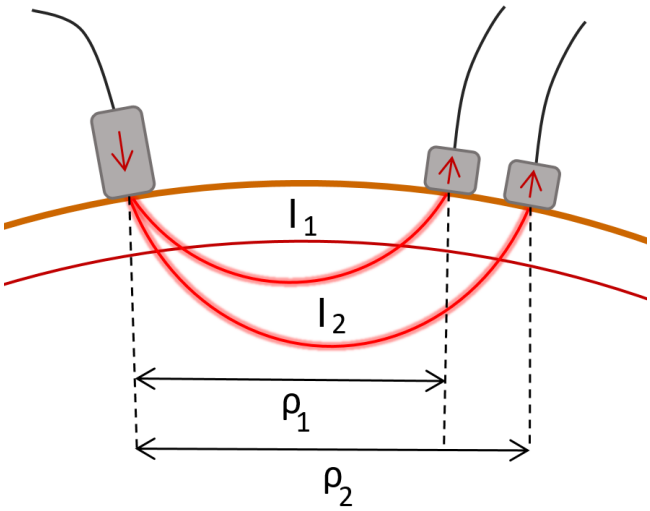

Figure 3.6: Diagram of a multidistance NIRS approach. Light emitted from the light source (left) travels through the outer layer and the inner layer in tissue before reaching the two detectors (right). The contribution of the outer layer is considered equal at both distances, hence cancels out when measuring the slope of light attenuation/reflectance against distance.

Table 3.1 shows a summary of different CW NIRS measurement methods developed for the measurement of StO_2. While a few algorithms used in commercial systems are included, most manufacturer's algorithms are not published. Out of the main published algorithms to recover StO_2, two have been selected to be used in this work, spatially resolved spectroscopy (SRS) and broadband fitting (BF). The application of the algorithms to multidistance broadband NIRS data is explored in Chapters 6 and 7.

3.4.4 Spatially resolved spectroscopy

SRS is a multidistance approach based on the solution to the diffusion equation with ZBC. ZBC reflectance is defined in Eq. (3.31); and for large detectors spacings, where $\rho^2 >> z_0^2$, is equal to:

$$R_{SRS}(\rho) = z_0 \mu_{eff} \frac{\exp(-\mu_{eff}\rho)}{2\pi\rho^2}. \tag{3.35}$$

Attenuation A can be calculated from Eq. (3.35) and Eq. (3.8):

$$A = -\log_{10}(R(\rho)) = -\frac{1}{\ln(10)} \ln(R(\rho)), \tag{3.36}$$

leading to

$$A_{SRS} = \frac{1}{\ln(10)} \Big[\mu_{eff}\rho + 2\ln\rho - \ln\frac{z_0\mu_{eff}}{2\pi} \Big]. \tag{3.37}$$

By making the assumption that $\mu_a + \mu_s' \approx \mu_s'$ (typically valid in human tissue [108]) and differentiating Eq. (3.37) with respect to ρ, we obtain the slope of attenuation against distance:

$$\frac{\partial A}{\partial \rho} = \frac{1}{\ln(10)} \Big(\sqrt{3\mu_a\mu_s'} + \frac{2}{\rho} \Big). \tag{3.38}$$

The attenuation derivative is measured through the multidistance approach. First, attenuation for each detector is calculated as the logarithm of the ratio of the initial intensity I_0 and the measured intensity I:

$$A = \log_{10} \frac{I_0}{I}. \tag{3.39}$$

Secondly, the slope of attenuation with respect to distance $\frac{\partial A}{\partial \rho}$ is approximated by fitting the relationship between SDS and attenuation with a linear relationship.

To quantify μ_s', the linear dependence of scattering on wavelength, $\mu_s' = a\lambda + b$, is used and written in the form of $\mu_s' = k_{SRS}(1 - h\lambda)$. h is the normalised slope of μ_s' along λ and was experimentally measured to be $h = 0.00063\ \mathrm{mm^{-1}nm^{-1}}$ in the adult head [112, 25]. The scattering assumption applied to Eq. (3.38) introduces a scaled $k_{SRS}\mu_a$:

$$k_{SRS}\mu_a(\lambda) = \frac{1}{3(1-h\lambda)} \left(\ln(10) \frac{\partial A(\lambda)}{\partial \rho} - \frac{2}{\rho} \right)^2, \tag{3.40}$$

leading to a scaled concentration of oxy- and deoxyhaemoglobin obtained by measuring attenua-

tion at at least two wavelengths;

$$\begin{bmatrix} k_{SRS}\mu_{a,\lambda_1} \\ k_{SRS}\mu_{a,\lambda_2} \end{bmatrix} = \ln(10) \begin{bmatrix} \varepsilon_{HHb,\lambda_1} & \varepsilon_{HbO_2,\lambda_1} \\ \varepsilon_{HHb,\lambda_2} & \varepsilon_{HbO_2,\lambda_2} \end{bmatrix} \begin{bmatrix} k_{SRS}c_{HHb} \\ k_{SRS}c_{HbO_2} \end{bmatrix}, \tag{3.41}$$

with the solution

$$\begin{bmatrix} k_{SRS}c_{HHb} \\ k_{SRS}c_{HbO_2} \end{bmatrix} = \frac{1}{\ln(10)} \begin{bmatrix} \varepsilon_{HHb,\lambda_1} & \varepsilon_{HbO_2,\lambda_1} \\ \varepsilon_{HHb,\lambda_2} & \varepsilon_{HbO_2,\lambda_2} \end{bmatrix}^{-1} \begin{bmatrix} k\mu_{a,\lambda_1} \\ k\mu_{a,\lambda_2} \end{bmatrix}. \tag{3.42}$$

The authors of SRS refer to their measure of StO_2 as the tissue oxygenation index, TOI, which is equal to StO_2 [25]:

$$TOI = \frac{k_{SRS}c_{HbO_2}}{k_{SRS}c_{HbT}} \times 100\% = \frac{c_{HbO_2}}{c_{HbT}} \times 100\% = StO_2. \tag{3.43}$$

3.4.5 Broadband fitting

The broadband, single distance algorithm to measure StO_2 has no official name yet; it has been referred to as "hyperspectral NIRS" [139]. Such terminology can lead to confusion with other hyperspectral imaging methods [140], it is hence referred to as *broadband fitting* (BF) in this work.

BF uses a model of light propagation in a semi-infinite homogeneous medium. Such model selection is suitable for the use of BF to recover StO_2 from measurements in the neonatal head, where signal contamination from extracerebral tissue is small at SDS of 3 cm and above [121]. Reflectance obtained from the solution to the diffusion equation obtained with EBC, R_{EBC}, is in Eq. (3.33) and is characterised in terms of μ_a and μ_s'. The aim of the algorithm is to recover the optical properties of the illuminated tissue through the comparison of the model R_{EBC} to the measured broadband reflectance R_M. The measured reflectance is calculated from the measured signal, the reference spectrum and dark noise:

$$R_M = \left(\frac{signal_\lambda - dark_\lambda}{reference_\lambda - dark_\lambda}\right). \tag{3.44}$$

The dependence of the model on the optical properties of the medium is described in terms of the effective attenuation coefficient μ_{eff}, $\mu_{eff} = \sqrt{3\mu_a(\mu_a + \mu_s')}$. The comparison of the model to the measured data is obtained through least-squares fitting, where μ_s' and μ_a are iteratively updated until the difference between the two data sets is minimised.

The updates of μ_s' and μ_a are achieved through the optimisation of 5 different fitting parameters: water fraction WF, c_{HbO_2}, c_{HHb}, a and b, originating from the definitions of μ_s' and μ_a.

μ_a is calculated from the concentrations of the chromophores HHb, HbO_2 and water. While additional compounds absorb light in the BF wavelength range (650–850 nm), their contribution is weaker than the absorption by water and haemoglobin [141].

$$\mu_a(\lambda) = c_{HbO_2}\alpha_{HbO_2}(\lambda) + c_{HHb}\alpha_{HHb}(\lambda) + WF\mu_{a_{H_2O}}(\lambda) \tag{3.45}$$

where α is the specific absorption coefficient. The relationship between μ_s' and wavelengths λ is described by the exponential approximation to Mie scattering normalised at a selected wavelength, usually 500 nm, 800 nm or 1000 nm [104]:

$$\mu_s'(\lambda) = a\left(\frac{\lambda}{wavelength}\right)^{-b}, \tag{3.46}$$

where a is the scattering amplitude and equal to μ_s' at the selected normalisation wavelength, *wavelength*; b is scattering power.

The optimisation routine is performed in the first and second spectral derivative space to emphasise absorption features of the individual chromophores. The fitting procedure is split into three steps to target individual spectral features of the chromophores [142]:

1. WF is found by fitting the second derivative of R, $\frac{\partial^2 R}{\partial \lambda^2}$, between 825 and 850 nm, in the range of prominent water absorption features.

2. After fixing the found water fraction WF, c_{HHb} is found by fitting $\frac{\partial^2 R}{\partial \lambda^2}$ between 700 and 800 nm, as this range has a distinct 760 nm HHb feature.

3. For the last step, c_{HHb} is also set constant and c_{HbO_2}, a and b are determined from fitting the first spectral derivative of R, $\frac{\partial R}{\partial \lambda}$, 680 to 845 nm.

Oxygenation is then expressed in terms of tissue oxygen saturation StO_2:

$$StO_2 = \frac{c_{HbO_2}}{c_{HHb} + c_{HbO_2}} \times 100\%. \tag{3.47}$$

3.5 Summary

Near-infrared spectroscopy measurements of haemoglobin concentration are based on the relative transparency of light in the near-infrared region. Continuous-wave systems emit light continuously into tissue, and the reflected light is collected in a detector on the tissue surface. The fluctuations in the signal are attributed to the changes in the concentrations of oxygenated and deoxygenated haemoglobin, or other chromophores of interest, offering a simple and non-invasive way of real-time measurements of oxygen delivery.

Absolute measurements of tissue oxygenation are the subject of cerebral oximetry. It measures an indicator of tissue saturation, StO_2, a relative measurement of oxygenated haemoglobin concentration and informs on the balance between cerebral oxygen supply and demand. Many different algorithms to measure StO_2 with CW NIRS have been developed. They are based on the approximation of light transport in tissue with the diffusion equation, and are able to account for scattering losses. A popular setup is the use of multidistance measurements of light attenuation to decrease the influence of superficial tissue layers on the measurement, and quantify StO_2.

Table 3.1: Methods for the measurement of cerebral StO_2 with CW NIRS. SD - single-distance, MD - multidistancem, BB - broadband

Author (year)	Setup	Description
Matcher (1995) [112]	MD	Known as *spatially resolved spectroscopy*, SRS. Measurements of attenuation at a few discrete wavelengths and multiple SDS give $\partial A(\lambda)/\partial\rho$. R_{ZBC} is used to calculate $\mu_a \times \mu_s'$, an an approximation of the wavelength dependence of scattering leads to a scaled μ_a. Multilinear regression of these estimates using the spectra of HHb and HbO_2 leads to StO_2. SRS widely used for the measurement of StO_2 as it is implemented in the commercial NIRO machines (Hamamatsu, Japan) [25] and it has been shown the multidistance approach applied does increase the sensitivy of the measurement to the intracranial signal [143].
Liu (1995) [144]	MD	Measured reflectance is approximated by a linear dependence on source-detector separation $\log[\rho^2 R(\rho,\rho_0)]$. Measurements are conducted at at least 2 cm separation at discrete wavelengths. The slope of the reflectance approximation versus ρ gives μ_{eff}. μ_a and μ_s' can be quantified with respect to a calibration sample with known attenuation properties. c_{HHb} and c_{HbO_2} are calculated from μ_a and lead to StO_2.
Hueber (1999) [145]	MD	The method is an extension to SRS, which uses at least two detectors and two light sources in a symmetrical arrangement, each detector collects light from both sources. The slope is calculated from all four intensity measurements, cancelling out the coupling factors of each source and detector, reducing the influence of movement artifacts [100].

Author (year)	**Setup**	Description
Benni (2002) [146]	SD	The method used in the FORE-SIGHT oximeter (CAS Medical Systems, US) is based on a single distance measurement at a few wavelengths. Light is emitted at different wavelengths and the signal intensity is measured as a function of wavelength. A calibration of the system using empirically determined SvO_2 and SaO_2 values then relates the attenuation measurements to StO_2.
Yeganeh (2012) [26]	SD BB	In this work referred to as *broadband fitting*. The method is based on a single-distance broadband (680 - 845 nm [147]) reflectance measurement. The reflectance is compared to a theoretical model of reflectance, R_{EBC}, in a least-squares fitting procedure. The fitting is performed is the first and second spectral derivative space, as it decreases the influence of detector coupling errors [138] and makes spectral features of different chromophores more prominent. The fitting recovers μ_s' and μ_a, leading to StO_2.
Kleiser (2018) [12]	MD	The algorithm applied in the OxyPrem v1.3 instrument is based on SRS, but with a different MD setup with 4 wavelengths, 2 detectors and 4 light sources. This creates two regions of interest, inner and outer, which have different SDS and depth sensitivity, giving two different StO_2 measurements and their mean value. The instrument is also self-calibrating, which enables the compensation for local inhomogeneity, such as birth marks or hair underneath the probes, giving a robust StO_2 measurement.
Deepak Veesa (2019) [148]	MD	An expansion of SRS through accounting for scattering losses. It is assumed that $\mu_s'(\lambda) = aS(b,\lambda)$, where $S(b,\lambda) = (\lambda)^{-b}$, and the ZBC reflectance model is fitted with unknown normalised chromophore concentrations aC_j and the scattering amplitude b.

Chapter 4

Cerebral oximetry: application in neonatal care

The measurement of oxygenation StO_2 in the brain with NIRS, cerebral oximetry, is used in the clinical care to detect hypoxia. The following chapter describes the establishment of StO_2 in intensive care and the various challenges which hinder its spread among units; later sections focus on the application in the NICU. The last section includes a review of clinical StO_2 measurements in neonates with brain injury.

4.1 Cerebral oximetry in the intensive care

Brain oximetry is used in the critical care for the detection of hypoxia and hyperoxia; the aim is to deepen the clinician's understanding of brain physiology and pathophysiology and guide the development of injury management strategies to prevent severe brain injury. Brain injury can occur during surgery or in the postoperative period; cerebral oximetry has been applied in cardiac surgery, pediatric surgery, traumatic brain injury, carotid endarterectomy and other situations [4, 149]. Cerebral oximetry is also suitable for the use in the NICU for monitoring of preterm and full term infants; several complications can lead to issues with cerebral oxygen supply in the neonatal brain, such as birth injuries and congenital malformation [103]. Cerebral oximetry in term infants with brain injury is the focus of this work.

Standard methods currently used to assess cerebral haemodynamics include jugular venous oximetry, trans-cranial Doppler or EEG. However, jugular venous oximetry is invasive and can miss regional pathologies and trans-cranial Doppler and EEG are difficult to operate. Thus, cerebral oximetry is currently the only simple to use, non-invasive method of cerebral oxygenation monitoring and has the potential to be the answer to the demand for a real-time bedside cerebral haemodynamic monitoring tool providing data from several brain regions simultaneously [150]. Another advantage is its portability and relatively low cost. Neonates are a particularly interesting subject for NIRS as light attenuation in the thin skull is weaker and there are fewer issues with

probe/tissue contact due to hair.

4.1.1 Establishing cerebral oximetry in the neonatal care

Cerebral oximetry can be used as a trend monitor in neonatal brain injury and can provide clinically important information to guide treatment [5]. It is still far from being a perfect monitoring tool - the development of all physiological monitors is driven by the need for an "ideal" clinical tool, which would be a monitor that provides a continuous or easily repeatable measurement of reliable and reproducible regional and global functional data in real-time and non-invasively [151]. Cerebral oximetry does not fulfil all these needs, neither does any other currently used neurological monitor. However, the main reason why cerebral oximetry is suitable for neonatal monitoring is that it allows measurement for extended periods of time without disturbing the infants and can be easily combined with other monitoring modalities.

The application of near-infrared spectroscopy in neonates has been first published in 1985 in a study by Brazy et al., who demonstrated bedside monitoring of haemoglobin and CCO concentration changes in preterm infants [2]. Significant correlation between central venous oxygen saturation and StO_2 in children has been shown in a study by Nagdyman et al. [152], who also compared StO_2 to jugular bulb oxygenation SjO_2 in children a year later and found significant correlation [153]. In a different study, NIRS was used to monitor venous oxygen saturation in mechanically ventilated paediatric patients and validated against invasively measured blood samples [154]. These studies demonstrate that even though there are still many issues in cerebral oximetry waiting to be resolved; using StO_2 trend monitors can yield important clinical information and cerebral oximetry is being nowadays used in the neonatal intensive care, e.g. in preterm care, neonatal surgery, during respiratory support, ductal surgery or red blood cell transfusion [155, 156, 157].

A recent (2018) worldwide survey conducted across 235 NICUs showed that only 85 (36%) owned a NIRS device for research or clinical application. The majority of those units did not use NIRS on a regular basis. The main reasons for not using/purchasing NIRS was the lack of research evidence, cost and no clinical advantages. Most units without access to NIRS did not plan to obtain a system [7]. The survey shows that more clinical evidence showing benefits of NIRS is needed and that there are many challenges facing cerebral oximetry and hindering it from spreading among clinics.

4.1.2 Challenges

Cerebral oximetry techniques have been in development since the 1990s; some challenges remain unsolved and prevent it from reaching its potential as a self-sufficient clinical monitor. These

include a lack of standardisation leading to differences in readings of different oximeters, setting reference ranges and poor precision and sensitivity of the measurements.

4.1.2.1 Physiological background of StO_2

Cerebral oximetry measures the oxygenation of a unknown mixture of venules, arterioles and capillaries (mostly under 100 μm, rarely above 200 μm in diameter [158, 159]) in the tissue underneath the sensor, the measured value of StO_2 is an average of the oxygenation of the illuminated tissue. StO_2 is a simple assessment of the complex underlying physiology influenced by various physiological processes, such as changes in pressure, partial pressure of carbon dioxide, cerebral blood flow or oxygen extraction. For a simplified illustration of the volume interrogated by tissue oximetry, StO_2 is determined by SaO_2, volumes of arterial and venous blood V_a and V_v, CBF, $CMRO_2$, the oxygen capacity of blood defined by haemoglobin concentration c_{Hb} and the oxygen binding capacity of haemoglobin k_{Hb} (1.306 mL of oxygen/g of haemoglobin) [10]:

$$StO_2 = SaO_2 - \frac{V_v}{V_v + V_a} \times \frac{CMRO_2}{CBF\ c_{Hb}k_{Hb}} \times 100\% \tag{4.1}$$

The arterial:venous volume ratio is not known. During instrument validation, an assumption of the arterial:venous volume ratio to approximate the influence of the saturations of the individual compartments is used. However, given the various layers of different tissue types illuminated; the ratio varies by measurement location, inter-subject and also during pathology and other physiological processes [4, 10].

Multiple studies have explored whether StO_2 can be used as a surrogate measurement of SvO_2. While the correlation is usually statistically significant due to the oximeter calibration and the venous drainage anatomy and physiology, the slope of the relationship has been repeatedly shown to be below 0.5 with wide limits of agreement [159].

The relationship between SaO_2 and cerebral StO_2 is affected by the presence of autoregulation. The main difference between the two quantities is that SaO_2 captures global oxygenation, while StO_2 measures regional oxygenation. If changes in SaO_2 occur, the corresponding fluctuations of cerebral StO_2 are reduced because of autoregulation [98]. Wolf et al. [160] measured SpO_2 and StO_2 in preterm neonates while repeatedly inducing SpO_2 changes in the range 99–85%. StO_2 correlated with SpO_2 but the change in StO_2 was by mean 3.3% smaller [160]. Hunter et al. [98] evaluated the correlation between StO_2 and SaO_2 measured with a blood gas analyser in stable preterm infants and found no correlation. It is likely that no correlation was found as the infants have likely developed cerebral autoregulation by the time the study was conducted [98]

and the small changes in SaO_2 did not affect StO_2.

The complex physiological background of the StO_2 signal illustrates the difficulty of using StO_2 as a standalone description of cerebral haemodynamics and it is up to the clinician to interpret the value. Different processes can lead to the same response in StO_2. An example can be arterial vasodilation or venous passive contraction, which both result in an increase in StO_2. The response of the signal to these events can however differ at the limits of cerebral autoregulation (described in section 2.2.1). In some cases, pathophysiologies might occur and yet be invisible to the StO_2 signal; e.g. during cerebral blood flow interruption in brain cell death, metabolism decreases but the venous compartment can be supplied with oxygenated blood from extracerebral tissue, thus maintaining StO_2 within the normal range [103]. Pathologies can lead to change in optical properties of the medium and assumptions in algorithms calculating StO_2 may no longer hold; it is unclear how stable the SRS algorithm is during processes such as hypothermia or hypovolemia [4].

The use of an in-house developed broadband NIRS system in this application was beneficial as it not only gave the opportunity to use a broadband NIRS system and recover additional information about the optical properties of the tissue but also ensured transparency of data collection without any instrument calibration assumptions, as present in commercial NIRS systems [22], and update the hardware as needed. As various physiological and pathological processes can lead to a change in StO_2, it is common in research to compare the measurement to a different, standard cardiovascular dynamics monitoring technique. StO_2 is often compared to perfusion CT or xenon enhanced CT, cerebral perfusion pressure, partial pressure of oxygen in extracellular fluid in the brain, transcranial Doppler or Lac/NAA [103, 161]. Nevertheless, more information is needed about the sensitivity and specificity in detecting true alterations in the oxygenation of the tissue.

4.1.2.2 Validation

Many studies have explored the potential of tissue oximetry to be used in the intensive care and help with diagnosis or treatment planning [4]. The disadvantage of these studies is a lack of uniformity regarding protocol, site and devices, leading to inhomogeneous results. As the StO_2 signal is an average of the oxygenation of the illuminated tissue and the individual components are unknown, validation of the measurement is challenging. The use of a validation technique is crucial for standardisation of different instruments and measurement techniques. Currently, there are two proposed means of validation: phantom measurements and *in vivo* validation.

Optical phantoms are objects that mimic the optical properties of biological tissue and are used for evaluating the performance of NIRS devices, their advantages are adjustable optical prop-

erties and low variation [162, 163]. Phantoms can be either solid (e.g. out of resin) or liquid (e.g. filled with blood) and can match the scattering and absorption properties of tissue over broad wavelength ranges. Dynamic phantoms have the advantage of changing optical properties, they can simulate saturation/desaturation of tissue [164, 165]. Another alternative to dynamic phantoms is the use of 3D printed phantoms for the performance assessment of oximeters [166].

In an effort to standardise instrument performance assessments and allow for reliable system comparison, three measurement protocols, which use solid phantoms as standardised assessment tools, have been developed. The basic instrumental performance (BIP) protocol [167] is focused on the characterisation of an instrument without a measuring object. It has been primarily developed for use in TR NIRS and assesses parameters not used in CW systems, such as shape of the response function or nonlinearity of timing electronics. The MEDPHOT protocol [168] has been designed to define procedures applicable to all NIRS instruments and to characterise them in terms of measurement results and key features. The measurements use 32 optical phantoms with different μ_a and μ_s' and evaluates the accuracy, linearity, noise, stability and reproducibility of the system. The nEUROPt protocol [169] has been designed to assess the ability of the systems to detect, localise and quantify changes in optical properties in tissue. Using a solid phantom with a movable inclusion with different optical properties allows to test the depth sensitivity and resolution of the systems. It has been primarily designed for the use in TR systems but can be applied with other modalities too. To show the advantage of using the three protocols and to demonstrate the need for standardisation, a recent study of 10 different NIRS instruments from 7 institutions applied the BIP, MEDPHOT and nEUROPt protocols to TR, FD and CW systems, including CYRIL [170].

The comparison of instruments can be also achieved through simultaneous measurements with different devices on one phantom, as demonstrated with a homogeneous blood-lipid phantom with changeable oxygenation [163], also in two-layer blood phantoms, where the first, solid layer simulates the optical properties of the neonatal skin and skull, and the second layer is liquid, simulates the brain and has adjustable optical properties [8, 165]. The studies also present linear conversions from the readings of one oximeter to a different one for comparison and suggest the use of such phantoms for the characterisation of oximeters [165].

The use of phantoms as a mean of direct validation of the quality of the StO_2 measure is not standardised yet; phantoms can not be used as direct validation of the quality of the StO_2 measure as oximeters can respond differently to phantom measurements than to *in vivo* human studies due

to background optical properties [171]. A different approach is to use a weighted blood reference; taking invasive samples of arterial blood and venous blood (arterial blood can be taken from the radial artery, venous blood from the jugular bulb) and measuring their saturation while the subject is being monitored with an oximeter. These studies are generally performed in healthy adults or patients requiring a jugular catheter. Such measurements are challenging in neonates and are hence not representative of the whole population. StO_2 measures combined oxygenation from arteries, veins and capillaries, instruments use an arterial-venous ratio to account for the different influence of each component, Eq. (4.1). Various ratios of jugular bulb saturation SjO_2 and arterial oxygen saturation SaO_2 are used for the calculation of StO_2 as commercial systems use different assumptions. INVOS (Medtronic, USA) studies use a 75:25 SjO_2:SaO_2 ratio [172, 173, 174]; other studies use a 70:30 SjO_2:SaO_2 ratio [171, 175, 176, 177]. Many *in vivo* NIRS validation studies have been performed but it is not possible to draw any firm conclusions, as the studies are very heterogeneous and apply different protocols. They showed poor measurement precision, suggesting that NIRS estimates local tissue oxygenation, whereas the blood samples reflect regional oxygenation. The studies also showed an oxygenation level-dependent bias, the difference between StO_2 and the reference increased with decrease of saturation [10]. The invasiveness of the measurement and the uncertainty of the arterial-venous ratio, which can also change with location, pathology and over time and does not account for the differences between subjects, are among the disadvantages of *in vivo* validation [165, 178]. Additionally, as it is not possible to induce deep hypoxia in healthy adults (SaO_2 below $\sim$ 50–70% can be dangerous), the validity of pathological StO_2 readings cannot be assessed, in contrast to liquid phantoms, which can be fully oxy- or deoxygenated (StO_2 reference ranges are discussed later in this chapter).

4.1.2.3 Inhomogeneous oximeter readings

A major concern is the difference in the readings of various oximeters due to the lack in standardisation protocols. Multiple studies demonstrated disparities in studies collected *in vivo*: Komiyama et al. [179] compared the performance of two SRS oximeters, NIRO 300 (Hamamatsu, Japan) and OM-200 (Shimadzu Corporation, Japan) during arterial occlusion and found significant correlation between muscle oxygen saturation measurements at rest but significant differences during arterial occlusion. Oxygen saturation measured with NIRO 300 was compared to regional cerebral oxygen saturation measured with INVOS 5100 (Medtronic, USA) during hyperoxia and hypoxia in Thavasothy et al. [180], showing similar values, but large inter- and intra-individual differences between the readings of the two monitors. Differences caused by using sensors either for adult

or neonatal/paediatric use from the same manufacturer in the same subject were found in other studies, with the neonatal readings being 10–15% higher [181, 182]. Hessel et al. [183] used two different oximeters in their study in term infants, INVOS 5100C with the OxyAlert neonatal sensor and FORE-SIGHT (Casmed, USA) with the Small Dual sensor. The authors report difference between the readings, up to 20% in the area of low oxygenation. Schneider et al. [184] compared the performance of 4 different oximeters in measurements in preterm infants, concluding that there are significant differences between readings of NIRO 200 (Hamamatsu, Japan), INVOS 5100C, FORE-SIGHT and SenSmart X-100 (Nonin, USA).

Vascular occlusions of the human arm offer an uncomplicated mean of performing a controlled rapid tissue oxygenation changes. Hyttel-Sorensen et al. [185] used the NIRO 300 and 200NX, the INVOS 5100 and OxyPrem systems and used them simultaneously on the forearm during a cuff occlusion. The results showed similar StO_2 between NIRO 200NX and the INVOS system, and a different NIRO 300 reading. The OxyPrem had a significantly lower dynamic range and a lower mean StO_2. Another cuff occlusion study used the INVOS 5100C, FORE-SIGHT and Nonin EQUANOX (Nonin, USA); INVOS gave significantly higher steady state results than FORE-SIGHT and EQUANOX had a steep decline in StO_2. The results indicated that good repeatability came at the expense of low oxygenation sensitivity [186]. Steenhaut et al. [187] compared NIRO 200NX, INVOS 5100C and FORE-SIGHT systems in a vascular occlusion test and concluded that the speed of response between the instruments varied. Additionally, the instruments were used in a MBLL mode and a StO_2 mode, and it has been shown that MBLL responded to oxygenation changes more promptly than StO_2 measurements. Such inter-instrument differences highlight that inhomogeneous readings are also caused by the algorithms used to analyse the raw data.

The use of phantoms offers a more controlled environment and is suitable for the comparison of systems. Hyttel-Sorensen et al. [163] compared multiple oximetry systems on a dynamic phantom and showed differences between the INVOS 5100C with an adult and an paediatric sensor, the NIRO 300 and the OxyPrem, an in-house designed system. Bigger differences were observed in lower saturations, pair-wise comparison showed simple linear relations. A similar study has been conducted by Kleiser et al. [8, 165]: 5 different systems were tested on a two-layer phantom in two different studies (OxyPrem, NIRO 200NX, FORE-SIGHT ELITE, SenSmart X-100 and OxiplexTS (ISS, USA) as reference). The differences particularly in low saturation regions and the presence of linear relationships between the instrument readings were confirmed.

The potential causes for the disparities are different engineering techniques of the devices, signal processing and algorithms. It has been shown that the assumptions of brain water content affect StO_2 [188], the selection of extinction spectra [189], and the selection of how to account for absorption in StO_2 measurements affects the results too [190]. Other causes of bias and variability can be partially caused by assumptions of tissue homogeneity and layer thickness, unaccounted chromophores, the impact of venous and arterial blood volume, and systemic bias such as skin pigmentation or gender [8, 112, 178, 180, 191]. To conclude, the studies suggest that the absolute measurements are currently not sufficiently precise for oximetry to be used as a stand-alone assessment of tissue oxygenation but that the devices can be used as trend monitors.

4.1.2.4 Influence of extracerebral layers

One of the most important challenges in NIRS is that emitted light travels through several extracerebral layers before it eventually reaches the tissue of interest, the brain. Figure 4.1 shows the different tissue layers illuminated in a multidistance cerebral oximetry setup; in adults, light has to travel through more than 1 cm of extracerebral tissue before reaching the brain. All these layers contribute to the measured StO_2 signal.

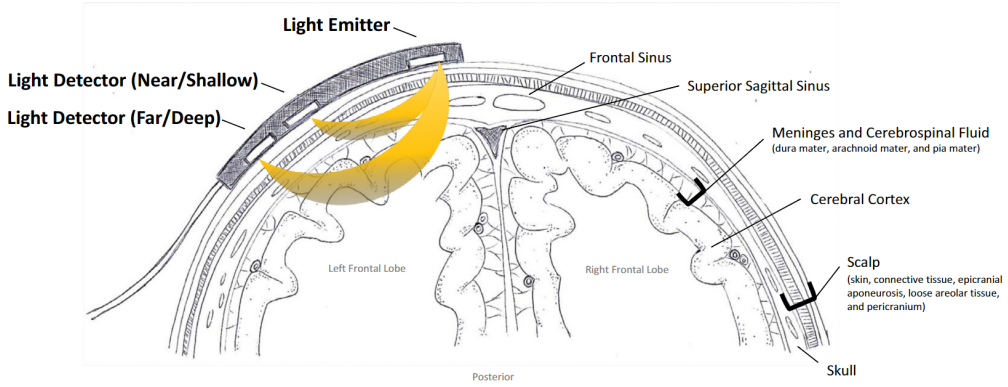

Figure 4.1: Axial cross-section diagram of a multidistance oximetry measurement. Emitted light travels in a curvilinear path and travels through different tissue layers before reaching the brain; StO_2 is the average oxygenation of the illuminated area. Taken from [159], reproduced with permission of Elsevier.

FD and TR systems are capable of distinguishing between extracerebral and brain signal components [192, 193] and CW systems can use multidistance setups to obtain a more brain-specific signal. The multidistance approach to CW oximetry measurements has been developed to minimise the impact of the extra-cerebral layer by using a detector close to the light source and at least one further away [100]. The light reaching the detector further away travels through deeper layers than the proximal detector while the extra-cerebral signal component is the same;

the influence of the extra-cerebral layer can be subtracted from the distal measurement. Several variations of this technique are commercially used with different SDS. However, studies in healthy adult volunteers have shown that the extra-cerebral signal reduces the brain-signal specificity of multidistance NIRS measurements [9, 194]. Commercial systems use other algorithms that should decrease the impact of extracranial signal components but a study conducted with INVOS 5100C, FORE-SIGHT and the Nonin EQUANOX on healthy adult volunteers showed that all systems were affected by the extracranial signal component to different extents [9].

Some StO_2 calculation algorithms do not apply any superficial signal subtraction so a strong influence of the superficial layer is expected. To overcome this, light transport models can be extended to the solution of the diffusion equation for a semi-infinite two-layer medium [125]. However, this is not necessary in the case of monitoring infants: the neonatal skin and skull are very thin (around 5 mm [108]) and the influence of the extra-cranial signal component is small [120, 121].

Another way of overcoming the contamination of the signal with extracranial components is removal of superficial signals in post-processing, which is common in differential spectroscopy. A short separation channel ($\sim$ 5–10 mm) collects data only from superficial layers, while light from a long separation channel ($\sim$ 30–50 mm) travels deeper in tissue. The haemoglobin concentration changes collected with the short separation channel can be removed from the long separation channel in post-processing [195]. The optimal short separation distance is 8.4 mm in a typical adult and only 2.15 mm in a neonate [196]. The short separation for neonates poses an engineering challenge because of the high collected light intensity and the required miniaturisation of the patient-end of the system.

4.1.2.5 Precision

Precision refers to the agreement between repeated measurements and consists both of repeatability and reproducibility. Repeatability is the variability in repeated measurements in identical circumstances, reproducibility accounts for repeated measurements with changed circumstances, for example, change of observer or instrument. While results in research come from measurement averages, treatment decisions in clinical practise are often based on single measurements, hence, high precision is desired in clinical care. A reasonable precision to aim for is 2–3%, which corresponds to the spontaneous variability over time in stable patients [197].

Dullenkopf et al. [181] measured the precision of the NIRO 300 and the INVOS 5100 in anaesthetised children; the precision of NIRO 300 was 6.1% for 4 cm interoptode distance and

7.8% for 5 cm. Precision of INVOS 5100 of a paediatric sensor was worse than with the adult sensor, 4.7% and 6.1%, respectively. Sorensen et al. [198] investigated the precision of NIRO 300 in premature infants and measured the precision of a single measurement of StO_2 to be 5.2%, insufficient for clinical use. Arri et al. [199] found that the precision of StO_2 measurements with the OxiplexTS decreased with the increase of tissue homogeneity from 11% to 2% in term infants and also in preterm infants, from 5.6% to 4.6%. Hyttel-Sorensen et al. [185] measured the reproducibility of 4 devices, INVOS 5100, 5.4%; NIRO 200NX, 4.4%, NIRO 300, 4.1% and OxyPrem, 2.7%. The precision of OxyPrem was improved to 1.85% in Kleiser et al. [12] study through the removal of systemic physiological fluctuations, which could be the major cause of variation between repeated StO_2 measurements [12, 200]. Hyttel-Sorensen and colleagues account the lack of reproducibility of cerebral oximetry to optical heterogeneity. They have also pointed out that studies, where sensors are repositioned at different sites show similar results to studies where the probes are placed on the same site [185]. More research is needed to understand the true reason for the variation in StO_2 measurements, which can also be subject-dependent. Until precision is improved in all clinical oximeters, it is suggested that in order to compensate for the lack of precision in cerebral oximetry measurements, StO_2 should be used mainly as a trend monitor and the absolute value should not be a standalone indicator of the patient's haemodynamics [197].

4.1.2.6 Reference ranges

The advantage of having a reading that gives an absolute value of regional oxygenation is that it would give a immediate assessment of the wellbeing of the patient. However, inter-individual differences in oxygen saturation and the dynamic error of readings are a major limitation of present cerebral oximetry as it is difficult to set StO_2 intervention thresholds, which would guide the treatment.

Reference ranges allow for an immediate assessment of the patients health by comparing the measured value to the published ranges. StO_2 reference ranges for healthy full term neonates immediately after birth were measured in 354 term infants with an INVOS 5100 [201] and also in a smaller cohort of 140 term infants with a NIRO 200NX [202]. Reference ranges are also available for preterm infants, measured in a large cohort (999 infants) with the INVOS 4100/5100 [203]. Intervention thresholds are used to assess the severity of hypoxia and to warn the clinician. These can vary among systems. The INVOS 7100 intervention guidelines by the manufacturer suggest that a normal range is 58–82%, the intervention threshold occurs at a 20% change from baseline or when StO_2 is below 50%, critical thresholds are at 25% difference from baseline or absolute

values below 40% [204].

Tomlin et al. [11] used three different oximeters on 10 healthy adult volunteers and induced hypoxia: when SpO_2 measured with pulse oximetry showed a reading of 70%. Subjects were simultaneously monitored with the INVOS 5100C and EQUANOX 7600, or INVOS 5100C and FORE-SIGHT. The percentage change in INVOS readings was more similar to changes in SpO_2 than what was measured with FORE-SIGHT and EQUANOX. The threshold of a 10% change from baseline, considered an early indicator of hypoxia, was reached by all systems in all subjects, but at different times. While INVOS detected the intervention threshold of 20% in all subjects, EQUANOX detected it only in one and FORE-SIGHT in none. These results highlight the need for different intervention thresholds for different instruments and also the differences between oximeters related to speed of response and sensitivity. The SafeBoosC III clinical trial focused on demonstrating the feasibility of measuring tissue oximetry in preterm infants used an intervention threshold of 55% in the INVOS 5100, with normal ranges 55–85% [205]. These values were linearly transformed to corresponding threshold values for different instrument using the linear relationships measured in lipid phantoms [8]; e.g. 66% for the FORE-SIGHT system or 61% for a NIRO [206].

Overall, several aspects of oximetry need to be improved to reliably use reference ranges. First, reference ranges need to be set for different subject groups based on sufficient sample sizes. Secondly, while linear transformations can be useful for inter-instrument comparison in a research setting, it can cause complications in a clinical environment. Additionally, the dynamic response of all systems should be validated in terms of the instrument range and temporal sensitivity.

Despite the challenges outlined, cerebral oximetry has the potential to become a monitor to predict outcomes and guide therapy to prevent poor outcomes, as shown in many studies measuring StO_2 in a clinical setting to test whether it is a useful indicator of patient wellbeing (described in following sections). An initiative to demonstrate the potential of cerebral oximetry in neonatal care are the SafeBoosC clinical trials, focused on the outcomes of NIRS monitoring combined with a treatment guideline in premature infants. SafeBoosC phase II was a multicentre randomised clinical trial which enrolled 166 extremely preterm infants. NIRS cerebral monitoring was started at 3 hours after birth and lasted until 72 hours, the experimental group had visible StO_2 readings while the control group was blinded. The experimental group was treated with dedicated treatment guidelines related to cerebral oximetry readings [205]. The trial has shown that with cerebral monitoring and a treatment guideline, cerebral oxygenation can be stabilised and the burden of

hypoxia was reduced to less than half [207]. By the end of 2019, the third phase of the trial started, aiming to involve 1000+ international patients. The objective is to examine whether it is possible to reduce the risk of death or severe brain injury at 36 weeks of age from 34% in the control group to 26% in the patients in the experimental group [208]. If the outcome of these trials is successful, a combination with the introduction of more validation and standardisation in the field will hopefully lead to an increased interest in cerebral oximetry in the clinical care.

4.2 Cerebral oximetry in hypoxic-ischaemic encephalopathy

Infants diagnosed with HIE could benefit from cerebral monitoring as this type of neonatal encephalopathy is caused by a failure of sufficient oxygen delivery. Severe cases of HIE can be accompanied by cerebral hyperoxygenation, abnormally increased perfusion and a lack of cerebral autoregulation [15]. In 2004, cerebral oximetry was first applied in HIE patients, the aim was to evaluate whether StO_2 is different in healthy neonates compared to injured ones. The authors, Huang and colleagues [17], found lower oxygenation in HIE infants and a different response to inhaling oxygen and an abnormal decrease of deoxyhaemoglobin concentration when inhaling oxygen due to slow blood flow. More studies exploring the potential of cerebral oximetry in HIE monitoring followed - this section provides an overview of cerebral oximetry measurements in HIE. Additionally, in order to understand the value of StO_2 measurements in infants with HIE, a short summary of cerebral oximetry measurements in healthy neonates is presented first.

4.2.1 StO_2 in healthy newborns

Measurements in healthy infants are mostly focused on the period following transition and start very shortly after birth, some follow up the progression of oxygenation during the first days of life. This timescale matches up with the monitoring of infants with HIE, where the aim is to measure StO_2 as soon as possible after birth to catch the therapeutic window.

Most publications report an increase of StO_2 within the first 10 minutes of life. INVOS 5100 system was the system of choice in most publications, reaching similar values at 2 minutes of life, between 39% and 42% [201, 209, 210]. This is followed by a steep increase - a higher StO_2 at 3 minutes was reported; reaching 44% [211] or 53% [183]. The increase continues over time, to 69% (5 min) [209], 76% (7 min) [211] and 77% (15 min) [201]. The trend agrees with studies performed with other oximeters. A value of 77% at 7 minutes was also measured with an EQUANOX system [212]; and Almaazmi et al. [210] reported a median StO_2 of 73% at 8 min with a FORE-SIGHT system. These measurements are similar to StO_2 collected in healthy adults

[213].

Some cerebral oximetry studies were performed with multiple oximeters to compare their results. Simultaneous measurements with an INVOS and FORE-SIGHT report a higher reading with FORE-SIGHT by 9% at 3 minutes, but only of 4% at 8 minutes [183], highlighting the need for instrument validation. Ziehenberger et al. [214] measured different values with the NIRO 200NX from the INVOS 5100 in the first minutes of life, 35%, and 50%, respectively. Given the dramatic increase of oxygenation within a few minutes of life, such a difference could be due to the differences in the temporal dynamic response of the systems.

Oxygenation keeps evolving even after the first few minutes of life. A change in oxygenation between 10 and 15 minutes was also reported by Bernal et al. [215], followed by a decrease of StO_2 during the first 120 hours after birth. While Hessel et al. [183] measured a decrease in StO_2 between day 1 and 2 from 86% to 78% with an INVOS 5100C, FORE-SIGHT measured an increase of 4% from 82% to 86%.

Franceschini [216] reported no change in oxygenation over a large time window of up to one year. Reference measurements were collected by Spinelli et al. [108] who measured optical properties in healthy term neonates with a TR system in a range 68–75 % (25th–75th percentile). The StO_2 = 75% collected by Arri et al. [199] on day 1 falls within the same range and is a little lower than StO_2 = 78% measured by Bailey et al. [217] in healthy term infants within the first two days. Another reason for different readings might be differences in gestational age of the patients; Farzam et al. [191] reported an increase of StO_2 with gestational age.

Overall, oxygenation increases during the first few minutes in healthy term infants. This could be caused either by an increase in cerebral oxygen delivery or a decrease in oxygen consumption following transition (section 2.2.3.2); it seems that oxygen supply to the brain is established very quickly and plateaus after a few minutes. It has been shown that the increase in SpO_2 takes longer, suggesting a preference of oxygen supply to the brain compared to the rest of tissue [209].

Oxygenation starts decreasing after around 15 minutes of life, eventually reaching values reported in adult subjects. The overall decrease of oxygenation in the few days after birth can be caused by further development of the cerebrovascular tone and changes in chemoreceptor and baroreceptor control of breathing [215].

4.2.2 StO_2 in newborns with HIE

HIE is an injury with the speed of progression depending on the severity of the primary hypoxic insult. It has been the aim of many cerebral oximetry research studies to capture the development

of the injury and to evaluate whether it is possible to obtain an understanding of the complex underlying pathophysiology just from a brief StO_2 measurement. This section provides an overview of published cerebral oximetry measurements in HIE; the aim is to summarise the measurement conditions and results and to obtain an understanding of the relationship between StO_2 and the physiology of HIE.

The literature search was focused on cerebral measurements in term infants diagnosed with hypoxic brain injury. Different combinations of terms were used for a search in the PubMed database and gave the following number of results:

- "NIRS" AND "neonatal encephalopathy": 11 articles
- "oxygen saturation" AND "neonate": 260 articles
- "oxygen saturation" AND "therapeutic hypothermia": 46 articles
- "NIRS" AND "therapeutic hypothermia": 23 articles

More studies were found through the references of the articles. Studies that monitored infants diagnosed with HIE, measured cerebral StO_2, used it as a individual biomarker and reported StO_2 were included. Studies that enrolled only preterm infants were excluded as the response to brain injury differs in the immature brain and so were studies monitoring infants with brain injury following surgery. Overall, 28 cerebral oximetry studies in term infants with HIE were included in this review. Table 4.1 is a summary of all found studies including the patient size, age, time of the study, used instrument and study result.

The use of oximetry in monitoring of asphyxiated/hypoxic infants has been demonstrated in several studies. However, the relationship between StO_2 and severity of brain injury seems inconsistent.

StO_2 lower in adverse outcome (1 study)

Huang et al. [17] monitored 16 term infants with HIE within the first few days of life with a TR system. 16 HIE patients were monitored on day 2, 25 infants in the healthy control group on days 2 or 3. StO_2 was significantly lower in HIE infants - 53% in sick infants versus 62% in healthy subjects. The authors suggest that StO_2 was lower because all HIE infants had a cerebral oedema causing intracranial hypertension decreasing the blood flow and increasing the degree of hypoxia [17].

StO_2 higher in adverse outcome (10 studies)

Toet et al. [84] monitored 18 asphyxiated infants and found that StO_2 increased within 6 to 48 hours of life in infants with an adverse outcome and was also higher than in the favourable outcome group. StO_2 did not change significantly in favourable outcome patients. While no difference in StO_2 was detected between the two groups within the first 24 hours, StO_2 of the sick patients increased on day 2, while it remained stable in the positive outcome group; eventually being almost 20% lower than in the negative outcome group. A similar pattern in StO_2 was discovered by Zaramella et al. [218]. Dehaes et al. [95] monitored 10 term infants with moderate/severe HIE treated with TH and found a higher StO_2 in patients undergoing TH than in the control group. Cerebral oximetry was performed during TH, during rewarming and post-TH, covering a time range from 6 to 305 hours. Healthy infants were monitored from 13 to 77 hours of life. However, the authors concluded that StO_2 is less sensitive to therapy and metabolic disturbances during the first days of life than other parameters, such as $CMRO_2$ [95].

Ancora et al. [219] did not have a healthy control group but measured StO_2 in infants with moderate/severe HIE treated with therapeutic hypothermia and found higher StO_2 values in neonates with an negative outcome. These findings were similar to Lemmers et al. [220], who found differences in StO_2 between adverse and a favourable outcome after day 1.

Higher StO_2 in moderate/severe HIE was also measured by Jain et al. [18]. The authors measured StO_2 for at least 48 hours until 54 hours after birth during TH. The rate of the rise in StO_2 increased with injury severity during the first 24–26 hours of life. Higher StO_2 (over 90%) in severely injured patients was reported by Arriaga-Redondo et al. [221] compared to moderate HIE.

A significant increase in StO_2 within the first days of life was found by Peng et al. [222], who measured an increase in StO_2 both in infants with a favourable and an adverse outcome, the latter group, however, had higher baseline values. The authors suggest that the increase represents the evolution of brain perfusion and metabolism in asphyxiated newborns during hypothermia, that the extraction of oxygen is maximal during day 1 and then decreases. Niezen et al. [223] reported adverse outcome in infants with higher StO_2 values but only after 48 hours of life.

StO_2 measured in 11 HIE infants by Nakamura et al. [224] suggest that the timing of monitoring has a significant effect on the prognostic value of StO_2 - a significantly higher StO_2 was found in adverse outcome only at 24 h and 48 h, but not at 6 h and 72 h.

No difference in StO_2 (7 studies)

Goeral et al. [225] measured StO_2 from the onset of TH for 102 hours. The study reports no difference between favourable and negative outcome; they did find an increase of StO_2 during cooling but it was not significantly different from a healthy control StO_2. The increase of StO_2 shows the influence of hypothermia on cerebral perfusion and metabolism [225]. Similar findings were reported by Wintermark et al. [226], who found no difference in StO_2 between moderate and severe injury, but the increase in StO_2 over time was more pronounced in severe injury. StO_2 was also not related to outcome by Burton et al. [227], Lee et al. [19], Shellhaas et al. [228] and Grant et al. [229].

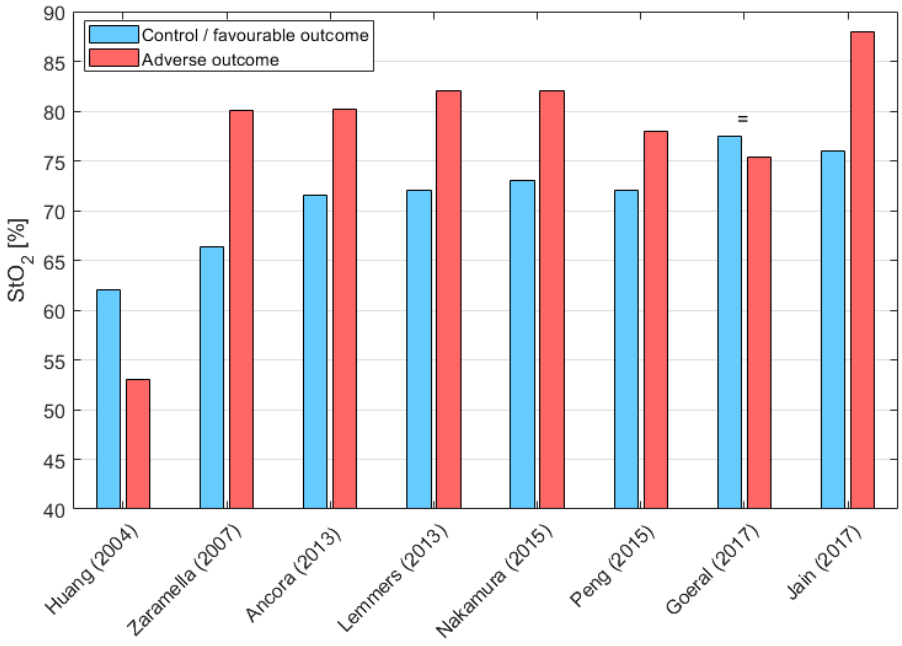

Figure 4.2: Average StO_2 values reported in neonates with HIE compared to a healthy control or favourable outcome group. For studies where StO_2 was reported on multiple days, values measured at 24 h were included. The "=" symbol indicates that there is no difference in StO_2 between both groups.

Figure 4.2 shows the average StO_2 values reported in studies focused on assessing the prognostic value of StO_2. Most studies that identified a higher StO_2 in the adverse outcome group than in the control/favourable outcome group reached similar baseline values. The StO_2 in control/favourable outcome infants are similar to the ranges obtained in healthy subjects, described in section 4.2.1.

Overall, most studies suggest that StO_2 is higher in severe HIE and that this difference is more significant over time [220, 223], an increase in StO_2 and abnormally high values could be caused

by a mismatch between perfusion and metabolism; as secondary neuronal injury progresses, cerebral metabolism gradually declines and causes an increase of StO_2. Such hypothesis agrees with the findings of Forman [230], who reported an increase of oxygenation during therapeutic hypothermia, but did not compare the sick infants to a control group. Their values measured with an INVOS system are higher than StO_2 measurements with the same system in different studies (e.g. [215, 211]).

Higher StO_2 in the negative outcome group might be due to the severe injury of the neurons and consequently a decrease in oxygen utilisation, and to the phenomenon of luxury perfusion, when perfusion exceeds metabolic demands, increasing cerebral oxygen delivery [222]. The increase of StO_2 during treatment in severe HIE has prognostic value but might limit the significance of cerebral oximetry for diagnosis in the first days of life, as it is not observable until later [223].

Given the contradictory results of other studies, drawing firm conclusions in the patterns of StO_2 during HIE is difficult. Many factors affect cerebral haemodynamics creating a variability in StO_2 results, including the administration of TH or sedative and anti-epileptic drugs, seizures, changes in oxygen supply, hypo/hyperventilation and fluctuations in haemoglobin levels [227].

Another contributing factor is the pattern of the injury - MRI has shown that most HIE cases develop one of two types of injury patterns; watershed injury or basal ganglia/thalamic, the second pattern leads to a more severe injury [85]. It is possible that the sensitivity of oximetry monitoring with probe placement on the forehead is affected by injury patterns. A recent study by Tian et al. [231] has shown that NIRS measurements are sensitive to tissue heterogeneity amongst brain regions caused by lesions. Cerebral haemodynamics in mild HIE was shown to be heterogeneous across different brain regions, while cerebral autoregulation remained intact [231].

While some of these factors are outside of the control of the researchers, a certain level of standardisation could aid the creation of HIE StO_2 reference ranges. An important step would be the unification of measurement times, as many studies have shown a change in StO_2 over time and the predictive value of cerebral NIRS is time-dependent [223, 225]. Additionally, differences in the oxygenation of the left and right hemisphere can arise during arterial desaturations [232] or due to the injury pattern, probe placement should also be unified. Whole-head coverage would be ideal, but is often not possible due to simultaneous EEG measurements. The differences in cerebral oximeter readings were already discussed and also highlighted in section 4.2.1, standardisation of the instruments could improve comparability of study results. However, one has to keep in mind that HIE is a highly complex injury with different patterns of progression. Using just one mea-

surement number to understand the intricate patterns of oxygen delivery and metabolism in such a fragile environment will be prone to misjudgement and more information about the pathology is required before drawing conclusions. Such steps are supported by multiple studies which looked at the relationship between StO_2 and other clinical variables, such as blood pressure, cerebral blood flow or EEG patterns [233].

4.2.3 Summary

Cerebral oximetry with continuous wave NIRS offers a real time, non-invasive assessment of the balance between cerebral oxygen supply and demand. While its ability to detect local hypoxia in the clinical setting has been shown in many studies, the overall benefit of cerebral oximetry in the clinical care is still subject to thorough scrutiny, particularly due to a lack of standardisation and reference & intervention ranges.

Cerebral oximetry can be found in the neonatal intensive care and offers an insight into the patterns of oxygen consumption shortly after birth. In healthy infants, an increase is observed immediately after delivery as oxygen supply to the brain is established; this plateaus after a few minutes and does not change significantly in the first few days of life. This progression has been found to be different in infants with HIE. Many studies have shown an increase of oxygenation in patients with severe brain injury, as the metabolic demand of neurons during secondary brain injury decreases. However, the timing of StO_2 measurements plays a significant role as differences between the healthy and the injured brain are time-dependent. Additionally, the complex patho-physiological background of the injury makes interpretation of results challenging; some studies offer contradictory results regarding the prognostic value of StO_2 in HIE. The establishment of cerebral oximetry in neonatal care is hindered by a lack of clinical evidence, oximeter precision and a standardisation, leading to poor comparison between different instruments and algorithms.

Table 4.1: Published studies measuring brain tissue oxygen saturation in brain injured neonates. T - term, w - week/s, d - day/s, TH - therapeutic hypothermia, HIE - hypoxic-ischaemic encephalopathy

First author (year) ref.	Title	Participants	Time of study	Instrument	Average StO_2	Findings
Huang, Lan (2004) [17]	Assessment of the hypoxic–ischemic encephalopathy in neonates using non-invasive near-infrared spectroscopy	16 T HIE, 25 T healthy	d 2–18	TSNIR-3 [234]	healthy vs. HIE: 62±4% vs. 53±3%	Significant difference between sick and healthy, higher StO_2 in HIE.
Toet, Mona C. (2006) [84]	Cerebral oxygenation and electrical activity after birth asphyxia: their relation to outcome	18 T asphyxia	from d 1 for at least 48 h	INVOS 4100	65% (12 h), 84% (48 h) in adverse outcome	Increase of StO_2 over time in infants with adverse outcome, stable StO_2 in good outcome.
Zaramella, Patrizia (2007) [218]	Can tissue oxygenation index (TOI) and cotside neurophysiological variables predict outcome in depressed/asphyxiated newborn infants?	22 T NICU, 15 T control	d 1	NIRO 300	adverse vs. favourable vs. control: 80.1% vs. 74.7% vs. 66.4%	Increased StO_2 suggests worse outcome at 1 year.
Ancora, Gina (2009) [235]	Changes in cerebral hemodynamics and amplitude integrated EEG in an asphyxiated newborn during and after cool cap treatment	1 T, TH	30 min - 80 h	NIRO 200	56.1(11.1)% (pre-TH), 63.7(4.9)% (TH 2–8 h), 73.1(5.4)% (TH 68–74 h), 72.6(5.8)% (post-TH)	Improvement in StO_2 during TH, remained stable.
Grant, Ellen P. (2009) [229]	Increased cerebral blood volume and oxygen consumption in neonatal brain injury	43 T (14 brain injury, 29 no brain injury, 19 control)	First two weeks of life	Imagent (ISS, USA)	no averages reported	No significant difference in StO_2 between HIE or healthy.

First author (year) ref.	Title	Participants	Time of study	Instrument	Average StO_2	Findings
Gucuyener, Kıvılcım (2012) [236]	Use of amplitude-integrated electroencephalography (aEEG) and near infrared spectroscopy findings in neonates with asphyxia during selective head cooling	8 moderate, severe HIE, TH	before, during and after TH	NIRO 200	no averages reported	Seizures led to low StO_2, increased oxygenation during TH. Some had higher StO_2 after rewarming, one patient with seizures had low StO_2 even during TH. Patient with flat trace, continuous low voltage EEG patterns died despite normal StO_2 values.
Ancora, Gina (2013) [219]	Early predictors of short term neurodevelopmental outcome in asphyxiated cooled infants. A combined brain amplitude integrated electroencephalography and near infrared spectroscopy study	12 T moderate and severe HIE, TH	d 1	NIRO 200	adverse vs. favourable outcome: 80.0±10.5% vs. 66.9±7.0% (6 h), 79.7±9.4% vs. 67.1±7.9% (12 h), 80.2±8.8% vs. 71.6±5.9% (24 h)	Higher StO_2 with adverse outcome.
Lemmers, Petra (2013) [220]	Cerebral oxygenation and brain activity after perinatal asphyxia: does hypothermia change their prognostic value?	39 T HIE, TH	before, during and after hypothermia	INVOS 4100-5100	adverse vs. favourable: 63±10% vs. 68±14% (pre-TH), 82±7% vs. 72±9% (24 h), 83±9% vs. 75±8% (36 h), 83±10% vs. 76±8% (48 h), 79±10% vs. 72±9% (84 h)	Higher StO_2 in infants with adverse outcome from 24h onwards.
Shellhaas, Renée (2013) [237]	Limited short-term prognostic utility of cerebral NIRS during neonatal therapeutic hypothermia	18 T HIE, TH	during and after TH	INVOS 5100C	averages not reported	Cerebral StO_2 variability unrelated to short-term outcome.

First author (year) ref.	Title	Participants	Time of study	Instrument	Average StO_2	Findings
Shellhaas, Renée (2013) [238]	Sleep-Wake Cycling and Cerebral Oxygen Metabolism Among Critically Ill Neonates	10 T NICU, 4 HIE	median d 4, for several hours	INVOS 5100C	left vs. right: 76.6 (5.8)%. vs. 80.0 (7.8)% (awake), 78.2 (13.7)% vs. 79.0 (11.4)% (quiet sleep), 77.4 (8.0)% vs. 77.5 (8.2)% (active sleep)	StO_2 varies by sleep-wake state among critically ill neonates.
Dehaes, Mathieu (2014) [95]	Cerebral oxygen metabolism in neonatal hypoxic ischemic encephalopathy during and after therapeutic hypothermia	10 T HIE, 22 control	during and after TH	hybrid FD-NIRS–DCS	averages not reported	StO_2 higher in TH-HIE than in control group, no difference in StO_2 during TH and post-TH in HIE group.
Wintermark, Pia (2014) [226]	Near-infrared spectroscopy versus magnetic resonance imaging to study brain perfusion in newborns with hypoxic-ischemic encephalopathy treated with hypothermia	7 T, HIE	during and after TH	FORE-SIGHT	77.6±6.6% (severe HIE), 77.3±4.7% (moderate HIE)	Increase of StO_2 over time, more pronounced in severe HIE.
Burton, Vera Joanna (2015) [227]	A pilot cohort study of cerebral autoregulation and 2-year neurodevelopmental outcomes in neonates with hypoxic-ischemic encephalopathy who received therapeutic hypothermia	28 T, HIE	during and after TH	INVOS 5100	averages not reported	StO_2 not related to outcome.
Gagnon, Marie-Helene (2015) [239]	Effect of persistent pulmonary hypertension on brain oxygenation in asphyxiated term newborns treated with hypothermia	3 T, TH, with persistent pulmonary hypertension	During and after TH	FORE-SIGHT	averages not reported	SpO_2 desaturations caused decrease in StO_2 in all infants, more episodes during rewarming.

First author (year) ref.	Title	Participants	Time of study	Instrument	Average StO_2	Findings
Nakamura, Shinji (2015) [224]	Simultaneous measurement of cerebral hemoglobin oxygen saturation and blood volume in asphyxiated neonates by near-infrared time-resolved spectroscopy	11 HIE, 5 TH	From 6 h before TH, until 72 h	TRS-10 (Hamamatsu, Japan)	Adverse vs. favourable: 79.6±8.4% vs. 72.5±5.5% (6 h), 81.6±6.4% vs. 72.9±2.1% (24 h), 85.9±4.7% vs. 76.6±4.9% (48 h), 80.9±3.5% vs. 76.4±7.6% (72 h)	Significantly higher StO_2 in adverse outcome at 24 h and 48 h, no difference at 6 h and 72 h.
Peng, Shuo (2015) [222]	Does near-infrared spectroscopy identify asphyxiated newborns at risk of developing brain injury during hypothermia treatment?	18 T, TH	during and after TH	FORE-SIGHT	adverse vs. favourable: 78.3±4.0 vs. 72.3±3.5 (d 1), 82.3±4.1% vs. 78.7±3.8% (d 2), 84.0±2.7% vs. 80.6±3.6 (d 3), 84.3±2.0% vs. 79.0±3.8% (d 4)	StO_2 higher in infants with adverse outcome. Significant increase of StO_2 from day 1 to day 2 in both groups.
Shellhaas, Renée (2015) [228]	An Evaluation of Cerebral and Systemic Predictors of 18-Month Outcomes for Neonates With Hypoxic Ischemic Encephalopathy	18 T HIE, TH	During TH	INVOS 5100C	averages not reported, within normal range (> 70%)	StO_2 not related to outcome.
Chalak, Lina F. (2016) [240]	Cerebral hemodynamics in asphyxiated newborns undergoing hypothermia therapy: pilot findings using a multiple-timescale analysis	10 T, TH	during and after TH	INVOS 4100-5100	80±7% (TH), 80±8% (rewarming)	No difference in StO_2 between TH or rewarming.
Alderliesten, Thomas (2017) [241]	Brain oxygen saturation assessment in neonates using T2-prepared blood imaging of oxygen saturation and near-infrared spectroscopy	9 T (brain injury) , 6 PT	before and after MRI	INVOS 5100C	68.4±12.9% (pre-MRI), 70.3±18.5% (post-MRI)	A strong linear relation found between oxygen saturation measured by magnetic resonance imaging and StO_2.

First author (year) ref.	Title	Participants	Time of study	Instrument	Average StO_2	Findings
Forman, Eva (2017) [230]	Noninvasive continuous cardiac output and cerebral perfusion monitoring in term infants with neonatal encephalopathy: assessment of feasibility and reliability	20 T HIE	during and after TH	INVOS	80±9% (10 h), 85±6% (70 h), 85±5% (100 h)	Increase of StO_2 during TH.
Goeral, Katharina (2017) [225]	Prediction of outcome in neonates with hypoxic-ischaemic encephalopathy II: role of amplitude-integrated electroencephalography and cerebral oxygen saturation measured by near-infrared spectroscopy	32 T, moderate HIE, TH	for 102 h since start of TH	INVOS 5100C	abnormal vs. normal MRI: 75.4±7.9% vs. 77.5±7.3%	No difference in StO_2 with pathology.
Jain, Siddharth V. (2017) [18]	Cerebral regional oxygen saturation trends in infants with hypoxic-ischemic encephalopathy	21 T HIE, TH	until 54 h for at least 48 h	INVOS 5100	moderate/severe vs. none/mild : 87.6±8.5% vs. 76.4±10.1%	Increased StO_2 associated with moderate-severe brain injury.
Lee, Jennifer K. (2017) [19]	Optimizing cerebral autoregulation may decrease neonatal regional hypoxic-ischaemic brain injury	64 T HIE, TH	during and after TH	INVOS 5100	averages not reported	StO_2 unrelated to brain injury in any anatomic region.
Massa-Buck, Beri (2017) [97]	Significant correlation between regional tissue oxygen saturation and vital signs of critically ill infants	27 T and PT (NICU)	d 6	FORE-SIGHT Elite	averages not reported	Significant correlation between cerebral StO_2 and mean blood pressure.
Chock, Valerie Y. [242] (2018)	Renal Saturation and Acute Kidney Injury in Neonates with Hypoxic Ischemic Encephalopathy Undergoing Therapeutic Hypothermia	38 HIE TH	during and after TH	INVOS 5100C	averages not reported	Insignificant decrease of StO_2 over time after re-warming.

First author (year) ref.	Title	Participants	Time of study	Instrument	Average StO_2	Findings
Niezen, Caren K (2018) [223]	Amplitude-Integrated EEG and Cerebral Near-Infrared Spectroscopy in Cooled, Asphyxiated Infants	39 T HIE TH	during and after TH	INVOS 5100C	71% (6 h), 82% (24 h), 88% (48 h), 87% (72 h)	Increase of StO_2 during TH and rewarming, StO_2 ≥90% predictive for a severely abnormal outcome after 48 h.
Wu, Tai-Wei (2018) [243]	Hemodynamic Changes During Rewarming Phase of Whole-Body Hypothermia Therapy in Neonates with Hypoxic-Ischemic Encephalopathy	20 T HIE, TH	before, during and after TH	INVOS 5100C	averages not reported	StO_2 stable during measurement, above 80%.
Arriaga-Redondo, Maria (2019) [221]	Lack of variability in cerebral oximetry tendency in infants with severe hypoxic-ischaemic encephalopathy under hypothermia	16 T moderate HIE, 8 T severe, TH	from admission up to 12 h after rewarming	INVOS 5100C	averages not reported	Higher StO_2 in severe injury, increase of StO_2 within 72 hours of life.

Chapter 5

Instrumentation and data acquisition

Throughout this project, NIRS data obtained with various means have been used, including data from computational simulations, optical phantoms and data collected in human subjects. The following chapter describes the collection methodology for the majority of data in this work and the NIRS instruments used.

5.1 Instrumentation

All CW NIRS data used in this work was collected with CYRIL, CYtochrome Research Instrument and appLication, developed by Dr Gemma Bale during her PhD [20]. Designed for the monitoring of CCO in the neonatal intensive care, CYRIL is a unique imaging system, as it applies a broadband wavelength range and allows for a multidistance setup by using 8 different detector optodes, which are all simultaneously processed on a 2D charge-coupled device (CCD) chip.

The CYRIL system was built in 2013 and some changes to the setup have been introduced since then. To simplify the timeline of these updates and differentiate between work that was done before the start of this project and that which was done by me, the system will be mostly referred to as either CYRIL 1 or CYRIL 2, with the differences outlined below. The setup CYRIL 1 was designed by Dr Gemma Bale; CYRIL 2 is the updated version to fulfil the requirements of this PhD project.

5.1.1 CYRIL 1

The specific application of CYRIL in the NICU for CCO monitoring placed several requirements on the design of the instrument, related to safety or practicality:

- Use of a broadband light source to capture the broad spectral peak of oxidised CCO, which is otherwise difficult to distinguish from haemoglobin, due to the low concentration of CCO.
- The use of low and high-pass light filters either side of the NIR region to minimise heat

deposition on the fragile neonatal skin and avoid tissue damage from heat.

- Optional second light source to monitor both hemispheres independently by using one light source with 4 optodes each.
- A multidistance detector set up to measure tissue oxygenation or to allow for the separation of shallow tissue layer signals. Additionally, the detectors were not in a fixed configuration to be placed in any desired setup by creating custom probe holders.
- Measurements at 1 Hz for real-time imaging achieved through the use of fibre bundles with a high numerical aperture and a spectrometer with a high light throughput.
- To make the device MRI compatible, fibre probes were made out of MRI safe plastic. The fibres were 3 m long to place the device far from the cotside, out of the way of the clinical staff.
- Electrical safety was assured through the use of an uninterruptible power supply and the use of an isolation transformer.

The whole setup of CYRIL 1 can be seen in Figure 5.5. The standard set-up of CYRIL 1 was one light source and 4 detectors per brain hemisphere. The broadband light source was the ORIEL Fibre Optic Illuminator 77501 (Newport, USA) with a halogen white light bulb. Light filtered with a 610 nm long-pass and a 950 nm short-pass filter was collected into a custom made 3 m long fibre bundle (Loptek, Germany) and branched into two fibre heads with a diameter of 2.8 mm. Light from the tissue surface was collected by 8 detector fibre heads holding fibres of 1 mm diameter which transported it to the light detection system. The patient end of the detector fibres and the two light fibres held in a probe holder are shown in Figure 5.1.

At the spectrometer end, the 8 detector fibres were bundled in a metal ferrule in a vertical arrangement, Figure 5.2. This was coupled to the spectrometer slit, from which light travelled to the spectrograph, Acton LS785 (Princeton Instruments, USA) which diffracted light with a grating; spectral range of 136 nm. The wavelength range was selected to be 770–906 nm to capture the broad CCO peak. The diffracted light was focused at the CCD, a PIXIS 512f camera (Princeton Instruments, USA), which had a two-dimensional array of 512×512 detector pixels. The light from the 8 detectors arrived at the CCD in 8 distinct strips and allowed recording data from all detector fibres simultaneously. The surface of the camera chip was divided into 8 regions by binning, the counts within the binned regions were summed into individual spectra.

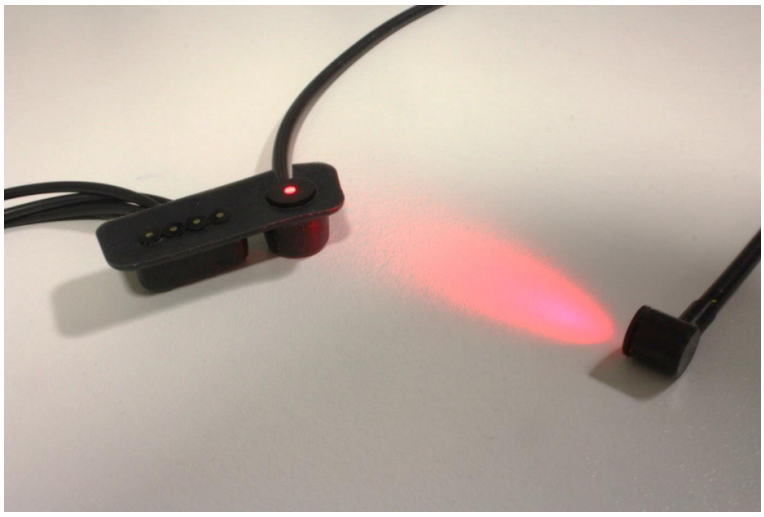

Figure 5.1: Patient end of CYRIL 1 with 4 detector fibres held in a probe holder and two source fibre heads. Taken from [111].

Figure 5.2: Input ferrule of the detector fibres at the spectrometer end. Taken from [111].

.

The patient-end part of the system was designed to be small to comfortably fit on the neonatal forehead. The light fibre bundle head was 10 mm in diameter and the detector bundle heads only 5 mm. The design of the light source and detector heads allowed for a custom detector setup. Depending on the requirements, probe holders were designed and 3D printed. The typically used detector arrangement was 4 detectors per light source, with the first detector 15 mm from

the light source and the other detectors placed consecutively, resulting in a setup with 15, 20, 25 and 30 mm SDS (measured from the centre of the fibres). A diagram of the optode setup on the patient end, with the probe heads held in place in a probe holder, is in Figure 5.3. The probe holder was designed in AutoDesk Inventor and 3D printed with a rubber-like black material, TangoBlack FLX973 combined with VeroWhitePlus. The material was selected to be flexible to allow for the curvature of the small neonatal head. The probe holder could be redesigned depending on the needs of the patient; the diagram in Figure 5.3 shows 1 light source with 4 detectors, different probe holders were designed for neonates with smaller heads, with one light source for all 8 detectors, as seen in Figure 5.4. The probe holder was attached to the skin using transparent double-sided tape. Figure 5.5 shows the system and the patient end of the system placed on an HIE patient.

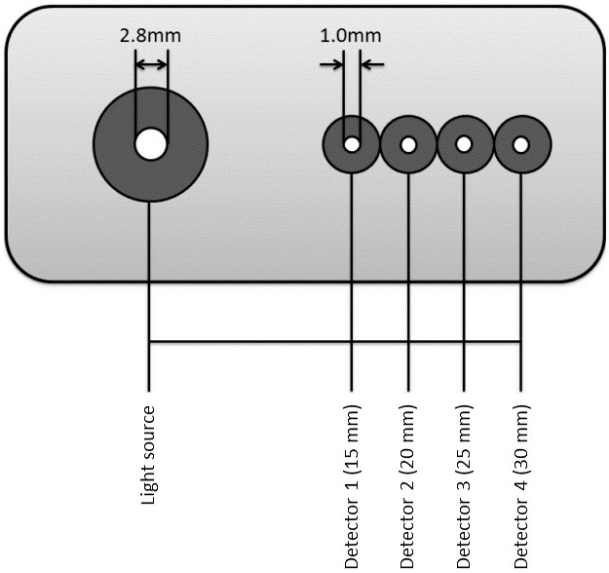

Figure 5.3: Patient end fibre arrangement in the probe holder. Taken from [111], edited.

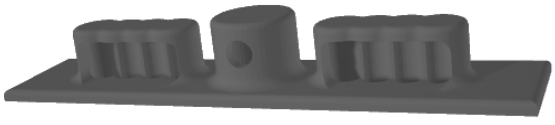

Figure 5.4: 3D design of the probe holder. This probe holder is designed for the use of one central light source head with 4 detectors on each side.

The CYRIL 1 system was operated through an interface (a VI, Virtual Instrument) developed in LabVIEW (National Instruments, USA). The aim was to make the software easy to use so that clinical personnel could operate the system. The user could change various settings, such as

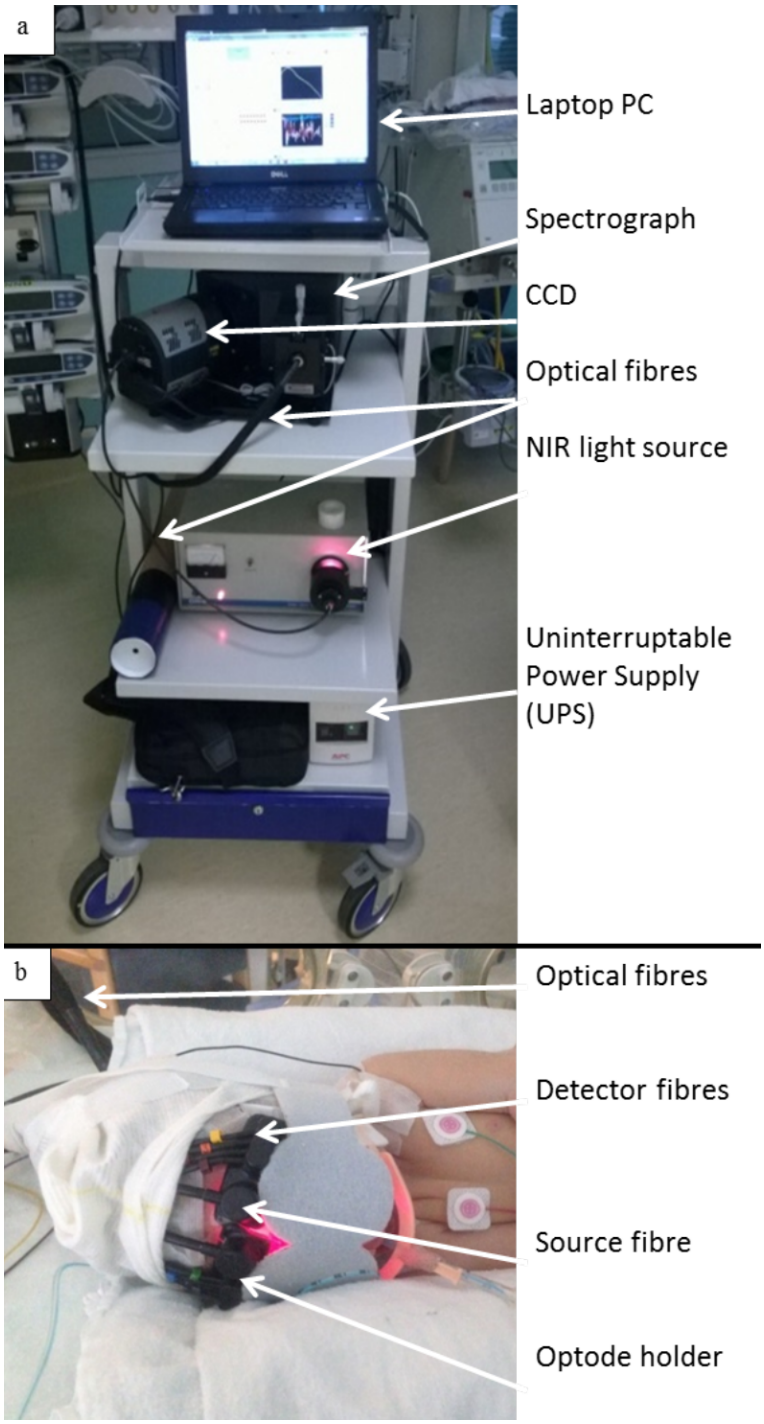

Figure 5.5: CYRIL 1 in the NICU. a) shows the setup with all individual components. b) shows the patient end, the patient is being monitored with both channels simultaneously. Taken from [111].

exposure and detector separation. The CCD binning was also operated by the LabVIEW interface, as that changed depending on the camera exposure and placement of the detectors. Figure 5.6 shows the binning region selection interface in LabVIEW. The VI displayed the collected spectra in real time for immediate quality assessment and calculated concentration changes real-time with

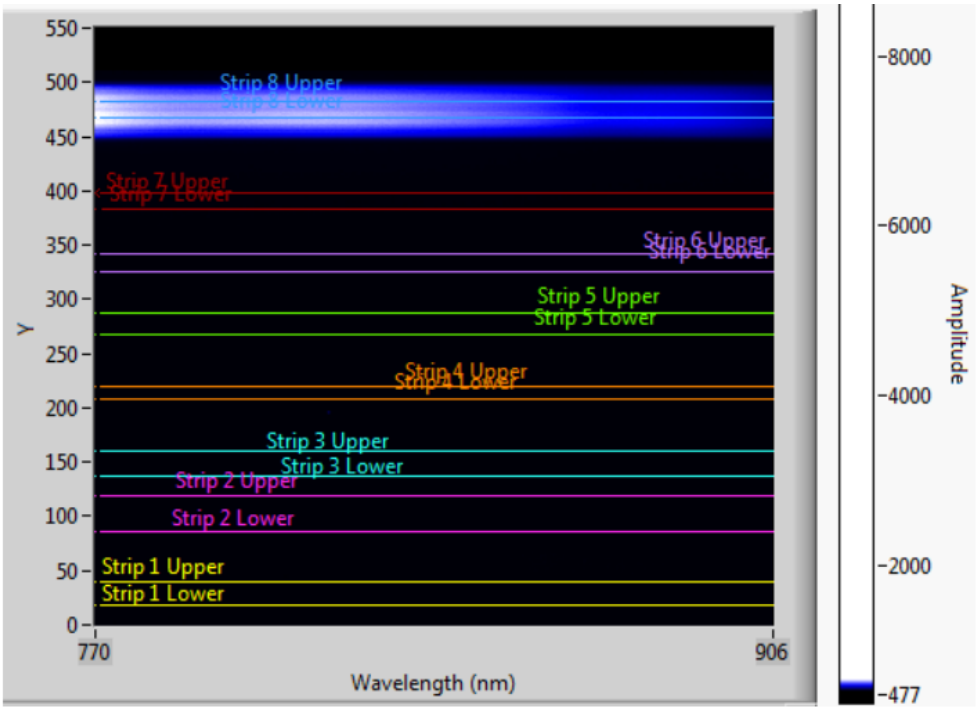

Figure 5.6: Setting CCD binning on CYRIL 1 in the LabVIEW user environment. The plot shows the CCD intensity map when only detector 8 is illuminated. Amplitude is in counts per pixel. The coloured lines, strips, divide the CCD area into discrete regions assigned to individual detectors. The user selects these strips by moving the lines up or down. Taken from [111].

MBLL and displayed the results; the user could send comments to be saved with a measurement timing file. The data were saved as spectra of counts against wavelength summed across the region specified by the binning; the output of the measurement would be a file for each detector with spectra collected at each exposition. The VI also saved a file with HbO_2, HHb, CCO and THb concentration changes. All files were saved in a .csv format.

The CYRIL 1 setup was used for data collection in UCLH for several years. In early 2018, the system returned to UCL for maintenance and further development.

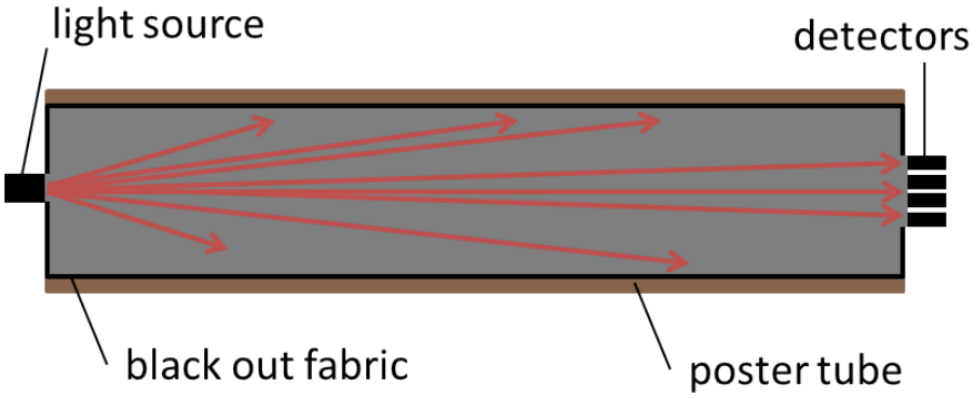

Figure 5.7: Measurement of reference spectra in a customised poster tube. Taken from [111].

5.1.1.1 Reference spectra collection

A reference spectrum is the measurement of the output spectrum of the light source and is used to account for the different bin widths of the CCD and as a measure of I_0. The intensity of the light source through free space with no attenuating medium is recorded. While the reference spectrum measurement is normally performed in a dark room, a poster tube lined with blackout rubberised fabric was created to be used as a simulation of a dark room in the hospital. Figure 5.7 shows the reference spectrum acquisition, in which the light source is placed at one end of the tube, with a set of 4 detectors from the same channel (1234 or 5678) placed opposite. The reference spectra were collected at a decreased exposure to prevent saturation of the CCD. The LabVIEW VI had a button which started a reference spectra measurement and saved the reference spectra in a .csv format.

5.1.2 CYRIL 2

The CYRIL 1 setup was designed for the use in the neonatal intensive care for the measurement of CCO changes. Once the purpose of the system shifted towards measuring oxygenation with broadband NIRS, some changes were introduced both to the hardware and software components. Some improvements to the CYRIL 1 setup were performed already throughout the first placement in UCLH, other were done for the purposes of this work; indicated where relevant.

5.1.2.1 Hardware changes

One of the difficulties encountered during the clinical measurements at UCLH performed by Dr Gemma Bale was that while asleep, neonates were often laying on their side and light source optodes could not be placed on either side of the forehead. Both optodes placed centrally were

causing crosstalk[1], so the light source fibre with two fibre heads was replaced with a optical fibre with a single head, which was placed centrally between two pairs of 4 detectors (probe holder for such setup is in Figure 5.4). The original light source was replaced with a more compact source, a white light source HL-2000-HP (Ocean Optics, USA) with a long 20 W lifetime tungsten halogen lamp. The broadband spectral range was reduced with a 650 nm long-pass NIR filter. Both the change to the light fibres and the light source were introduced before the start of this project.

CYRIL 1 was moved back to UCL for preparations for the next session of the Baby Brain Study, the measurement session performed for the purposes of this work. The new system setup will be referred to as CYRIL 2. I amended some of the system hardware: a new trolley, a new probe holder and new hard disk drives for storage were added. All work described from now on was done by me for the purposes of this project, unless specified.

The system was moved to a new, lockable storage unit. This allowed CYRIL 2 to be left unattended in the hospital for hours without the need of securing individual components to the trolley. The tidy appearance also improved the visual impact of the system.

The curvature of the head of the neonates caused the probe holder to lift off on the edges where the 30 mm detectors were placed. The probe holder design was amended to improve the contact between the skin and the fibre heads. The sides of the probe holder were widened; allowing more space for the placement of double sided tape. While keeping the probe holder small enough to fit on a neonatal forehead, tape could be placed on all four sides of the holder without covering any of the fibres, improving contact. The separation between the light source and the detectors remained unchanged; 15, 20, 25 and 30 mm on each side. The probe holders were 3D printed out of the materials TangoBlack+ and VeroClear. Figure 5.8 shows the new probe holder.

CYRIL 1 data was automatically stored in real time on the laptop PC used to operate the system. To protect the data in the case of a computer failure, the data collection procedure was changed. Two external 2 TB hard disk drives were connected to the laptop PC, and data was saved on both simultaneously during the measurement. This setup would protect the data even in the case of the failure of one data storage location. The updated system setup CYRIL 2 is displayed in Figure 5.9. Not all components are visible.

[1] Light from one channel reaching detectors from the other channel.

Figure 5.8: CYRIL 2 probe holder with widened sides. The light source is in the middle, with four detectors on each side.

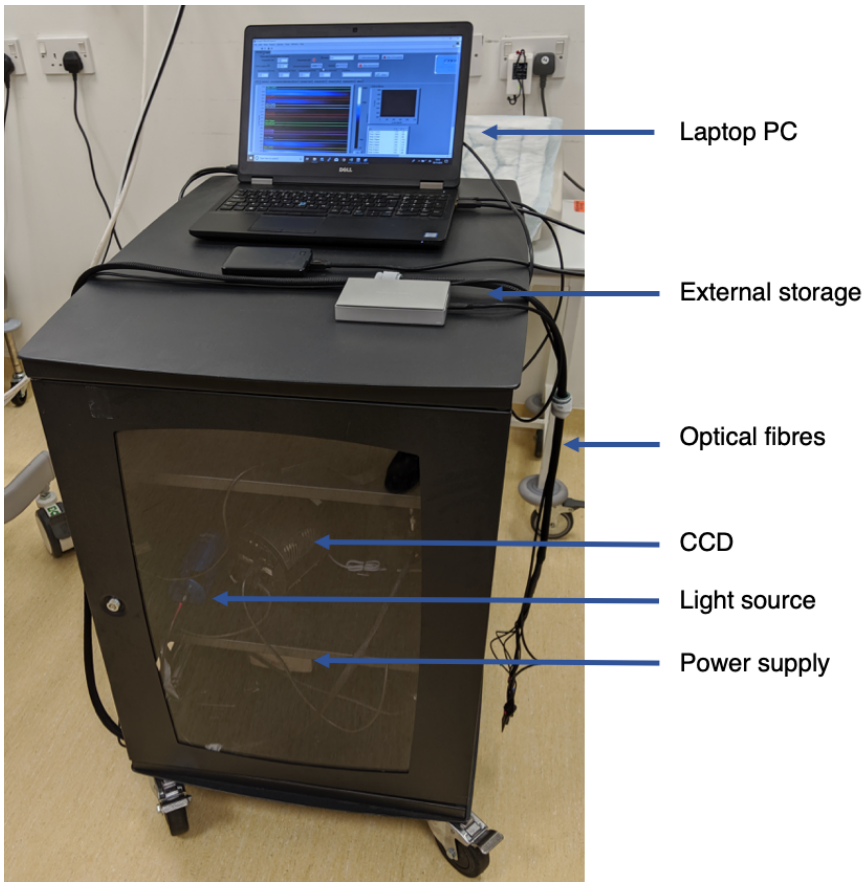

Figure 5.9: The CYRIL 2 setup. Note that not all components (e.g. the isolation transformer) are visible.

5.1.2.2 CCD calibration

The detection range of CYRIL 1, 770–906 nm, was specifically selected to capture the wide CCO peak with high resolution. However, there are other interesting spectral features of haemoglobin just outside this range, which could be useful for the measurement of StO_2. As seen on the spectra and their derivatives in Figure 3.5, additional spectral features which could be used in a broadband measurement of StO_2 are:

- The 730 nm water peak.
- The 760 nm HHb peak.
- Water features around 900 nm.

Therefore, to use the full potential of the broadband CCD, a new diffractive grating with a wider spectral range was installed in the spectrograph. The new grating had a spectral range of 207 nm, and the new spectral range was calibrated to 704–911 nm.

The CCD camera was calibrated to the new wavelength range 704–911 nm in 2016, before the work on this project started. Once CYRIL returned from the hospital in early 2018, I evaluated the calibration of the system to ensure that the system's performance was satisfactory. During calibration, the relationship between the pixels on the CCD chip in the x-axis and a corresponding wavelength is assessed. Calibration light sources that emit light at distinct wavelengths are used for this procedure.

The wavelength resolution of CYRIL 2 was tested by finding the minimum peak-to-peak separation of the calibration spectra that can be resolved. A calibration neon-argon lamp was used for the measurement, CAL-2000 (Ocean Optics, USA). The spectral lines of argon cover 704–911 nm, as seen in Figure 5.10; the length of the lines corresponds to the relative intensity at that wavelength. Figure 5.11 shows the calibration spectra at two different strips as measured with CYRIL 2. One strip is measured by detector 2, strip 71, the other by detector 6, strip 334. The grey lines are the spectral lines of argon. The calibration spectra were taken at an exposure of 1 s at a slit width of 15 μm, the different heights of the peaks correspond to the different intensity of the argon spectral lines.

The offset between the peaks measured by detector 2 and 6 was likely caused by chromatic aberation of light passing through the spectrometer lenses and reaching the CCD. The offset between detector 2 and argon is more prominent than between detector 6 and argon because detector

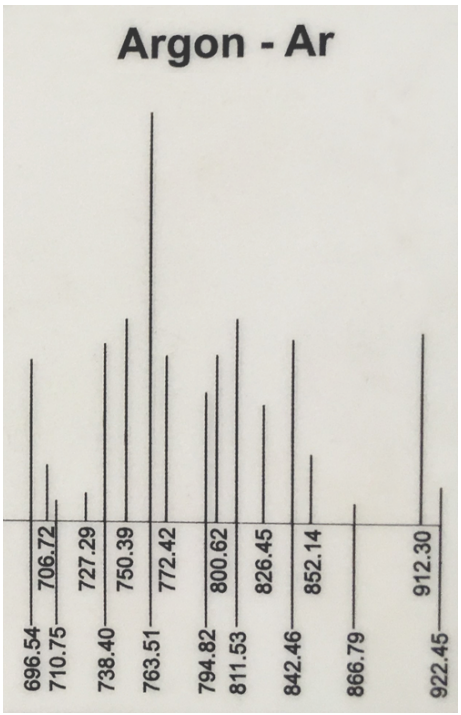

Figure 5.10: Spectral lines of argon emitted by a CAL-2000 calibration light source.

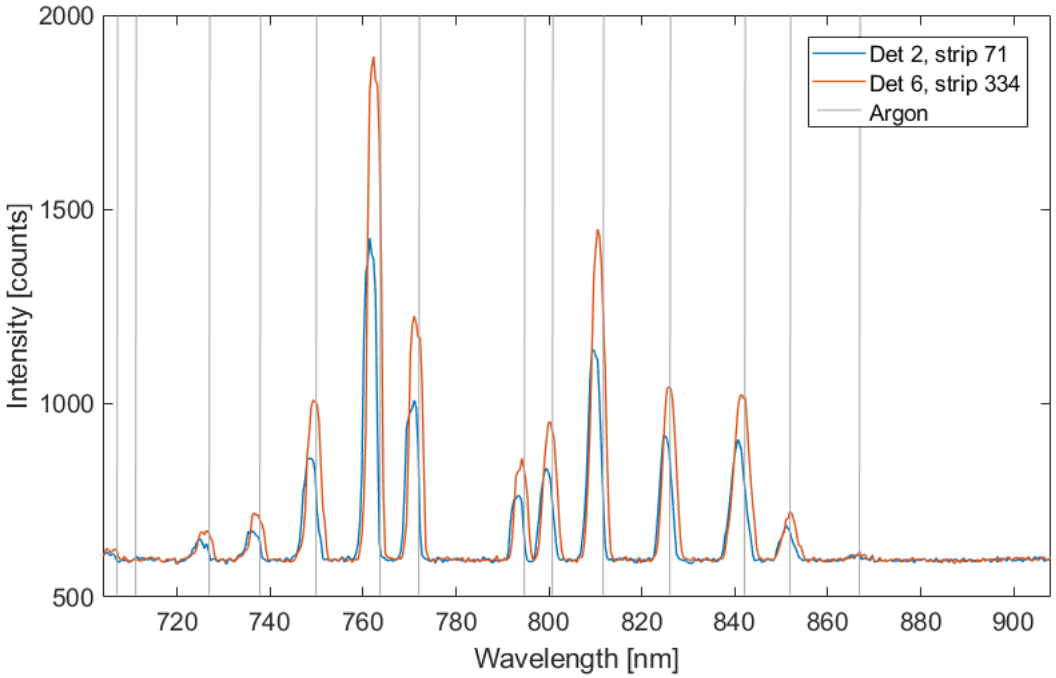

Figure 5.11: Argon spectrum measured with CYRIL. Depicted are spectra measured on strip 71, collected by detector 2, and strip 334, collected by detector 6.

6 illuminated pixels closer to the centre of the CCD. The difference in the height of the detectors 2 and 6 peaks was caused by the individual properties of the optical fibres and illumination angle.

As the CCD showed a distinct difference between the 794.82 and 800.62 nm peaks (argon emission lines in the CYRIL range closest to each other), the wavelength resolution of the system was below 5.8 nm. To further quantify the wavelength resolution, the full width at half maximum (FWHM) was calculated for three peaks: 763.51 nm, 794.82 nm and 826.45 nm. FWHM was calculated by subtracting the noise floor from the measurement and fitting the selected peaks with a Gaussian curve, which gave the standard deviation σ, FWHM = $2\sqrt{2\ln 2}\,\sigma$ [244]. Results are in Table 5.1. The resolution is wavelength and CCD strip dependent due to the relative position of the fibres to the CCD and the intensities of the emitted light.

Table 5.1: The wavelength resolution of CYRIL 2 calculated as the full width at half maximum (FWHM) of spectra with three different argon peaks. The resolution was measured with two different detectors, detector 2 (CCD strip 71) and detector 6 (CCD strip 334).

	FWHM at wavelength [nm]		
Detector	763.51	794.82	826.46
2	3.73	3.66	3.83
6	3.82	3.85	4.19

Additionally, the optical resolution of the system was calculated; it is limited by the resolution of the individual components and is dependent on the groove density of the diffracting grating, the width of the spectrograph entrance slit and the size of the CCD chip pixels [111]:

$$\begin{aligned} \text{Dispersion} &= \frac{\text{spectral range}}{\text{number of pixels}} = \frac{207}{512} = 0.40 \text{ nm/pixel}, \\ \text{Resolution} &= \text{slit width} \times \text{grating groove density} = 0.015 \times 600 = 9 \text{ pixels}, \\ \text{Optical resolution} &= \text{dispersion} \times \text{resolution} = 0.40 \times 9 = 3.6 \text{ nm} \end{aligned} \tag{5.1}$$

The optical resolution of 3.6 nm is smaller than the wavelength resolutions in Table 5.1 because of the coupling of the fibres to the spectrograph and the alignment of the CCD to the diffracted light beam. The resolution of the system was considered sufficient as spectral features of the chromophores of interest (HHb, HbO_2 and water) occur at a scale larger than 5 nm.

5.1.2.3 CCD data collection

Another issue identified during hospital data collection with CYRIL 1 was the setting of the binning of the CCD. Correct setting of the binning was important for the collection of high quality data, as that ensured that even detectors far away from the light source were measuring data with a

high signal-to-noise ratio (SNR); the sensitivity of a CCD detector strip was increased by widening the detection area. Widening the detection area too much lead to detector crosstalk. Detector crosstalk occurred when an area illuminated by light from one detector was covered by a binning region assigned to a different detector.

In the clinical environment, the setting was often changed as signal was differently attenuated in individual study subjects and one binning setting could not fit all. One problem that arose rather often was the saturation of the CCD camera, which was caused by a binning region detecting too much light, and either the binning strip had to be narrowed or exposure had to be decreased.

The saturation limit of the CCD was determined by the way the CCD was reading the data. In the CYRIL 1 setup, the data that the CCD sent to LabVIEW were 8 spectra collected at each time point. The CCD automatically summed the counts in the binning region (wavelength-wise) into spectra, which were sent to the computer. During readout of the detected counts, all pixels of the same wavelength within one region were read at once. The benefit was that it caused little noise, adding readout noise only once per wavelength. However, this batch data acquisition also meant that the sum of all counts detected by all pixels at the same wavelength in the binned region could not exceed 65535. This limit was determined by the data storage capabilities of the CCD and corresponds to the maximum value represented by an unsigned 16-bit binary number. It was often difficult to set the binning/exposure so that the detectors closest to the light source were not saturated and the detectors further away had sufficient signal without any crosstalk from other detectors.

A new CCD data collection approach was proposed for CYRIL 2; instead of collecting the summed spectra, the individual counts at each pixel were saved at each time point in form of a CCD snapshot. The spectra were binned and summed manually. The main advantages of such approach were:

1. No need to set binning individually for each patient.
2. As the CCD read out each pixel individually, the saturation limit applied only pixel wise, significantly decreasing the probability of detector saturation.

Potential drawbacks had to be addressed; further discussed in the next sections:

1. Need to manually select binning for each subject retrospectively.
2. Significant increase of the amount of data sent to the computer from the CCD, requiring more storage and potentially creating a bottleneck.

3. Readout noise added to each pixel.

Readout noise

The background noise levels were much higher in the manual summing spectra approach. In CYRIL 1, the readout of the CCD followed the direction of the x-axis (wavelength) and per each step, all pixels in the corresponding binning region (y-axis) were read simultaneously, adding only one readout noise component per step. In CYRIL 2, each pixel was read individually, hence the noise component increased with binning width. To overcome this, a background noise measurement was added to the measurement protocol to subtract it from each individual CCD capture. The measurement was performed with the spectrometer shutter closed for at least ten acquisitions, which were then averaged. Figure 5.12 shows the temporal stability of the background measurement in one pixel over time. The background noise could be summarised only in a short measurement; the mean noise value at pixel (250, 250) over 1000 acquisitions was 582.7 counts with a standard deviation of 3.3 counts. As the signal intensities collected in a tissue simulating solid phantom with CYRIL 2 at 30 mm exceeded 55 000 counts at maximum (771 nm), the error caused by averaging the background noise over a shorter period was negligible.

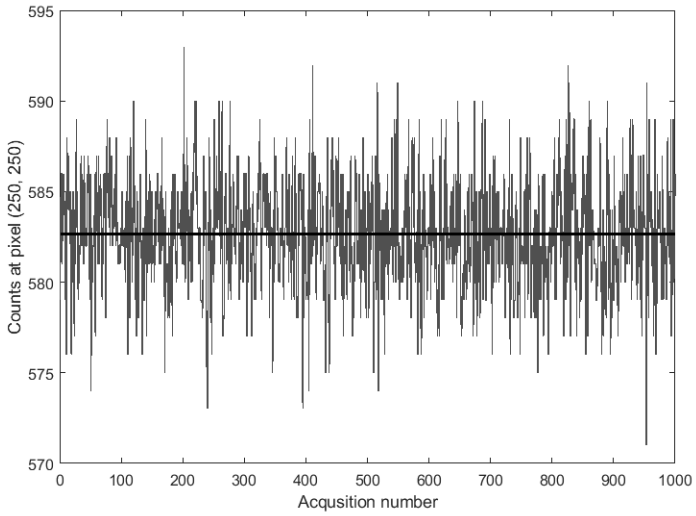

Figure 5.12: CCD background noise collected in pixel (250, 250) over 1000 acquisitions with the shutter closed. The solid line is the mean value.

The SNR of the measurement after removing the background level was measured using a solid tissue phantom (μ_a = 0.02 mm^{-1} and μ_s' = 0.9 mm^{-1}). 1000 measurements, 1 s exposure, with all 8 detectors in a standard setup (4 detectors on each side of the light source, 30–15 mm SDS) were averaged, noise was given by the standard deviation of the measurements. SNR in

dB at each pixel was calculated as 10×log of the fraction of the mean signal and the standard deviation; the SNR across the whole CCD for each pixel is shown in Figure 5.13. The SNR in the centre was lower as the detectors were placed further away from the light source, SNR increased towards the edges of the CCD as SDS decreased.

Summing the spectra further improved the SNR; when binning of a width of 20 across the pixels with the highest counts for each detector was used, SNR increased up to 1300 for detectors closest to the light source and to 350 for detectors furthest away. The improvement of the spectra is shown in Figure 5.14, the spectra are normalised to show the smoothing effect of binning.

Figure 5.15 shows a comparison of spectra of the broadband light source collected with both CYRIL 1 and CYRIL 2 (binned, post noise-removal). Normalising the spectra with the MATLAB (MathWorks, MA, USA) function *normalize* shows that changing the data readout methodology did not decrease the quality of the spectra.

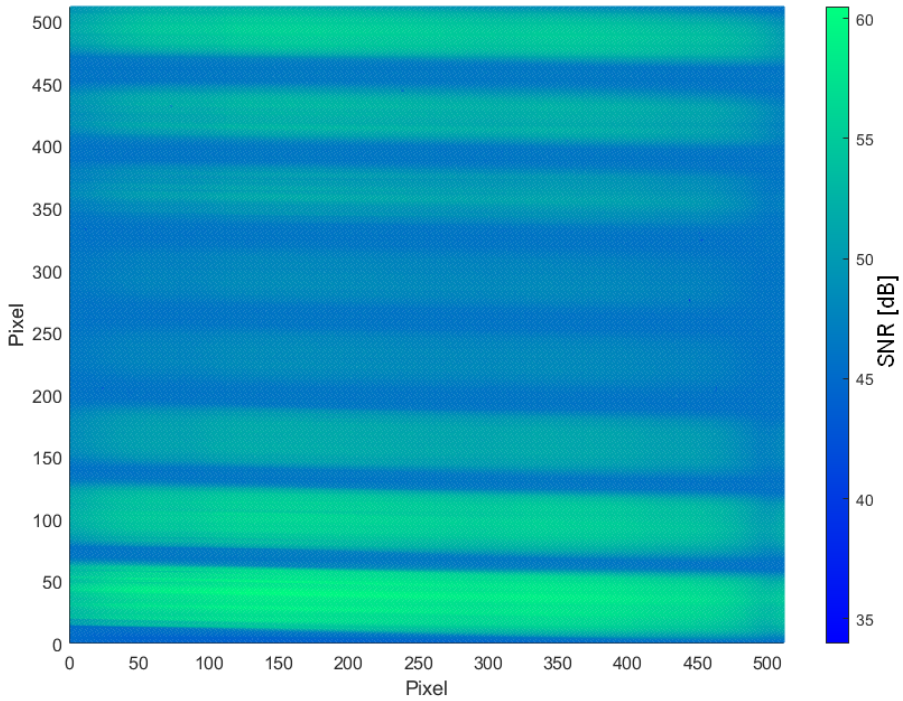

Figure 5.13: The pixel-wise SNR across the whole CYRIL CCD measured in a solid tissue phantom over 1000 acquisitions with all 8 detectors.

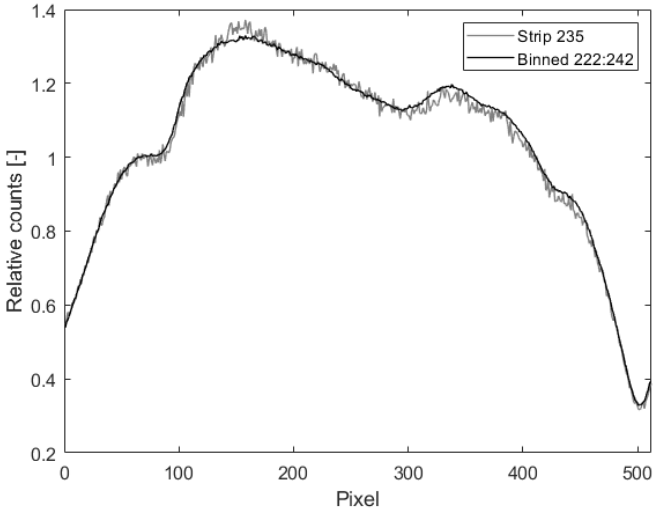

Figure 5.14: Spectra collected with Detector 4 at 30 mm separation in a solid tissue phantom with one individual pixel strip and when 20 strips are binned.

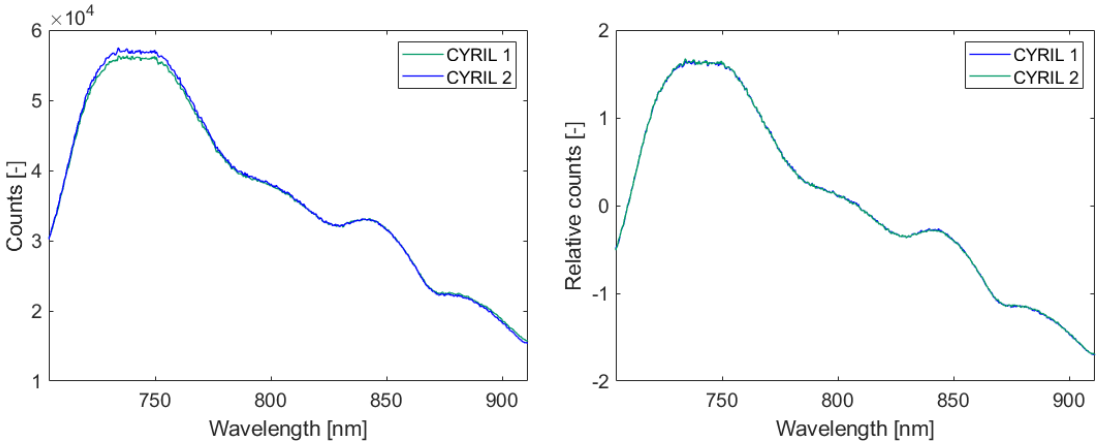

(a) Counts per pixel.

(b) Normalised counts per pixel.

Figure 5.15: Broadband light source spectra collected with the CYRIL 1 and CYRIL 2 setups at binning width = 16 with detector 1.

5.1.2.4 New LabVIEW software

A new LabVIEW VI for CYRIL 2 was created to facilitate the CCD data collection change. The front panel for the user to interact with was similar to the front panel design for CYRIL 1 for ease of use. The block diagram (the back end of the software) was designed to be readable, easy to follow and debug. The main difference between the new VI and the old CYRIL 1 VI was how the CCD sent data to the PC. With the new approach, the CCD sent to the computer snapshots of the CCD at each time point in the form of a 512 $\times$ 512 matrix, where the x-axis was calibrated for wavelength and the y-axis was used to select detector regions. The VI saved these snapshots in

the form of .csv files and it also automatically summed pixels in the regions of interest according to the binning to obtain spectra for a real-time MBLL calculation and display of spectra and concentrations.

The VI was built for two different uses; for the collection of data, and also for the displaying of data stored on the PC. When starting the VI, the data collection main setup window appeared, shown in Figure 5.16. The top section of the window was allocated for the measurement set up; changing the acquisition rate, file name or sending comments. The user could start and stop measurements or take individual snapshots of the CCD, which were displayed in the bottom left plot, amplitude was measured in counts per pixel. The CCD plot was divided into binning regions in an analogous manner as in the CYRIL 1 VI; the binning could be changed either by dragging the coloured lines or by rewriting the values in the bottom right table. This binning selection was only for the MBLL calculations performed real-time within the VI.

The plot on the right side was a y-axis view of the CCD, showing intensity peaks detected from 8 different fibres and allowing the user to check for detector crosstalk. Important indicators on the front panel included "Temperature Set?" and "Current Temperature". These checked the temperature of the CCD as soon as the user started the VI and initiated the cooling, the "Temperature Set?" indicator was red if the CCD was not cool enough. The user could not start measurements until the CCD was cooled down to -70 °C, the VI informed the user of the CCD status by opening a pop-up window with the text "System ready" and the "Temperature Set?" indicator turning green.

Once the measurement started, the user could see the spectra in real time in the "Spectra" tab, Figure 5.17. Concentration changes of HHb, HbO_2, CCO and THb at 30 mm SDS across the whole duration of the measurement were displayed in the "Concentrations: both sides, 30 mm" tab, shown in Figure 5.18. Concentration changes collected with other detectors were displayed in the "Channel 1 3", "Channel 2 7", "Channel 3 6" and "Channel 4 5" tabs, where a custom number of data points was displayed.

The CYRIL 2 measurement could be stopped any time with the "Stop measurement" button. For each measurement, a folder was created at the beginning of the measurement, called what the user specified in the field "File name". CCD snapshots, summed spectra for each detector, calculated concentration changes and a time file with measurement timings and comments were saved in real time in the form of .csv files.

The VI could also be used for the displaying of data collected with CYRIL. The measurement

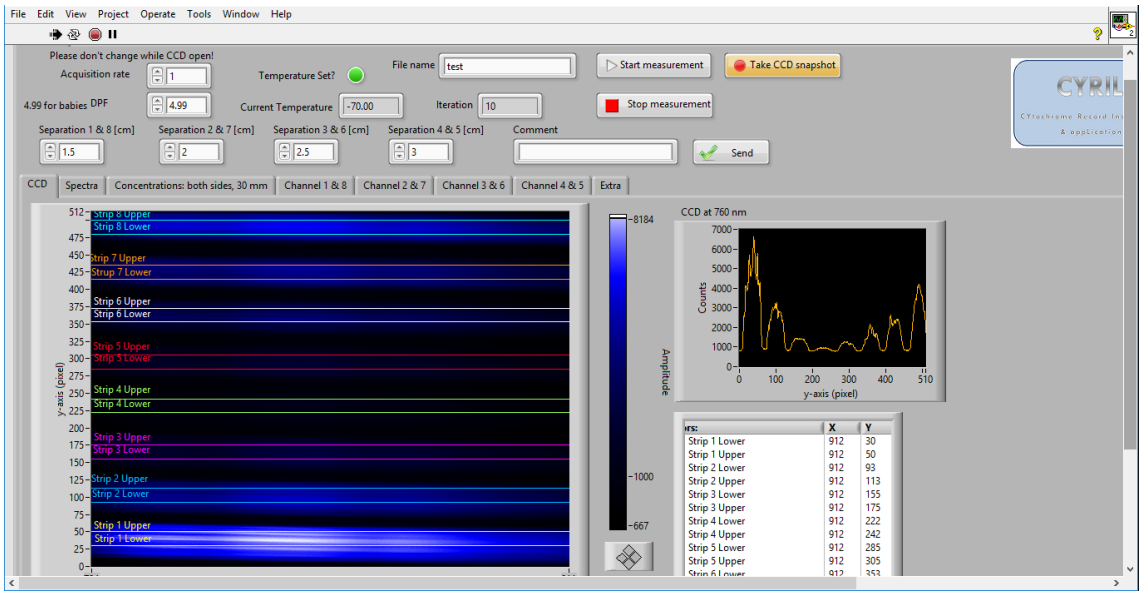

Figure 5.16: The data collection window of the CYRIL 2 VI. The VI informed the user that CYRIL was ready by changing the "Temperature Set?" indicator from red to green. The front panel was used to start/stop the measurement, collect CCD snapshots (single capture), set the file name, the DPF, the acquisition rate of the measurement and SDS. Comments could be also sent to be saved real-time. The CCD tab showed the default binning setting, which could be adjusted either by dragging the lines on the plot of the CCD or by updating the values in the table. An y-axis view of the CCD at 760 nm was shown to assess detector crosstalk.

of intensity was shown as counts over time at one wavelength. To see more than just the time trend over one wavelength, hovering the cursor over the plot showed the broadband spectrum at each time point; as seen in Figure 5.19.

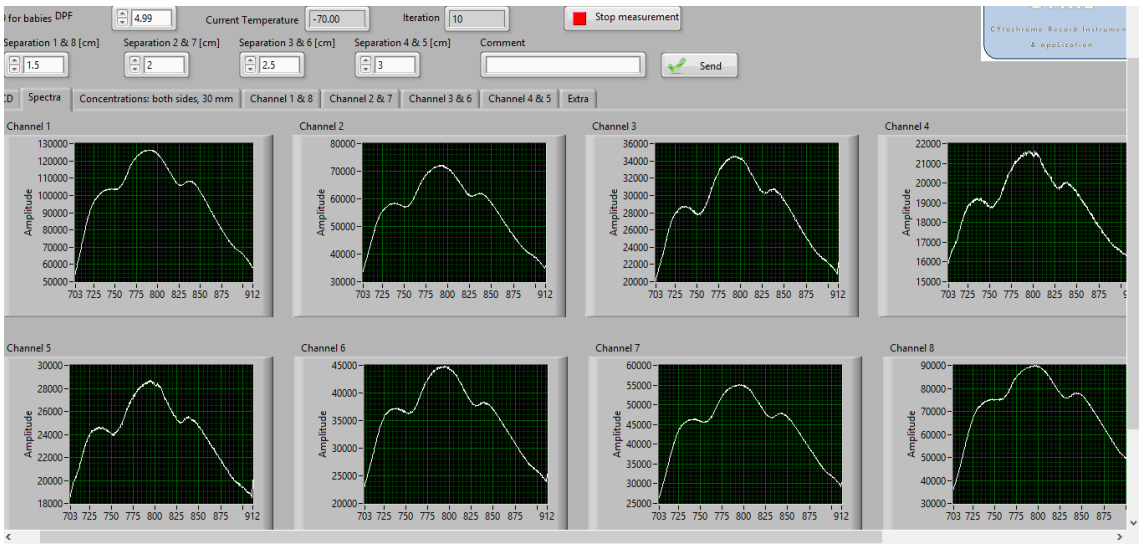

Figure 5.17: CYRIL 2 VI spectra display. Spectra summed according to the default binning setting were displayed for each detector. These spectra included readout noise for each pixel row.

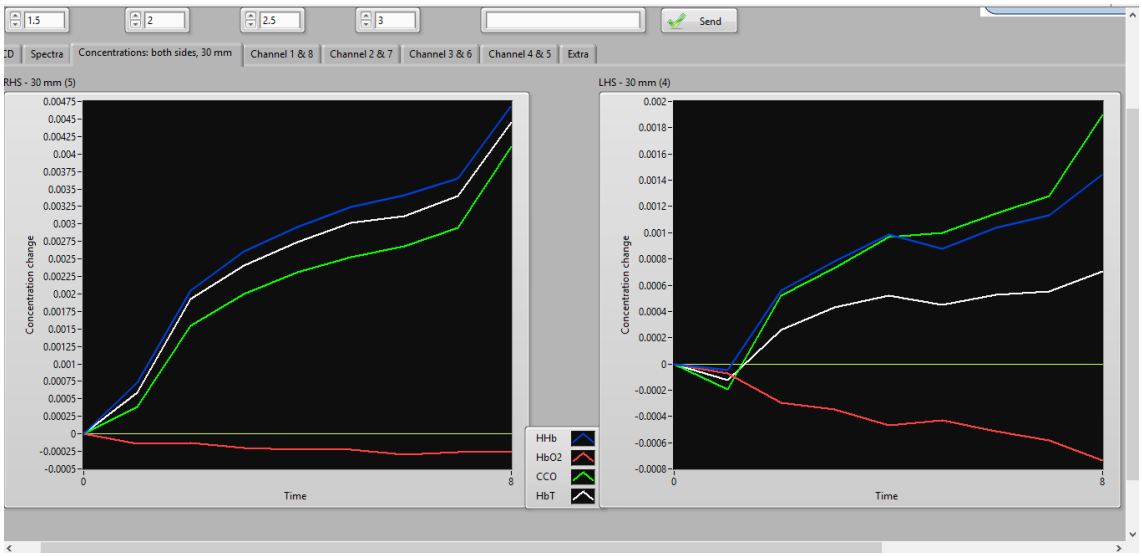

Figure 5.18: CYRIL 2 VI concentration calculated from data collected at 30 mm with detectors 4 and 5. MBLL was applied to spectra summed according to the default binning selection. In this tab, concentration changes from the start of the measurement were displayed.

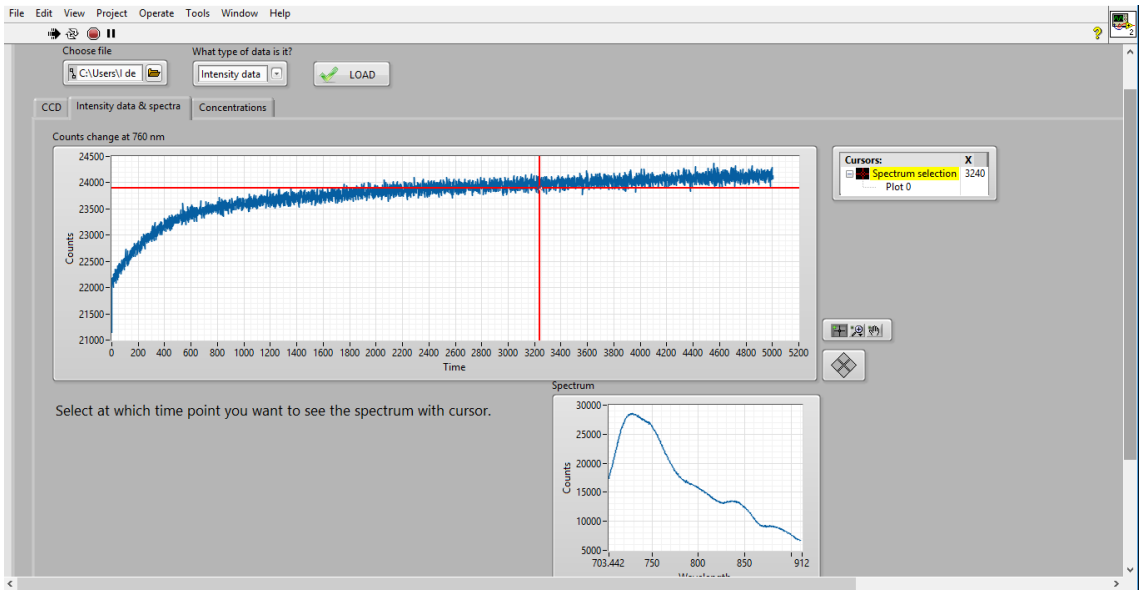

Figure 5.19: Example intensity data collected with CYRIL retrospectively viewed in the CYRIL 2 VI. Moving the cursor across the plot of counts against time displayed the corresponding spectrum below.

Binning selection

Predefined CCD binning values were used in the VI. These were selected to have the least crosstalk from other detectors. To evaluate detectors crosstalk and find suitable binning settings, images of the CCD were taken when illuminated by each detector individually. The detectors were placed on a tissue-mimicking phantom 15 mm apart from the light source, exposure was

set to 0.1 s. The phantom was a homogeneous slab with the optical properties $\mu_a = 0.02$ mm^{-1} and $\mu_s' = 0.9$ mm^{-1}. The 8 different CCD snapshots were then displayed in one plot of counts at 750 nm against pixel number, Figure 5.20. The 8 coloured peaks correspond to 8 detectors. Binning was then set to cover a region 20 pixels wide on the maximum of the peak, where crosstalk was minimal.

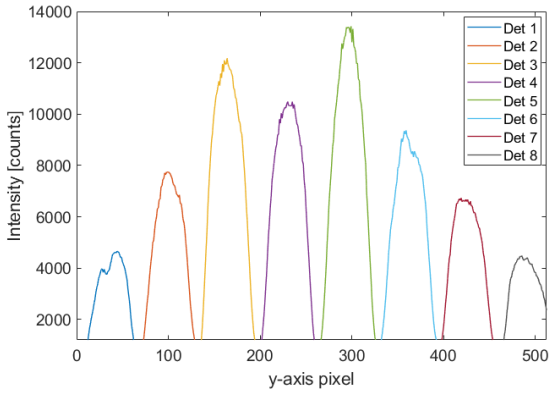

Figure 5.20: Detected counts against y-axis pixels for all 8 detectors when each detector illuminated individually placed on a tissue-mimicking phantom.

Data storage

A disadvantage of the new CCD data storage approach was the immense increase of data stored. While the size of 1000 measurements at an acquisition rate of 1 s with the old setup was only 3 MB, the equivalent measurement with the CCD snapshot approach was $\sim$ 1 GB. To deal with this amount of data, measurements were saved in real time on external hard disk drives with a memory of 2 TB each. While a USB 3.1 connection was fast enough to write data on the disks in real time, the bottleneck of the setup was the data readout, slightly increasing the acquisition rate specified by the user, a 1 Hz measurement was collected at about 0.95 Hz.

The differences between the VI used in CYRIL 1 and the new VI used in CYRIL 2 are summarised in Table 5.2. Figure 5.21 shows the steps of CYRIL 2 data collection with the new VI.

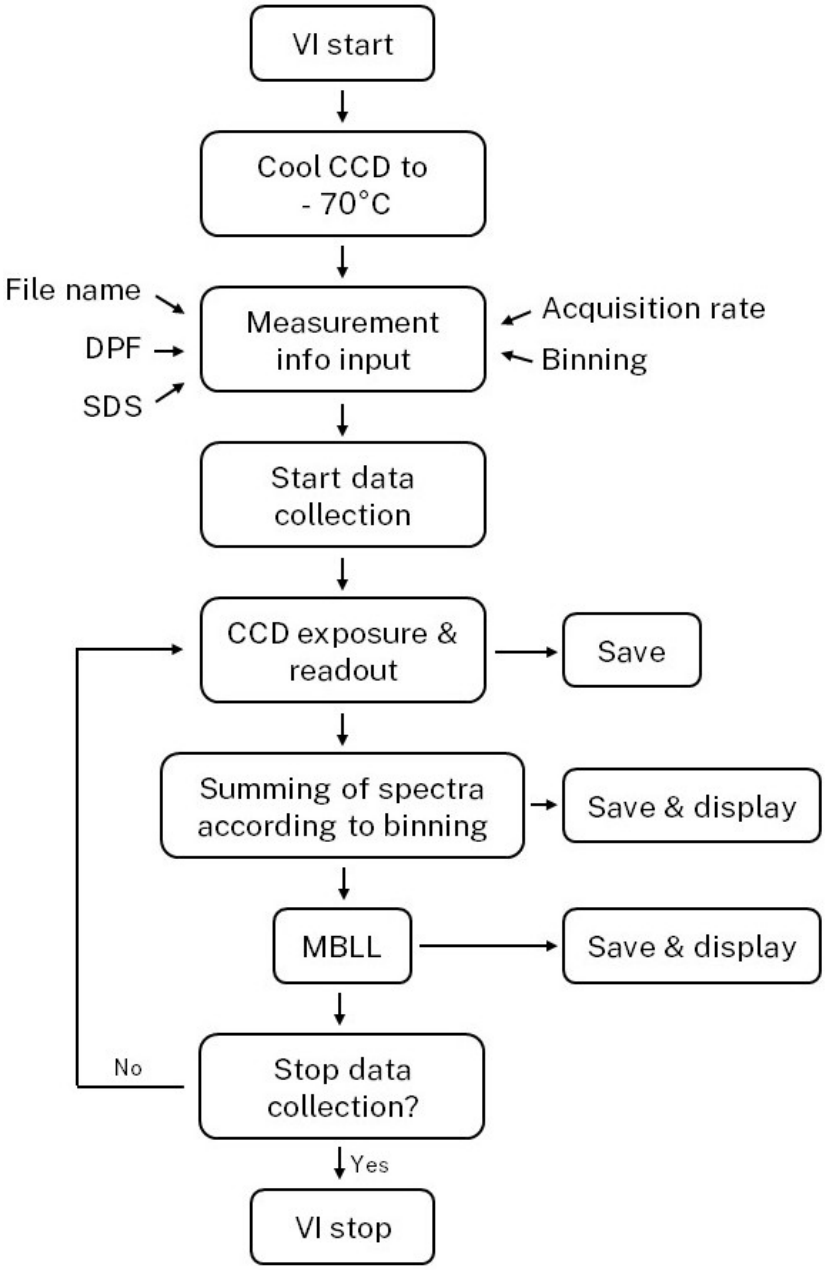

Figure 5.21: Flowchart summarising the process of CYRIL 2 data collection with the new VI.

Table 5.2: Differences between the original VI used in CYRIL 1 and a new version developed for the use in CYRIL 2.

	CYRIL 1 VI	**CYRIL 2 VI**
Temperature check	No	Before measurement start
Data readout	Across binning region, saves spectra	Pixel-wise, saves whole CCD
Noise reduction	Less readout noise	No
Real-time data display	Spectra and conc. changes	Spectra and conc. changes
Load data	No	Display saved .csv files
Data storage	On PC, one folder	2 external storage drives
Storage requirements	Faster readout, less data	Slower readout, more data

5.1.2.5 Reference spectra

The collection of reference spectra with CYRIL 2 was performed in the same manner as for CYRIL 1. A benefit of measuring the reference across the whole CCD was that it could be used for any binning setting and the clinical team did not have to collect a reference spectrum for each binning setup.

The use of a reference tube for the collection of reference spectra was validated with a dark room measurement. Spectra collected at an exposure of 0.1 s in a dark room and with the customised reference tube are in Figure 5.22. All spectra were normalised at 750 nm. 5 measurements were repeated for each mode; for the dark room, the position of the detector relative to the light source was changed. The detector was taken out of the detector holder in the tube measurements and put back in place in the holder. Figure 5.22a shows a slight offset between the two averaged spectra. This offset could be caused by the lower repeatability of the dark room measurement.

Comparing Figure 5.22b to Figure 5.22c shows that the repeatability of the poster tube measurement was higher; small differences between the 5 spectra collected in the dark room are visible, particularly in the 850 nm region. The dark room measurement was less repeatable because the positioning of the detectors to the light source was not fixed, which can cause uneven illumination. Overall, the customised poster tube was considered suitable for the collection of reference spectra and was used throughout this work.

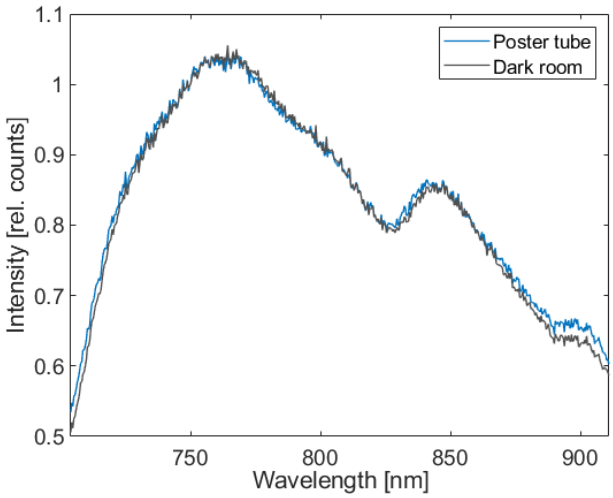

(a) Reference spectra collected in a dark room and in a poster tube with detector 4. Average of 5 measurements, normalised at 750 nm.

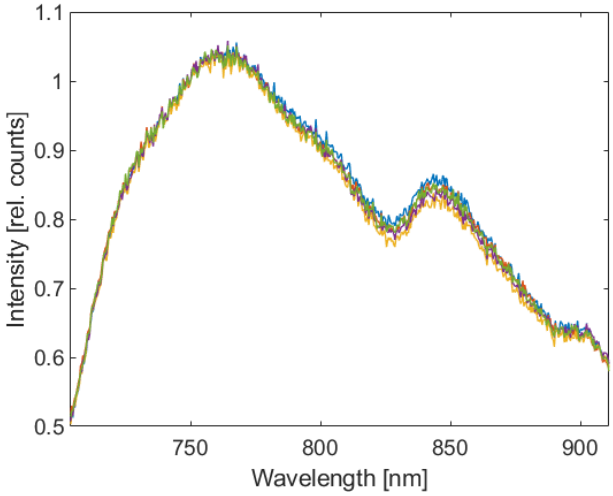

(b) 5 repeated measurements of reference spectra in a dark room, normalised at 750 nm.

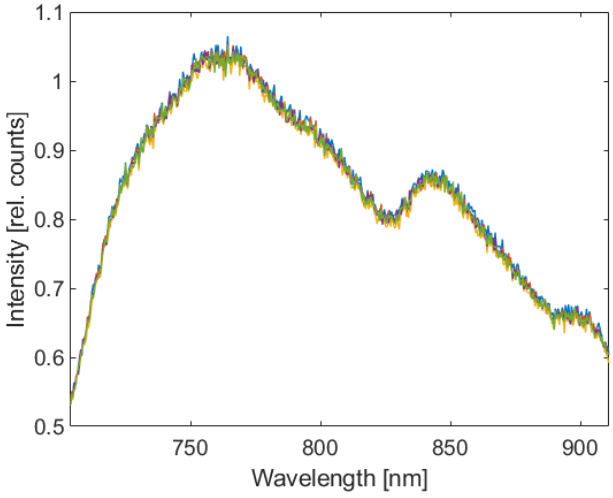

(c) 5 repeated measurements of reference spectra in a customised poster tube, normalised at 750 nm.

Figure 5.22: Reference spectra collected in a dark room and a customised poster tube.

5.1.3 TR NIRS MAESTROS

The second NIRS system used in this work was a TR system. As TR systems can measure μ_a and μ_s' directly, it was used during phantom studies to obtain a reference to compare CYRIL to. MAESTROS (Metabolism and hAemoglobin Evaluation via a Spectroscopic Time Resolved Optical System) was developed in-house at UCL [245, 113] and operated by Dr Frédéric Lange, who also analysed the data and provided μ_s', chromophore concentrations and StO_2. MAESTROS (shown in Figure 5.23) was designed to monitor c_{HHb}, c_{HbO_2} and c_{oxCCO}; its performance was assessed using the BIP and nEUROPt protocols and in optical phantoms [113].

The MAESTROS light source was a supercontinuum laser with 16 wavelengths. The individual wavelengths (selected between 780 and 900 nm) were tuned using a dual acousto-optic filter, splitting the initial light pulse into two beams. The light travelled via optical fibres to the sample (tissue). The reflected light was collected by up to four detectors placed at the desired SDS, which was 3 cm for phantom measurements in this work. The beam travelled through optical attenuators which adjusted the signal dynamics, and then reached a photomultiplier tube. The signal from the photomultiplier tube continued to a time correlated photon counting card, which measured the temporal point spread function of the detected pulse.

The acousto-optic filter wavelength selection was very fast; signal at each wavelength was acquired sequentially for 20 to 50 ms. The measurement was repeated several times and summed to obtain a good photon count. The fast switching enabled MAESTROS to run at a speed from 0.5 to 2 Hz depending on the number of wavelengths used [113].

5.2 NIRFAST simulations

NIRFAST (Near Infrared Fluorescence and Spectral Tomography) [23, 24] is an open-source software toolbox for MATLAB for multimodal optical imaging. It simulates the propagation of light in biological tissue; originally designed for the modelling of breast tissue with diffuse optical tomography, it can be used for single and multiwavelength spectral modelling and image reconstruction. NIRFAST also has the capability to combine measured data with 3D models to recover chromophore concentrations. In this work, NIRFAST was used to generate multiwavelength spectral data from CW NIRS multidistance measurements in a neonate. The aim was to obtain data simulating various NIRS measurement situations and to use this data to assess the performance of different StO_2 calculation algorithms. The benefits of using NIRFAST for performance assessment include the knowledge of the true value of the optical properties and the possibility to test the influence of ECT on the recovered StO_2.

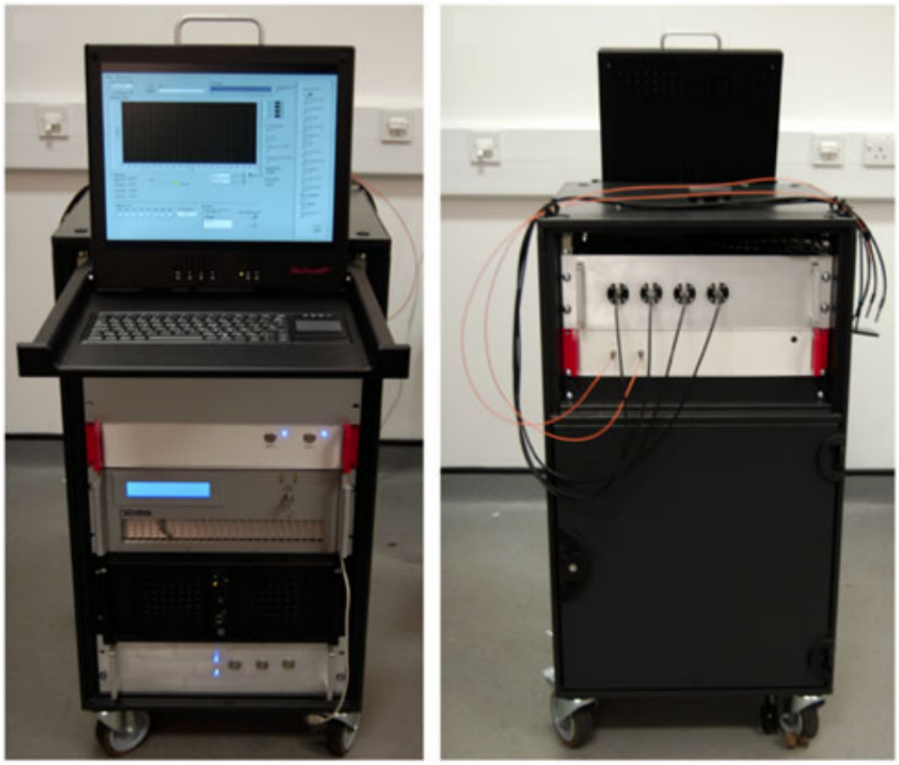

Figure 5.23: The MAESTROS system from the front (left) and the rear (right) side. Taken from [113].

NIRFAST uses a model of light transport in a turbid medium, the diffusion equation (Eq. (3.30)) applied with an air-tissue boundary represented by a index-mismatched type III condition (called Robin or mixed boundary condition), which assumes there are no photons coming into the object through the boundary unless they enter at the source position[2] [129]. NIRFAST applies the model in the volume (mesh) using the finite element method (FEM). In FEM, the mesh is subdivided into small elements connected at nodes. The diffusion equation is expressed as a system of linear algebraic equations, the fluence is approximated in each point. The light source is a Gaussian distributed source, assumed to be spherically isotropic and when centred one transport scattering distance ($1/\mu_s'$) within the outer boundary, the simulation accurately reflects experimental data [24]. In a generalised forward model, when used for CW NIRS, the user provides NIRFAST with a mesh with nodes and elements, assigns optical properties and light source/detector placements. The output of the forward model is intensity spectra with counts at each wavelength detected at each detector.

[2]Type III boundary conditions are more general than zero/extrapolated boundary conditions (both are type I, Dirichlet), but also more complex [132, 246].

5.2.1 Mesh

The mesh used for the simulation was created by Brigadoi et al. [247], who generated a series of meshes from MRI images of neonates of different gestational ages. The benefit of the models is that the MRI images were segmented and the resulting meshes have several tissue layers, giving the user the option to define optical properties individually for each layer: extracerebral tissue (ECT), cerebrospinal fluid (CSF), grey matter (GM), white matter (WM), cerebellum and brainstem. The layered structure of the mesh is shown in Figure 5.24. The 40-week GA model was selected as a representation of a full term neonate's head. The composition of the model was 26.5% ECT, 24.8% CSF, 25.7% GM, 18.9% WM, 0.8% brainstem and 3.3% cerebellum. (The majority of ECT is in the bottom part of the model and was not illuminated during the simulation.)

The meshes were in a mesh-based Monte Carlo (MMC) format, different from the mesh structure required for NIRFAST. A MMC mesh is saved in three different files; a mesh with the element and nodes, a data file containing the individual optical properties of the layers, and an input file specifying the properties of the light source and the detectors. NIRFAST works with a mesh structure, with all the needed information saved in one file. A custom MATLAB R2019a script was written to convert the MMC model into a NIRFAST mesh structure. The placement of the light source and the detectors was selected to mimic a clinical frontal lobe measurement (right hemisphere) with 5 detectors with separations 10, 15, 20, 25 and 30 mm [111], shown in Figure 5.25.

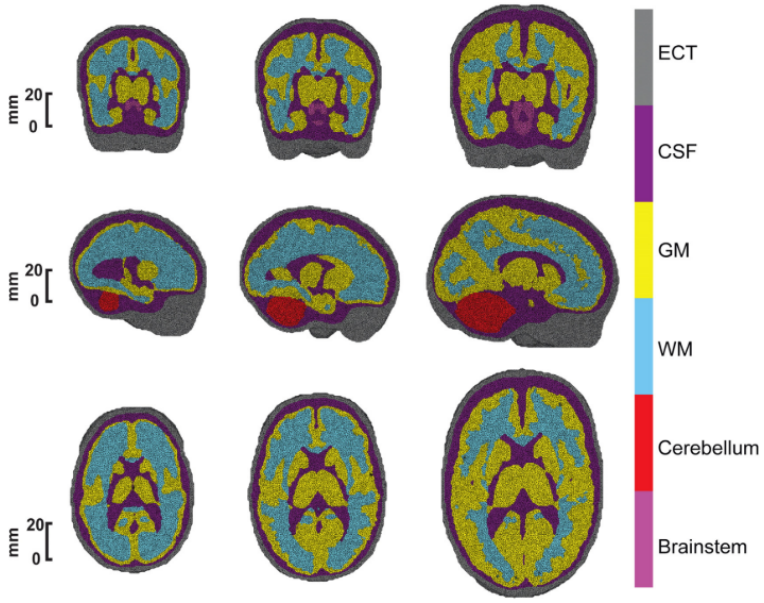

Figure 5.24: Multilayered tetrahedral meshes for example gestational ages (29, 35 and 44 weeks). The first row shows a coronal view of the mesh, the second row shows a sagittal view and the third show an axial view. In grey is displayed ECT, in purple CSF, in yellow GM, in cyan WM, in red the cerebellum and in violet the brainstem. Taken from [247], reproduced with permission of Elsevier.

While the high resolution of the mesh - maximal element size of 1 mm^3 [247] - is an advantage in terms of how accurately the mesh represents a neonatal head, the amount of nodes (805,537) is a considerable burden for the computational requirements of the simulation. Additionally, generating broadband spectra at hundreds of wavelengths increases these requirements as the fluence in the whole mesh is calculated for each wavelength separately. On a standard computer, generating spectra for one single broadband measurement could take several hours, up to days. The team behind NIRFAST have been developing a faster version of the toolbox, which uses the GPU architecture of the computer to parallelize the problem [248]. Although the NIRFAST GPU toolbox is not yet publicly available (as by October 2019), it was kindly provided for use on this project by the University of Birmingham NIRFAST team lead by Prof. Hamid Dehghani. With the upgraded toolbox, the generation of one data set with 301 wavelengths then took around 2.5 hours on a PC with a Intel(R) Core(TM) i7-8700 CPU @ 3.20, 32 GB RAM and a NVIDIA GeForce GTX 1080 Ti GPU.

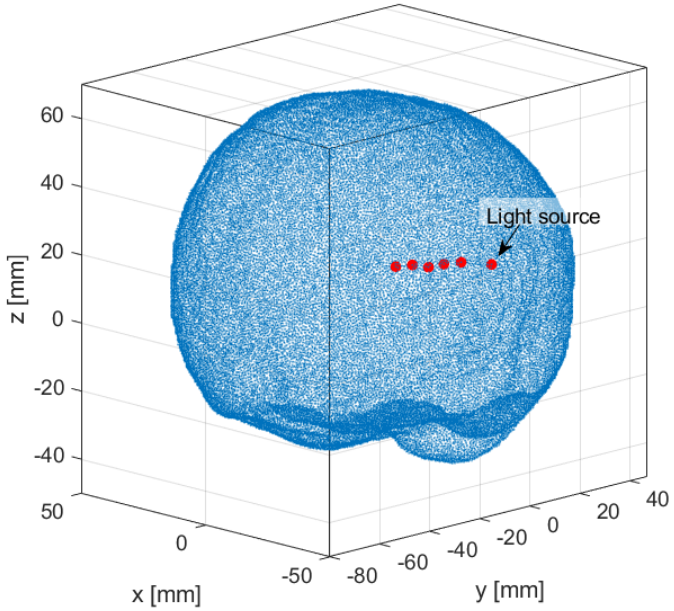

Figure 5.25: Detector and light source setup on the 40-week neonatal head mesh for NIRFAST simulations. The light source is on the right, next to the five detectors with separations 30, 25, 20, 15 and 10 mm, from left. The mesh is taken from [247].

5.2.2 Simulated models

NIRFAST was used to generate data from 650 to 950 nm at 1 nm steps. Optical properties were set either for a homogeneous model, where all layers were identical, or a heterogeneous model. In the heterogeneous case, the optical properties of the cerebellum and brainstem regions were set identical to white matter. The scattering model used in all simulations was $\mu_s' = a \times (\lambda/1000(\text{nm}))^{-b}$, where a is scattering amplitude and b is scattering power. Five different models were used in NIRFAST to obtain broadband data, the optical properties of each are in Table 5.3. Optical properties of the individual tissue layers were taken from [249], the refractive indices from [133]. Example spectra from models A, B, C and D1 are shown in Figure 5.26, where the difference between the models is the addition of water absorption or layered structure.

Table 5.3: The optical properties set in five different models of the neonatal head used for the generation of broadband spectra in NIRFAST. Models A and B are homogeneous models with and without water absorption; model C is a layered structure without water absorption. Models D1 and D2 are both layered with water absorption, the optical properties are different by 10%.

Model	Layer	WF [%]	c_{HbO_2} [μM]	c_{HHb} [μM]	a [$mm^{-1}\mu m^{-1}$]	b [-]	StO_2 [%]	n [-]
A	all	0	55.0	29.5	0.51	1.74	65.1	1.33
B	all	80	55.0	29.5	0.51	1.74	65.1	1.33
C	ECT	0	43.8	15.7	0.73	0.90	73.6	1.33
	CSF	0	0	0	0.30	~ 0	0	1.33
	GM	0	55.0	29.5	0.51	1.74	65.1	1.40
	WM	0	67.0	20.9	0.82	1.31	76.2	1.41
D1	ECT	30	43.8	15.7	0.73	0.90	73.6	1.33
	CSF	99	0	0	0.30	~ 0	0	1.33
	GM	80	55.0	29.5	0.51	1.74	65.1	1.40
	WM	80	67.0	20.9	0.82	1.31	76.2	1.41
D2	ECT	30	48.2	17.3	0.66	0.81	73.6	1.33
	CSF	99	0	0	0.27	~ 0	0	1.33
	GM	80	60.5	32.5	0.46	1.57	65.1	1.40
	WM	80	73.7	23.0	0.74	1.18	76.2	1.41

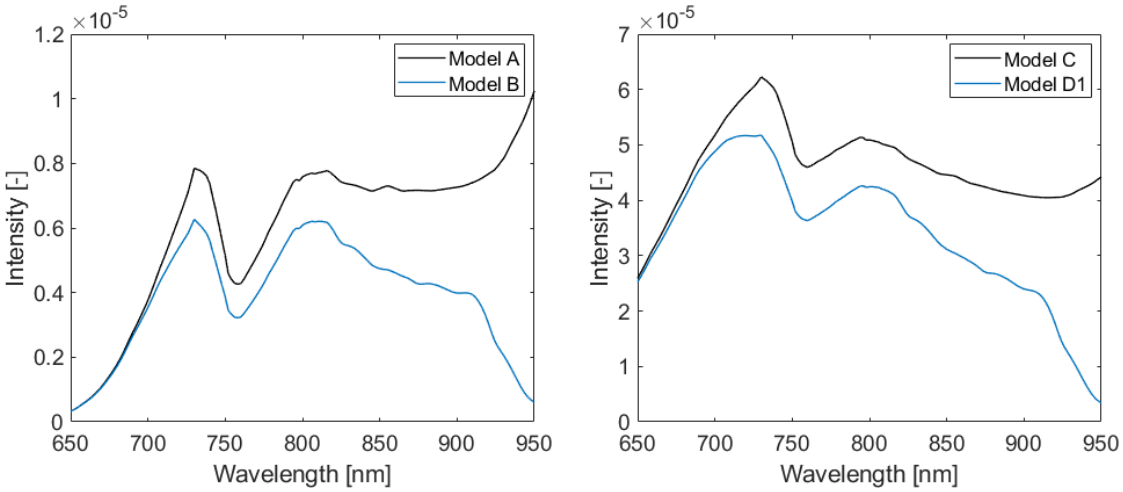

(a) Homogeneous models. **(b)** Heterogeneous models.

Figure 5.26: Spectra simulated with NIRFAST in models A (homogeneous, no water), B (homogeneous, with water), C (heterogeneous, no water) and D1 (heterogeneous, with water) at 30 mm SDS.

5.2.2.1 Tissue layer desaturations

Further work with NIRFAST was focused on the generation of data simulating tissue saturation and desaturation. The first desaturation model, referred to as model E, was performed similarly to the work described in [148].

Two head models were used, a homogeneous and a two layer model, where one layer was

considered ECT and the second layer, brain, was CSF, GM, WM, brainstem and cerebellum combined. The baseline optical properties were taken from [148], using the values of the brain for the second layer and the average of the skin and skull values for the first layer. The oxygenation of the homogeneous model was changed in 5 steps. During the desaturation, StO_2 was changed and total haemoglobin, c_{THb}, remained constant. In the heterogeneous case, the oxygenation of the second, deeper layer was changed while the first, surface layer remained constant. Ten simulations were performed in each step with scattering changed by up to +/- 30% to account for inter-subject variability.

The second desaturation model was focused on investigating simultaneous oxygenation changes in different tissue layers. In model F, both ECT and brain were oxygenated in a range StO_2 = 10–90 %. The baseline optical properties were the same as in model E. Model F involved 23 different combinations of ECT and brain oxygenations. Scattering remained the same in all simulations. Table 5.4 shows the used optical properties for both models, inspired by [148].

Table 5.4: The optical properties used in models E and F, simulating layer desaturations. The scattering properties in model E were changed 10 times by up to 30% for each of the five brain desaturation steps, resulting in 10 spectra for each step. In model F, scattering properties remained at the baseline values and 23 different combinations of ECT and brain oxygenation were used.

Layer	$\mathbf{c_{THb}}$	**a**	**b**	**Model E $\mathbf{StO_2}$**	**Model F $\mathbf{StO_2}$**
	[μM]	[mm$^{-1}\mu m^{-1}$]	[-]	[%]	[%]
ECT	59.5	1.56	1.07	80	10–90
Brain	76.0	0.80	1.61	50–80	10–90

5.3 Phantom measurements

Optical phantoms are tissue mimicking objects used for the evaluation of optical system performance used throughout system development and for the validation of systems (see section 4.1.2.2 for a description of the validation of brain oximetry measurements in phantoms). An ideal phantom medium is non-diffusive and transparent in the whole optical spectrum of interest. Scattering and absorbing centres can be added in a desired ratio to achieve the optical properties (μ_s' and μ_a) of biological tissue [250]. Optical phantoms used in NIRS can be solid or liquid. Solid phantom can be made out of epoxy resin, silicon rubber or 3D printed. Liquid phantoms are made of water and small fat droplets. Optical phantoms can be dynamic with changeable optical properties; solid phantoms can have an movable inclusion with different optical properties [169], liquid phantoms are filled with a medium with changeable optical properties. Phantoms can also be a combination

of both types of medium to obtain a better simulation of the optical properties of the human head; e.g. by using a two layer phantom with a top solid layer and a liquid phantom underneath [165].

Two different phantoms were used for acquiring data in this work; a homogeneous liquid phantom and a two-layer liquid phantom with solid windows. Both phantoms gave the user the option to use multiple NIRS systems simultaneously for system comparison.

The objective for using dynamic phantoms in this work was to simulate the measurement of StO_2 in biological tissue with the impact of instrumentation. The presence of a solid layer in the two-layer phantom was a closer approximation of the neonatal head than the homogeneous phantom. Both phantoms were used because if the homogeneous phantom was not used, it would be impossible to assess whether the source of StO_2 measurement errors in the two-layer phantom arose from the presence of solid layers or from the instrumentation.

5.3.1 Homogeneous phantom

The recipe for this liquid phantom was developed in-house motivated by the need for a optical phantom suitable for the quantification of CCO with NIRS [113] and is also suitable for StO_2 measurements. The phantom was filled with liquid that could be oxygenated and deoxygenated in cycles by blood and yeast; yeast consumes O_2 for aerobic respiration and also contains CCO. The phantom was oxygenated by bubbling O_2 gas through the liquid until it was fully oxygenated, yeast then deoxygenated the liquid. Typically, the oxygenation of the phantom was 100% at the beginning of the measurement due to the exposure to air; deoxygenation occured once yeast was added. Once the phantom was doexygenated, bubbling oxygen increased it again and the deoxygenation process started as soon as the bubbling of O_2 was stopped.

5.3.1.1 Measurement setup

An advantage of this phantom was its simplicity and quick preparation. A schematic of the phantom measurement setup is in Figure 5.27. The container was a metallic box (27 $\times$ 15 $\times$ 16 cm) with inner walls covered in black absorbing material to satisfy the semi-infinite boundary approximation. It was filled with 1425 ml of water mixed with phosphate-buffer (2 bags of PBS, P3813, Sigma-Aldrich, Germany) to maintain the pH of the solution at physiological values of pH = 7.4. Scattering centres were incorporated by adding 75 g of 20% Intralipid (Fresenius Kabi Italia, Italy); 15 ml of blood were added to the mixture for light absorption. After the initiation of the measurement 15 g of yeast were added. The container was placed on a hot stirring plate and kept at a temperature of 37 $\pm$ 1 °C with constant temperature monitoring using a sensor immersed into the liquid. The liquid was continuously stirred with a magnetic stirrer. An industrial O_2 tank

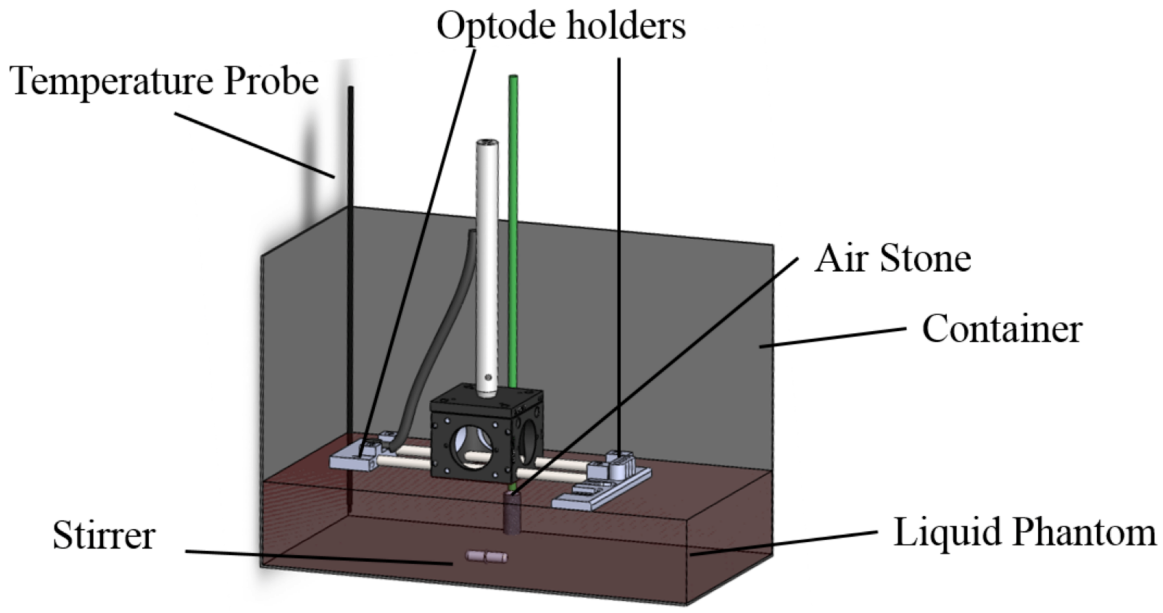

Figure 5.27: Schematic of the homogeneous phantom measurement setup. Optical fibres are not shown. Taken from [113].

was used for adding the gas; an air stone connected to the gas tank was placed at the bottom of the phantom. The O_2 content in the liquid was measured with a diffuse oxygen content probe. The data from the sensor was logged manually; when it was 0%, total deoxygenation was assumed, and values over 100% occurred when the phantom was fully oxygenated. The phantom was covered with plastic film to prevent gas exchange with the surrounding air. The oxygenation status of the solution was also tracked real-time with CYRIL, as it displayed concentration changes of HbO_2 and HHb calculated with MBLL and oxygenation/deoxygenation of the phantom would eventually reach plateaus. The protocol of the measurement is in Table 5.5.

Table 5.5: Liquid phantom measurement protocol.

Step	
1	Baseline
2	Add 15 g of yeast
3	Wait for plateau
4	Turn on O_2
5	Wait for plateau
6	Turn off O_2
7	Repeat step 3 to 6
8	Stop

Two NIRS instruments were used on the phantom simultaneously; the liquid surface area was big enough to ensure the individual system optodes would be far apart not to be affected by the

other device. Optode holders were 3D printed out of a rigid, black material and held the detector fibre heads in place. The SDS was 3 cm for each of the 4 MAESTROS detectors and 15, 20, 25 and 30 mm for each of the 4 CYRIL detectors used. The optode holders were placed on the surface of the liquid and slightly submerged to ensure no gas bubbles would be trapped below the optodes. The measurements were performed in a dark room to avoid interference by ambient light. The exposure was set to 1 s. After the measurements, the optode holders and the fibres were thoroughly cleaned with clinical sanitiser to prevent contamination.

5.3.2 Two-layer phantom

A two-layer phantom is a better replication of the human head than the homogeneous phantom as it can simulate the skull by introducing a solid layer on top of the liquid medium. A two-layer phantom with thin windows with the optical properties of the neonatal skull was developed at the Biomedical Optics Research Laboratory at the University Hospital Zurich, Switzerland, for simultaneous measurements of different NIRS systems and their comparison [165]. As the phantom setup is more complex than the homogeneous phantom, replication was not possible and the original phantom container was generously lent to our research group for a month in June 2018.

The design of the phantom was focused on simultaneous measurements with 4 different NIRS systems; an irregular octagonal shape with four wide and four narrow side faces enabled such setup. The container was 3D printed out of absorbing material to satisfy semi-infinite boundary conditions and each long side featured a window, which was covered with 2.5 mm thick silicone slabs with optical properties of the neonatal head [165]. The phantom was covered with a cap to isolate the phantom from ambient air; the cap featured slots for the placement of temperature and diffuse oxygen sensors and a tube to add O_2.

5.3.2.1 Measurement setup

The use of the phantom was equivalent to the homogeneous phantom, it was filled with a liquid solution which was deoxygenated and oxygenated in cycles. The recipe followed the instructions of the phantom authors [165]; it was filled with 2500 ml of water, 5 bags of phosphate-buffer, 74 ml of Intralipid, 20 ml of blood and 20 g of yeast. Temperature and diffuse oxygen content were monitored throughout the study, the phantom was kept at 37 ± 1 °C and continuously stirred with a magnetic stirrer. The measurement protocol was identical to the protocol in Table 5.5.

CYRIL and MAESTROS probes were placed on opposite sides of the phantom; the optodes were held by black rigid optode holders and attached to the silicon windows. The measurements

were performed in the dark to avoid contamination with ambient light. The setup of the phantom with the NIRS optodes and sensors attached is in Figure 5.28.

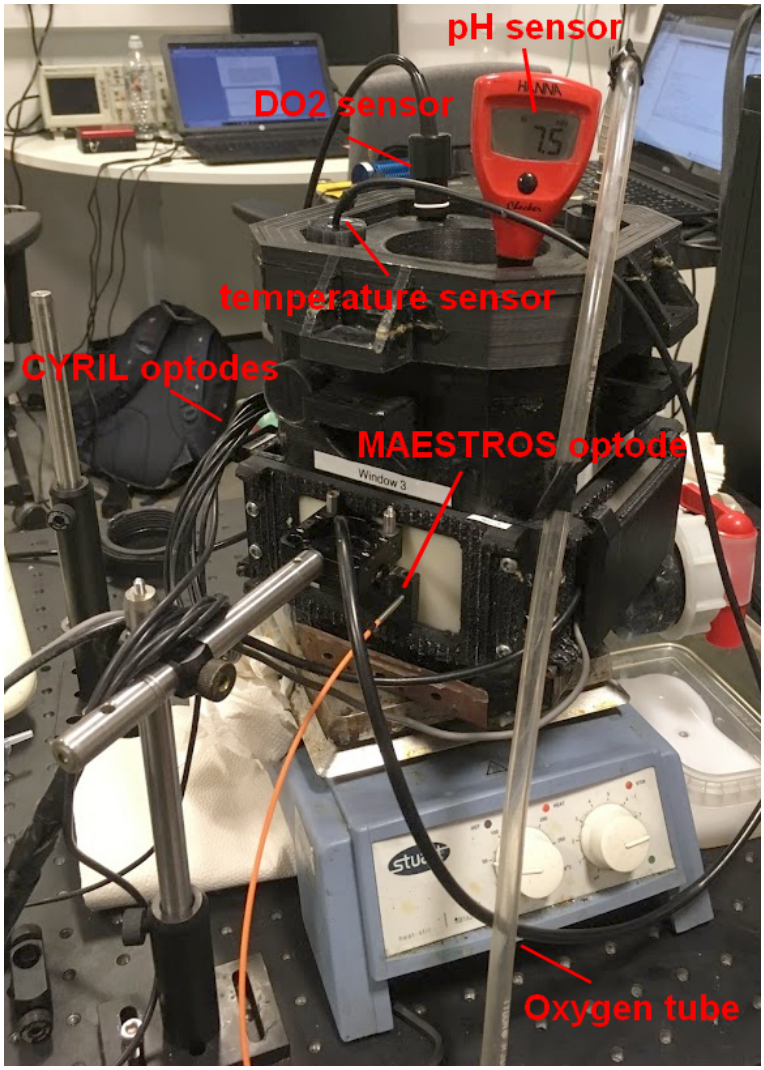

Figure 5.28: Two-layer phantom with sensors and NIRS optodes attached. DO2 sensor stands for diffuse oxygen content sensor.

5.4 Neonatal studies

The clinical application of this work is focused on the use in neonates diagnosed with HIE. NIRS data from this patient group have been collected through a collaboration with the Institute of Women's Health at UCLH and UCL, the Baby Brain Study. Data collection was performed at the NICU at UCLH, ethical approval for the Baby Brain Study at UCLH, London was obtained from the North West Research Ethics Centre (REC reference: 13/LO/0106).

The data analysed in this work was collected in two different study sessions; one set of mea-

surements was collected primarily for the monitoring of CCO ("session 1"), the study was set up by Dr Gemma Bale. The instrument used was CYRIL 1 and the data was collected between December 2013 to November 2015. The second set of the measurements ("session 2") was conducted for the purposes of this work. The instrument used was CYRIL 2 and the study lasted throughout 2019.

5.4.1 Monitoring neonates with HIE: session 1

The objective of the first session of the data collection in infants with HIE was to measure changes in CCO concentration with bNIRS at the NICU cotside in the first days of life. Parents of term or preterm infants born or transferred to UCLH for acute brain injury treatment were approached for the study. Children with congenital malformations were excluded. Written, informed consent was obtained from parents before each study.

Treatment and monitoring at the NICU included continuous 10 channel EEG monitoring with a Nicolet monitor (Natus Medical Incorporated, USA). Intellivue monitors (Philips Healthcare, UK) collected physiological data, saved in real time in the CYRIL 1 computer using the ixTrend software (ixitos GmbH, Germany). The monitor collected SpO_2 measurements with pulse oximetry from the foot or hand, heart rate by ECG, respiratory rate, mean arterial blood pressure from an intra-arterial catheter and the partial pressures of O_2 and CO_2 measured transcutaneously. Infants with HIE were treated with TH, their temperature was lowered to to 33.5°C using a cooling mattress beginning as soon as possible in the first 6 hours of life for 72 hours, followed by a 16 hour rewarming period in which their temperature was raised by 0.5°C every 2 hours. The patients were intubated and ventilated during hypothermia. After rewarming, MRS was performed to measure the Lac/NAA ratio. The infants were sedated either intravenously with morphine or orally with chloral hydrate.

The CYRIL 1 NIRS optodes were placed on each side of the forehead, each channel with four detectors was monitoring haemodynamics in one hemisphere. The forehead placement was selected as it was free from EEG electrodes and hair. The probe holder was attached to the skin with double-sided tape. The probes were tucked underneath the EEG cap and covered with blackout fabric to reduce interference from ambient light. The infants were positioned in the supine position throughout the study. NIRS data was collected during hypothermia or during the rewarming period, the studies started as soon as possible after birth. Enrolled infants which were not diagnosed with HIE were monitored with NIRS as soon as possible after birth. The aim was to collect data for 4–6 hours each day during hypothermia and rewarming (day 1–4) and before and

after MRS. Data was collected at with exposure 1 s at sampling frequency of approximately 1 Hz (exposure + processing time).

The data was later used in this project to calculate StO_2; the methodology and results are discussed in Chapter 6.

5.4.2 Monitoring neonates with HIE: session 2

The second measurement session at the UCLH NICU was performed with CYRIL 2 for the purposes of this project. The measurements were also part of the Baby Brain Study; the aim was to measure StO_2 in infants with HIE as soon as possible after birth, for at least one hour daily. As the use of CYRIL in the NICU was already well established thanks to the work of Dr Gemma Bale and the clinical team, little changes were introduced to the measurement protocol. The details the motivation for the work, the protocol and results are discussed in Chapter 9.

5.5 Summary

This chapter described the data collection for the majority of work described in this thesis. Computational simulations were performed with NIRFAST, a software toolbox for MATLAB. It was used to generate broadband spectra in a model of a neonatal head. A broadband multidistance NIRS system CYRIL collected data in dynamic tissue mimicking phantoms during oxygenation/deoxygenation cycles. The system was also used in the clinic to collect data in neonates.

The motivation for the use of simulated spectra was the controllability of the environment: the user provides NIRFAST with a model with defined optical properties and a desired NIRS measurement setup. The result of the simulations are spectra at selected wavelengths. Several different measurements in a 40-week old neonatal head mesh were simulated with NIRFAST; including homogeneous and heterogeneous mesh models with or without absorption by water. To evaluate the sensitivity of StO_2 measurements, desaturations in the brain or extracerebral tissue were also simulated.

Hardware and software changes were introduced to the system for the purposes of this project, including a new LabVIEW user environment and amendments to the data storage methods to simplify the use of the system in the clinic and obtain more information about the measurement. CYRIL 2 was used to collect data in tissue-simulating phantoms; a homogeneous phantom and and also a two-layered phantom. The benefit of work with phantoms was the ability to assess the system performance in a controlled environment. The data described will be further used for the assessment of various NIRS algorithms in the following chapters.

Broadband multidistance intensity spectra were collected with CYRIL, an in-house built CW NIRS system. Before the start of this project, infants with HIE in the NICU at UCLH were monitored from as soon as possible after birth and during TH for several hours. The analysis of this data is described in the next chapter.

Chapter 6

Application of spatially resolved spectroscopy in broadband NIRS

Spatially resolved spectroscopy is a commonly applied StO_2 measurement algorithm thanks to its simple implementation and the ability to decrease the influence of superficial layers. It is applied both commercially and in research and it was the first choice for an algorithm to calculate tissue oxygenation from broadband data collected with CYRIL 1. In this chapter, the algorithm is applied to data collected in the NICU with the aim of exploring its application to CYRIL data.

6.1 Motivation

The main goal of this work was to develop a novel algorithm to measure StO_2, BRUNO, which would recover StO_2 with high precision and accuracy and track brain signals with minimal ECT signal contamination. The development of BRUNO started with prior knowledge about StO_2 measurements - multiple StO_2 algorithms have already been described (see Table 3.1). Among those are two algorithms, spatially resolved spectroscopy (SRS) and broadband fitting (BF), which are of particular interest for BRUNO development. The idea for the novel algorithm was to combine SRS and BF, benefiting from both the multidistance approach in SRS and the use of broadband spectra in BF. The initial step of BRUNO development was to thoroughly explore these algorithms to identify their strengths, weaknesses and applicability to CYRIL data. The first algorithm to be explored was SRS.

SRS is a multidistance approach to measure tissue oxygen saturation commonly applied in commercial NIRO systems and research systems [251], also in a broadband NIRS setting [213]. The data collected with CYRIL 1 in the NICU (described in section 5.4.1) had not yet been used to calculate oxygenation and this gave the opportunity to explore the application of SRS to bNIRS data and obtain tissue oxygenation values for infants with HIE in the first days of life.

The summary of StO_2 measurements in HIE patients in Table 4.1 shows that the findings are inconsistent - most studies report an increase in HIE with poor outcome but some also found no difference between the subject groups or a lower StO_2 in HIE. While the subject-dependent physiological background of HIE progression contributes to the disagreement in study results, drawing firm conclusions on the prognostic value of oximetry in HIE is burdened by the causes facing all cerebral oximetry applications, discussed in section 4.1.2, including poor accuracy and inter-instrument comparability. The presence of different data analysis algorithms implemented in instrumentation (which are often not published) could contribute to the disparities. The aim of the work described in this chapter was to investigate how much SRS algorithm implementation affects the recovered StO_2. The algorithm gives the NIRS instrument developer the freedom of choice of which wavelengths to use, for example, or how to account for scattering. The specific setting of the algorithm could have an impact on the use of tissue oximetry as a prognostic tool in HIE.

Preliminary work on this topic was published by Kovacsova et al. [252]; the authors suggest that changing the SRS approach can cause different results. To explore this further, more approaches were included in this study, the data analysis method was updated and relationships between StO_2 and HIE severity were scrutinised.

6.2 Confounding factors in SRS

The SRS algorithm, described in section 3.4.4, can be implemented with slightly different settings; it does not assume any "fixed" light-source detector separations or wavelengths. There are several aspects of the algorithm that were investigated for the purposes of this study:

Wavelength selection : The SRS algorithm is typically applied with only a few wavelengths; when it was introduced in the NIRO 300, the wavelengths 775, 810, 850 and 905 nm were used [25]. The current NIRO system, NIRO 200NX, applies three wavelengths: 735, 810, 850 nm [253]. Several other NIRO wavelength combinations were reported, such as 775, 810, 847 and 919 nm (NIRO 300) [254] or 775, 825, 850 and 904 nm (NIRO 300) [181]. The choice of wavelengths is determined by the effort of spreading the wavelengths evenly across the near-infrared range and the availability of light sources. With the growth of interest in bNIRS, broadband systems have been used for the recovery of oxygenation with broadband SRS: Steimers et al. [255] used broadband SRS (720–860 nm) to measure oxygenation in the calf and thigh during exercise. Tachtsidis et al. [256] used a hybrid multidistance FD and broadband system and combined absolute scattering measurements with broadband SRS. Phan et al. [213] developed a multidistance broadband system that measures tissue oxygen saturation with broadband SRS (740–900 nm). The studies did not

investigate how changing the wavelength selection would affect the results.

Chromophores : The number of chromophores that can be accounted for in NIRS is limited by the number of wavelengths used. The main chromophores of interest in differential NIRS are HHb and HbO_2, background absorption is subtracted during data analysis. In SRS, the main absorbers of interest are also HHb and HbO_2 [25]. However, background absorption is no longer subtracted and other chromophores contribute to light absorption, mainly water and melanin [141]. If these chromophores are not accounted for, absorption by these compounds is then incorrectly assigned to haemoglobin absorption and can lead to errors [257, 258]. Using a broadband spectrum gives the opportunity to include the absorption by additional chromophores and increase the accuracy of StO_2 measurements. Eq. (6.1) shows how water can be added to SRS and accounted for, or any other chromophore of interest. However, adding chromophores increases the computational burden and in the case of water, creating a pseudo-inverse of the extinction matrix can cause erroneous negative concentrations of water due to the ill-conditioning of the linear system [258]. The relative contribution of additional chromophores to the total absorption depends on the wavelength range; melanin and CCO absorption is very weak in CYRIL wavelengths (770–906 nm) [141]. In the work in this chapter, the effect of water absorption was investigated.

$$\begin{bmatrix} kc_{HHb} \\ kc_{HbO_2} \\ kc_{H_2O} \end{bmatrix} = \frac{1}{\ln 10} \begin{bmatrix} \varepsilon_{HHb,\lambda_1} & \varepsilon_{HbO_2,\lambda_1} & \varepsilon_{H_2O,\lambda_1} \\ \ddots & \ddots & \ddots \\ \varepsilon_{HHb,\lambda_n} & \varepsilon_{HbO_2,\lambda_n} & \varepsilon_{H_2O,\lambda_n} \end{bmatrix}^{-1} \begin{bmatrix} k\mu_{a,\lambda_1} \\ \ddots \\ k\mu_{a,\lambda_n} \end{bmatrix} \tag{6.1}$$

Scattering : SRS uses an estimate of the scattering coefficient μ_s' to account for scattering losses; assuming a linear decrease of scattering with wavelength: $\mu_s' = k_{SRS} \times (1 - h\lambda)$. NIRO systems use the value $h = 6.3 \times 10^{-4} \text{mm}^{-1}\text{nm}^{-1}$, which was measured by Matcher [112] in the adult head (7 subjects). It was calculated by measuring μ_s' at different wavelengths, approximating the relationship with $\mu_s' = a\lambda + b$ and taking h as the ratio of the slope of the regression to its intercept $\frac{a}{b}$ [112]. Scattering changes following brain injury [259] which raises the question whether a universal value of h can be applied in different situations. To test this, one can calculate h by using published values of scattering in the human head shown in Table 6.1. The studies were selected because they all feature different subject groups.

SDS : SRS is based on measurements from at least two SDS to measure the attenuation slope, a higher number theoretically improves the accuracy, as it can correct for non-linearity, which could arise, for example, due to coupling issues (Figure 6.1). The selection of separation is a

Table 6.1: h calculated from published μ_s' measurements by calculating the ratio of the slope a and the intercept b in the approximation $\mu_s' = a\lambda + b$.

Study	Subjects	**h** [$\times 10^{-4}$ $mm^{-1}nm^{-1}$]
Matcher (1997) [107]	7 healthy adults	4.5
Highton (2016) [259]	21 brain injured adults	5.4
Kurata (2016) [260]	60 neonates at NICU	3.5
Spinelli (2017) [108]	33 healthy neonates	4.6

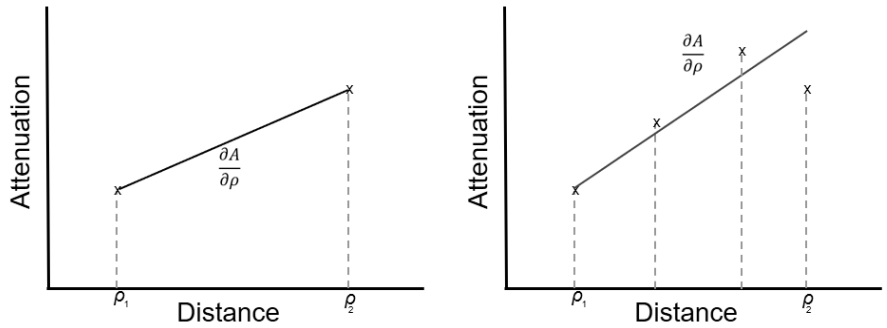

Figure 6.1: The increase of attenuation over distance and the improvement of the estimation of $\frac{\partial A}{\partial \rho}$ by increasing the number of light source-detector distances.

compromise between collecting enough light while reaching deep tissue; NIRO systems have a separation between the light source and the detectors of an average 3–5 cm; two detectors are placed very close to each other [185].

6.3 Method

The data used for this chapter was collected during the first session of the Baby Brain Study at the NICU at UCLH, published by Bale [16]. The measurement system CYRIL 1 and the data collection protocol are described in sections 5.1.1 and 5.4.1.

6.3.1 Patients

NIRS spectral data were acquired from 47 (15 female) neonates born or transferred to the NICU at UCLH for treatment of acute brain injury, all data were collected between November 2013 and December 2015. The patients were monitored during the first days of life. Out of the 47 subjects, 41 neonates were diagnosed with moderate (n = 27) or severe (n = 14) HIE, 3 infants with stroke, 2 were preterm and 1 infant was diagnosed with intraventricular haemorrhage. The average gestational age was 39 weeks $\pm$ 19 days, birth weight 3.2 $\pm$ 0.7 kg.

At least one NIRS measurement was obtained for each infant from day 1 to day 11, duration from 10 min to 18 h. Some infants were monitored on only one day, others on several different

occasions during the first 11 days of life.

Reference spectra were collected irregularly on the occasion of changing the binning setting; it was noted which reference spectrum belonged to which patient.

6.3.2 Data selection

Intensity spectral data were analysed in MATLAB R2019a. For the purposes of this study, only 600 s long parts of the measurement were analysed to decrease computational burden. The sections were selected manually by visual inspection of the intensity data; Figure 6.2 shows an example of data selection process. Intensity values at 820 nm, collected with all 4 detectors, were normalised to the maximum and plotted over time. The user moved a cursor to select a section to analyse. The selection criteria for data analysis were for the region to be flat with constant intensity and minimal artefacts. If a measurement did not have a noise-free region, it was excluded. If a measurement had many flat sections that could potentially be used, only one was chosen. In total, 121 data sets were selected for analysis, treated as independent samples. Only one measurement from one infant per day was used.

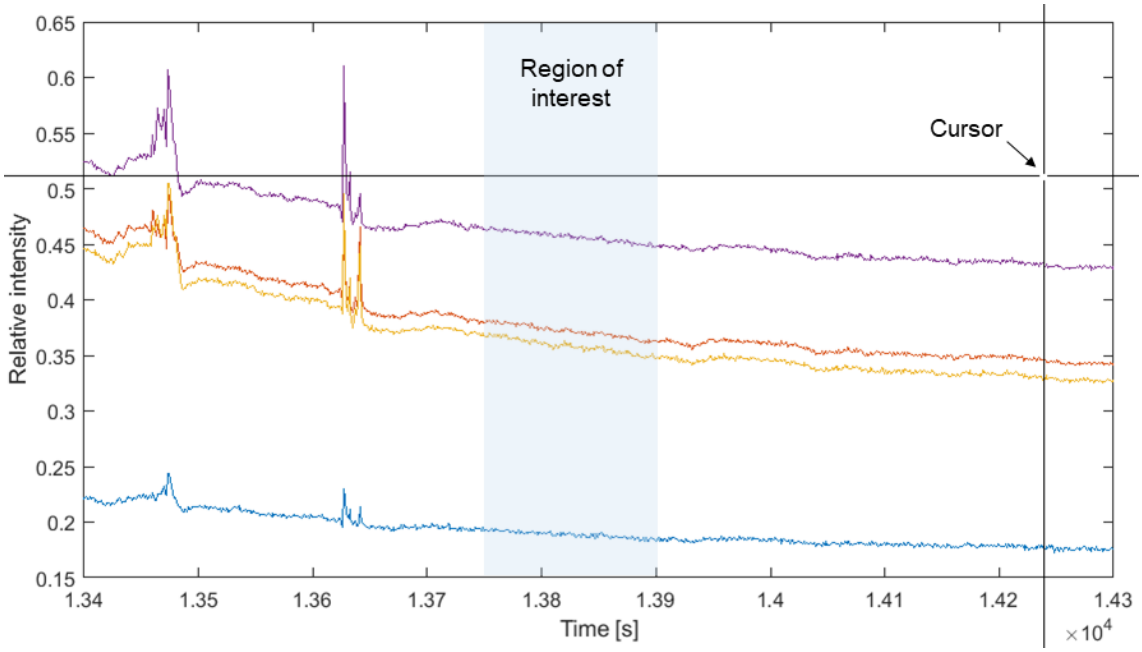

Figure 6.2: Example of data selection for the SRS investigation. Intensity collected with 4 detectors at 820 nm was normalised to the maximum and plotted over time. The user selected a flat region with little artefacts with the cursor (highlighted in light blue).

6.3.3 Data analysis

For the investigation of effects of changing different aspects of SRS, all 121 data sets were analysed with different versions of SRS. These are further referred to as "approaches" and are described

below:

Approach 1, *Broadband* : The first version is SRS applied to the standard CYRIL 1 setup; using broadband 770–906 nm data collected with all 4 detectors at 15, 20, 25 and 30 mm SDS, describing the wavelength dependence of the scattering coefficient with $h = 0.00063$ mm^{-1}nm^{-1}. Only oxy- and deoxy-haemoglobin absorption was assumed.

Approach 2, *Water* : This approach accounted for the concentration of water additionally to oxy- and deoxy-haemoglobin. To assure that non-negative water concentrations would be not calculated during the pseudo-inversion of the extinction matrix, a least-squares solver with a MATLAB non-negative constraint was used, *lsqnonneg*.

Approach 3, *Scattering* : Different values of h can be obtained depending on the measurement of μ_s'. For this approach, the following values were used, taken from Table 6.1: $h_H = 0.00054$ mm^{-1}nm^{-1}, $h_K = 0.00035$ mm^{-1}nm^{-1} and $h_S = 0.00046$ mm^{-1}nm^{-1}. The measurement by Matcher was excluded as the result was similar to the Spinelli value h_S.

Approach 4, *Wavelength* : Instead of the whole broadband spectrum, only a few discrete wavelengths were used in this approach to resolve the concentrations of oxy- and deoxy- haemoglobin. Those were selected to be 775, 810 , 850 and 905 nm as used by Suzuki et al. [25], 775, 825, 850 and 904 nm as used by Dullenkopf et al. [181] and 775, 810 and 850 nm to see the impact of adding the fourth wavelength 905 nm. Other combinations of wavelengths mentioned in section 6.2 were not included as they are outside of the CYRIL 1 wavelength range.

Approach 5, *Distance* : The SDS and the number of detectors used on the estimation of the slope of attenuation against distance, $\frac{\partial A}{\partial \rho}$, were changed. CYRIL 1 measured data with 4 detectors 30, 25, 20 and 15 mm far from the light source. Due to the design of the instrument, it was not possible to decrease the inter-detector spacing below 5 mm, which would resemble the standard NIRO setup. The additional combinations of 3 or 2 detectors applied in this approach were:

2 detectors	**3 detectors**
20 and 15 mm	25, 20 and 15 mm
25 and 15 mm	30, 20 and 15 mm
30 and 15 mm	30, 25 and 15 mm
25 and 20 mm	30, 25 and 20 mm
30 and 20 mm	
30 and 25 mm	

Each approach was investigated independently from the others; the other parameters remained as in the *Broadband* SRS approach. Approaches *Scattering*, *Distance* and *Wavelength* had several

sub-approaches. In total, there were 18 approaches resulting in 18 different StO_2 measurements for each data set. Figure 6.3 shows a summary of the data analysis with SRS in form of a flow chart.

6.3.4 Data classification

StO_2 obtained for each section with each approach were averaged over the time window. They were rated as "valid", if the mean was between 40–100%. The lower threshold of 40% was selected based on available StO_2 in HIE from literature, Figure 4.2, and the upper threshold of 100% was determined by the definition of StO_2.

Next to rating the validity of StO_2, the quality of the slope was also evaluated. The linearity of the slope informs on the homogeneity of tissue; a linear slope suggests that tissue is homogeneous. It is assumed that attenuation increases linearly with short SDS; that $A(\rho_1,\lambda) < A(\rho_2,\lambda)$, where $\rho_1 < \rho_2$ (Figure 6.1). If this was the case for all ρ, the slope was labelled "regular", otherwise, it was "irregular". Additionally, in the case of large inhomogeneities, the slope can become negative; $\frac{\partial A}{\partial \rho}(\lambda) < 0$ between two SDS, indicating a decrease of attenuation with distance. The slope was assessed at three wavelengths; 775, 810 and 850 nm during the first time-point in the 600 s measurement and was rated as "irregular" or "negative" if it was decreasing or negative at any of the wavelengths, between any two SDS combinations.

6.3.5 Relationship between HIE severity and StO_2

Out of each approach, the sub-approach with the most "valid" StO_2 was used as a representation to obtain StO_2 for neonates with HIE. Measurements in infants with HIE, who had "valid" StO_2, "regular" and "positive" slopes for all 5 approaches, were used. The StO_2 were grouped according to severity, moderate and severe, and by the day of measurement. Firstly, it was assessed whether there are differences in StO_2 measurements depending on the severity of injury for each approach. Secondly, the change of StO_2 over time was evaluated.

6.3.6 Statistical analysis

Statistical analysis was performed in MATLAB 2019a. The mean, median, standard deviation, 25th and 75th percentile were calculated out of all averaged StO_2 values for each approach. After testing the data for normality, the non-parametric, distribution-free Sign test was used to assess differences between the individual approaches. The Sign test evaluates the hypothesis that the distribution of the differences between two data sets has a zero median to assess consistent differences between the approaches [261]. An approach was considered different if $p < 0.05$. Correlation between the approaches was measured using Spearman's rho (ρ_s), a non-parametric test measuring

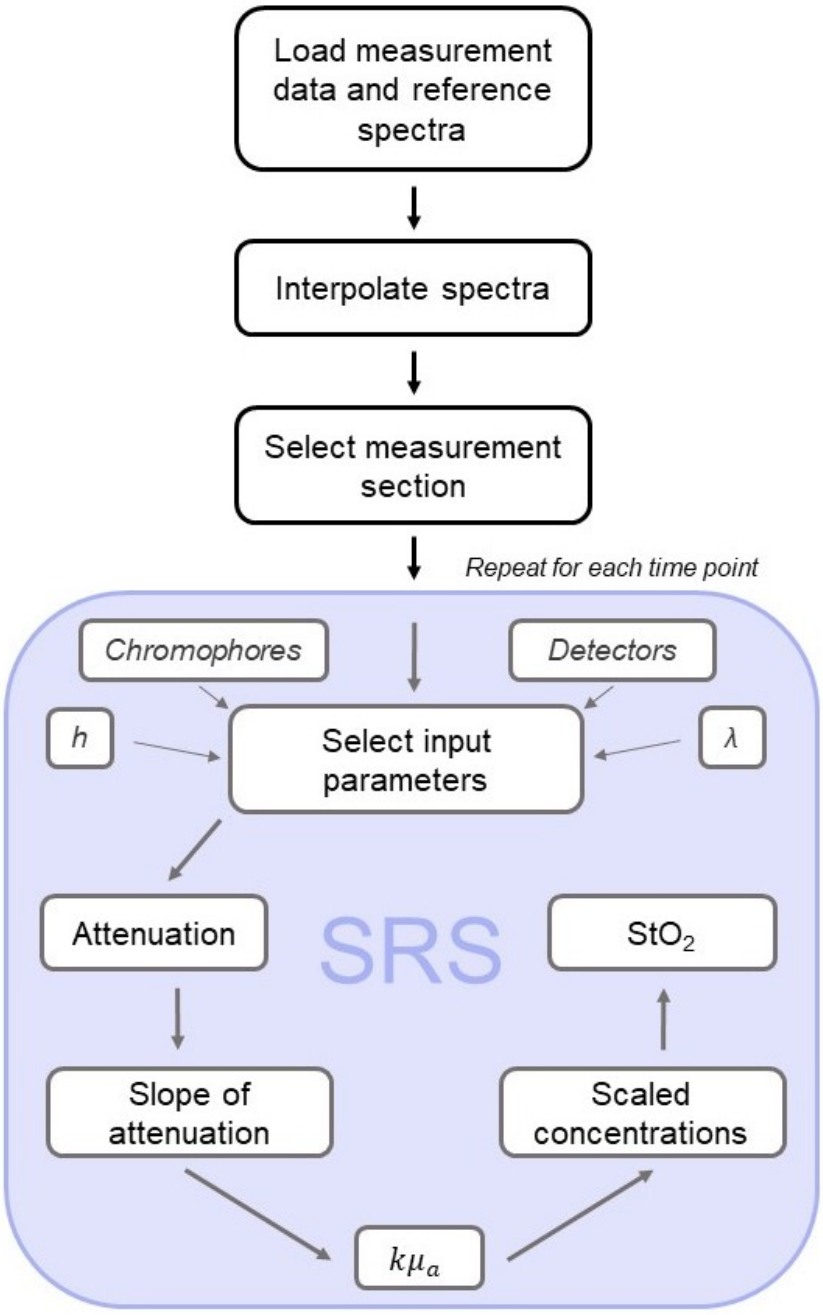

Figure 6.3: The steps taken in analysing measurements with SRS. The SRS section is repeated for each time point and for each approach (18 approaches in total). The interpolation of spectra was performed to transform CYRIL 1 wavelengths corresponding to each pixel to integer wavelengths.

the strength of association; where $\rho_s = 1$ is perfect positive correlation, $\rho_s = -1$ is perfect negative correlation, there is no correlation if $\rho_s = 0$.

The StO_2 of neonates with HIE are reported as the mean $\pm$ standard deviation. To assess the difference between StO_2 in the HIE severity groups, a Mann-Whitney U test was used. The test is a non-parametric test assessing whether two independent samples were selected from populations having the same distribution. The StO_2 grouped by severity were considered different if $p < 0.05$.

6.4 Results

121 sets 600 s long were selected and used in the analysis, resulting in 2178 average StO_2 values; shown in Table 6.2. Using only a few wavelengths and resolving for haemoglobin across 4 detectors gave the most "valid" StO_2 values: approach *Wavelengths* (775, 810, 850 nm) gave 115 out of 121 StO_2 between 40 and 100%. On the contrary, using only two detectors, *Distance* (25,30 mm), gave 23 "valid" measurements, with many StO_2 below 0%. The amount of "valid" StO_2 of the other approaches was between 61 and 107, with approaches using only 2 SDS in the lower-scoring half. The different distributions of StO_2 are also notable - while using only three wavelengths (*Wavelengths* (775, 810, 850 nm)) gave quite a narrow distribution of StO_2 with an interquartile range of 15%, the approach *Distance* (15, 20, 30 mm) resulted in a broader distribution with an interquartile range of 26%. Figure 6.4 shows StO_2 acquired in one subject with a few approaches. The measurement had "valid" and "regular" attenuation slopes; the range of StO_2 obtained with different approaches was wide, including results with negative StO_2 or an StO_2 above 100%.

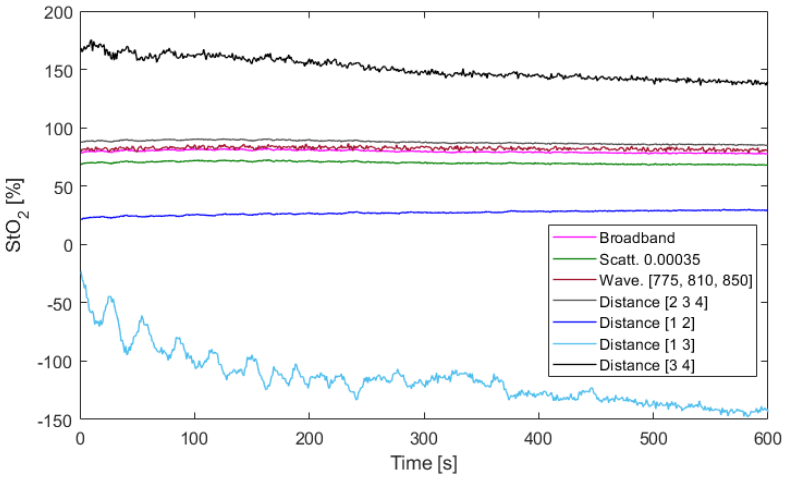

Figure 6.4: StO_2 acquired using 7 different approaches in a measurement which had "positive" and "regular" attenuation slopes. Distance [2 3 4] corresponds to SDS 20, 25, 30 mm; [1 2] to 15, 20 mm, [1 3] to 15, 25 mm and [3 4] to 25, 30 mm.

Table 6.2: StO_2 values in % obtained for each approach and sub-approach with the absolute and relative amount of "valid" StO_2 per approach. The mean, median, standard deviation (σ), 25th percentile (Q1) and the 75th percentile (Q3) were calculated from all 121 measurements.

Approach	**Sub-approach**	**Valid StO_2**	**% Valid**	**Mean**	**Median**	σ	**Q1**	**Q3**
Broadband		99	82	63	61	35	60	75
Water		97	80	52	54	21	42	67
Scattering	0.00046 $mm^{-1}nm^{-1}$	88	73	57	54	34	43	67
	0.00054 $mm^{-1}nm^{-1}$	91	75	59	57	34	46	70
	0.00035 $mm^{-1}nm^{-1}$	85	70	54	52	34	41	65
Wavelength	775, 810, 850, 905 nm	106	88	62	60	27	50	71
	775, 810, 850 nm	115	95	65	63	19	57	72
	775, 825, 850, 904 nm	107	88	62	61	25	52	72
Distance	15, 20, 25 mm	84	69	79	75	50	28	93
	15, 20, 30 mm	95	79	64	59	43	48	74
	15, 25, 30 mm	94	78	61	61	34	49	73
	20, 25, 30 mm	62	51	55	50	65	32	73
	15, 20 mm	83	69	57	64	67	48	78
	15, 25 mm	84	69	79	75	50	58	93
	15, 30 mm	94	78	61	59	35	49	72
	20, 30 mm	62	51	55	50	65	32	73
	20, 25 mm	61	50	75	73	69	48	110
	25, 30 mm	23	19	25	22	79	-7	48

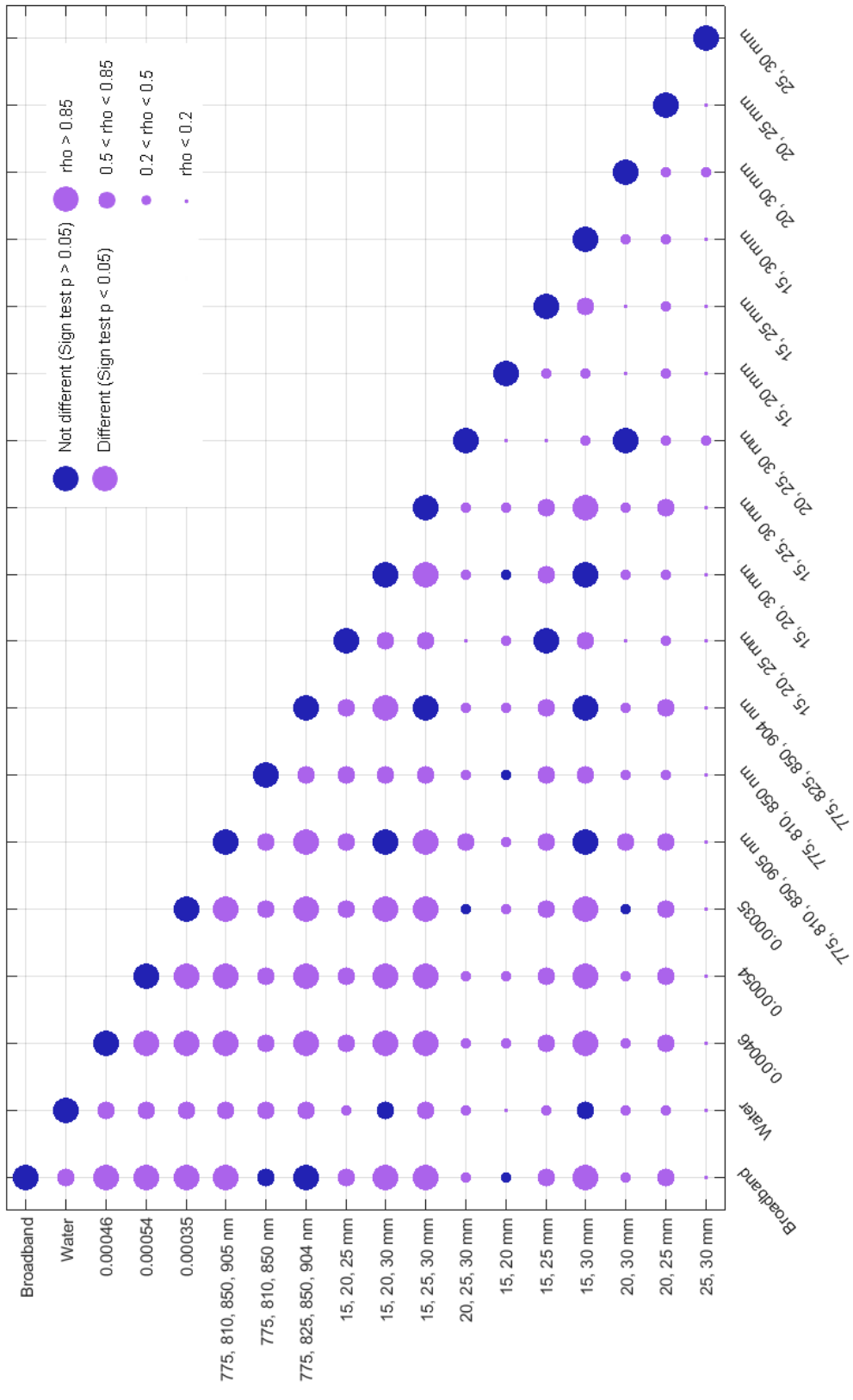

Figure 6.5: Correlation map of different SRS approaches. The colour of the dots corresponds to the strength of the relationship between the approaches assessed with the Sign test; the size o the dots corresponds to the correlation measured with Spearman's Rho.

As testing the data for normality showed that neither of the approaches resulted in a normal distribution of StO_2, the non-parametric Sign test was used to find differences between two approaches by assessing whether the difference between them has a zero median. The results are shown in Figure 6.5, where a dark spot indicates no difference ($p > 0.05$), a light spot shows differences ($p < 0.05$). Most of the approaches gave different results.

Additionally to looking at similarity, the correlation between approaches was measured with the Spearman's Rho ρ_s. The size of the dots in Figure 6.5 corresponds to the strength of correlation.

The two *Wavelength* approaches (775, 810, 850 nm) and (775, 825, 850, 904 nm) had a higher amount of "valid" StO_2 than *Broadband* but the mean and median StO_2 were very similar. Both of the *Wavelength* approaches had a wider distribution, and, in particular, ρ_s was lower between (775, 810, 820 nm) and *Broadband*, ($\rho_s = 0.7$, than when comparing *Broadband* to (775, 825, 850, 904 nm), $\rho_s = 0.9$. Low correlation and differences were also found between *Broadband* and *Distances*.

h is a constant used to account for scattering and changing it affects the relative contribution of scattering to attenuation, Eq. (3.40). Changing the value of h in *Scattering* acted as a constant offset; all correlated highly with *Broadband* but changed the median and mean StO_2, while the interquartile range was maintained. The higher h was, the higher StO_2. A difference in h of 0.0001 $\text{mm}^{-1}\text{nm}^{-1}$ led to a difference in StO_2 of $\sim 4\%$, hence the possible change of "valid" StO_2 with h.

Adding a wavelength to the *Wavelength* approach, from (775, 810, 850 nm) to (775, 810, 850, 905 nm) significantly changed the result, with a correlation of $\rho_s = 0.75$. The correlation between (775, 810, 850, 805 nm) and (775, 825, 850, 905 nm) was higher, $\rho_s = 0.99$. Even though the mean and median of the approaches were identical, the Sign test rejected the hypothesis of a zero median of differences with $p = 0.02$.

Changing the SDS led to the weakest correlation with other approaches, particularly in detector combinations with just two detectors or combinations which excluded the nearest detector at 15 mm. The approach *Distance* using just 25, 30 mm correlated the least with other approaches. The Sign test showed no difference between *Distance* (20, 30 mm) and *Scattering* (0.00035 $\text{mm}^{-1}\text{nm}^{-1}$), $p = 0.86$, the mean StO_2 were very similar, even though correlation was weak, $\rho_s = 0.44$.

The quality of the attenuation slope was assessed through testing whether it was "regular" and "positive". Example of a measurement with a "positive" and "regular" slope is in Figure 6.6,

a measurement with a "irregular" and "positive" slope is in Figure 6.7 and a measurement with a "negative" and "irregular" slope is in Figure 6.8.

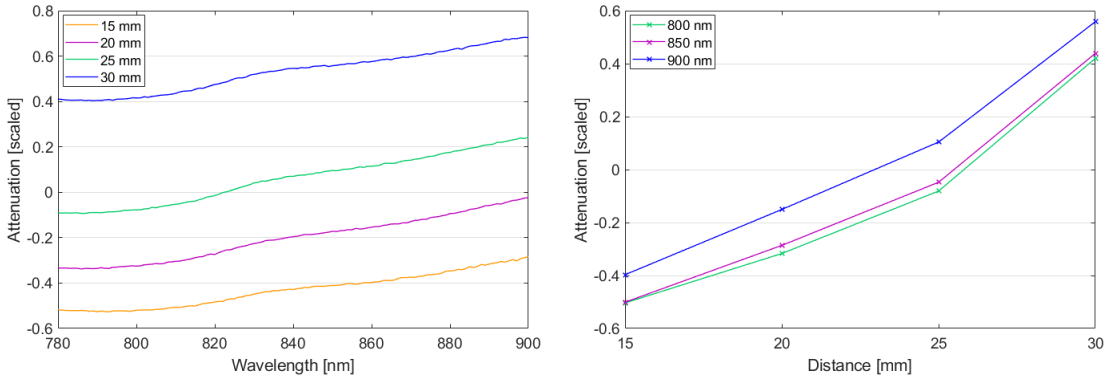

(a) Attenuation **(b)** Attenuation slope

Figure 6.6: Attenuation leading to a "regular", "positive" slope.

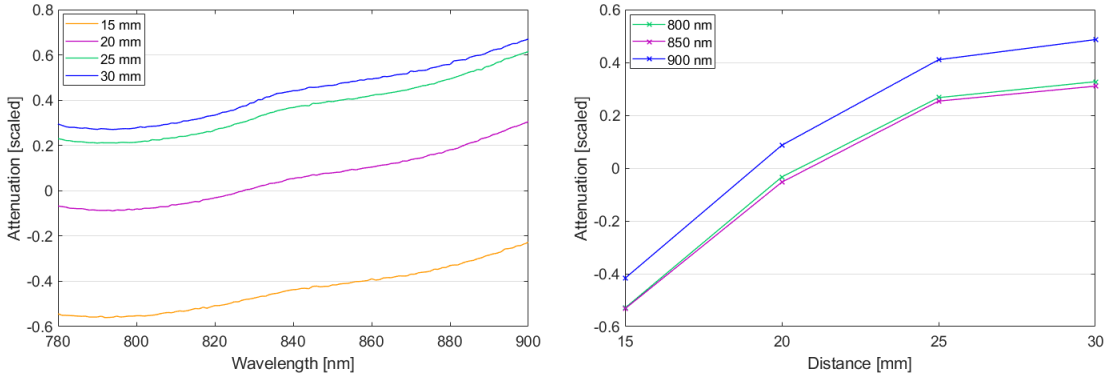

(a) Attenuation **(b)** Attenuation slope

Figure 6.7: Attenuation leading to a "irregular", "positive" slope.

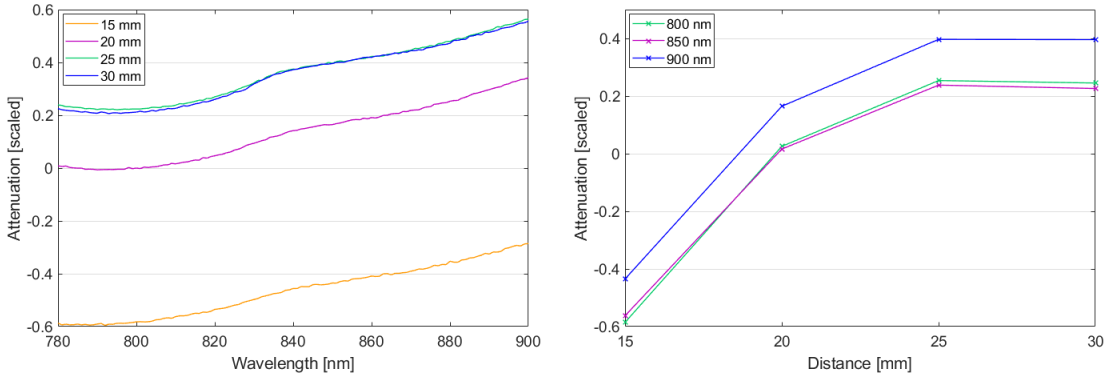

(a) Attenuation **(b)** Attenuation slope

Figure 6.8: Attenuation leading to a "irregular", "negative" slope.

Table 6.3 shows the amount of "regular" and "positive" slopes grouped by light-source detector separation, summarising a total of 1331 measurements. For 15, 20, 25, 30, the results shown are from the approach *Broadband*. Using all four detectors had the highest rate of non-linearities (102 were "regular"). The lowest number of positive slopes was found using only the furthest away detectors, 25 & 30 mm, which led to 9% of the slopes to be negative. The measurement at 20, 30 mm had all slopes "regular" and "positive". As expected, the amount of "positive" slopes was always higher than or equal to the amount of "regular" slopes. The relationship between "valid" StO_2 and the slope is further explored in Table 6.4. The total amount indicates the amount of StO_2 measurements obtained with all combinations of SDS. It shows that the majority (790 out of 1331) of "valid" StO_2 come from a "positive", "regular" slope. However, in 435 cases, even though the slope was "regular", StO_2 was still not "valid". In 36 cases was a "valid" StO_2 without a "regular" and "negative" slope.

Table 6.3: The regularity and positivity of the slope calculated across different light-source detector separations.

Separation	Regular slope	% Regular	Positive slope	% Positive
15, 20, 25, 30 mm	102	84	115	95
15, 20, 25 mm	109	90	116	96
15, 20, 30 mm	110	91	115	95
15, 25, 30 mm	108	89	115	95
20, 25, 30 mm	107	88	121	100
15, 20 mm	110	91	111	92
15, 25 mm	115	95	116	96
15, 30 mm	115	95	115	95
20, 30 mm	121	100	121	100
20, 25 mm	120	99	120	99
25, 30 mm	108	89	110	91

6.4.1 StO_2 in neonates with HIE

Out of the 18 SRS versions, the sub-approaches with the highest amount of "valid" StO_2 were selected for each approach. These 5 sub-approaches were: *Broadband*, *Water*, *Scattering* (0.00054 $mm^{-1}nm^{-1}$), *Wavelength* (775, 810, 850 nm) and *Distance* (15, 20, 30 mm). In this subsection, the sub-approaches will be referred to only with the name of the approach they represent.

Table 6.4: StO_2 "validity" corresponding to the regularity and positivity of the slope.

Valid StO_2	Regular slope	Positive slope	Total
✓	✓	✓	790
✓	×	✓	15
✓	✓	×	0
✓	×	×	36
×	✓	✓	435
×	×	✓	35
×	✓	×	0
×	×	×	20

Out of the 121 measurements in total, 68 were collected in 32 infants with HIE on different days and gave "valid" StO_2 for all of the five sub-approaches. The slopes were "positive" and "regular". Out of 68, 23 analysed data sets were from 11 severely injured patients, 45 from 21 moderately injured patients; mean gestational age of the neonates was 39 weeks. Measurements were collected on different days of life ranging from day 1 to day 12. Each neonate was monitored at least once, one infant was monitored on 5 different days. Due to the small amount of measurements taken at days 8–12, they were added to the group of measurements at day 7. Table 6.5 shows average StO_2 for each approach for both severity groups and also the p-values obtained with the Mann-Whitney U test. Significant differences in the mean StO_2 depending on severity were found in 3 approaches: *Broadband*, *Scattering* and *Distance*; StO_2 was higher in moderate injury than in severe injury. Figure 6.9 shows the StO_2 values recovered for the severe and moderate groups with different SRS approaches.

Table 6.5: Mean StO_2 [%] (standard deviation [%]) in HIE grouped by severity for 5 different approaches. The Mann-Whitney U-test was used to find differences between severities, the null hypothesis of both distributions being equal was rejected if $p < 0.05$.

Severity/Approach	Broadband	Water	Scattering	Wavelength	Distance
Severe (n = 23)	60 (12)	58 (11)	56 (11)	65 (9)	58 (13)
Moderate (n = 45)	66 (11)	60 (11)	62 (11)	67 (9)	65 (11)
p-value	0.02	0.23	0.02	0.39	0.01

Table 6.6 shows the mean StO_2 values for each day, the change of StO_2 over time can be seen in Figure 6.10. There is an indication of a rise in StO_2 throughout the first days of life. Grouping the data by HIE severity shows that a rise in StO_2 during the first 5 days is more prominent in

infants with severe HIE, Figure 6.11.

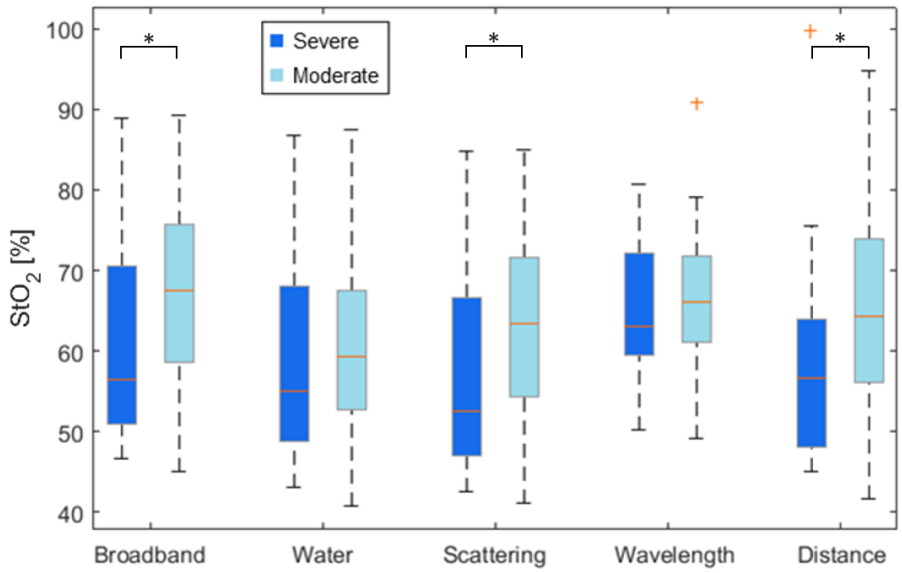

Figure 6.9: StO_2 recovered in severe and moderate HIE with different SRS approaches. Significant difference ($p < 0.05$) was found between severe and moderate groups in the approach *Broadband*, *Scattering* and *Distance*.

Table 6.6: Mean StO_2 [%] (standard deviation [%]) in HIE grouped by day of life for 5 different approaches. Measurements are the number of measurements for each group: severe (S) and moderate (M) HIE.

		Approach				
Day	**Sample**	**Broadband**	**Water**	**Scattering**	**Wavelength**	**Distance**
1	2 S, 6 M	65 (13)	60 (10)	61 (13)	67 (7)	62 (13)
2	8 S, 13 M	58 (7)	54 (7)	54 (8)	63 (7)	55 (8)
3	4 S, 12 M	69 (11)	63 (13)	65 (11)	69 (10)	68 (12)
4	4 S, 7 M	68 (10)	63 (11)	64 (10)	70 (8)	65 (9)
5	2 S, 4 M	72 (15)	67 (15)	68 (15)	71 (8)	73 (19)
6	0 S, 1 M	71 (-)	64 (-)	68 (-)	67 (-)	70 (-)
7+	3 S, 2 M	56 (7)	52 (5)	52 (7)	57 (3)	54 (6)

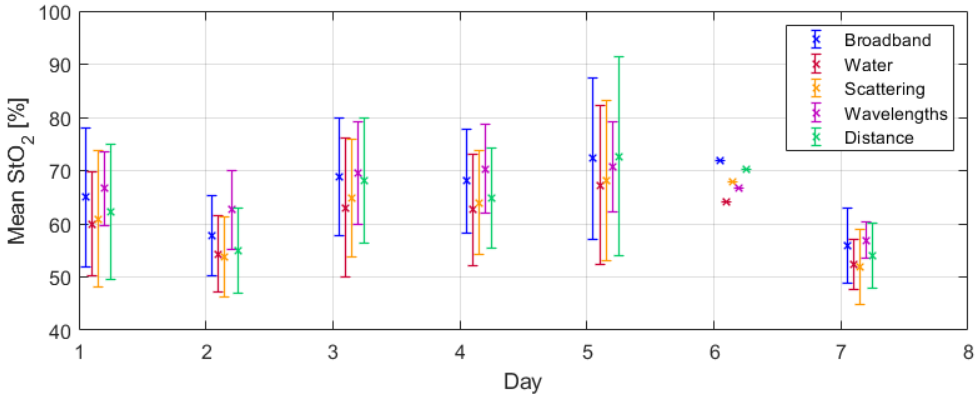

Figure 6.10: Change of StO_2 in HIE neonates during the first days of life calculated with 5 different SRS approaches.

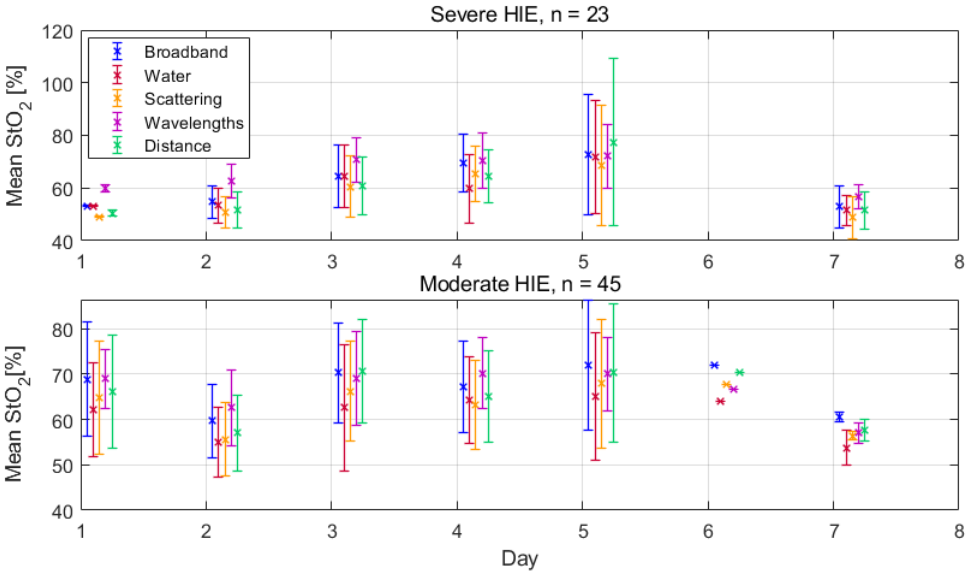

Figure 6.11: Change of StO_2 in HIE neonates during the first days of life calculated with 5 different SRS approaches and grouped by HIE severity, n = 68.

6.5 Discussion

Analysis with 18 different implementations of SRS, called approaches, of 121 sets of broadband NIRS data collected in neonates with HIE during the first days of life evaluated the impact of SRS implementation on the measured StO_2. The resolved chromophores, wavelengths, scattering assumptions and SDS were changed and the resulting StO_2 was averaged across all 121 measurements. These StO_2 values were labelled as "valid", if they were in the region between 40–100%.

The length of the original data collected varied; to improve computational burden and to

exclude errors due to artefacts, a 600 s long section was manually selected from each data set. The aim was to select a stable region; the study was not focused on quantifying the dynamics of changes in oxygenation. During the data selection, the collected intensity measurement was normalised to compare it to the values from other detectors with different intensity counts. The process of normalisation could have made some smaller artefacts less visible. To overcome this, the selection process had two stages, in the first, the whole measurement was shown to the user who then selected a region that looked suitable for analysis, had little noise and was stable. In the second stage, this region was zoomed into and the user confirmed their selection.

In most neonates, more than one data set was collected. Attenuation was calculated from the data and reference spectra. The measurements were considered independent even though some bias was introduced by the use of reference spectra, which were only collected when the binning of the CCD was changed. The same reference spectrum was then used for all neonates monitored with the same binning setting. Hence, if an error occur ed in the reference spectrum measurement, multiple data sets were affected.

The StO_2 calculated with different approaches was averaged, it summarised the whole 600 s measurement. As it has been shown that the dynamic responses of oximeters to changes in saturation are different [11]; the regions for analysis were selected to be as flat as possible to reduce errors in comparison. The selection of "valid" boundaries was based on published StO_2 values in neonates. The lowest reported StO_2 in Figure 4.2 is 53%, and 40% was selected as a boundary to allow for outliers.

Statistical analysis of the approaches showed that most gave different results. One has to keep in mind that the non-parametric test used for this analysis is the Sign test, which compares the median of the differences between the paired measurements. This omits information on the magnitude of the observations. Other statistical tests might be more suitable, such as the Wilcoxon Signed-Rank test, or Passing-Bablok regression [262], which has been specifically designed for method comparison. Nevertheless, the distributions of StO_2 did not fulfil the assumptions of either of these test: the Wilcoxon test requires symmetry, whereas the Passing-Bablock regression assumes linearity. As the sample of 121 values was relatively small, the Sign test had rather less power than other non-parametric methods, or a parametric equivalent (e.g. a paired t-test), and had less chance of detecting a true effect where one exists [263].

Measurements of correlation inform on how similar the trends in StO_2 among different methods are. Combining the information from the Sign test with Spearman's Rho ρ_s in Figure 6.5 and

the statistics in Table 6.2 show that most approaches behaved differently, resulting in many StO_2 for each measurement. The main findings can be summarised as followed:

- It was not uncommon for StO_2 to be be outside the 0–100% interval, as seen in Figure6.4. An StO_2 below 0% occurred either when c_{HHb} was negative and larger than c_{HbO_2}, or when c_{HbO_2} was negative. A negative c_{HHb}, smaller than c_{HbO_2}, led to StO_2 above 100%. Negative concentrations are physiologically impossible and were hence caused by errors in the measurement. To further explore the impact of measurement error on negative/too large StO_2 values, the StO_2 grading system should expanded beyond "valid", also classify StO_2 specifically below 0% or above 100%.

- The addition of water as an absorbing chromophore significantly changed the StO_2. One source of error in the *Water* approach is the pseudo-inversion of the extinction matrix. Due to a large difference between the extinction coefficient of water and haemoglobin (ε_{H_2O} is $\sim 10^6$ smaller than ε_{HbO_2} in the selected wavelength range), the condition number of the matrix is very large, 2.3×10^7 for 771–906 nm, compared to the condition number when resolving just for haemoglobin, 7. To improve the solution of the equation $[k_{SRS}c] = [\varepsilon^{-1}] \cdot [k\mu_a]$, a non-negativity constraint can be applied to exclude solutions with negative concentrations. However, the water concentrations resolved were often very small, sometimes it was zero and the resulting StO_2 was equal to the StO_2 calculated with *Broadband*. Perhaps a more robust way of accounting for water would be assuming a constant water concentration, however, as brain water content differs between adults, term and preterm infants and also during brain injury, a fixed concentration assumption can lead to additional measurement errors [188, 264]. It has been shown that also the way water absorption is accounted for in the calculation of μ_a affects StO_2 [190]. A limitation of the exploration of the impact of water absorption in this work is that it was only used with broadband wavelengths, specifically applied to CYRIL. Given the weaker absorption by water in shorter wavelengths, up to $\sim$ 850 nm, it is possible that the impact of water on SRS would be less at those wavelengths.

- The h values used in this analysis were measured in several patient groups (healthy adults, brain injured adults, healthy neonates and neonates at the NICU) and led to different results; scattering assumptions caused a shift in the StO_2. Even though the offset was relatively small, around 3% in StO_2 if h changed by 10^{-4}, it significantly affects the accuracy of the measurement and makes the use of reference ranges and intervention thresholds difficult.

In order to improve the measurement of StO_2 with SRS, it would be useful to change h depending on which patient is being monitored, or even emit this prior assumption on tissue scattering, as demonstrated by Deepak Veesa and Dehghani [148]. Removing the dependence of StO_2 on h improved the accuracy of StO_2 recovery in NIRFAST simulations [148].

- The selection of wavelengths significantly affected the result, even excluding just one wavelength, 905 nm, changed the amount of "valid" StO_2. The potential causes for this include that 905 nm is at the end of CYRIL's CCD detection region and the counts at those pixels are very low. Also water absorption is much stronger at 905 nm than at lower wavelengths, combining the *Wavelength* (775, 810, 850 nm) approach with *Water* could obtain a more robust measure of StO_2 at those wavelengths. It is important to note that using a broadband light source and selecting only specific wavelengths in CYRIL is not equivalent to using a light source that emits at only specific wavelengths, such as LEDs or laser diodes used in commercial systems. The results of this analysis might be different if instead of just selecting wavelengths out of the broadband spectrum during SRS, a different light source with specific wavelengths was used.

- Changing which detectors were used had an impact on the calculated slope. The combinations of detectors that used the closest and furthest away detector had the highest amount of "valid" StO_2. They also had high correlation with 4 other detector approaches. This shows that most of the information about the slope of attenuation comes from the edge detectors. The sub-approach with the lowest success rate is 25, 30 mm. These detectors suffer from more measurement noise as they receive less signal than detectors closer to the light source, additionally, they are also more likely to suffer from poor tissue contact due to the curvature of the neonatal forehead. Most calculated StO_2 values include an error arising from the fact that the distance between the detectors was not negligible compared to the spacing between the light source and the detectors, one of the assumptions made when using ρ in Eq. (3.40). A more suitable version of the equation can be found in [251], later used in this work in Chapter 9.

Most of these findings, such as the offset introduced by h, the effect of SDS and the absorption by water, are relevant for any application of SRS. The selection of wavelengths and its impact on StO_2 is only relevant to CYRIL 1 in this investigation as it is instrumentation-dependent.

Assessments of the slope helped explain why some of the StO_2 were outside of the "valid"

range. "Positivity" informed on whether attenuation is increasing with distance, as expected. If it was not "positive", it implied significant measurement errors, such as issues with coupling, leading to a decrease in counts. The lowest amount of "positive" slopes in Table 6.3 was with SDS 25, 30 mm, 91%. This is also visible in Figures 6.7 and 6.8; the trend of the slope flattens with detector separation. Using additional SDS can improve the slope measurement; it increases the linearity of the attenuation slope, as seen on the diagram in Figure 6.1. SRS can benefit from more than two SDS as one can detect faulty SDS and exclude them from the measurement.

The assessment of "regularity" informs on the trend of the attenuation, as incorrect coupling can lead to $A(\rho_1,\lambda) < A(\rho_2,\lambda)$, where $\rho_1 < \rho_2$. If this is not large, the slope will remain "positive". Using all 4 SDS led to the lowest amount of "regular" slopes, 84%, because a slope was labelled as "not-regular" even when just one SD in the whole set had incorrect counts. A small offset from "regularity" can still maintain linearity and the measurement is not affected. Hence the amount of "regular" slopes increased when excluding the faulty SDS. Perhaps a better way of assessing this trend would be the measurement of linearity through R^2 (measure the goodness of fit of linear regression models) and using it to assess how well the linear fit matches to the data. That would require a selection of threshold R^2 values. A similar assessment of tissue homogeneity was used by Arri et al. [199], who looked at the correlation between the SDS and the mean intensity, modulation amplitude and phase shift measured with a FD NIRS system. High values of the correlation coefficient indicated high tissue homogeneity.

As seen in Table 6.4, 15 "valid" StO_2 had a "irregular" slope, which was "positive". In 36 cases, even a "non-positive" slope did not lead to a StO_2 outside the 40–100%, suggesting that an error in the measurement can still give a "valid" StO_2 measurement.

Slope characteristics which can be described by the selected metrics, however, do not explain all errors in the measurement: 435 StO_2 values were not "valid" even though the slope was "regular" and "positive". This was caused by many different issues, such as issues with the reference spectra (which led to the wrong quantification of attenuation), measurement noise or poor coupling to tissue.

Looking at the StO_2 values measured in neonates and relating them to severity of measurement showed different results depending on the selected approach. Grouping the StO_2 from 5 different approaches (*Broadband*, *Water*, *Scattering* (0.00054 $\text{mm}^{-1}\text{nm}^{-1}$), *Wavelength* (775, 810, 850 nm) and *Distance* (15, 20, 30 mm)) according to HIE severity has shown that depending on which approach is used, the relationship between severity and StO_2 changes. While

Water and *Wavelength* showed no difference in StO_2 with severity, *Broadband*, *Scattering* and *Distance* do, giving higher StO_2 values for moderate injury. These findings agree with Huang et al. [17], who measured lower oxygenation in HIE injury than in the control group, explaining that this is due to intracranial hypertension. The reported HIE StO_2 was 53%, the control group's StO_2 was 62%, values similar to the StO_2 reported in Table 6.6. On the contrary, no difference found between severity with the approaches *Water* and *Wavelength* agrees with other studies [19, 95, 225, 226, 227]

Contrasting results of assessing HIE severity with StO_2 measurements suggest that inconsistencies among studies focused on measuring brain oxygenation in HIE could be caused by more factors than the pathologies in the individual subjects, which vary and lead to different physiological responses, but also the different NIRS systems used and the application of individual data processing algorithms. Huang et al. [17] measured oxygenation with an in-house built CW system based on a multidistance approach, Dehaes et al. [95] used a hybrid FD-DCS system; Goeral et al. [225], Lee et al. [19] and Burton et al. [227] used INVOS systems and Wintermark et al. [226] monitored with the FORE-SIGHT device. All these systems use different engineering solutions and algorithms to calculate oxygenation from the raw data, which makes comparison difficult. Additionally, algorithms in systems produces by the same manufacturers can change over time, for example, the current NIRO 200NX uses different wavelengths than used in older NIRO versions [25, 253]. As this can possibly lead to different results, the comparability and suitability of such measurements for HIE severity assessment needs to be investigated.

While the use of linear transformation to shift StO_2 collected in one device to make it equivalent to a different system's reading is possible [165], it does not fix the problem of different instrument sensitivities [11]. In order to use StO_2 as a reliable biomarker in HIE, it is firstly crucial to ensure that the measurements are validated and it is possible to assume that the reading of one machine is comparable to a different machine. A study focused on measuring the relationship between StO_2 and HIE severity in term infants using different oximeters in the same subjects could help establish whether the sensitivity to severity is an issue among many oximetry systems, or whether it is only a problem of the device used in this study, CYRIL 1.

While the results suggest a small increase of StO_2 over the first 5 days of life, Figure 6.10, particularly in severely injured neonates, Figure 6.11, it is difficult to assess the trend. Due to the inconsistent sample size of measurements on different days, statistical significance of the findings was not investigated. The trend of StO_2 over time was also influenced by the approach selected

for the data analysis, approach *Wavelength* gave a flatter, more stable response. An increase of oxygenation over time in studies focused on StO_2 in infants treated with TH was reported in multiple studies [18, 222, 226, 225, 221], but no difference in StO_2 during and after rewarming was also found [240]. These differences could be because of the different sample sizes and rates of severe/moderate injury. As the progression of oxygenation could vary with injury severity, an increase of oxygenation over time in more severe HIE cases could be due to the worsening of the perfusion-metabolism mismatch, which can be related to an increase of luxury perfusion or worsening of cortical injury. Secondary injury leads to a decline in metabolism, which increases StO_2 [18]. StO_2 is more stable in milder injury, as perfusion matches the metabolic needs of the brain, an increase of oxygenation has not been shown in healthy infants [217].

A more thorough investigation of the relationship between severity/StO_2 and StO_2 development over time requires a large sample size and the collection of data in a consistent manner. NIRS measurements should be performed on the same days for all neonates, continuously. In this retrospective study, the reason why data was not collected on the same days for all infants was that neonates were monitored depending on the availability of the measurement device and the primary focus of the data collection was to collect NIRS data continuously for several hours.

Nevertheless, this investigation highlights that one of the reasons leading to inconsistent reported results in brain oximetry studies might not only be the engineering of instruments, but also the algorithms applied. There is a need to avoid contradictory results obtained just by amending the SRS algorithm used, as this could potentially lead to incorrect diagnosis and severity assessments in patients with HIE.

6.6 Conclusion

The purpose of this study was to investigate the SRS algorithm to identify how it could be implemented in the novel algorithm BRUNO and how it can be best applied to data collected with CYRIL 1. The exploration of SRS also led to a demonstration of how data collected with one instrument can lead to different StO_2 by implementing SRS with different settings. Various inputs have been changed - the wavelengths used, how scattering is accounted for, SDS and whether the absorption by water is accounted for. All these amendments led to different StO_2 values, mostly significantly different. Correlation between the approaches was also low, suggesting there was straightforward linear relationship explaining the differences. The approach with the highest rate of "valid" StO_2 values was *Wavelength* (775, 810, 850 nm). However, as no true values of StO_2 were available, it was not possible to say whether that implementation of SRS in CYRIL 1 really

was the best option. SRS will be compared to a known truth later in this work in Chapter 8.

SRS assessment

Overall, the strengths of the SRS algorithm are:

- Superficial layer removal: one of the main advantages of the SRS approach is the removal of the influence of a superficial layer through the calculation of the attenuation slope $\frac{\partial A}{\partial \rho}$. This ability of the SRS algorithm will be addressed later in section 8.7.1. The novel algorithm, BRUNO, should also be based on an attenuation slope measurement.

- Low computational requirements is a desirable property as it allows real-time measurements. Keeping the computational burden minimal will be crucial when developing a new StO_2 algorithm.

- Multidistance setup: if more than two detectors are applied, the multidistance setup can decrease the impact of errors arising from coupling issues from a single detector as demonstrated through the increase of "valid" StO_2 values when using more detectors. Measurements with 4 detectors will hence be also implemented when designing BRUNO.

Limitations identified when applied to data collected with CYRIL 1:

- Scattering assumption: the use of the scattering scaling factor h simplifies the calculation but also introduces an offset if it is not correct for the tissue monitored. It is desired that the new algorithm, BRUNO, does not assume any fixed scattering properties.

- Wavelength selection: the application of the algorithm to CYRIL 1 data has shown inconsistencies of results when the wavelengths are changed. To explore the implications of wavelength selection on SRS further, two versions of SRS are used later in this work; one, where the whole broadband spectrum is used, and one, where only selected wavelengths are used (775, 810, 850 nm). BRUNO will be also based on a broadband measurement, the advantages of this will be presented in the next chapter.

- Resolving water: the algorithm has been shown not to be very robust when accounting for the concentration of water when used with broadband wavelengths. The absorption of water will not be assumed when using SRS further in this work. However, as water absorbs strongly in the longer wavelengths, the ability to account for water absorption will be implemented in BRUNO.

StO_2 in neonates with HIE

The data was collected in infants with HIE undergoing treatment at the NICU and the obtained StO_2 values were linked to the severity of brain injury using 5 different SRS approaches. It has been shown that the relationship of StO_2 HIE injury severity was inconsistent among the different approaches - while the approaches *Broadband*, *Scattering* and *Distance* showed differences in StO_2 between patients with severe and moderate HIE, the approaches *Water* and *Wavelengths* did not. This agrees with current research - most published research suggests a difference in StO_2 depending on severity, but not all. However, a higher StO_2 is usually reported in the severe HIE group, in contrast to this work, where moderate HIE lead to higher StO_2. The change of StO_2 over time was also studied, but no strong conclusions were drawn due to the inconsistent sample size.

In order to establish reference values for the use of StO_2 as a quick assessment of cerebral haemodynamics and for HIE diagnosis, results published from different studies must be comparable. This investigation suggests that the differences between StO_2 values and relations to HIE severity among published studies do not have to be caused only by the different pathologies, oximeters or timings of the measurement, but also the different algorithms applied. The introduction of standardisation of oximeters and protocols describing validation and measurement execution would increase the reliability of oxygenation measurements.

Chapter 7

Measuring tissue saturation with single-distance broadband NIRS

A multidistance approach is not the only way of measuring StO_2 with CW NIRS - it can be achieved with single-distance NIRS measurement by use of broadband spectra. The aim of this chapter is to explore the broadband fitting algorithm; the focus is on the application of the algorithm to broadband NIRS data obtained in NIRFAST simulations to identify the strengths and limitations of using single-distance bNIRS to quantify StO_2.

7.1 Motivation

Broadband fitting is a CW NIRS technique in which a spectrum is collected with a single detector. Instead of using a multidistance approach, this method applies broadband measurements to recover a full spectrum with various absorption features corresponding to the attenuating substances. These features are amplified through spectral differentiation and the measured reflectance spectra are compared to their corresponding models from diffusion theory. As the fitting is performed through an iterative recovery of chromophore concentrations and scattering amplitude and power, the main strength of the method is the recovery of absolute μ_a and μ_s' values to obtain StO_2 [26, 139]. BF has been used in many applications; to measure cerebral blood flow and cerebral tissue oxygenation in infants [142], cerebral oxygenation and optical properties in piglets [139, 147] and phantoms [26]. The measured StO_2 in infants agrees with reference ranges introduced in Chapter 4 and validating the method in Monte Carlo simulations showed high accuracy when recovering optical properties [139].

One of the advantages of BF is that it does not rely on an assumption of tissue scattering, in contrast to SRS. This property is one example of how the design of BRUNO can benefit by implementing similar methods as used in BF, the absence of a fixed h when describing μ_s' (like

in SRS) could increase the accuracy of StO_2 recovery. The aim of this chapter is to explore the application of BF as an algorithm to calculate StO_2 with bNIRS data and to scrutinise its properties and implementation on bNIRS data. This step is crucial in finding the best way of combining BF with SRS in the development of BRUNO.

7.2 Implementation of broadband fitting

The BF algorithm is described in section 3.4.5; some properties of BF originating in the algorithm design are:

- BF uses a broadband spectrum ($\sim$ 650–850 nm), allowing for the monitoring of more chromophores than just haemoglobin and for a quantification of scattering.
- A single-distance CW NIRS measurement does not allow the separation of the extracranial signal components. This contamination is weak for thin neonatal skulls [139].
- The spectral differentiation removes baseline-offset artefacts originating from poor fibre-tissue coupling [26, 138].

Figure 7.1 shows a reflectance spectrum R_M and the model R_{EBC} fitted to the reflectance derivatives $\partial R_M/\partial\lambda$, $\partial^2 R_M/\partial\lambda^2$. The data was collected in a liquid phantom. The process of BF is summarised in a diagram in Figure 7.2.

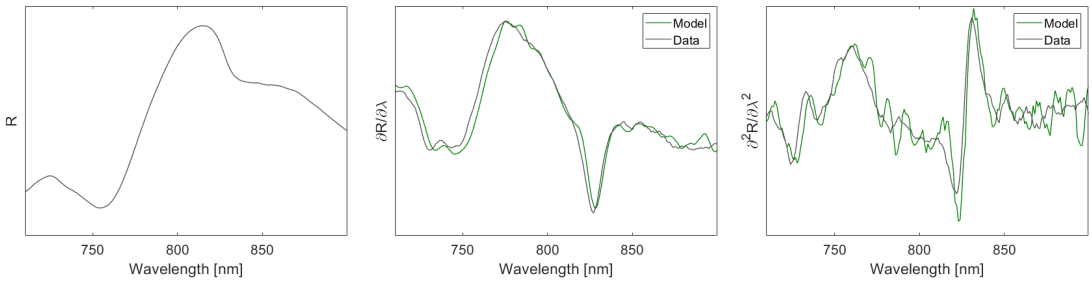

(a) Measured reflectance.

(b) First spectral derivative of reflectance.

(c) Second spectral derivative of reflectance.

Figure 7.1: BF applied to a reflectance measurement in a liquid phantom. The measured reflectance R_M (a) is twice differentiated (b,c) and compared to the theoretical model R_{EBC}.

Strengths and limitations of BF will be identified through the implementation of the algorithm in bNIRS data obtained in NIRFAST simulations. The CYRIL 1 data collected in infants used for the exploration of SRS was not suitable due to the insufficient wavelength range. The use of NIRFAST enables a direct assessment of accuracy of StO_2 recovery. Unless specified, the algorithm was applied as described in section 3.4.5 using a custom MATLAB script.

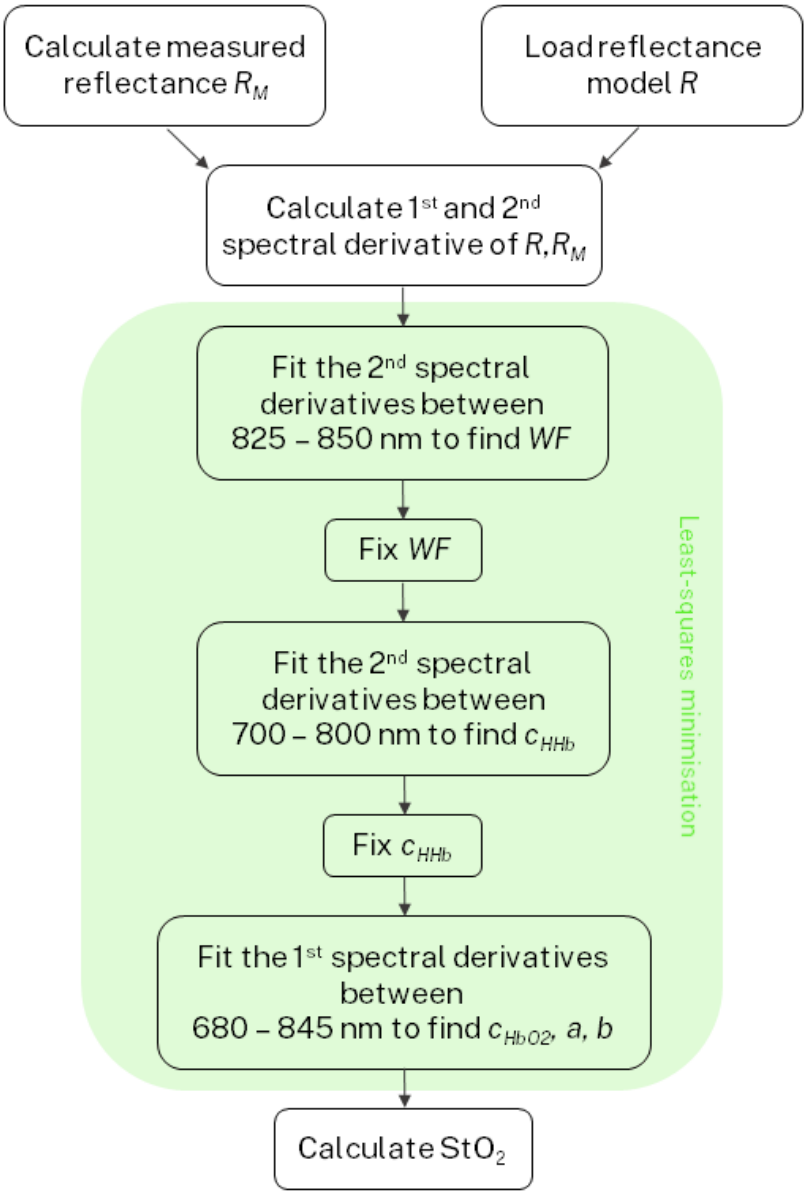

Figure 7.2: Flowchart describing the process of recovering StO_2 with BF. The theoretical model is loaded once but evaluated with different optical properties in each iteration during the least-squares minimisation.

One of the main aspects of BF is the process of fitting the theoretical model R_{EBC} to the measured data R_M, in the least-squares minimisation routine (highlighted in green in Figure 7.2). A close fit of the model to the data is crucial for correct results. The aim of the optimisation routine performing the fitting is to minimise the difference between the model and the measured data. This can be achieved through least squares fitting; a method of minimising the sum of the squares of the offsets between the fitted curve and the data points, the residuals. The use of solvers that allow

for the setting of boundary conditions for the fitting parameters improves speed and accuracy. The authors of BF suggest the use of *fminsearchbnd*, a bound nonlinear programming solver available online [147, 265]. This solver offered fast and repeatable results and used throughout this work for all model fitting.

7.2.1 Coupling of μ_a and μ_s'

One of the main challenges in measuring absolute quantities with CW NIRS is the difficulty in separating the effect of scattering and absorption on light in tissue. The dependence of reflectance on wavelength in the definition of the BF reflectance model in Eq. (3.33) is given by μ_{eff}, $\mu_{eff} = \sqrt{3\mu_a(\mu_a + \mu_s')}$. A change in μ_{eff} at a single wavelength can be attributed to changes in either μ_a or $\mu_s'(\lambda)$, and an infinite amount of combinations of μ_a or μ_s' can lead to the same μ_{eff}. The algorithm itself can also contribute to the crosstalk, the limits set on the amount of function evaluations and function tolerance determine which result is already deemed "good" enough. Using broadband data constraints the amount of solutions to the least-squares problem, as the conditions need to be satisfied at each wavelength. Boundary conditions also help guide the optimisation closer to the correct solution.

A coupling between μ_a and μ_s' is a common issue in CW NIRS measurements [266] and it is important to quantify its effect on StO_2. To measure this impact, 81 reflectance models were generated by evaluating the reflectance model (Eq. (3.33)) at a constant μ_a but different μ_s'. Chromophore concentrations were the same in all models; $WF = 0$, $c_{HHb} = 29.5$ μM, $c_{HbO_2} = 55$ μM. The different values of μ_s' for each model were obtained by changing the scattering parameters a and b; they ranged 0.26–0.77 $\text{mm}^{-1}\mu\text{m}^{-1}$ and 0.87–2.61, respectively. Examples of a few μ_s' used when generating different reflectance models are shown in Figure 7.3.

The generated models were used as input data for BF and only μ_a was recovered with BF; μ_s' remained fixed by setting all boundary conditions for a, b equal to the true value. The lower boundary condition for c_{HHb} and c_{HbO_2} was 0 μM; upper boundary were 200 μM. The recovered c_{HHb} and c_{HbO_2} obtained from combinations of nine a and nine b values are in Figure 7.4a and Figure 7.4b.

The recovered concentrations c_{HHb} and c_{HbO_2} increased with the decrease of a and b. As μ_s' decreased, the light attenuation was attributed to higher μ_a. While the fixed scattering values were changed by 50% from the true value, the change in the recovered concentrations was wider: 10.7–86.5 μM (36 - 293% of the true value) for c_{HHb} and 25.6–133.4 μM (47–243% of the true value) for c_{HbO2}.

This shows that despite μ_a being identical in all 81 models, the recovered haemoglobin concentrations varied significantly with the change in μ_s', suggesting that BF is not suitable for the recovery of c_{HHb} and c_{HbO_2} individually.

The next step was to assess the robustness of StO_2 towards these scattering changes. The change of StO_2 with a and b is shown in Figure 7.4c. The change in StO_2 was lower than in c_{HHb} and c_{HbO_2}. All StO_2 values were between 59.7% and 70.5%, the true value was 65.1%. Even though the changes in c_{HHb} and c_{HbO2} were very large, the relative content of c_{HbO_2} in c_{THb} did not change and kept StO_2 mostly stable, suggesting a resistance of StO_2 towards crosstalk.

An increase of residuals of the fit with increased mismatch between the truth and the recovered parameters was observed. Figure 7.5 shows the residuals when recovering StO_2. The sum of residuals is the lowest for the true value setting of a and b. The banana-like shape of the low residual region corresponds to similar μ_{eff} values.

In conclusion, μ_s' and μ_a are connected; if BF is to be used for the estimation of absolute optical properties, both μ_a and μ_s' need to be found accurately. Crosstalk between the fit parameters can be reduced by setting adequate boundary conditions. While the recovered haemoglobin concentrations can by vastly overestimated by incorrectly measuring the scattering parameters; the measurement of StO_2 is less sensitive to crosstalk and can be measured with higher precision than μ_a and μ_s'.

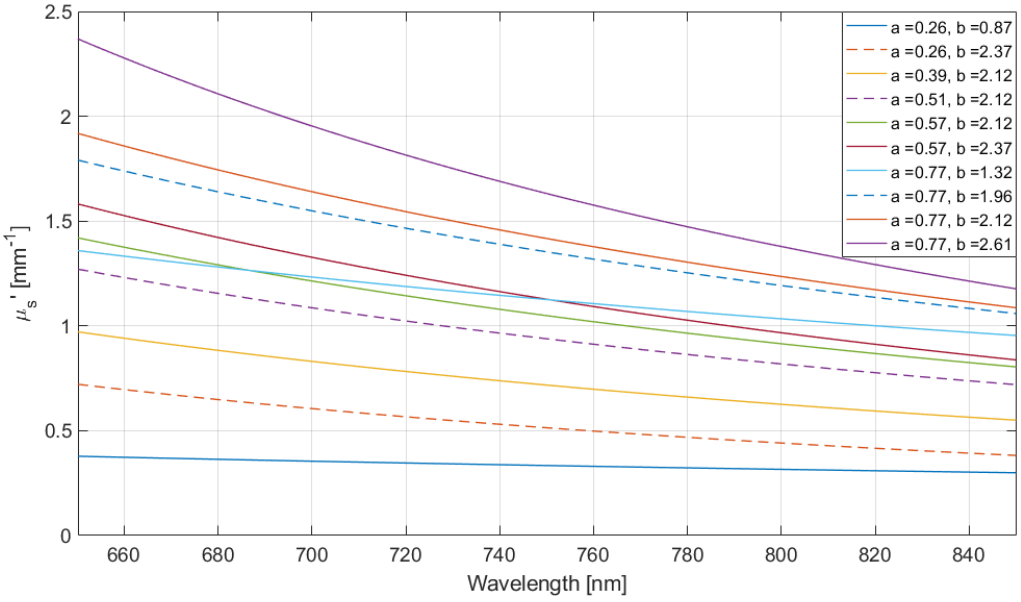

Figure 7.3: Examples of μ_s' used when generating models of reflectance used for the recovery of μ_a with BF. a is reported in $\mathrm{mm}^{-1}\mu\mathrm{m}^{-1}$. The range of a was 0.26–0.77 $\mathrm{mm}^{-1}\mu\mathrm{m}^{-1}$ and the range of b was 0.87–2.61.

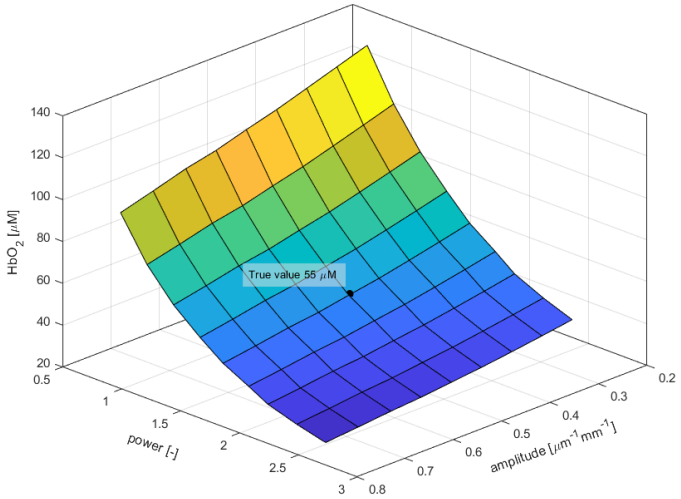

(a) c_{HbO_2}.

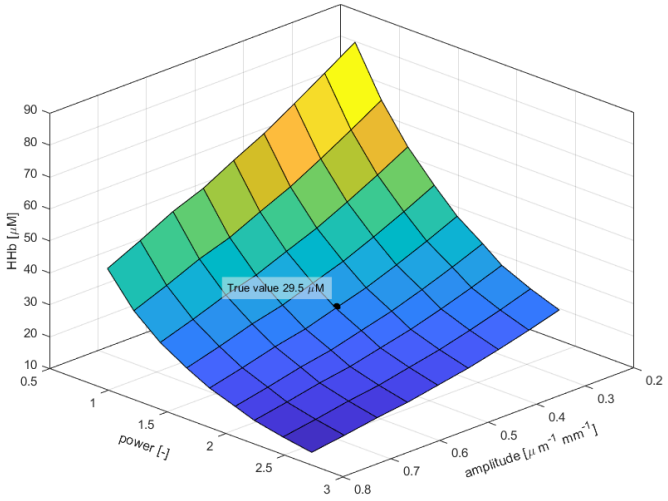

(b) c_{HHb}.

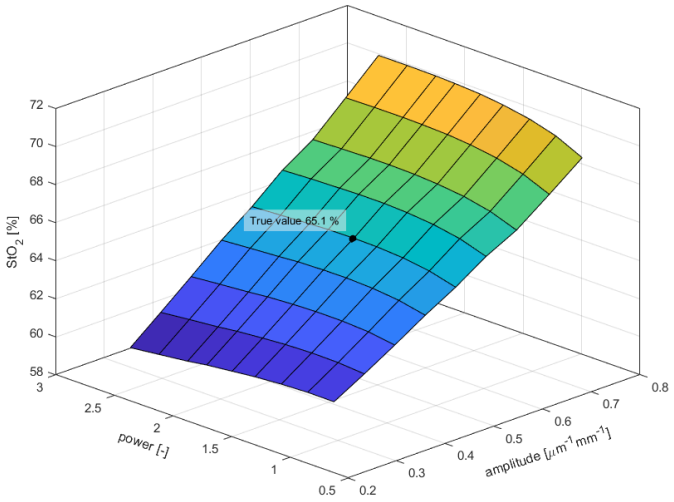

(c) StO_2.

Figure 7.4: c_{HHb}, c_{HbO_2} and StO_2 recovered with BF while scattering parameters a, amplitude, and b, power, were fixed at constant values.

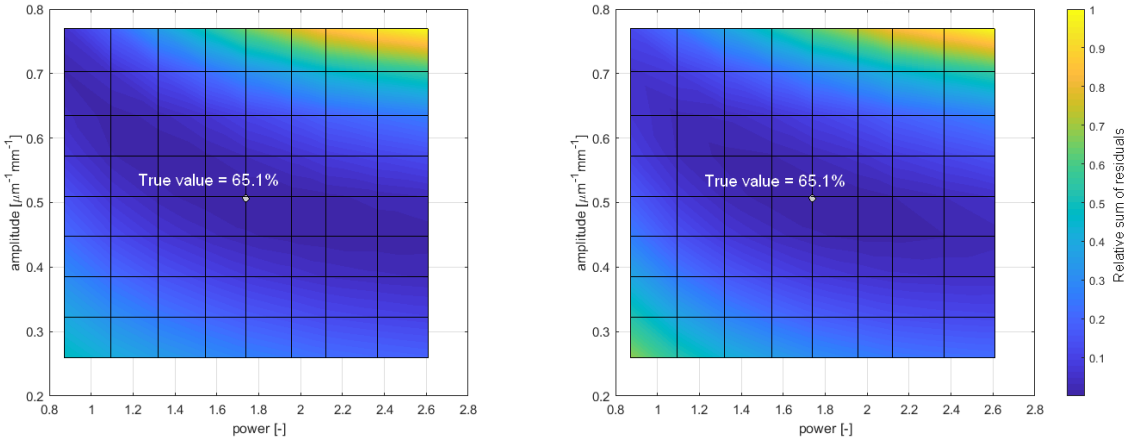

(a) First derivative fit. **(b)** Second derivative fit.

Figure 7.5: Sum of residuals when using *fminsearchbnd* in BF to recover StO_2 when keeping the amplitude a and power b of scattering fixed.

7.2.2 Wavelength selection

Wavelength selection is a property that strongly influences the accuracy of an algorithm, as shown already in the exploration of SRS. In BF, the fitting process is divided into three different steps across specific wavelength ranges across 680–845 nm. While the wavelength selection in BRUNO will be different than BF due to the CYRIL 2 system measuring across 704–911 nm, similar steps can be undertaken when designing the BRUNO fitting to ensure maximal accuracy of StO_2 recovery.

The wavelength intervals in BF were selected according to chromophore's spectral features. The previous section has shown the significant effect of crosstalk between absorption and scattering when fitting the reflectance data to the model. While using a broadband spectrum and setting adequate boundary conditions reduces the amount of possible solutions, targeting specific features of the reflectance spectrum for the recovery of specific parameters is an additional way of guiding the least-squares fitting algorithm to the right solution.

BF is designed to recover also the concentrations of water. Water was not discussed in the previous sections; from now on, a water content of 80% is assumed.

Differentiation is used in other NIRS algorithms to improve the visibility of spectral features [137, 135]. An important feature is the 760 nm HHb feature seen both in the 1st and 2nd derivative spectra, Figure 7.6. When c_{HHb} is recovered with BF, data measured at wavelengths around this feature, at 700–800 nm, are used to decrease the potential for crosstalk with other chromophores.

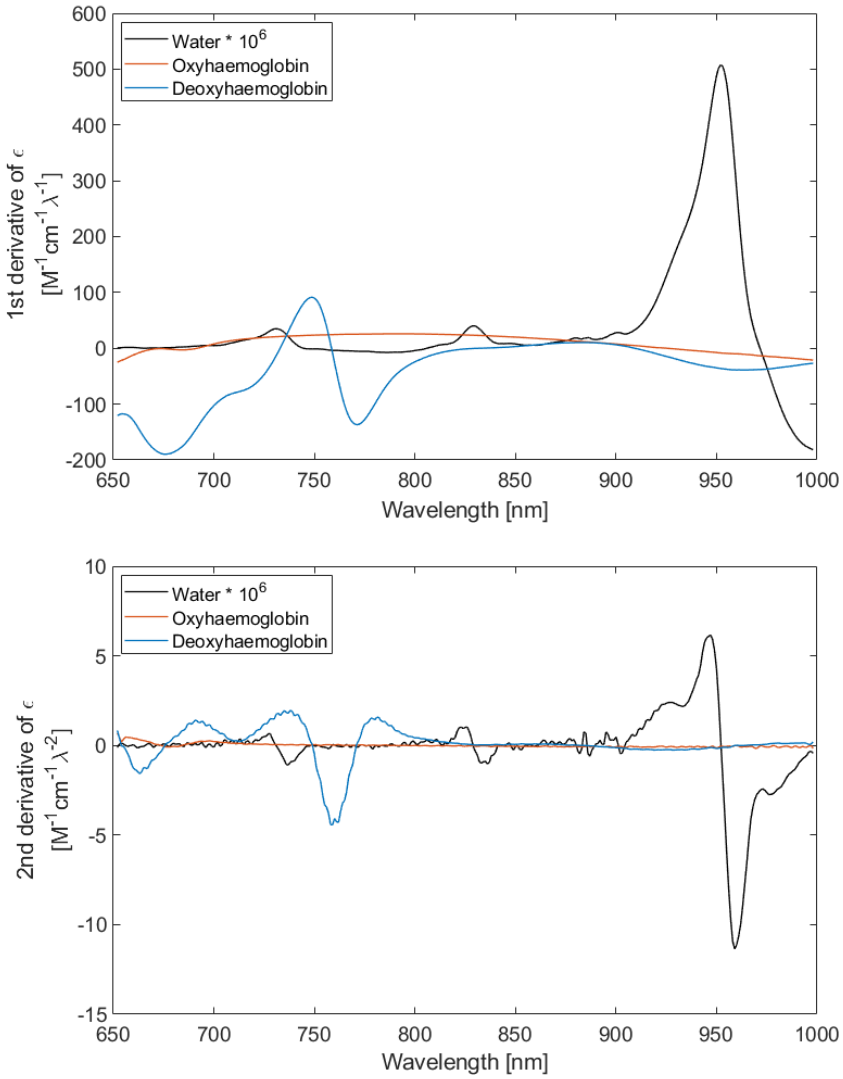

Figure 7.6: Spectral derivatives of HHb, HbO_2 and H_2O extinction spectra. Measured by [136].

The HHb peak of interest overlaps with a water feature at 740 nm in the 2nd spectral derivative. To overcome this potential for crosstalk when recovering both chromophores, BF first fits for water in a region of another significant water feature, 840 nm. Once the fitting algorithm finds a suitable value of WF, BF sets this as a constant and fits for only c_{HHb} and the other 3 parameters across the 760 nm feature in the second step. Recovering c_{HbO_2} is more difficult, as it lacks any significant spectral features. To estimate c_{HbO_2}, a and b; c_{HHb} and WF are set as constant and BF fits over the rest of the spectrum in the 1st derivative. This approach does not completely eliminate the effect of crosstalk as μ_s' is sought for simultaneously with μ_a in all steps.

The wavelength region to use for the fitting of individual parameters can be identified by differentiating $\frac{\partial^m R}{\partial \lambda^m}$, where m = 1,2, with respect to each of the five parameters. This shows how

changing each parameter affects $\frac{\partial^m R}{\partial \lambda^m}$. The derivatives are shown in Figure 7.7.

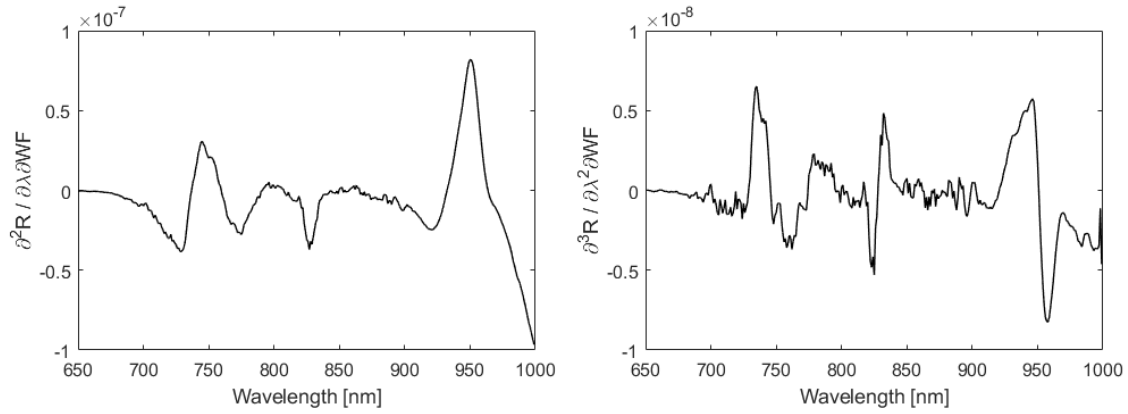

(a) Water fraction WF

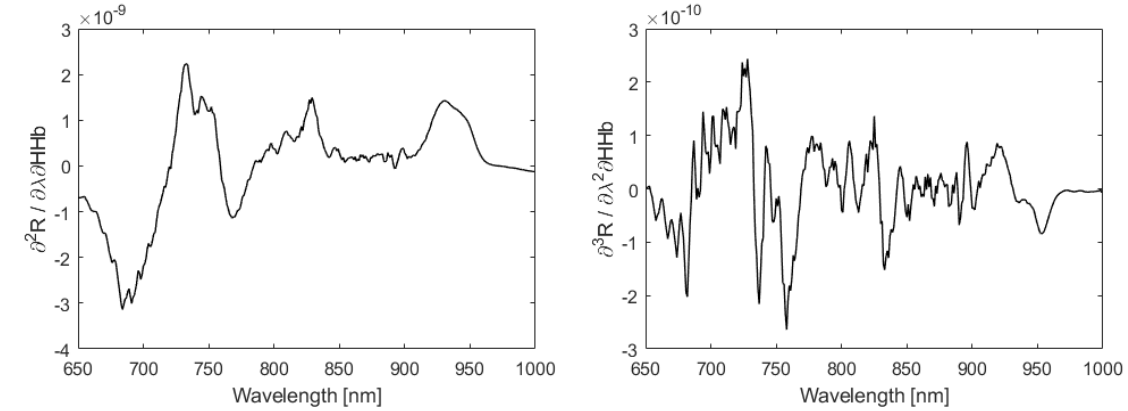

(b) HHb concentration c_{HHb}

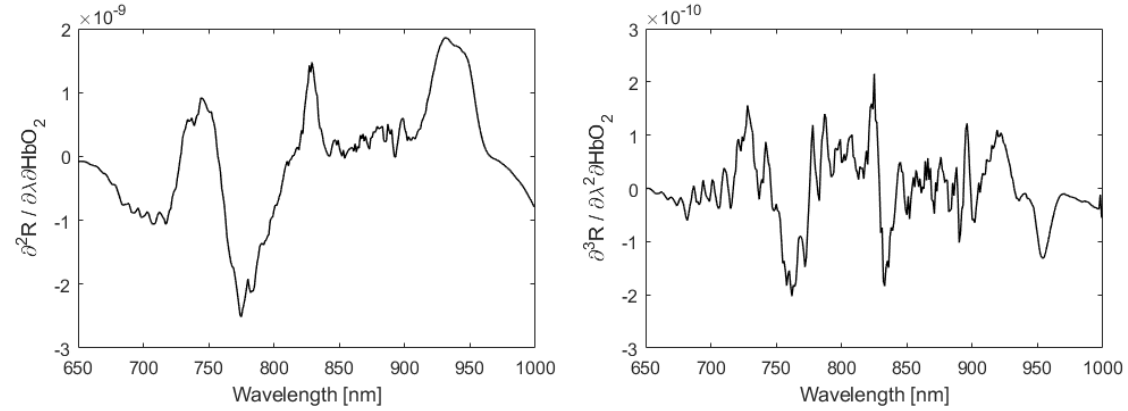

(c) HbO_2 concentration c_{HbO_2}

Figure 7.7: The 1st and 2nd spectral derivatives of $\frac{\partial R}{\partial param}$. The function was evaluated at $WF = 0.8$, $c_{HHb} = 29.5\ \mu$M, $c_{HbO_2} = 55\ \mu$M, $a = 0.5\ \text{mm}^{-1}\mu\text{m}^{-1}$ and $b = 1.7$.

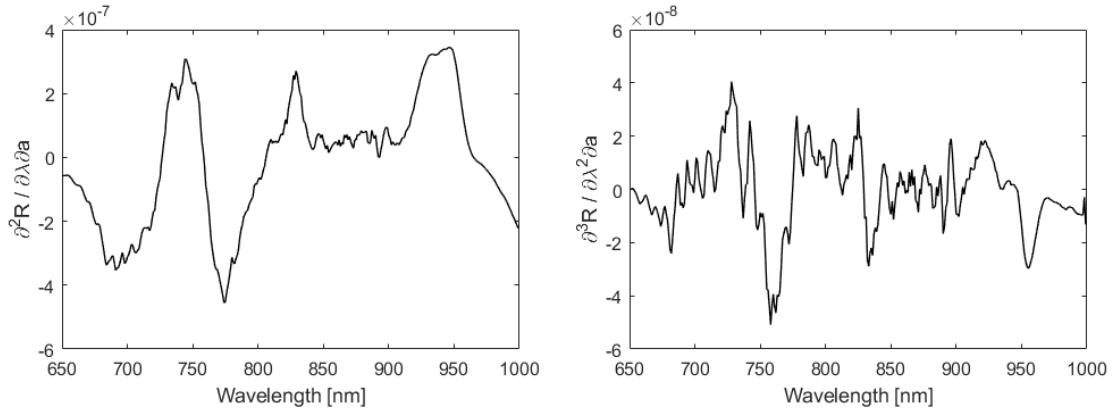

(d) Scattering amplitude a

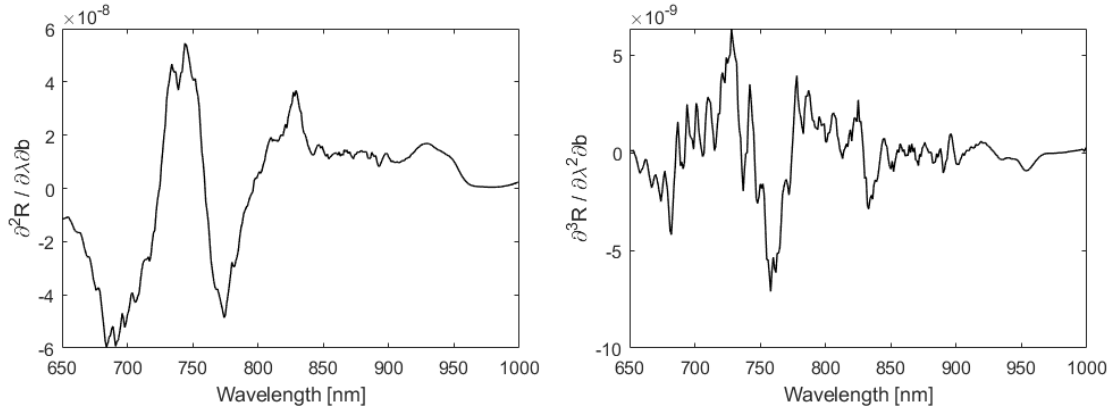

(e) Scattering power b

Figure 7.7: The 1st and 2nd spectral derivatives of $\frac{\partial R}{\partial param}$ (cont.). The function was evaluated at $WF = 0.8$, $c_{HHb} = 29.5$ μM, $c_{HbO_2} = 55$ μM, $a = 0.5$ mm$^{-1}\mu$m^{-1} and $b = 1.7$.

The patterns in Figure 7.7 indicate the impact of changing a parameter on $\frac{\partial R}{\partial \rho}$ and $\frac{\partial^2 R}{\partial \rho^2}$. The similarity to the spectral features seen in Figure 7.6 is expected. For example, if WF is changed, $\frac{\partial R}{\partial \rho}$ changes the most around 950 nm as that is where water absorption is the strongest. $\frac{\partial^2 R}{\partial \rho \partial WF}$ still contains the spectral features of other chromophores HHb and HbO_2 in the 700–900 nm range, they are smaller relative to the 950 nm peak as changing WF does not affect $\frac{\partial R}{\partial \rho}$ much in that wavelength region. A strong water spectral feature is also seen in $\frac{\partial^3 R}{\partial \rho^2 \partial WF}$ at 825 nm but the same feature is much smaller in $\frac{\partial^3 R}{\partial \rho^2 \partial c_{HHb}}$ and $\frac{\partial^3 R}{\partial \rho^2 \partial c_{HbO_2}}$. Hence, if the 825 nm peak is used in BF for the recovery of WF, crosstalk from other chromophores will be minimal. Fixing WF at the recovered value during the next step in BF, where c_{HHb} is estimated by fitting between 700–800 nm; this process accounts for the absorption by water and decreases parameter crosstalk.

The derivative spectra of a, b and HbO_2 were very similar, showing that the last fitting step is particularly sensitive to crosstalk between scattering and absorption. μ_a is by then, however, limited by the fixed values of WF and c_{HHb}.

To explore how beneficial it is to split the fitting process into three steps instead of doing just one, data from model B (homogeneous with water absorption) was analysed with BF across 680–850 nm either a one-step process or a three-step process. The boundary conditions used are in Table 7.1; the results are reported in Table 7.2.

Table 7.1: Boundary conditions for the analysis of model B with BF.

	WF [%]	c_{HHb} [μM]	c_{HbO_2} [μM]	a [mm$^{-1}\mu$m^{-1}]	b [-]
start	64	23.6	66.0	0.61	1.39
LB	40	14.8	27.5	0.26	0.87
UB	100	44.3	110.0	0.76	2.61

Table 7.2: Fitting spectra from simulation B with BF either across the whole spectrum at once or with first fitting for WF, then c_{HHb} and other parameters. WF was fitted for over 825–850 nm, c_{HHb} over 700–800 and the other parameters were recovered across 680–845 nm.

Fitting	WF [%]	c_{HHb} [μM]	c_{HbO_2} [μM]	StO_2 [%]	a [mm$^{-1}\mu$m^{-1}]	b [-]	Duration [s]
1 step	58.2	17.5	27.5	61.2	0.36	2.57	4.28
3 steps	42.3	16.3	29.4	64.4	0.72	1.46	6.84
Truth	80.0	29.5	55.0	65.1	0.51	1.73	

The comparison of performing BF over 3 steps or 1 step is in Table 7.2. StO_2 was more accurate when found in three steps but crosstalk was not eliminated, as seen in Figure 7.8. Targeting the water peak by fitting across 825–850 nm did not lead to a correct evaluation of the water concentration, instead, scattering was overestimated, as seen in Figure 7.8a. Figure 7.8b shows that the absorption coefficient recovered both in 1-step process and 3-step process were very similar; the main difference was in the recovery of μ_s'. While the underestimation of μ_a in the 3-step process was balanced by an overestimated μ_s', the 1-step fitting also underestimated μ_s', causing an underestimation of μ_{eff} and StO_2.

Fitting over the whole spectrum at once did not lead to an advantage except for a decrease in execution time; hence, the 3-step fitting was considered suitable as suggested by the authors of BF.

7.2.3 Absorption by water

It is possible that the decrease addition of a third chromophore, water, could decrease the accuracy of StO_2 recovery with BF, as some absorption by haemoglobin might be attributed to the absorption by water instead, or opposite.

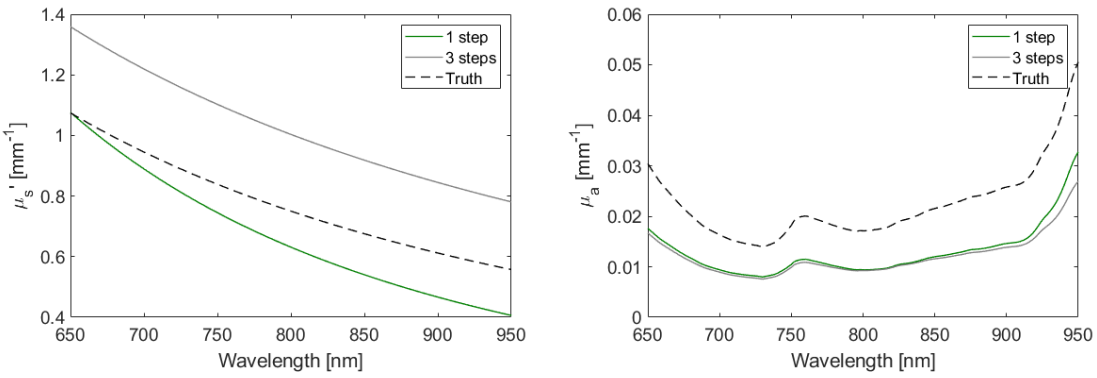

(a) μ_s' **(b)** μ_a

Figure 7.8: Scattering and absorption recovered with BF in fitting in 1 or 3 steps in data from model B compared to the truth.

To see how StO_2 is affected by the assumed water fraction, all boundary conditions of WF were set to a constant value, fixing the output WF (the true WF in the input model was 80%). The other 4 parameters were recovered from model B spectra. The fitting was performed over 3 steps with $fminsearchbnd$. The effect of not allowing the optimisation routine to change WF is shown in Figure 7.9.

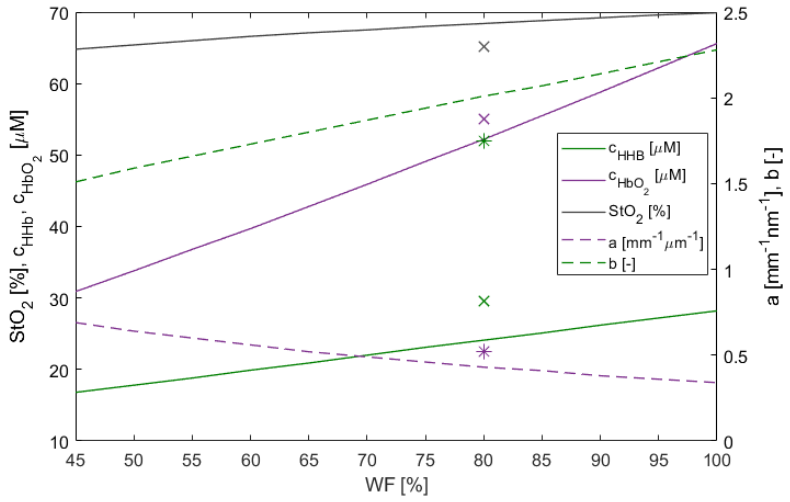

Figure 7.9: The effect of WF set to a specific value (x-axis) on the recovery of c_{HHb}, c_{HbO_2}, a, b and StO_2 with BF. The true WF in the used model was 80%. The ground truth of c_{HHb}, c_{HbO_2} and StO_2 at 80% WF are indicated with crosses, the ground truth of a, b are indicated with stars.

Both c_{HHb} and c_{HbO_2} increased with the increase of water concentration, leading to a rise of StO_2. It is likely that the strong absorption features of water were incorrectly assigned to haemoglobin absorption instead, a crosstalk could be present not only between μ_a and μ_s', but also between the individual chromophores due to the overlapping spectral features. The maximal error

in StO_2 estimation occurred at 100% WF and was 4.8%. The accuracy of StO_2 recovery was much higher than the accuracy of other parameters recovery.

An overestimation of μ_a was balanced by a decrease in μ_s'; visible when plotting μ_a and μ_s' for the different values of WF, Figure 7.10. The stabilising of μ_{eff} when absorption increased as scattering decreased is shown in Figure 7.11. In Figure 7.11a, μ_{eff} was calculated from the individual optical properties recovered in Table 7.9; in Figure 7.11b only μ_a was changed while μ_s' remained at the same value, calculated from parameters at WF = 80%. The change in μ_{eff} with WF was much larger.

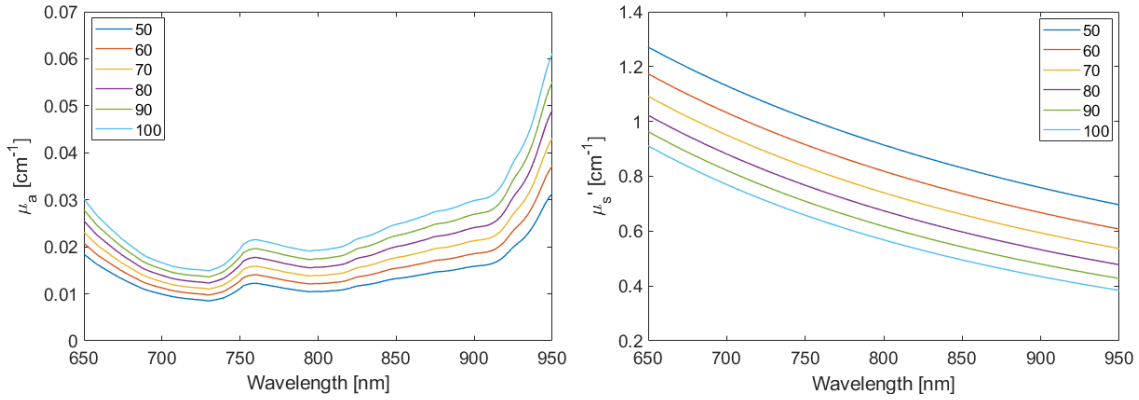

(a) μ_a **(b)** μ_s'

Figure 7.10: The recovered μ_a and μ_s' retrieved with BF when WF was set to different values. WF reported in %.

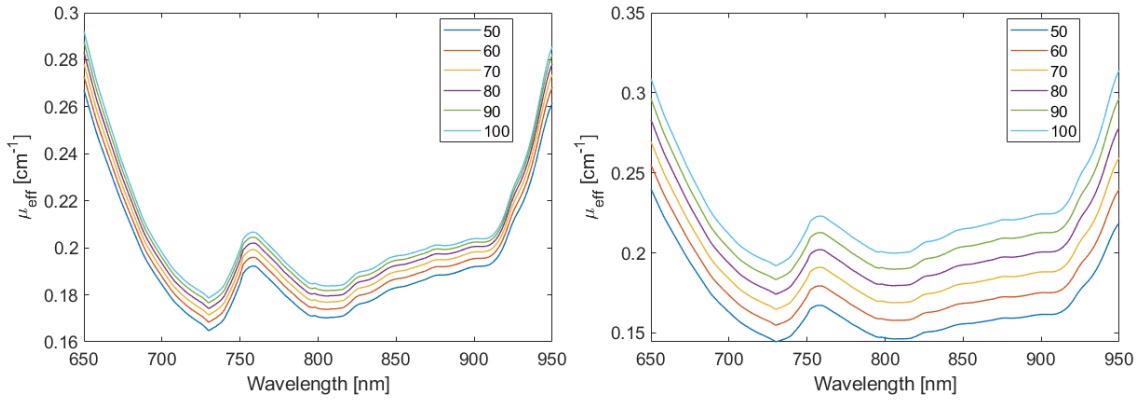

(a) μ_{eff} **(b)** μ_{eff} when μ_s' constant.

Figure 7.11: The recovered μ_{eff} from optical properties retrieved with BF when WF was set to different values. WF reported in %. In (b), μ_s' remained constant and was equal to $\mu_s' = 0.43\frac{\lambda}{1000}^{-2.01}$.

7.3 Discussion

The aim of this chapter was to explore the application of the BF algorithm to broadband NIRS data obtained in NIRFAST simulations. The application of BF to NIRFAST data highlighted properties of the algorithm, which will be relevant when combining BF with SRS in the development of the novel algorithm, BRUNO, such as the crosstalk between scattering and absorption or fitting wavelength selection.

The crosstalk between μ_a and μ_s' is present in CW measurements of attenuation data. It is impossible to separate the impact of scattering and absorption in with BF, as attenuation of the signal can be attributed to either. In theory, there is an infinite amount of combinations of μ_a and μ_s', which would lead to the same μ_{eff}. In BF, the amount of possible solutions is restricted through the use of broadband spectra and the setting of boundary conditions. It this work, boundary conditions were derived from the true values of concentrations and scattering. In a real NIRS measurement, the user can guide the setting of boundary conditions from reference values of tissue optical properties.

Although the sample size of spectra was too small for algorithm validation, the results show that StO_2 can be recovered with high precision using BF. The accuracy of the individual fitting parameters (WF, c_{HHb}, c_{HbO_2}, a, b) was lower, because μ_s' was often overestimated, leading to a reduced μ_a. However, as the reduced absorption led to a decrease in both c_{HHb} and c_{HbO_2}, StO_2 remained close to the correct value. While an impact of water absorption on the estimation of haemoglobin absorption was found, the effect on StO_2 was small.

The lack of accuracy when estimating μ_s' and μ_a identified in this work has been reported elsewhere. The performance of the BF algorithm was recently validated in a study by Kewin and colleagues [139]. An animal model was simultaneously monitored with a broadband system and a TR system. Additionally, Monte Carlo simulations were used to acquire 500 spectra at different StO_2 values. The authors found that the precision of estimating StO_2 was higher than the precision of c_{HHb} and c_{HbO_2}, showing that the algorithm can converge to the correct StO_2 even if μ_a is inaccurate. Similar results were reported in another study where spectra were simulated with NIRFAST; optical parameters were recovered with a higher error than StO_2 [267].

The potential increase of the accuracy of BF by using different fitting algorithms or changing the fit options was not explored in this work, *fminsearchbnd* was used in BF. Using a different optimisation routine could potentially improve the result, particularly using solvers which find a global solution. It is however possible that the improvement achieved through a better fitting

process would be negligible compared to the measurement errors present in NIRS measurements, such as noise or coupling artefacts. Nevertheless, a better performing least-squares algorithm would also increase the duration of the fitting, which is not desired for real-time measurements.

The work in this chapter is not a complete exploration of the behaviour of BF. Additional aspects which could affect the accuracy of the method include:

- The selection of correct haemoglobin specific extinction coefficient spectra is important for when recovering absolute concentrations with NIRS [268, 269]. To avoid issues related to incorrect extinction coefficients, default NIRFAST extinction spectra, which are part of the properties of the mesh, were used in this study for both data generation and analysis.

- The effect of the mismatch of the refractive index n on the boundaries of different tissue types in the mesh was not investigated as the absolute true values of parameters are not known in the heterogeneous NIRFAST simulations. To be able to assess the accuracy of BF, mostly homogeneous mesh data was used, where the refractive index was identical in all nodes.

- The presence of noise in the data was briefly explored when comparing different least-squares fitting methods. Noise did decrease the accuracy of the method, particularly because it gets amplified through the differentiation. The use of smoothing filters is hence necessary. A five-step moving average filter was used in this work, as used by the authors of BF [139]. The use of de-noising algorithms for BF was also suggested in other work [270] but was not implemented here. It is not assumed that the absence of de-noising is the cause of discrepancies between the results presented here and in literature [147, 139] because the majority of the analysed spectra was noise-free.

- BF uses a EBC model as it is a more precise estimation of light propagation in tissue than ZBC used in SRS. Using ZBC in BF was not investigated.

- The sensitivity of the algorithm to ECT is likely increased due to the absence of multiple detectors. This will be further investigated in the next chapter.

All the findings of this chapter were important when developing BRUNO, which is a combination of SRS and BF by measuring a broadband attenuation slope against distance $\frac{\partial A}{\partial \rho}$. Fitting this measurement to a theoretical model of this slope means that the BRUNO algorithm should have similar properties to BF: crosstalk is present, water absorption has to be accounted for and the computational burden is increased compared to SRS.

7.4 Conclusion

The use of BF to recover StO_2 from bNIRS data was demonstrated. The design of the algorithm was investigated and how the individual selection of aspects, such as wavelength selection, affect the final result. Several properties of BF were highlighted:

- BF has the ability to recover StO_2 with high accuracy even if the other fitting parameters are incorrect. The inability to recover μ_a and μ_s' accurately is attributed to parameter crosstalk. StO_2 is more robust to crosstalk than μ_a. This crosstalk is independent of the measurement algorithm and is a property of the reflectance model used.
- BF benefits from bNIRS measurements by targeting different spectral features of chromophores to improve the precision of the measurement. The fitting of the theoretical model to the data in three steps improves the accuracy of StO_2 recovery.

Limitations of BF include:

- If incorrect boundary conditions are set, the algorithm will not lead to the desired results and will converge at the boundary. If StO_2 was recovered with a large error, it is likely that the parameters converged at the boundaries. In such case, adjusting the boundary conditions should always be guided by a visual assessment of the fit.
- The computational requirements of the algorithm are much higher than SRS and could potentially hinder BF from being used in real-time. The aim in BRUNO development will be to decrease this, perhaps by using simpler light transport in tissue models.
- Applicable only in infants as it does not include any means of removing extracerebral layer contamination.

Chapter 8

Development of a novel brain oximetry algorithm

The investigation of the application of SRS and BF to NIRS data to understand the behaviour of the algorithms created a basis for the development of the novel StO_2 algorithm BRUNO. The following chapter guides the reader from the initial algorithm proposal through the development process and evaluation using NIRFAST and phantom data up to the last section, where the performance of the novel algorithm is compared to BF and SRS.

8.1 Requirements

The aim of this PhD project was to develop a novel algorithm to measure StO_2 with multidistance CW NIRS; to obtain a measure of StO_2 sensitive to cerebral tissue and track oxygenation with high accuracy, dynamic range and precision. The result was BRoadband mUltidistaNce Oximetry; BRUNO. Overall, two main requirements guided the development:

1. The algorithm had to be compatible with the measurement device CYRIL, with the broadband wavelength range (704–911 nm, resolution < 4 nm) and a multidistance light detection setup with minimal separation of 5 mm between optodes.

2. A requirement was set by the desired application of the algorithm; in the NICU for the monitoring of infants with HIE. The size of the neonatal head impacts the assumptions of light transport in tissue.

The idea was for the algorithm to benefit from both SRS and BF: obtain a brain-specific measurement through a multidistance setup and use the broadband spectrum for a measure of StO_2 free from SRS scattering assumptions. A brief comparison of SRS and BF is in Table 8.1.

Table 8.1: Comparison of spatially resolved spectroscopy (SRS) and broadband fitting (BF). ZBC: zero boundary conditions, EBC: extrapolated boundary conditions, SD: single-distance, BB: broadband, MD: multidistance.

	SRS	**BF**
Diffusion equation boundary conditions	ZBC	EBC
Set up	MD	SD BB
Accounting for water absorption	×	✓
Broadband spectrum	×	✓
Homogeneous tissue model	✓	✓
Low computational requirements	✓	×
Lower noise amplification	✓	×
No boundary conditions needed	✓	×
No prior scattering assumption	×	✓
Reduction of superficial layer signal contamination	✓	×
Unique solution	✓	×

Both SRS and BF are based on modelling tissue as a homogeneous medium. Keeping this assumption for neonates is sufficient as the extracerebral tissue layer in the neonatal head is very thin and errors arising from using such models are small [121]. However, while SRS uses the ZBC when modelling light transport in the tissue, BF uses EBC. EBC provide a more precise model of light transport but also increases the computational requirements.

An important advantage of SRS is the multidistance set up, which reduces the signal contamination from extracerebral layers. The single-distance BF measurement is influenced by the extracranial signal contamination more than SRS and the three-step fitting process adds to computational requirements of the algorithms. The advantages of BF lie in the reduction of coupling errors through differentiation [138] and the ability to account for attenuation by water absorption and scattering. While SRS does account for scattering as well, the use of the fixed h is a disadvantage.

Another difference between SRS and BF lies in the number of unique solutions. While SRS has one solution, the fitting routine in BF tries to find the optimum solution within the given boundary conditions. Boundary conditions are used to constrain the amount of possible solutions, as the optimisation has no unique solution. This is why the computational burden of SRS is much lower.

Most weaknesses of either algorithm can be addressed by the other. For example, one of the main drawbacks of BF, the use of only one SDS, can be solved by implementing a multidistance measurement. This could be applied to BF by measuring a slope of reflectance against distance instead of reflectance. If a broadband attenuation slope was measured in SRS, the algorithm would

no longer have to rely on h. It is likely that these improvements would increase the accuracy of StO_2 calculation and perhaps also affect other performance indicators, such as sensitivity or dynamic range.

Such combination of SRS and BF led to BRUNO. It combined the strengths of both methods: the brain-specificity and efficiency of SRS and the ability to account for μ_s' with BF, while keeping the computational requirements low to allow for real-time measurements.

8.2 Proposed algorithm

Combining the goals set in the previous section, the novel algorithm should:

- Use a multidistance setup to measure the slope of attenuation over distance and reduce the impact of extracranial signal components.
- Use broadband spectra to obtain a complete assessment of attenuation in the selected NIR wavelength range.
- Apply differentiation to correct for coupling errors and highlight spectral features.
- Use a model of light transport that can be solved in real-time over a broad range of wavelengths.

Combining these criteria led to the proposed algorithm BRUNO. The idea was to retrieve StO_2 with broadband CW NIRS based on a multidistance measurement of the slope of light attenuation A against distance ρ, $\frac{\partial A}{\partial \rho}$, dependent on the optical properties of the medium (μ_{eff}). One can then obtain a measure of scattering and absorption in the interrogated tissue by fitting the measured slope to a theoretical model over a broadband wavelength range. The fitting is performed in a manner similar to BF; the attenuation slope depends on $\mu_{eff}(\mu_a, \mu_s')$, the fitting parameters are absorption and scattering described in terms of chromophore concentrations and scattering amplitude a and power b:

$$\mu_s'(\lambda) = a\left(\frac{\lambda}{1000(nm)}\right)^{-b}, \tag{8.1}$$

$$\mu_a(\lambda) = c_{HbO_2}\alpha_{HbO_2}(\lambda) + c_{HHb}\alpha_{HHb}(\lambda) + WF\mu_{a_{H_2O}}(\lambda) \tag{8.2}$$

The fitting is performed in the spectral derivative space to decrease the influence of coupling errors, other baseline offsets and highlight spectral features.

The individual steps in BRUNO's design, such as wavelength or model selection, will be discussed further. The aim was to create a novel algorithm to obtain an as accurate measurement

of StO_2 as possible. The algorithm development was data driven, guided by evaluating the accuracy of StO_2 recovery from data collected in NIRFAST simulations and phantom measurements described in Chapter 5.

While in theory the algorithm could be used for the individual recovery of μ_s' and μ_a, the accuracy of estimating these parameters was not considered a criterion of BRUNO performance due to the presence of crosstalk between μ_s' and μ_a, already identified in the previous chapter.

8.3 Data preparation

Before the algorithm started being developed, NIRS data had to be prepared for analysis. While the broadband spectra obtained with NIRFAST did not need any pre-processing, the data from dynamic phantom measurements had to be synchronised with the TR data collected with MAESTROS and the attenuation slopes were calculated. All TR data analysis was performed by Dr Frederic Lange and will not be described here (details can be found in [113]), the provided StO_2 was used.

8.3.1 Homogeneous phantom data preparation

The protocol for phantom data collection is introduced in section 5.3.1. The phantom data analysed in this chapter was collected with detectors 3, 4, 5 and 6 at 30–15 mm SDS; CYRIL 2 data collection protocols were used. The phantom measurement consisted of 4 oxygenation-deoxygenation cycles within 45 minutes. The pre-processing of the data were performed in MATLAB and included background noise subtraction, summing spectra across the CCD according to binning, interpolation and attenuation/reflectance calculation.

The CCD binning for the summing of spectra was selected to cover the peaks of the detection areas as described in Chapter 5. The effect of changing the binning width on a spectrum collected with the furthest away detector, detector 3, is shown in Figure 8.1; increasing the bin width reduced the noise and increased the number of counts. A bin of width 20 pixels was used for all spectra as it is a compromise between maximal counts and minimal detector crosstalk.

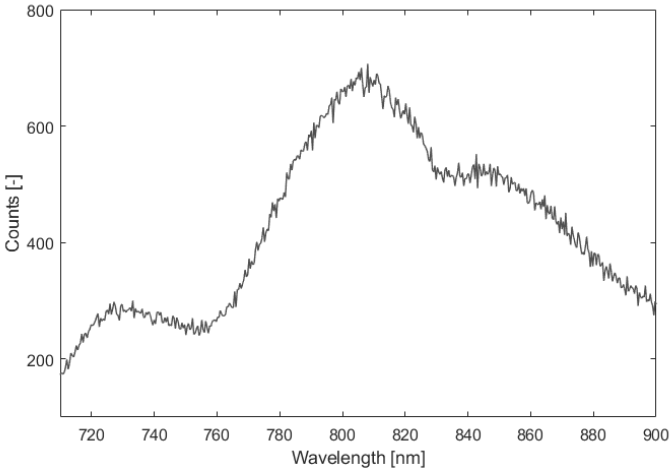

(a) Strip 143, bin width = 1 pixel.

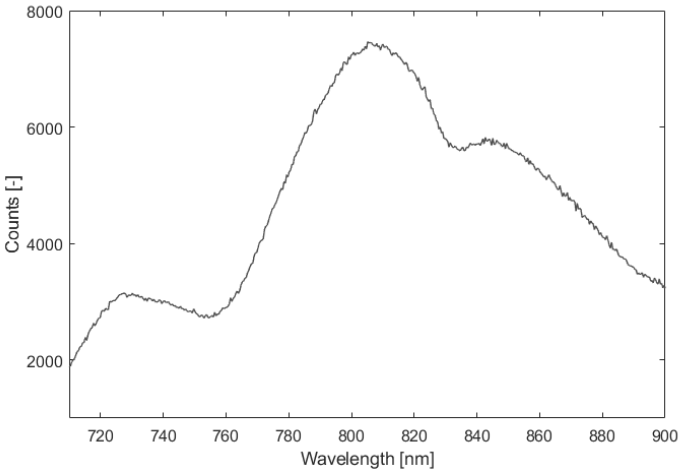

(b) Strips 138 to 148, bin width = 10 pixels.

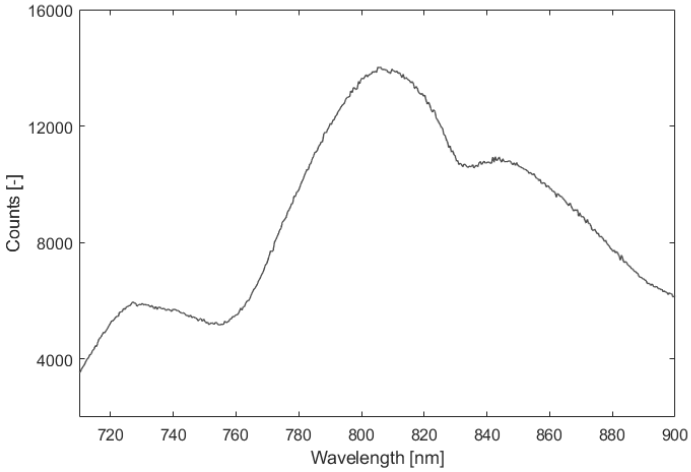

(c) Strips 133 to 153, bin width = 20 pixels.

Figure 8.1: The effect of CCD bin width on the quality of a spectrum collected at 30 mm separation, exposure 1 s.

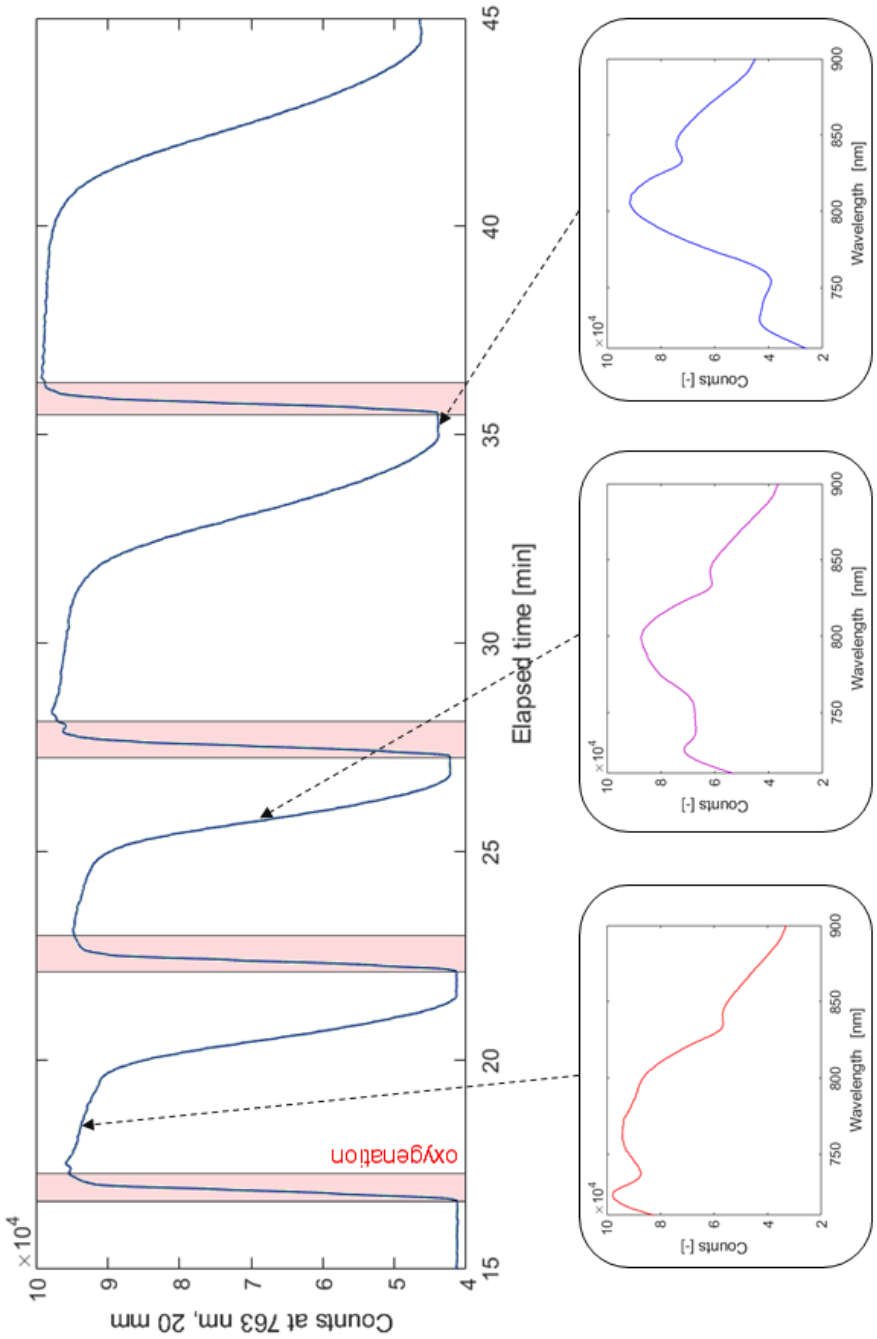

Figure 8.2: The change of absorption throughout the oxygenation-deoxygenation cycles in a homogeneous dynamic phantom collected at 20 mm SDS.

The spectra shown in Figure 8.1 were collected during a deoxygenated phase of the phantom, note the dip at 760 nm corresponding to strong HHb absorption. The change of the spectral shape throughout several cycles of the phantom measurement is shown in Figure 8.2, which follows counts at 763 nm where absorption with HHb dominates, hence an increase in counts is observed when the oxygenation of the phantom increases. The intensity plot does not show the beginning of the measurement where blood and yeast were added to the mixture. The sections highlighted in red show when oxygen was being added into the mixture; oxygenation plateaued for a few minutes following the oxygenation before yeast started consuming the oxygen.

Note that throughout this chapter, even though the CCD of CYRIL was calibrated to 704–911 nm, spectra are shown from 710–900 nm and data is also analysed in that range. This is because the output of the light source peaks at $\sim$ 760 nm and the count rate is much lower at the edges of the spectral range; there are no spectral features of interest (HHb, HbO_2, water) in the excluded wavelengths. Attenuation and reflectance at two different stages of the phantom cycle are shown in Figure 8.3, calculated using the reference spectra.

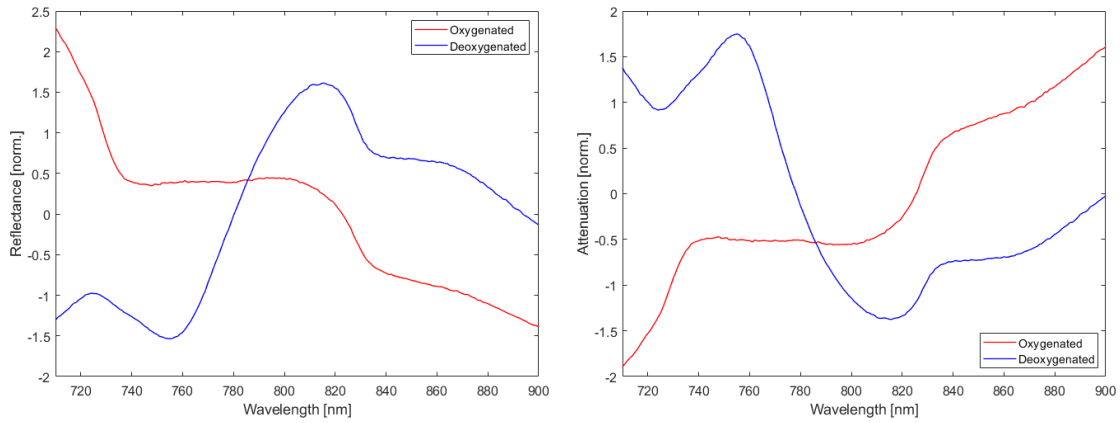

(a) Reflectance **(b)** Attenuation

Figure 8.3: Reflectance and attenuation collected at 20 mm SDS during complete oxygenation and deoxygenation of the homogeneous phantom. Both quantities were normalised with the MATLAB function *normalize*.

Oxygenation measured with the MAESTROS system was used as a reference. Figure 8.4 shows the change in StO_2 during the four oxygenation-deoxygenation cycles compared to counts measured with CYRIL. The synchronisation of both systems was performed manually by starting data collection in both systems simultaneously.

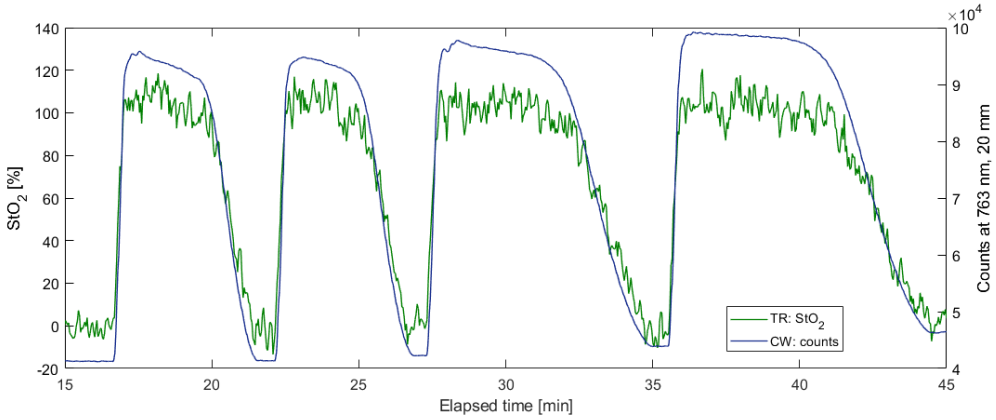

Figure 8.4: The oxygenation of the homogeneous phantom measured with the TR system MAESTROS compared to CYRIL counts at 763 nm during 4 phantom cycles.

8.3.1.1 Slope calculation & differentiation

The algorithms to calculate StO_2 used either spectral derivatives of the reflectance (BF) or the slope of attenuation against distance (SRS and BRUNO).

Reflectance differentiated with respect to wavelength is shown in Figure 8.5, the reflectance spectra were smoothed with a 5-step averaging filter *smooth* in MATLAB before differentiation.

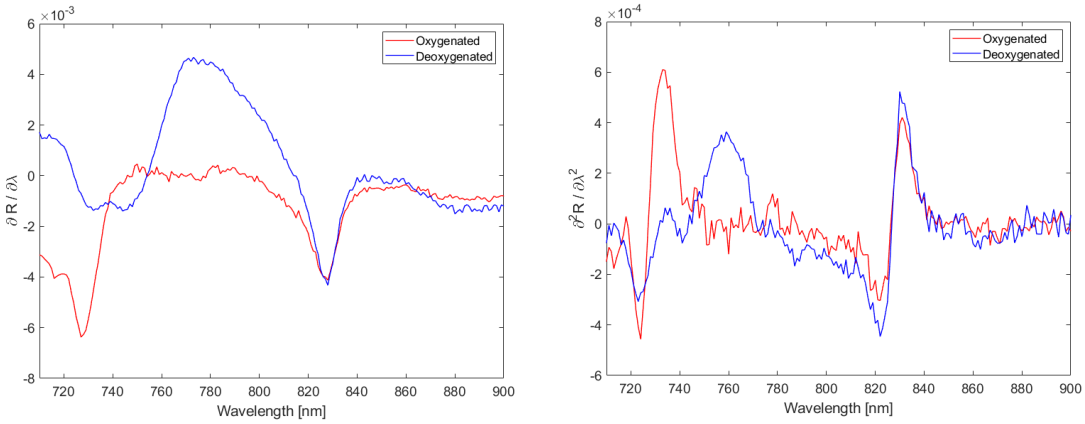

(a) $\frac{\partial R}{\partial \lambda}$ **(b)** $\frac{\partial^2 R}{\partial \lambda^2}$

Figure 8.5: The first and second spectral derivatives of reflectance during complete oxygenation and deoxygenation of the homogeneous phantom at 30 mm.

The linearity of the increase of attenuation with distance was assessed at three wavelengths; 750 nm, 800 nm and 850 nm by finding R^2. The increase of attenuation with distance remained linear throughout the whole measurement with $R^2_{750} = 0.98$, $R^2_{800} = 0.99$ and $R^2_{850} = 0.99$. High linearity of the change of attenuation over distance indicated that the medium was homogeneous. In the case of heterogeneity in the path, the change in optical properties would affect the increase

in attenuation at the affected separation.

$\frac{\partial A}{\partial \rho}$ was calculated across all four detectors. The data were smoothed with a 5-step averaging filter before differentiation. The slopes collected in an oxygenated and deoxygenated phantom and their corresponding spectral derivatives are shown in Figure 8.6.

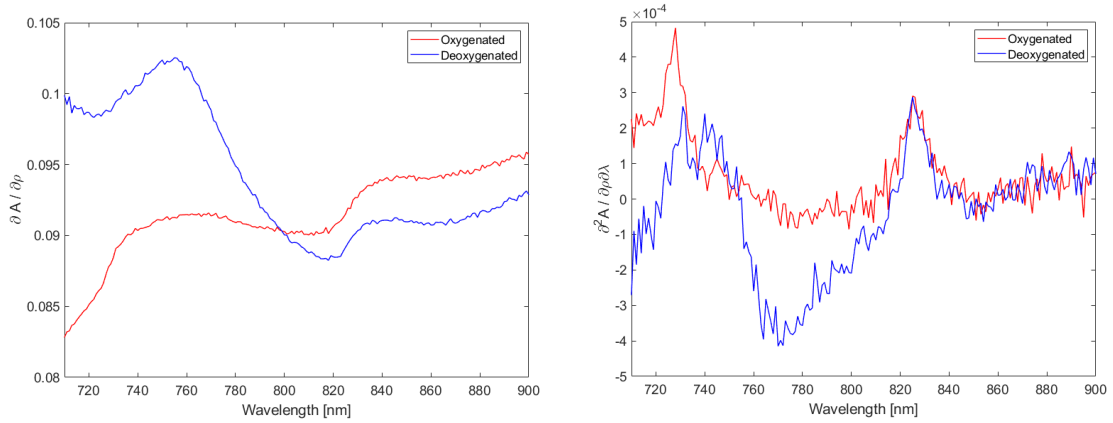

(a) $\frac{\partial A}{\partial \rho}$ **(b)** $\frac{\partial^2 A}{\partial \rho \partial \lambda}$

Figure 8.6: The attenuation slope and the derivative of the attenuation slope with respect to wavelength during complete oxygenation and deoxygenation of the homogeneous phantom.

8.3.2 Two-layer phantom data preparation

Analogously to the homogeneous phantom; data were collected at 15–30 mm SDS in the two-layer phantom. The data analysis followed the same steps as before. The only difference was in the binning of the data. At the time of the two-layer study (July 2018), the data acquisition based on capturing the whole CCD was not yet used and spectra were summed during CCD data readout. The spectra were summed according to the binning selected during the measurement setup. (In the homogeneous phantom, in January 2019, the whole CCD readout data processing was already applied. The two data acquisition methods are described in detail in section 5.1.2.3.)

Due to the two-layer nature of the phantom, the sensitivity of the measurement to the liquid part of the phantom increased with SDS; higher SDS improved the visibility of haemoglobin spectral features. Figure 8.7 shows the difference between spectra collected during oxygenation and deoxygenation of the phantom at 15 and 30 mm SDS; the deoxyhaemoglobin absorption feature at 760 nm is more pronounced at 30 mm SDS.

SDS also affected attenuation, Figure 8.8, and reflectance, Figure 8.9. The data collected at 15 mm were noisier than in the homogeneous phantom. Decreased SNR at short separations, 15 mm, was not observed in the homogeneous phantom data. The difference is caused by the

two CCD readout methods used; whole CCD readout (homogeneous phantom) or binned CCD readout (two-layer phantom). The two-layer phantom measurement had very narrow binning at 15 mm SDS not to saturate the CCD. The bin width remained the same for reference measurement, where care has to be taken not to saturate the CCD at the furthest SDS with the widest bins. As all detectors were illuminated equally during the reference measurement, the signal intensity was much lower with narrow bins, hence the decrease of SNR when calculating attenuation and reflectance at 15 mm SDS.

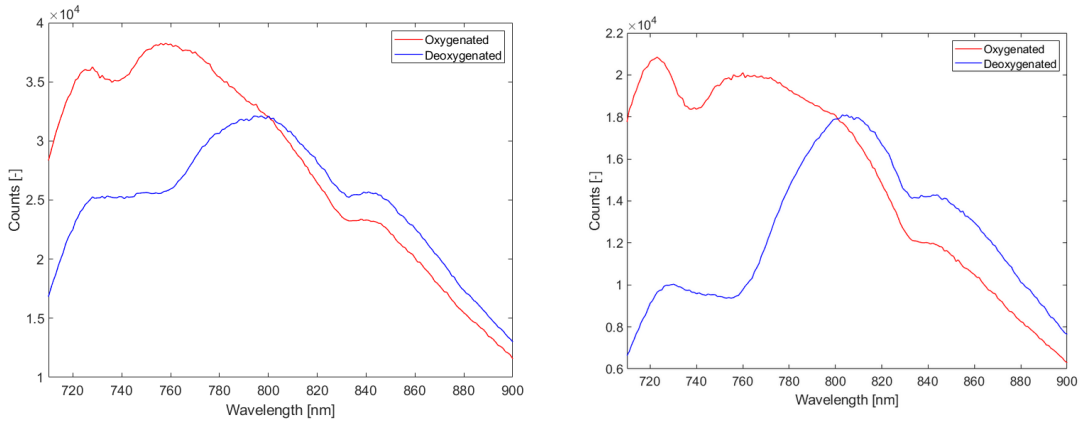

(a) 15 mm SDS **(b)** 30 mm SDS

Figure 8.7: Spectra collected in a two-layer phantom at 15 and 30 mm SDS during phantom oxygenation and deoxygenation.

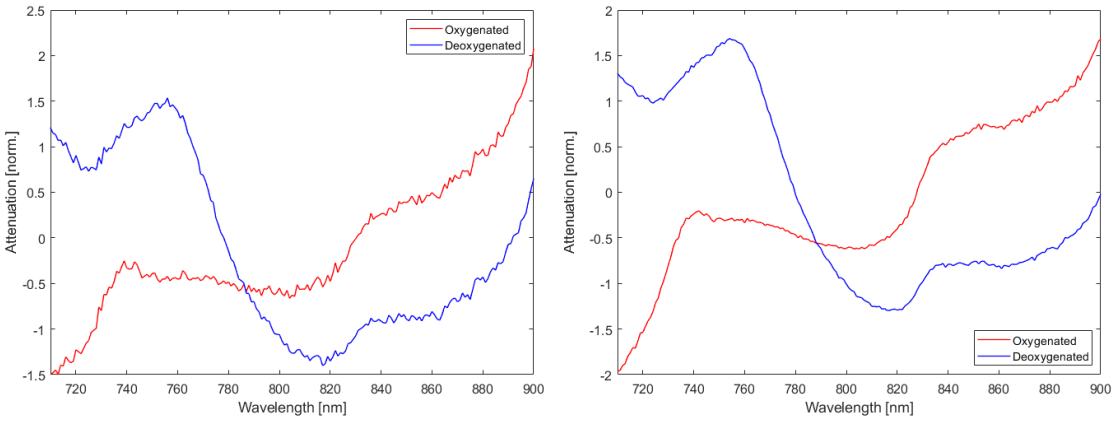

(a) 15 mm SDS **(b)** 30 mm SDS

Figure 8.8: Attenuation collected at 15 and 30 mm SDS during complete oxygenation and deoxygenation of the two-layer phantom. The quantities were normalised with the MATLAB function *normalize*.

MAESTROS was used simultaneously with CYRIL and measured StO_2, Figure 8.10 shows the change of counts at 20 mm measured with CYRIL at 763 nm and the change of MAESTROS-

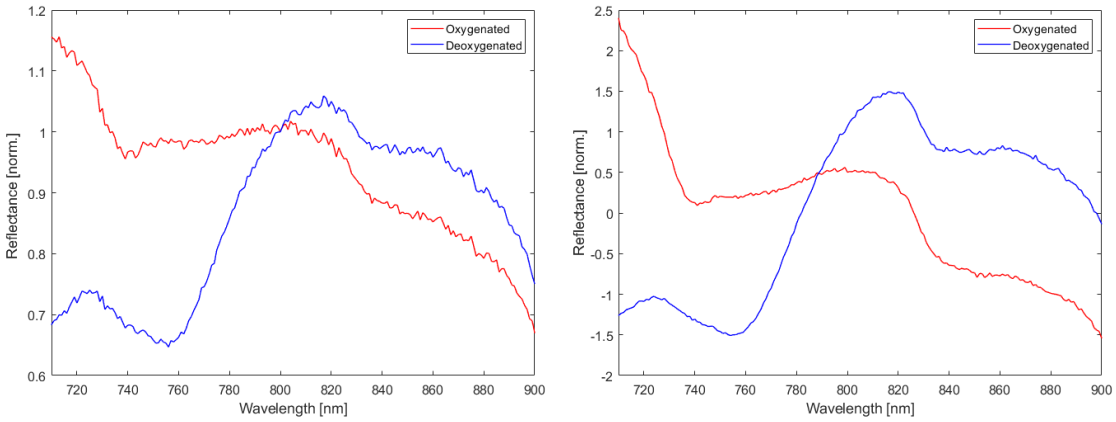

(a) 15 mm SDS **(b)** 30 mm SDS

Figure 8.9: Reflectance collected at 15 and 30 mm SDS during complete oxygenation and deoxygenation of the two-layer phantom. The quantities were normalised with the MATLAB function *normalize*.

measured StO_2 throughout two deoxygenation/oxygenation cycles.

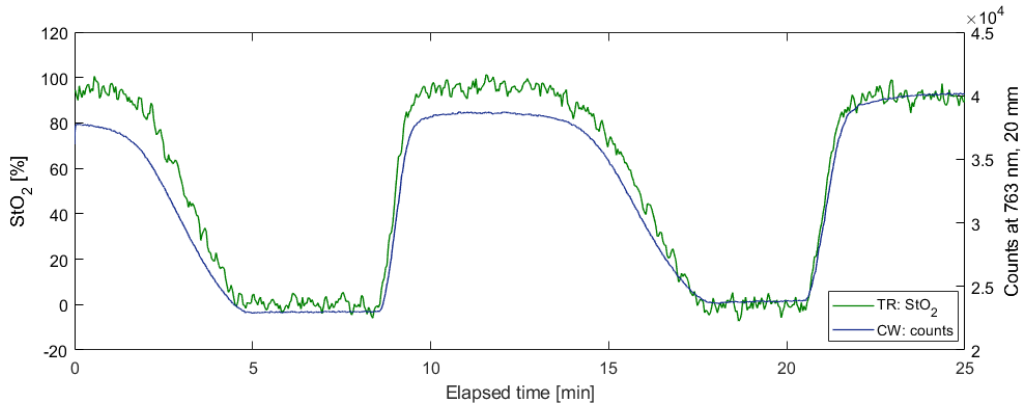

Figure 8.10: The oxygenation of the two-layer phantom measured with the TR system MAESTROS compared to CYRIL counts at 763 nm during 2 phantom deoxygenation cycles.

8.3.2.1 Slope calculation & differentiation

The decrease of attenuation with distance was linear with an average $R^2_{750} = 0.98$, $R^2_{800} = 0.99$ and $R^2_{850} = 0.98$, not different from the homogeneous phantom. The presence of heterogeneity was barely reflected in the slope as the contribution of the superficial layer was equal at all SDS. $\frac{\partial A}{\partial \rho}$ and its derivative with respect to wavelength in the two-layer phantom are shown in Figure 8.11. Compared to the homogeneous phantom, Figure 8.6, the spectral feature at 730 nm is less obvious.

The first and second spectral derivatives of reflectance at 30 mm are shown in Figure 8.12 and look very similar to the reflectance spectra in the homogeneous phantom, Figure 8.5, as the impact of the thin layer absorption was negligible at 30 mm SDS and the detector collected signal mainly from the liquid part of the phantom.

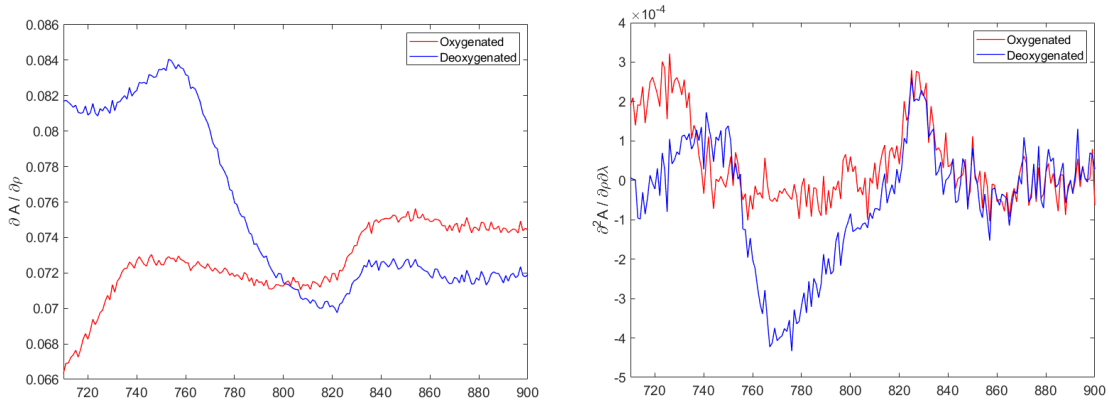

(a) $\frac{\partial A}{\partial \rho}$ **(b)** $\frac{\partial^2 A}{\partial \rho \partial \lambda}$

Figure 8.11: The attenuation slope and the derivative of the attenuation slope with respect to wavelength during complete oxygenation and deoxygenation of the two-layer phantom.

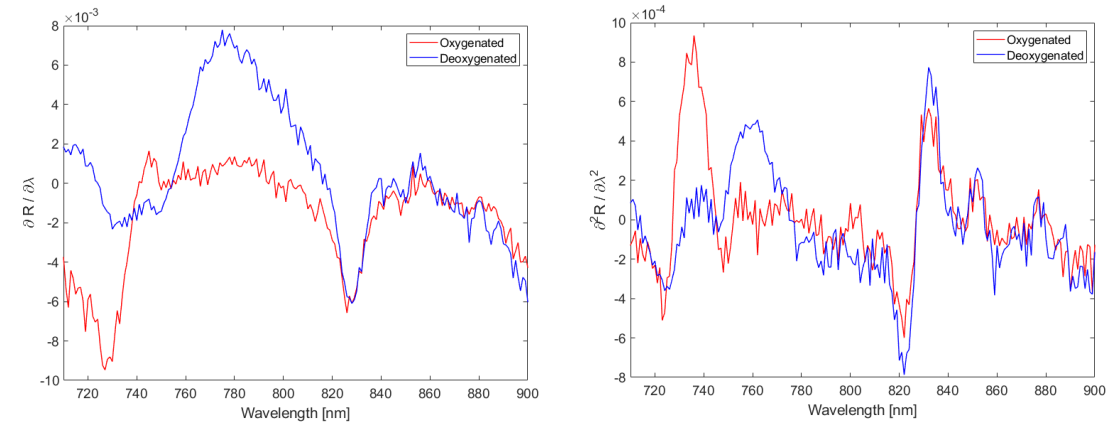

(a) $\frac{\partial R}{\partial \lambda}$ **(b)** $\frac{\partial^2 R}{\partial \lambda^2}$

Figure 8.12: The first and second spectral derivatives of reflectance during complete oxygenation and deoxygenation of the two-layer phantom at 30 mm.

The phantom data will be further explored later in this chapter: it will be used for the demonstration of the performance throughout the development of BRUNO and it will be analysed with BF and SRS to compare their performance to BRUNO.

The boundary conditions in Table 8.2 will be used for BF and BRUNO analysis of both data sets. The optical properties were set from MAESTROS results and the concentration of water in the phantom recipes.

Table 8.2: Boundary conditions for analysing phantom data with BRUNO.

	WF [%]	**c_{HHb} [μM]**	**c_{HbO_2} [μM]**	**a [mm$^{-1}\mu$ m^{-1}]**	**b [-]**
Start	100	20	20	1	3
LB	97	0	0	0	0
UB	100	40	40	2	4

8.4 Model selection

The first step of developing BRUNO was the selection of a model of light transport in tissue. As mentioned in section 3.4, different models can be used to approximate the behaviour of light in tissue. The description of the neonatal head as a homogeneous slab model is sufficient; a difference, however, lies in the selection of boundary conditions when solving the diffusion equation, as they led to different models of reflectance R. In this application, the choice is between using zero boundary conditions reflectance, R_{ZBC}, (used in SRS) or the reflectance obtained with extrapolated boundary conditions, R_{EBC} (used in BF). Once a reflectance model is defined, the model of the slope of attenuation against distance is obtained from R using the relation

$$\frac{\partial A}{\partial \rho} = -\frac{\partial}{\partial \rho}\big(\log_{10}(R(\rho)\big). \tag{8.3}$$

In the following section, different solutions to the diffusion equation will be examined in order to find a suitable model of the slope of light attenuation for the new algorithm BRUNO. The requirements for the model were that it should lead to accurate results at speeds suitable for real-time execution.

8.4.1 ZBC model

The solution to the diffusion equation with zero boundary conditions is

$$R_{ZBC}(\rho) = \frac{z_0}{2\pi r_1^2}\Big(\frac{1}{r_1} + \mu_{eff}\Big) exp\big(-\mu_{eff} r_1\big), \tag{8.4}$$

where $r_1^2 = z_0^2 + \rho^2$ and μ_{eff} is the effective attenuation coefficient when scattering is much stronger than absorption $\mu_a \ll \mu_s'$: $\mu_{eff} = \sqrt{3\mu_a\mu_s'}$. Assuming large detector spacing, $\rho^2 \gg z_0^2$, $z_0/\rho \approx 0$, leads to

$$R_{ZBC}(\rho) = z_0\mu_{eff}\frac{\exp(-\mu_{eff}\rho)}{2\pi\rho^2}. \tag{8.5}$$

The assumption of $\mu_a \ll \mu_s'$ was not utilised in the definition of μ_{eff} of BF, section 3.4.5, but can be found in the derivation of SRS equations and is typically valid in tissue [109].

Attenuation A_{ZBC} is then equal to

$$A = -\log_{10}(R_{ZBC}) = -\frac{\ln(R_{ZBC})}{\ln 10} = \frac{1}{\ln 10}\left[(\mu_{eff}\rho) + 2\ln\rho - \ln\frac{z_0\mu_{eff}}{2\pi}\right]. \tag{8.6}$$

If the detectors measuring the attenuation are close together with respect to the distance from the source ρ, $\frac{\partial A}{\partial \rho}$ is obtained by differentiation:

$$\frac{\partial A_{ZBC,C}}{\partial \rho} = \frac{1}{\ln 10}\left(\sqrt{3\mu_a\mu_s'} + \frac{2}{\rho}\right), \tag{8.7}$$

where $A_{ZBC,C}$ stands for the attenuation measured at close separation between detectors relative to ρ.

However, CYRIL can use a light source-detector set up where the closest detector is 15 mm far from the light source and the furthest detector 30 mm, hence, the assumption of small inter-detector spacing (close, C) no longer applies. In that case, the slope of attenuation is approximated by evaluating $\frac{\partial A}{\partial \rho}$ at the long distance, d_L, and the short distance, d_S [251]:

$$\frac{\partial A_{ZBC,F}}{\partial \rho} = \frac{A(d_L) - A(d_S)}{d_L - d_s} = \frac{1}{\ln 10}\left(\sqrt{3\mu_a\mu_s'} + \frac{2\ln\frac{d_L}{d_S}}{d_L - d_S}\right), \tag{8.8}$$

where $A_{ZBC,F}$ stands for the attenuation measured at far separation between detectors relative to ρ, (far, F).

8.4.2 EBC model

Solutions to the diffusion equation with EBC are a more precise approximation of light transport in tissue than those with ZBC. The reflectance obtained with EBC is

$$R_{EBC}(\rho) = \frac{1}{4\pi}\left[z_0\left(\mu_{eff} + \frac{1}{r_1}\right)\frac{\exp(-\mu_{eff}r_1)}{r_1^2} + (z_0 + 2z_b)\left(\mu_{eff} + \frac{1}{r_2}\right)\frac{\exp(-\mu_{eff}r_2)}{r_2^2}\right], \tag{8.9}$$

where $D = \frac{1}{\mu_a + \mu_s'}$ is the diffusion coefficient and the effective attenuation coefficient is given by $\mu_{eff} = \sqrt{3\mu_a\mu_s'}$. It is also assumed that $z_0^2 \ll \rho^2$, hence $r_1^2 = \rho^2$ and $r_2^2 = (z_0 + 2z_b)^2 + \rho^2$. For biological tissue, z_b is given by [134]:

$$z_b = \frac{1 + 0.493}{1 - 0.493}2D. \tag{8.10}$$

Attenuation A_{EBC} can be obtained from R_{EBC} in the same manner as shown in Eq. 8.6, and two different models of the slope of light attenuation can be calculated for detector spacing smaller than ρ, $\frac{\partial A_{EBC,C}}{\partial \rho}$, and detector spacing similar to ρ, $\frac{\partial A_{EBC,F}}{\partial \rho}$. The derivation of A_{EBC} and the slope models from R_{EBC} was performed in MATLAB. In total, 4 different models of the attenuation slope were tested: $\frac{\partial A_{ZBC,C}}{\partial \rho}$, $\frac{\partial A_{ZBC,F}}{\partial \rho}$, $\frac{\partial A_{EBC,C}}{\partial \rho}$ and $\frac{\partial A_{EBC,F}}{\partial \rho}$.

The optical properties of GM, as used in NIRFAST mesh model B (homogeneous with water absorption, described in Table 5.3) were used in the analysis.

8.4.3 Impact of light source-detector separation

The first assessed attenuation slope model aspect was the impact of SDS. Figure 8.13a shows the 4 different attenuation slope models evaluated at different SDS. The decrease of the separation between the detectors made the model $\frac{\partial A_F}{\partial \rho}$ identical to $\frac{\partial A_C}{\partial \rho}$ both for ZBC and EBC. The difference between EBC and ZBC models increased at short SDS because the EBC models were better at approximating behaviour of light closer to the light source.

As the proposed algorithm should fit the model to the data in the spectral derivative space, the behaviour of the differentiated models $\frac{\partial^2 A}{\partial \lambda \partial \rho}$ was investigated; they are shown in Figure 8.13b. All 3 ZBC models are overlapping because the distance terms in Eq. (8.6) and (8.7) are independent of wavelength. On the other hand, the spectral derivatives of $\frac{\partial A_{EBC}}{\partial \rho}$ do not overlap, because distance ρ is included in the r_1 and r_2 terms in Eq. (8.9) and these are not removed through differentiation.

As the spectral derivatives of $\frac{\partial A_{ZBC,C}}{\partial \rho}$ and $\frac{\partial A_{ZBC,F}}{\partial \rho}$ are identical; both models are the same when used to calculate StO_2. Hence, only one model will be investigated further in this section, $\frac{\partial A_{ZBC,C}}{\partial \rho}$, and will be compared to both versions of the $\frac{\partial A_{EBC}}{\partial \rho}$ models.

The independence of $\frac{\partial A_{ZBC}}{\partial \rho}$ can be beneficial when applied to NIRS data, as, due to the curvature of the neonatal head, the input SDS (SDS set in the probe holder) can be different than the "real" separation between the detectors. A mismatch could decrease the accuracy of $\frac{\partial A_{EBC}}{\partial \rho}$ model's prediction. The effect of head curvature on slope models was not explored in this work.

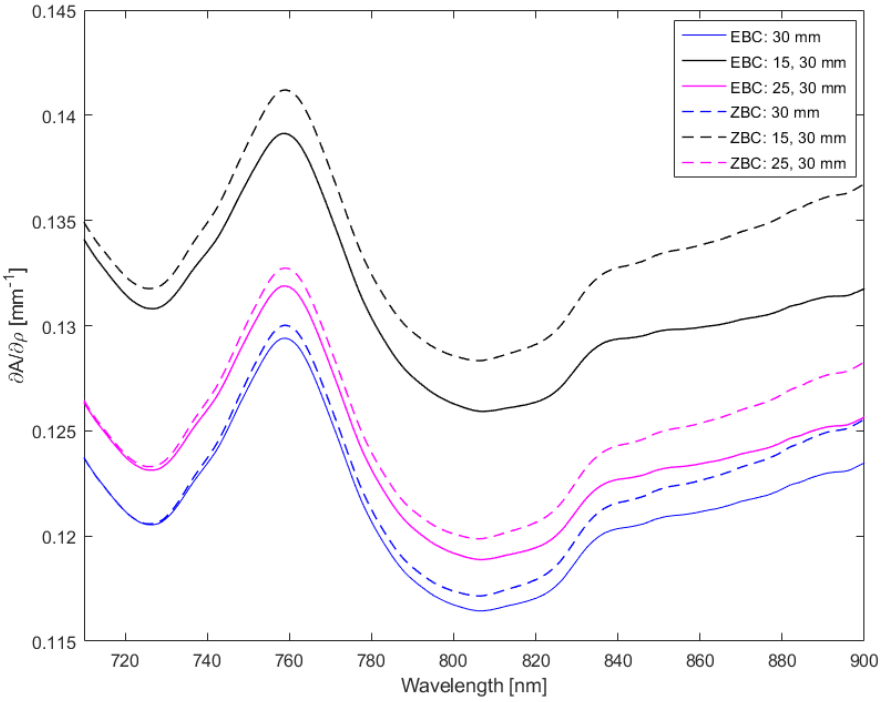

(a) Different $\frac{\partial A}{\partial \rho}$ models evaluated at different ρ, resp. d_L, d_S.

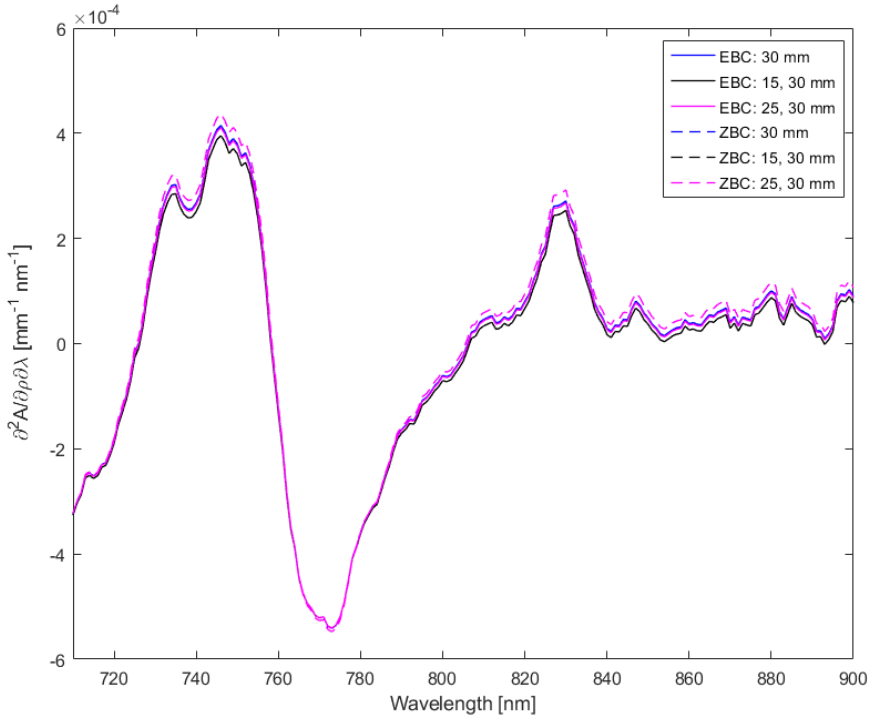

(b) Different $\frac{\partial^2 A}{\partial \rho \partial \lambda}$ models evaluated at different ρ, resp. d_L, d_S. All ZBC models are overlapping.

Figure 8.13: Comparison of the slope of attenuation obtained with models utilising EBC or ZBC. The models are evaluated with optical properties of grey matter. For ZBC, $\frac{\partial A_{ZBC,C}}{\partial \rho}$ was evaluated at 30 mm and $\frac{\partial A_{ZBC,F}}{\partial \rho}$ was evaluated at 15, 30 mm and 25, 30 mm. For EBC, $\frac{\partial A_{EBC,C}}{\partial \rho}$ was evaluated at 30 mm and $\frac{\partial A_{EBC,F}}{\partial \rho}$ was evaluated at 15, 30 mm and 25, 30 mm.

8.4.4 Scattering & absorption crosstalk

The presence of crosstalk between μ_s' and μ_a was already shown in BF in Chapter 7. As the source of crosstalk is the dependence of reflectance on μ_{eff}, it is also expected to be present when recovering StO_2 from $\frac{\partial A_{ZBC}}{\rho}$ or $\frac{\partial A_{EBC}}{\rho}$.

To demonstrate the relationship between μ_s' and μ_a and its effect on StO_2, 81 attenuation slope models were generated for $\frac{\partial A_{ZBC}}{\rho}$, $\frac{\partial A_{EBC,C}}{\rho}$ and $\frac{\partial A_{EBC,F}}{\rho}$. The absorption remained the same in all and was based on WF = 80%, c_{HHb} = 29.5 and c_{HbO_2} = 55μM, StO_2 = 65.1%. The scattering parameters a and b were different in each of the 81 models. 9 different values of a were used, 0.26–0.77 mm$^{-1}\mu$m^{-1}, and 9 values of b, 0.87–2.61. The used μ_s' are shown in Figure 7.3. The generated models were used as input data for BRUNO and only μ_a was recovered. The optimisation routine *fminsearchbnd* was used in BRUNO.

Figure 8.14 shows how StO_2 changed with the selection of amplitude a and power b for $\frac{\partial A_{ZBC}}{\rho}$ and $\frac{\partial A_{EBC,F}}{\rho}$ (the result was identical to $\frac{\partial A_{EBC,C}}{\rho}$). The black dots indicate the true value of StO_2; the recovered values diverged from the truth with increased mismatch of the amplitude a, but remained quite stable for different b, highlighting a weaker effect of b on StO_2.

$\frac{\partial A_{ZBC}}{\partial \rho}$ and $\frac{\partial A_{EBC}}{\partial \rho}$ followed the same trend of dependence of StO_2 on a and b, however, the range of StO_2 was narrower for $\frac{\partial A_{ZBC}}{\partial \rho}$; suggesting that the crosstalk between scattering and absorption was weaker. This is likely due to the increased complexity of $\frac{\partial A_{EBC}}{\partial \rho}$ compared to $\frac{\partial A_{ZBC}}{\partial \rho}$.

These results suggest that crosstalk between μ_s' and μ_a does not automatically prevent the recovery of an accurate StO_2 but it can lead to errors when looking for the individual fitting parameters. Similar findings were observed when investigating crosstalk in BF. The offset from the truth caused by incorrect scattering was smaller for the $\frac{\partial A_{ZBC}}{\partial \rho}$ than for $\frac{\partial A_{EBC}}{\partial \rho}$.

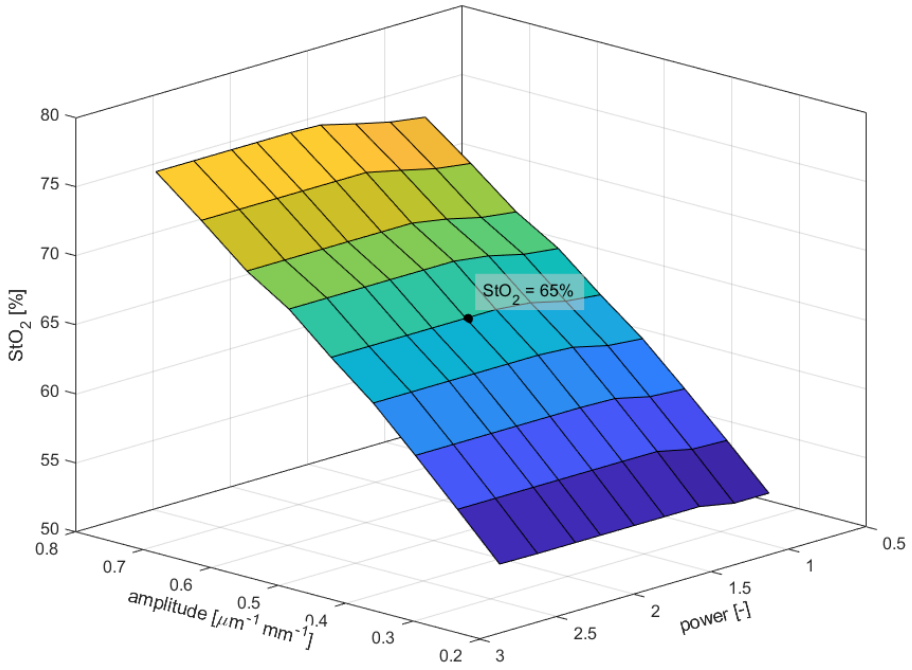

(a) ZBC

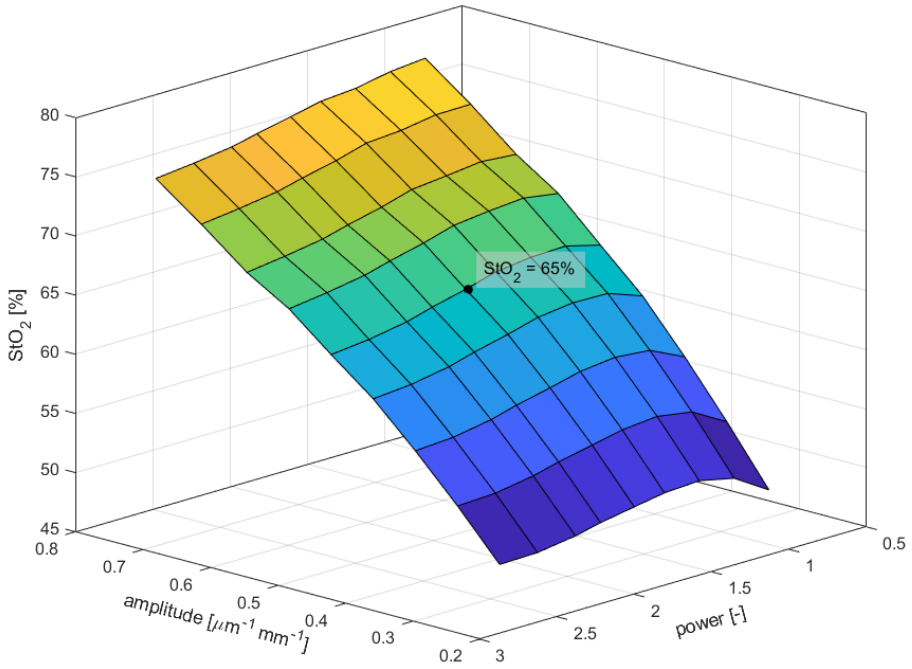

(b) EBC, F

Figure 8.14: StO_2 recovered with BRUNO using $\frac{\partial A_{ZBC}}{\partial \rho}$ or $\frac{\partial A_{EBC,F}}{\partial \rho}$ while scattering parameters a, amplitude, and b, power, were fixed at constant values.

8.4.5 Model performance

8.4.5.1 NIRFAST data

NIRFAST simulations were used to assess the accuracy of BRUNO and the computational requirements. As the aim of this work was to develop a real-time algorithm; a complicated model could bear a significant computational burden and make real-time measurements impossible.

Spectra simulated with NIRFAST were analysed with the 3 different attenuation slope models; $\frac{\partial A_{ZBC}}{\partial \rho}$, $\frac{\partial A_{EBC,C}}{\partial \rho}$ and $\frac{\partial A_{EBC,F}}{\partial \rho}$. The NIRFAST simulated spectra obtained in model E, step-wise desaturations of brain tissue (Table 5.4), were used for the comparison, as the set included 50 spectra with different, but known, optical properties.

Table 8.3 shows the StO_2 values recovered with $\frac{\partial A_{ZBC}}{\rho}$ and $\frac{\partial A_{EBC}}{\rho}$. The fitting was performed for the homogeneous and heterogeneous models over 710–900 nm in the first spectral derivative space with $fminsearchbnd$. To demonstrate the effect of noise on the performance of BRUNO, 1% amplitude random noise was added to the spectra from the homogeneous model.

StO_2 was recovered with high accuracy in both homogeneous models, adding noise increased the computational burden and standard deviation of StO_2, particularly in the last step at true StO_2 = 50%. Using BRUNO to recover measurements in two-layer NIRFAST models showed high sensitivity to the brain signal and all three slope models recovered StO_2 with high accuracy. The error of the measurement increased with the increase of the difference between the oxygenation of the brain and ECT layers.

The main difference between the models was the speed, ZBC was the fastest model in all three cases.

8.4.5.2 Phantom data

Phantom data are more challenging than NIRFAST simulations and represent a more realistic NIRS measurement scenario. The absolute truth was not known, so MAESTROS was used as the gold standard.

Table 8.3: Mean StO_2 (standard deviation) recovered from spectra acquired in model E, homogeneous with and without 1% amplitude noise added and in model E, heterogeneous. The used models were $\frac{\partial A_{ZBC}}{\partial \rho}$ and $\frac{\partial A_{EBC}}{\partial \rho}$. The duration was measured as the time it took to perform least-squares fitting on all 50 spectra. Standard deviation rounded to one decimal place is in brackets. For the heterogeneous, the true oxygenation in the brain layer is reported, ECT layer was 80% in all steps.

	StO_2 [%]		
Truth	**EBC, C**	**EBC, F**	**ZBC**
	Homogeneous model		
90.0	89.9 (0.1)	90.0(0.1)	89.8 (0.0)
80.0	79.9 (0.0)	79.9 (0.0)	79.8 (0.0)
70.0	69.9 (0.1)	70.0 (0.3)	69.8 (0.0)
60.0	60.0 (0.1)	60.1 (0.3)	59.9 (0.0)
50.0	50.3 (0.1)	50.4 (0.3)	50.2 (0.0)
Duration [s]	28.4	18.9	6.1
Truth	**Homogeneous model with noise**		
90.0	89.8 (0.5)	89.8 (0.5)	89.7 (0.5)
80.0	80.4 (1.0)	80.4 (1.0)	80.3 (1.0)
70.0	70.0 (0.9)	69.9 (0.9)	69.8 (0.9)
60.0	60.0 (0.9)	60.0 (0.9)	59.9 (0.9)
50.0	50.6 (2.7)	50.6 (2.7)	50.5 (2.7)
Duration [s]	242.2	182.8	153.0
Truth	**Heterogeneous model**		
90.0	89.4 (0.0)	89.5 (0.0)	89.4 (0.1)
80.0	80.2 (0.0)	80.2 (0.0)	80.2 (0.0)
70.0	71.2 (0.1)	71.1 (0.1)	71.1 (0.0)
60.0	62.2 (0.1)	62.1 (0.1)	62.1 (0.1)
50.0	53.1 (0.2)	53.1 (0.2)	53.0 (0.1)
Duration [s]	31.0	25.1	6.6

Homogeneous phantom

Data collected in the homogeneous phantom was analysed with BRUNO with 3 different attenuation slope models: $\frac{\partial A_{ZBC_C}}{\partial \rho}$; $\frac{\partial A_{EBC_C}}{\partial \rho}$ and $\frac{\partial A_{EBC_F}}{\partial \rho}$. The analysis was performed over 710–900 nm with *fminsearchbnd*.

Figure 8.15 shows BRUNO applied to homogeneous phantom spectra at three different points of the oxygenation cycle; at maximal and minimal oxygenation and at halfway deoxygenation, which was selected as the middle point between the counts at maximal and minimal oxygenation.

The BRUNO fit changed depending on the oxygenation; one of the main spectral features observable is the 830 nm water peak, which does not change during the cycle. The oxygenation state changes the features at 720–800 nm. A slight offset is visible between the peak of the models at 731 nm and the data peak at 728 nm in all three figures. This offset is within the resolution of CYRIL's CCD, which is around 4 nm, and is explained in section 5.1.2.2.

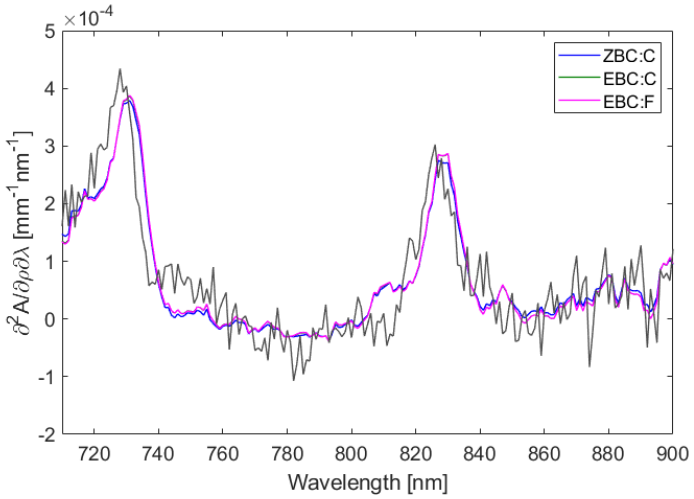

(a) Oxygenated phantom

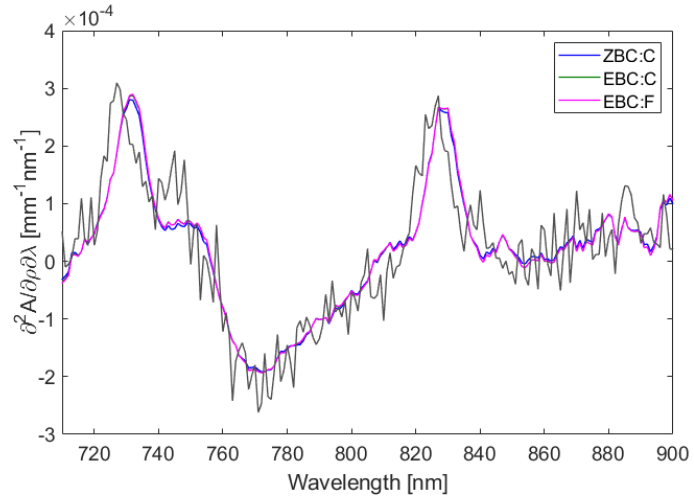

(b) Mid-deoxygenation

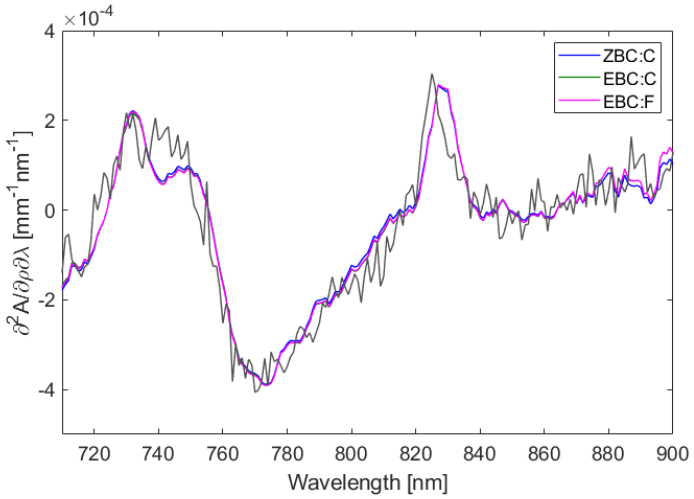

(c) Deoxygenated phantom

Figure 8.15: The comparison of different light transport models when applied in BRUNO to $\frac{\partial A}{\partial \rho}$ collected the homogeneous phantom during different parts of the oxygenation cycle.

Both $\frac{\partial A_{EBC}}{\partial \rho}$ models overlapped, even though they had a different ρ dependence. However, they did not lead to the same results, as shown in Figure 8.16, where the results are compared to the MAESTROS StO_2 reference measurement. The displayed data were smoothed with a 5-point averaging filter. Several conclusions can be drawn from Figure 8.16:

- All models recovered a smooth StO_2 response that follows the oxygenation trend. The saturation at 100% is flat because of the boundary conditions; c_{HHb} converged to 0 μM.
- The biggest differences in the measured StO_2 was when it was below 20%. Such low saturation values however, never occur in the clinical setting - the SafeBoosC clinical trial uses a hypoxic threshold of 55% [207]. The accuracy of the measurement at those points is not a priority.
- $\frac{\partial A_{EBC}}{\partial \rho}$ had a smaller dynamic range causing a delay in the recovery of deoxygenation. While $\frac{\partial A_{ZBC}}{\partial \rho}$ followed the trend of MAESTROS over the whole duration of the measurement; the measurement with $\frac{\partial A_{EBC}}{\partial \rho}$ models was delayed by 30 s during the deoxygenation stages leading to a difference in StO_2 of up to 20%. Even though such rapid changes in StO_2 are unlikely in the clinic, a delayed response is undesirable as hypoxia can lead to damage within a few seconds.

Measuring the duration of BRUNO analysis of all 2368 spectra showed another strong advantage of using $\frac{\partial A_{ZBC}}{\partial \rho}$; similarly to the simulation results, it was much faster. $\frac{\partial A_{ZBC}}{\partial \rho}$ analysis took 65 s, $\frac{\partial A_{EBC_C}}{\partial \rho}$ took 379 s and $\frac{\partial A_{EBC_F}}{\partial \rho}$ took 210 s.

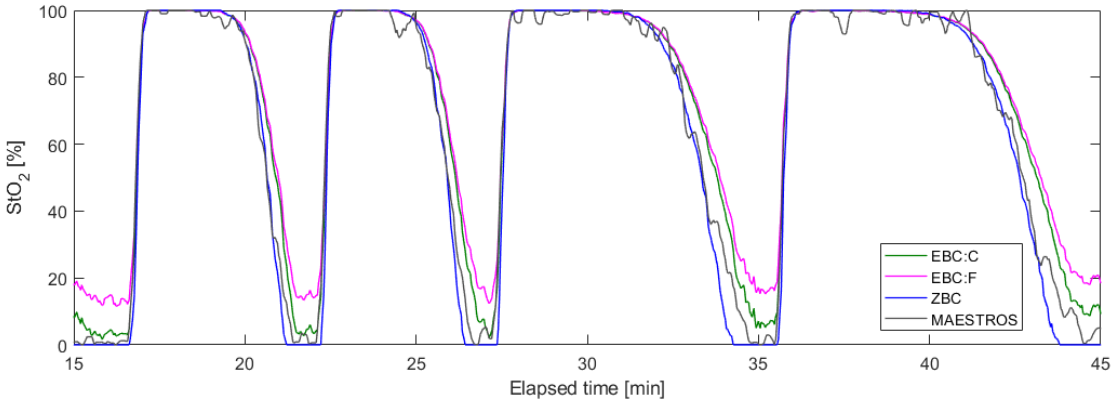

Figure 8.16: StO_2 in the homogeneous phantom measured with MAESTROS compared to BRUNO analysis with 3 different $\frac{\partial A}{\partial \rho}$ models.

Two-layer phantom

The analysis of the NIRFAST and homogeneous phantom data showed that using $\frac{\partial A_{ZBC}}{\partial \rho}$ is faster and leads to better results; the application of BRUNO to the two-layer data was used to assess whether the presence of another layer affects the performance.

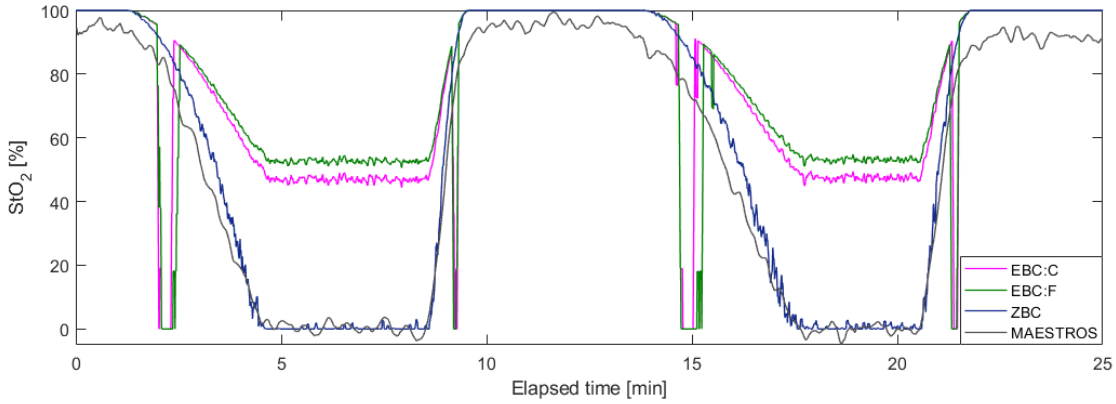

Figure 8.17: StO_2 in the two-layer phantom measured with MAESTROS compared to BRUNO analysis with 3 different $\frac{\partial A}{\partial \rho}$ models.

Figure 8.17 shows StO_2 recovered with the three BRUNO slope models compared to the TR reading in the two-layer phantom; the data were smoothed with a 5-step smoothing filter. The performance of BRUNO was worse than in the homogeneous phantom:

- The StO_2 recovered with $\frac{\partial A_{EBC}}{\partial \rho}$ models included artefacts which visually resemble movement artefacts. However, as these did appear in $\frac{\partial A_{ZBC}}{\partial \rho}$, they were related to the models. Looking at the BRUNO fit before and during the artefact, Figure 8.19, shows what led to the difference in results. Despite the data looking very similar, $\frac{\partial A_{EBC}}{\partial \rho}$ models converged to the wrong solution. The likely reason is the high amount of noise in the data. The increase of noise compared to the homogeneous phantom was not because of the additional layer but because of the data acquisition. More noise was present in the two-layer phantom due to the absence of noise subtraction in the data analysis and fewer collected counts. $\frac{\partial A_{ZBC}}{\partial \rho}$ appeared to be more resistant towards noise.

- The baseline values of $\frac{\partial A_{EBC}}{\partial \rho}$ models were at $\sim$ 60%, compared to the 0% MAESTROS baseline. While $\frac{\partial A_{ZBC}}{\partial \rho}$ and $\frac{\partial A_{EBC}}{\partial \rho}$ fits looked identical, there was a difference in the recovered μ_s' and μ_a, shown in Figure 8.18; $\frac{\partial A_{EBC_F}}{\partial \rho}$ overestimated attenuation.

- While $\frac{\partial A_{ZBC}}{\partial \rho}$ was robust towards the increase of noise, it did not match MAESTROS' reading at high oxygenation. The offset was also visible throughout the deoxygenation. MAE-

STROS found an oxygenation baseline at 96%. Other published work with the same phantom shows the maximal oxygenation in a range $\sim$ 90–100% depending on the instrument used [165]. The difference in the reading between MAESTROS and ZBC BRUNO is not assumed to be due to the addition of the extra layer, as it is very thin and at MAESTROS' 3 cm SDS, its impact should be negligible [271].

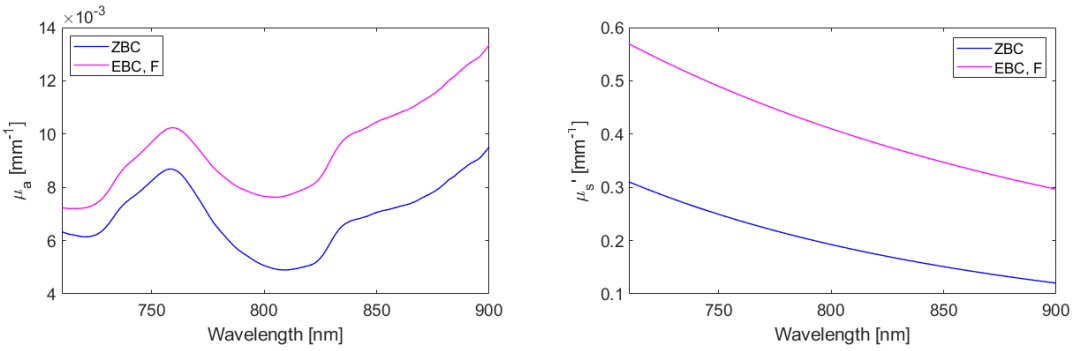

(a) μ_a **(b)** μ_s'

Figure 8.18: The comparison of μ_a and μ_s' recovered with $\frac{\partial A_{ZBC}}{\partial \rho}$ and $\frac{\partial A_{EBC,F}}{\partial \rho}$ at the same point during phantom deoxygenation. StO_2(ZBC) = 0%; StO_2(EBC,F) = 52.5%.

8.4.6 Model selection: conclusion

The use of three different models of the slope of light attenuation in tissue to recover StO_2 with BRUNO was demonstrated. The models were compared based on their accuracy, speed, crosstalk between μ_a and μ_s', the influence of SDS and were also applied to data collected in NIRFAST simulations and phantoms.

Overall, $\frac{\partial A_{ZBC}}{\partial \rho}$ was selected for use, because:

- The first spectral differential of the model is independent of SDS. This is useful because the real distance between the detectors and the light is shorter than the distance designed in the probe holder due to the curvature of the neonatal head.
- The model is more likely to converge to a correct value of StO_2 than $\frac{\partial A_{EBC}}{\partial \rho}$ if incorrect μ_a or μ_s' are recovered.
- While, theoretically, $\frac{\partial A_{EBC}}{\partial \rho}$ are a more precise approximation of light transport than $\frac{\partial A_{ZBC}}{\partial \rho}$, the accuracy of both models demonstrated on NIRFAST spectra (judged on the accuracy of StO_2 recovery) is comparable.
- $\frac{\partial A_{ZBC}}{\partial \rho}$ has lower computational requirements and converges to the solution quicker than other

models. This is important as fast execution is crucial for the design of a real-time measurement algorithm.

- Application to phantom data showed greater agreement between $\frac{\partial A_{ZBC}}{\partial \rho}$ and the MAESTROS reference measurement and also a lower sensitivity to noise than $\frac{\partial A_{EBC}}{\partial \rho}$.

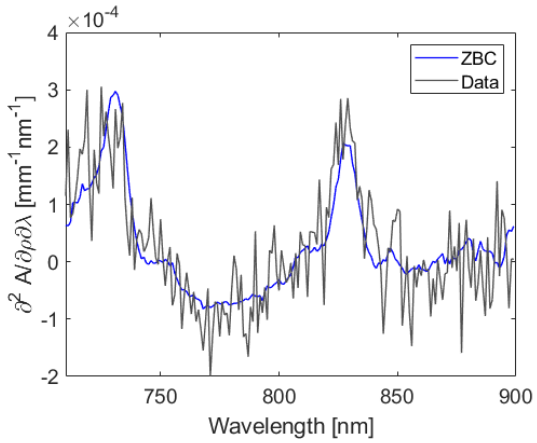

(a) Before artefact: ZBC leading to an StO_2 = 92.7%

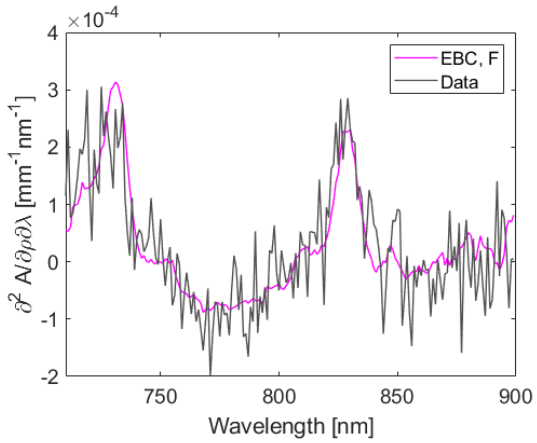

(b) Before artefact: EBC, F leading to an StO_2 = 95.3%.

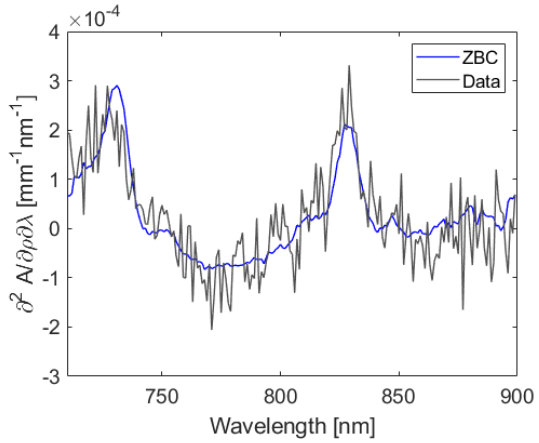

(c) During artefact: ZBC leading to an StO_2 = 91.0%.

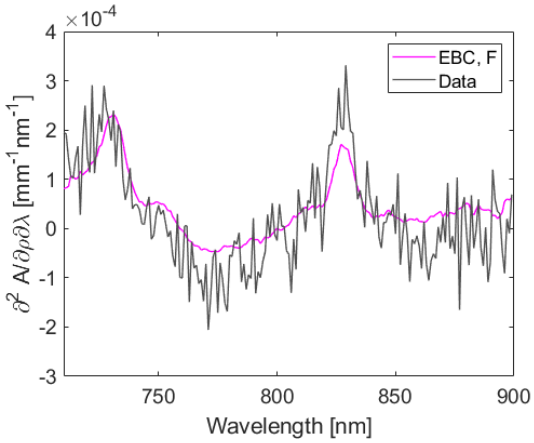

(d) During artefact: EBC, F leading to an StO_2 = 0%.

Figure 8.19: BRUNO with $\frac{\partial A_{ZBC}}{\partial \rho}$ and $\frac{\partial A_{EBC,F}}{\partial \rho}$ before and during a measurement artefact in the two-layer phantom. Note the difference in the closeness of the model fit to the data in figure (c) vs. (d).

8.5 Additional algorithm considerations

The selection of the model of light transport significantly affected the performance of BRUNO. There are other additional algorithm aspects which need to be selected, such as wavelengths, over which the spectrum is fitted, or chromophores.

8.5.1 Wavelength selection

The first constraint on the wavelength selection of BRUNO was the compatibility with the CYRIL 2 wavelength range, 704–911 nm. In this range, the main absorption features include a HHb feature at 760 nm, a 740 nm water feature, and a water feature at 840 nm. These could be targeted in BRUNO similarly to the BF fitting process.

BRUNO uses first spectral derivatives of the slope model as differentiation amplifies spectral features of chromophores in a spectrum which is otherwise quite featureless, Fig. 8.13a. The use of second spectral derivatives was not considered as noise would be the preliminary source of contrast after the attenuation slope calculation and double spectral differentiation.

So far, the least-squares fitting for 5 parameters was performed across the whole spectrum for all wavelengths at the same time. The aim of this section is to investigate whether using only selected sections of the spectrum (similarly to BF) for the fitting of individual chromophores would improve the algorithm performance.

The impact of each parameter on the spectral derivative of the slope model, $\frac{\partial^2 A}{\partial \rho \partial \lambda}$, was assessed, Figure 8.20. Each of the five parameters affected the model in a different manner; this was shown through differentiation: the individual derivatives of $\frac{\partial^2 A}{\partial \rho \partial \lambda}$ with respect to each parameter show how each parameter affects the model across the whole spectrum. The behaviour only across the 704–911 nm wavelength range was studied as it is the wavelength range of CYRIL 2.

The differentiation with respect to each parameter showed that they do affect the spectrum in various patterns, with WF and c_{HHb} having the most distinct spectral features. The WF peaks at 730 and 830 nm correspond to the known WF peaks in the second spectral derivative space of extinction spectra, Figure 7.6 and the large HHb feature at 760 nm is also seen in $\frac{\partial^3 A_{ZBC}}{\partial \rho \partial \lambda \partial c_{HHb}}$. The water and HHb features of $\frac{\partial^2 A}{\partial \rho \partial \lambda}$ were seen before in the phantom spectra in Figure 8.6. While some spectral features of HbO_2 are visible in Figure 8.20c, they overlap with the spectral features of HHb.

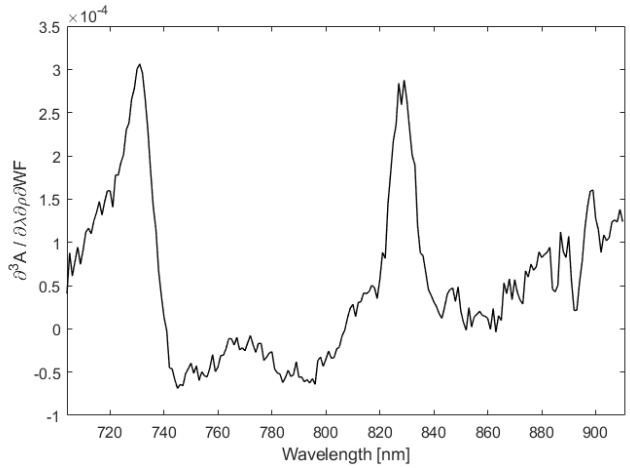

(a) WF

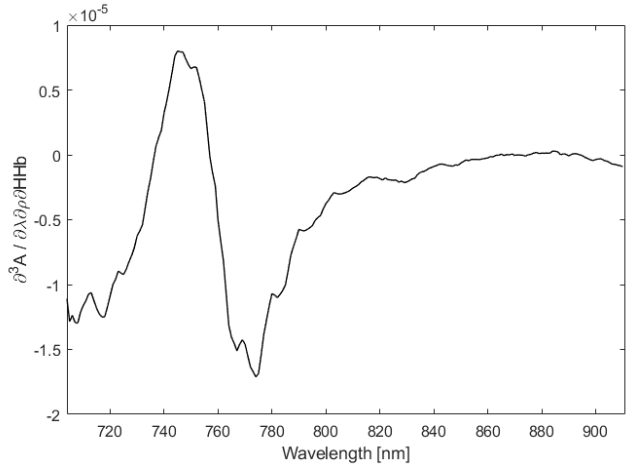

(b) c_{HHb}

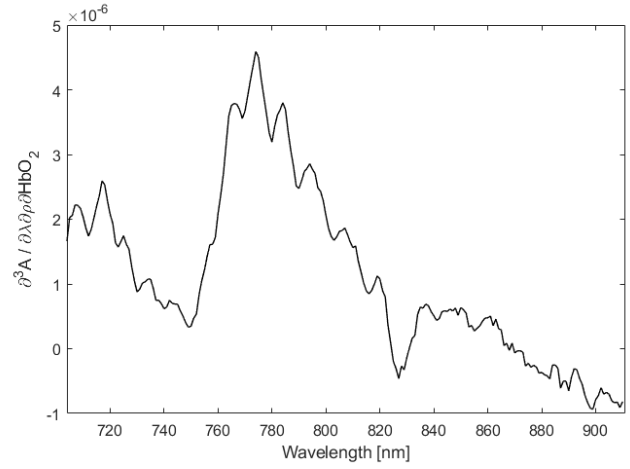

(c) c_{HbO_2}

Figure 8.20: Differentiating $\frac{\partial^2 A_{ZBC}}{\partial \rho \partial \lambda}$ with respect to each parameter. The function is evaluated at $WF = 0.8$, $c_{HHb} = 29.5\ \mu$M, $c_{HbO_2} = 55\ \mu$M, $a = 0.5\ \text{mm}^{-1}\mu\text{M}^{-1}$ and $b = 1.7$.

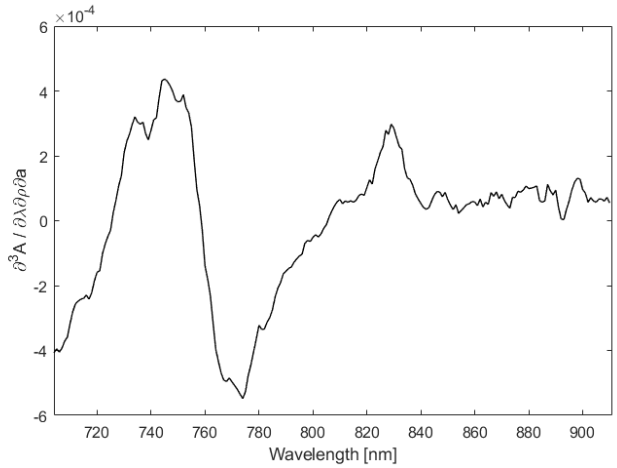

(d) a

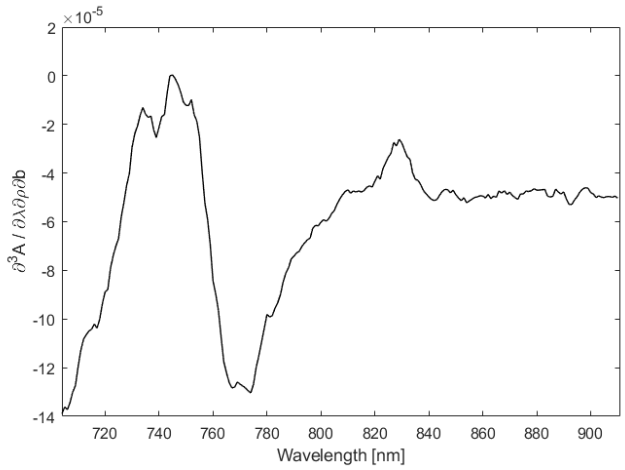

(e) b

Figure 8.20: Differentiating $\frac{\partial^2 A}{\partial \rho \partial \lambda}$ with respect to each parameter (cont.). The function is evaluated at $WF = 0.8$, $c_{HHb} = 29.5$ μM, $c_{HbO_2} = 55$ μM, $a = 0.5$ mm$^{-1}\mu$M^{-1} and $b = 1.7$

The shape of $\frac{\partial^3 A_{ZBC}}{\partial \rho \partial \lambda \partial a}$ and $\frac{\partial^3 A_{ZBC}}{\partial \rho \partial \lambda \partial b}$ is a combination of the spectral features of the three chromophores; scattering acts as an amplifier of those features. The HHb feature at 720–780 nm is particularly prominent in $\frac{\partial^3 A_{ZBC}}{\partial \rho \partial \lambda \partial a}$ and $\frac{\partial^3 A_{ZBC}}{\partial \rho \partial \lambda \partial b}$. This explains the crosstalk; it is unclear whether to attribute a change in μ_{eff} to a higher concentration of a chromophore or to stronger scattering.

Given the significant water absorption feature at 830 nm, it might be beneficial to first fit for the concentration of water, fix WF, and then fit for the rest of the parameters.

NIRFAST simulations

Whether fitting first for WF between 810–850 nm, fixing the recovered parameter and then fitting for the rest of the parameters over the whole spectrum would be beneficial was tested by analysing a spectrum obtained in NIRFAST model B. The recovered StO_2 for BRUNO with only one fitting

step or with two is in Table 8.4.

The recovered StO_2 was identical in both cases. While fitting for water first did increase the duration by a fraction, the recovered parameters are similar. It is noticeable how fitting for water first overcompensated the water concentration compared to an overall fit. In both cases, scattering amplitude was overestimated at the cost of reduced haemoglobin concentrations.

Table 8.4: Fitting spectra from model B with BRUNO either across the whole spectrum at once or with first fitting for WF. WF was fitted for over 810–850 nm, other parameters were recovered across 704–911 nm.

Fitting	**WF** [%]	$\mathbf{c_{HHb}}$ [μM]	$\mathbf{c_{HbO_2}}$ [μM]	$\mathbf{StO_2}$ [%]	**a** [$mm^{-1}\mu m^{-1}$]	**b** [-]	**Duration** [s]
1 step	86.4	13.5	25.0	64.9	0.64	1.79	0.39
2 steps	94.9	14.9	27.5	64.9	0.58	1.79	0.44
Truth	80.0	29.5	55.0	65.1	0.51	1.73	

Homogeneous phantom

The impact of fitting in one step compared to two steps was also assessed in the homogeneous phantom. Figure 8.21 shows that the result was identical and only the computational burden was increased; adding another fitting step increased the duration of the analysis from 64 s to 131 s. Overall, no benefit of splitting the fitting into two stages was found.

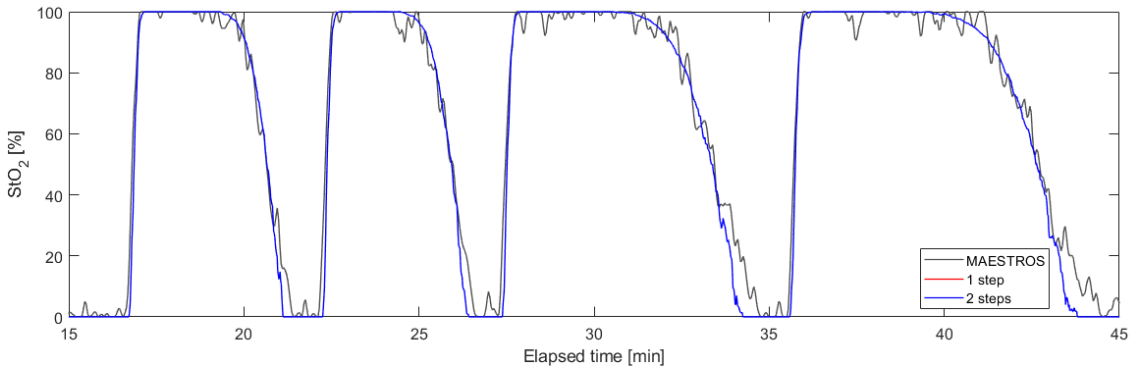

Figure 8.21: The comparison of fitting BRUNO in one or two steps to StO_2 measured with MAESTROS.

8.5.2 Chromophore selection

The absorption in tissue is dominated by water, HHb and HbO_2 and BRUNO is designed to account for the absorption by all three compounds. All three chromophores of interest have their specific spectral features shown in Figure 8.20. Other chromophores, such as melanin, fat or CCO are usually not considered in the calculation of StO_2 as their contribution to the total absorption is much weaker than the absorption by haemoglobin in the wavelength range of interest, 700–900 nm

[104, 141] and can not be accounted for when only a few wavelengths are used.

The absorption by these chromophores is however not zero and when the StO_2 algorithm is set not to account for their contribution to light attenuation, their absorption is attributed to the absorption by HHb or HbO_2, potentially decreasing the accuracy of the measurement. One example of a chromophore with non-negligible absorption is CCO. CCO has been subject to increased interest in the field of NIRS in the recent years and monitoring its concentration changes in the NICU can inform of HIE injury severity [16]. In fact, the instrument used in this work, CYRIL, was specifically designed to monitor CCO concentration changes. The challenge facing absolute measurements of CCO is its low concentration; about one order of magnitude lower than the concentration of haemoglobin [102].

To demonstrate the potential of BRUNO to recover absolute CCO concentrations, Figure 8.22 shows the effect of adding CCO to $\frac{\partial A^2}{\partial \rho \partial \lambda}$, assuming that the concentration of oxidised CCO, oxCCO, is 5μM, or that there is no contribution by oxCCO to the absorption. oxCCO increased the absorption of light in the tissue and caused a visible change in the slope model. As the oxCCO absorption is very broad, the addition of oxCCO to the model affects it across the whole spectrum.

While the change in the slope model could be quantified through accurate fitting, it was decided not to account for oxCCO absorption at this stage of BRUNO development. An additional fitting parameter would increase the computational burden. The broad spectral peak of oxCCO affects the slope model in the whole region of interest. Crosstalk between haemoglobin concentrations, scattering and oxCCO could occur, making an accurate assessment of oxCCO concentrations unlikely. As BRUNO is focused on the recovery of StO_2 and not absolute chromophore concentrations, accounting for oxCCO was decided to be excluded from the algorithm at this stage of development.

8.5.3 Source-detector separation

The topic of light source-detector spacing is briefly discussed when selecting the attenuation slope model. While the separation does not influence the selected $\frac{\partial A_{ZBC}}{\rho}$, the work in Chapter 6 has shown that it does affect the experimentally measured slope. Using all 4 detectors increases the robustness of the measured attenuation slope towards errors affecting only one detector; the linearity of the decrease of attenuation against distance is maintained despite potential offsets from linearity of one detector. Offsets from linearity were not observed in the phantom data (high R^2 throughout the measurement).

Using all four detectors is desirable even in the case of a perfectly linear increase of attenua-

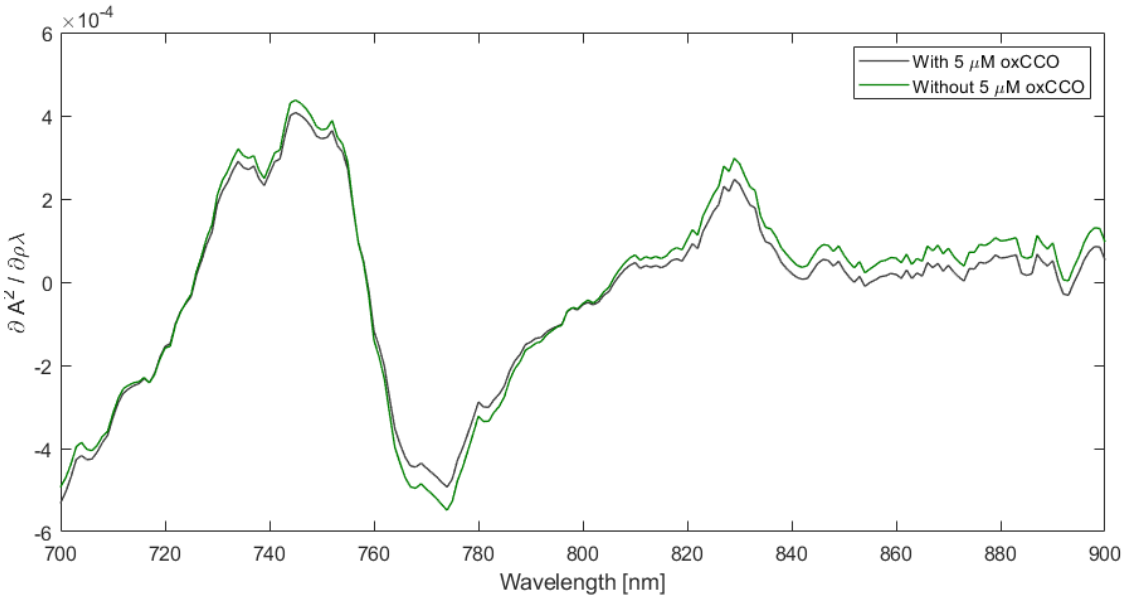

Figure 8.22: The effect of adding 5 μM oxCCO to $\frac{\partial^2}{\partial\rho\lambda}$ quantified at WF = 0.8, c_{HHb} = 29.5 μM, c_{HbO_2} = 55 μM, a = 0.5 mm$^{-1}\mu$m^{-1}, b = 1.7.

tion with distance; using close detectors reduces the noise in the measured slope. As further away detectors in CYRIL have a lower SNR, using only far separations would lead to a noisy slope. The advantage of using 4 detectors in a multidistance setup is shown in Figure 8.23. Spectral features of the slope are barely visible in the measurement using only far away detectors.

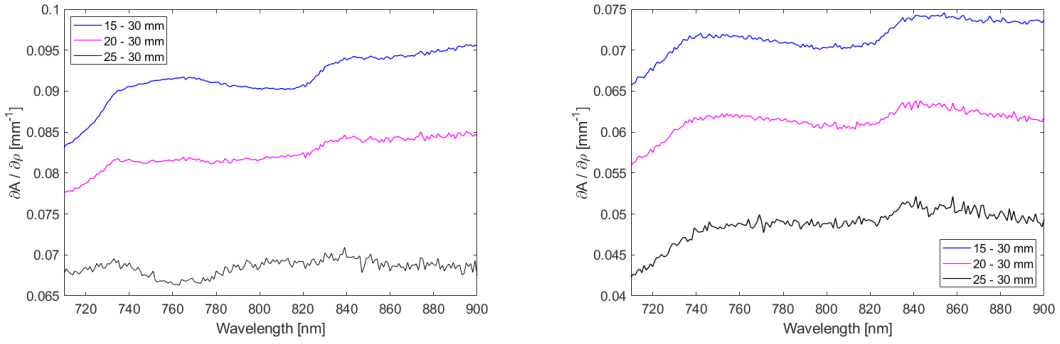

(a) Homogeneous phantom **(b)** Two-layer phantom

Figure 8.23: Attenuation slope $\frac{\partial A}{\partial \rho}$ measured across 4 (15–30 mm), 3 (20–30 mm), or 2 (25–30 mm) detectors in the phantoms during phantom deoxygenation.

8.6 BRUNO summary

The finalised process of recovering StO_2 from spectral data with BRUNO, also shown in Figure 8.24, is as follows:

- Measure attenuation A with at least two detectors in a multidistance setup.
- Calculate the slope of attenuation against distance $\frac{\partial A}{\partial \rho}$ across the detectors. If using CYRIL, use four detectors measuring at SDS from 15 to 30 mm.
- Generate a model of the attenuation slope $\frac{\partial A_{ZBC}}{\partial \rho}(\mu_a,\mu_s')$. Define the wavelength dependence of μ_a and μ_s', Eq. (8.2) and Eq. (8.1).
- Differentiate both $\frac{\partial A_{ZBC}}{\partial \rho}$ and $\frac{\partial A}{\partial \rho}$ with respect to wavelength. Smooth $\frac{\partial A}{\partial \rho}$ with an averaging filter prior to differentiation.
- Apply a least-squares minimisation process ($fminsearchbnd$) which will minimise the difference between $\frac{\partial A}{\partial \rho}$ and $\frac{\partial A_{ZBC}}{\partial \rho}$ by iteratively updating μ_s' and μ_a by changing their parameters a, b and chromophore concentrations. Perform the minimisation across the whole broadband spectrum, 710–900 nm if using CYRIL.
- Calculate StO_2 from the recovered c_{HHb} and c_{HbO_2}.

All necessary MATLAB scripts to run BRUNO on attenuation data are available on GitHub [272].

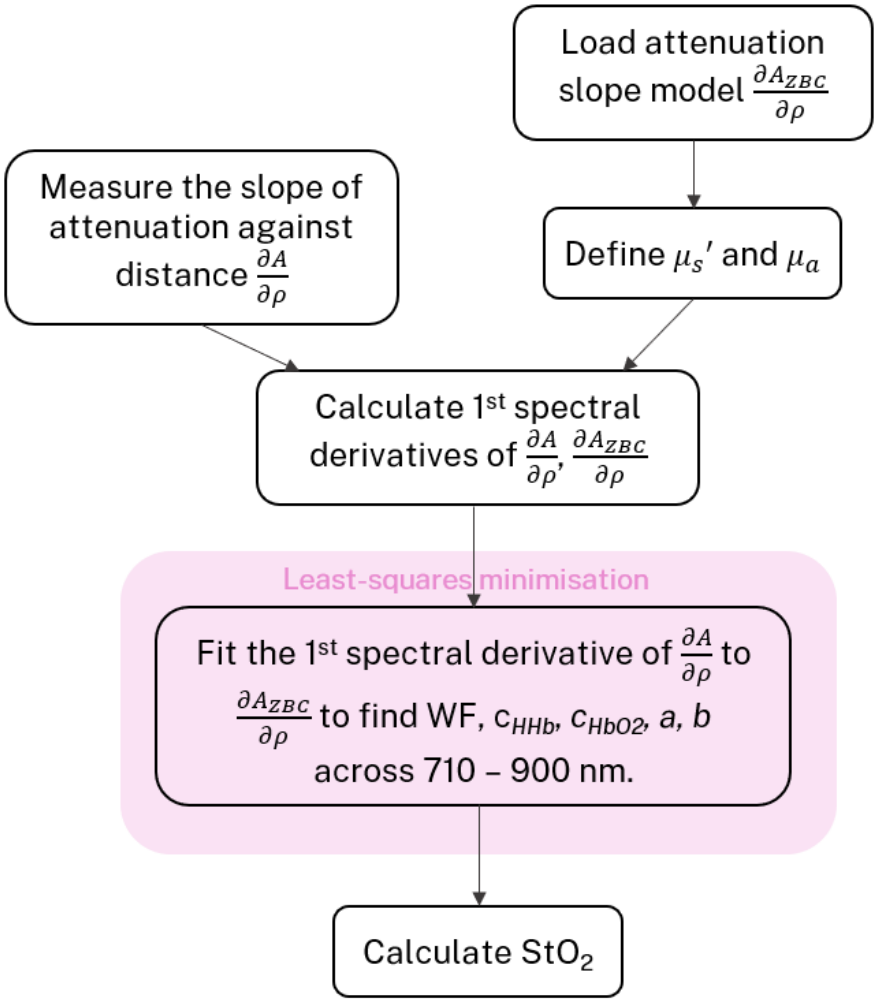

Figure 8.24: The process of calculating StO_2 with BRUNO. In the MATLAB implementation of BRUNO, $\frac{\partial A_{ZBC}}{\partial \rho}$ is first called as a symbolic function dependent on μ_{eff}. μ_a and μ_s' are then defined with the required parameters. The model is then evaluated during the least-squares minimisation procedure.

8.7 The performance of BRUNO

The data driven approach to the design of BRUNO, based on SRS and BF, was focused on improving the quality of StO_2 recovery by building on the individual strengths of both algorithms. The final step of BRUNO development is to compare the recovery of StO_2 with BRUNO to the oxygenation recovered with BF and SRS.

The application of BF to simulated data in this section was different compared to Chapter 7. The BF recommended wavelength range from 680 nm to 850 nm was used previously. In this chapter, the start of the broadband range was moved to 710 nm to make the results from NIRFAST simulations more comparable to measurements in a phantom, as CYRIL does not cover the required wavelengths below 700 nm. The other steps in the analysis were as described in Figure 7.2.

Two different versions of SRS were evaluated; one, where only discrete wavelengths were applied, and a broadband version. The discrete wavelengths were selected based on the results from the work in Chapter 6; 775, 810 and 850 nm. The broadband version covered the whole CYRIL range. As all 4 CYRIL detectors were used in the analysis, the attenuation slope model in SRS was changed from Eq. (8.6) to Eq. (8.7). A summary of the SRS algorithm is in Figure 6.3.

8.7.1 NIRFAST simulations

All NIRFAST simulations described in section 5.2 were used for the performance assessment, with spectra collected at 15, 20, 25 and 30 mm used for the attenuation slope calculation. The accuracy of the algorithms was determined by the accuracy of the recovered StO_2. Random 1% amplitude noise was added to all spectra. For models A, B, C, D1 and D2 , 50 spectra with noise were generated from each original noise-free spectra. In model E, 1% noise was added to each spectrum once. In model F, 1% noise was added to each spectrum 10 times, giving 10 spectra for each step.

The simulated models were described in detail in Tables 5.26 and 5.4; model A was homogeneous tissue without water absorption, B was a homogeneous tissue with water absorption, C was using heterogeneous tissue without water absorption, D1 and D2 were based on measurements in heterogeneous tissue with water absorption but with slightly different optical properties. The absolute truth for the heterogeneous simulations was not known but the recovered StO_2 was desired to be between the oxygenation of GM and WM. The analysis of all NIRFAST models was performed with the boundary conditions reported in Table 8.5. They were set wider than used previously, as if the true value of the parameters was not known, and to allow the quantification of low StO_2 values in model F.

Table 8.5: Boundary conditions for NIRFAST spectra analysis with BRUNO and BF. For models without water absorption, LB, UB and start of WF were set to zero.

	WF [%]	$\mathbf{c_{HbO_2}}$ [μM]	$\mathbf{c_{HHb}}$ [μM]	**a** [mm$^{-1}\mu$ m^{-1}]	**b** [-]
Start	70	50	50	1	1
LB	60	0	0	0.3	0.5
UB	95	100	100	2	3

The recovered StO_2 from models A, B, C, D1 and D2 with BRUNO, BF, SRS and BB SRS are shown in Figure 8.25. The black line indicates the true value for models A and B, oxygenation of GM. The dashed line lies on the true value of StO_2 in WM and the recovered StO_2 is expected to lie in the interval between truth GM and truth WM.

BF was strongly influenced by the addition of noise; the results of model D1 are particularly skewed, less so in model D2. The distribution of results in models A, B and C was more symmetrical around the median. The large standard deviation of BF in models D1 and D2 was caused by the algorithm converging to boundary conditions several times. While the difference between D1 and D2 was only a 10% change in optical properties, the algorithm was more unstable in D1. However, the median recovered oxygenation was still a value between GM and WM truth.

Out of all 4 algorithms, BRUNO recovered StO_2 with the highest accuracy in model A and B, and a value between the oxygenation of GM and WM in C, D1 and D2. The distribution of the results was narrow, suggesting a higher robustness towards noise than BF. The difference in the result between D1 and D2 was minimal.

SRS and BB SRS gave very similar results, only the distribution of SRS results was wider; suggesting that adding wavelengths increases the algorithm's robustness towards noise. The highest accuracy of SRS and BB SRS was in model C (heterogeneous, no water) and model B (homogeneous, with water). The results from model D1 and D2 are very similar, showing that the algorithms were not affected by small changes in μ_a and μ_s'.

Recovering StO_2 in models C and D did not inform sufficiently about the depth sensitivity of the algorithms; the models consisted of several different layers with varying oxygenations and the absolute truth was unknown. Models E and F, on the other hand, used a two-layer model with ECT and brain tissue, making tracking the sensitivity to brain tissue oxygenation easier.

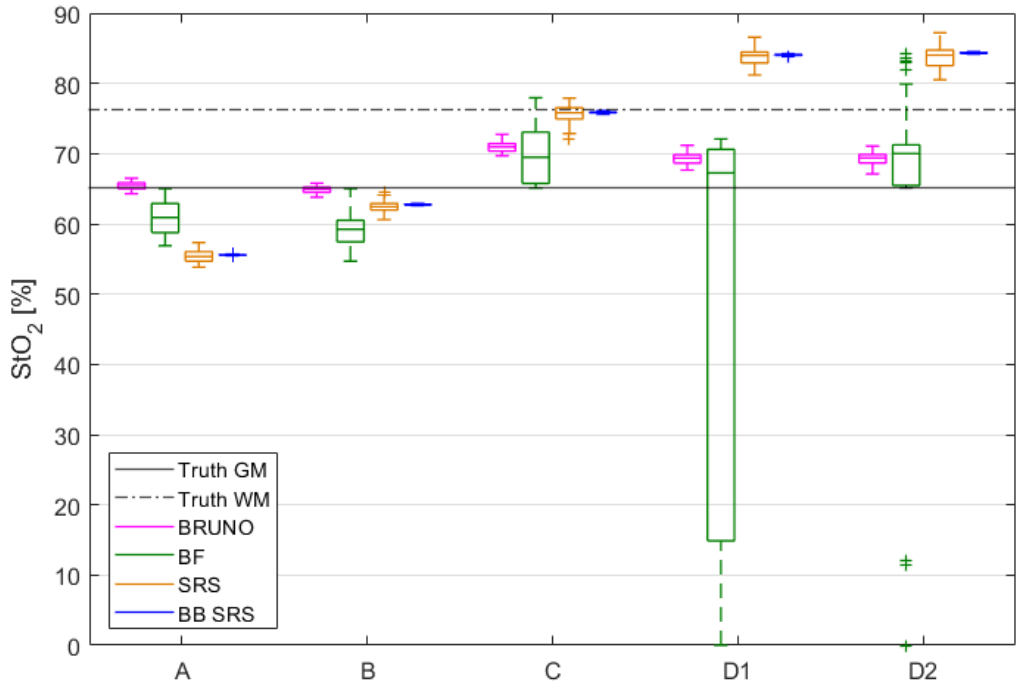

Figure 8.25: StO_2 recovered in 5 different models, n = 50. Model A is homogeneous tissue without water absorption (GM truth), B is homogeneous tissue with water absorption (GM truth), C is heterogeneous tissue without water absorption (GM WM truth), D1 and D2 are heterogeneous tissue with water absorption but slightly different optical properties (GM WM truth). Spectra were analysed with 4 different CW algorithms: SRS with 3 wavelengths (SRS), SRS with the whole broadband spectrum of CYRIL (BB SRS), BRUNO and BF.

Figure 8.26 shows the results of analysing model E, where homogeneous tissue with optical properties of the brain was oxygenated from 50% to 90%. Figure 8.27 shows the same oxygenation changes with a two-layer model, where brain was oxygenated and ECT oxygenation remained at 80%.

The accuracy of each method is visualised in Figure 8.28, showing the error of each method both in the homogeneous and heterogeneous models. The error was defined as the absolute difference between the true brain StO_2 value and the recovered value. All four algorithms recovered a brain-specific signal, the error between the true value and the recovered StO_2 increased with the difference between the oxygenation of brain and ECT.

BRUNO estimated oxygenation of the brain with the smallest error in both the homogeneous and two-layer model. The errors of BF were smaller than the errors of SRS and BB SRS but with a wide distribution, suggesting the method was less robust during changes in optical properties (scattering was changed ten times in each oxygenation step in this model). Using a broadband spectrum for SRS decreased the width of the distribution of errors, suggesting an increase of robustness, but it also decreased the accuracy. Interestingly, StO_2 from SRS and BB SRS maintained

a relatively constant offset from the truth in the two-layer model and became more accurate with lower StO_2 in the homogeneous model.

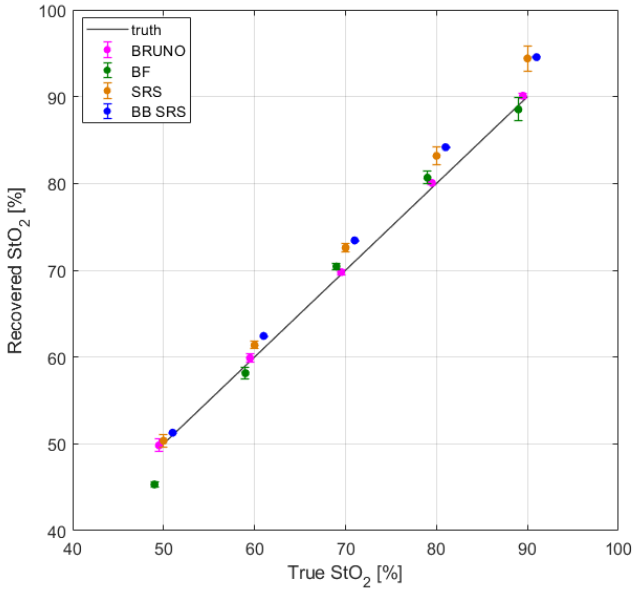

Figure 8.26: Recovering StO_2 from model E (homogeneous) during a brain tissue deoxygenation. Spectra were analysed with 4 different CW algorithms: SRS with 3 wavelengths (SRS), SRS with the whole broadband spectrum of CYRIL (BB SRS), BRUNO and BF.

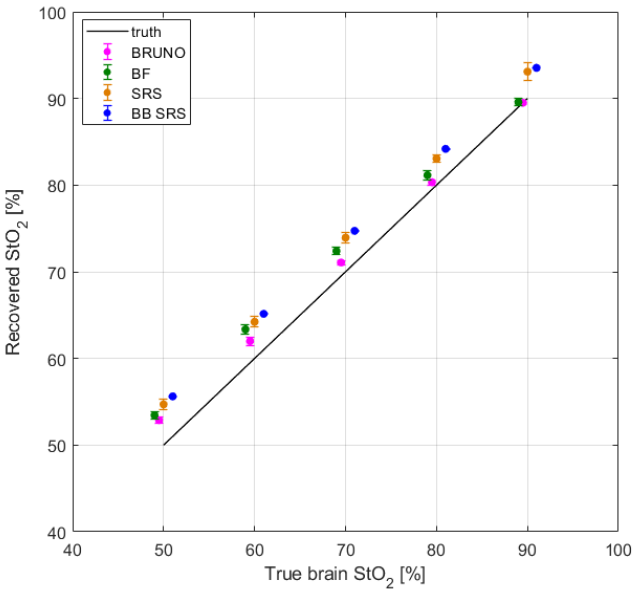

Figure 8.27: Recovering StO_2 from model E (two-layer) during a brain tissue deoxygenation. Spectra were analysed with 4 different CW algorithms: SRS with 3 wavelengths (SRS), SRS with the whole broadband spectrum of CYRIL (BB SRS), BRUNO and BF.

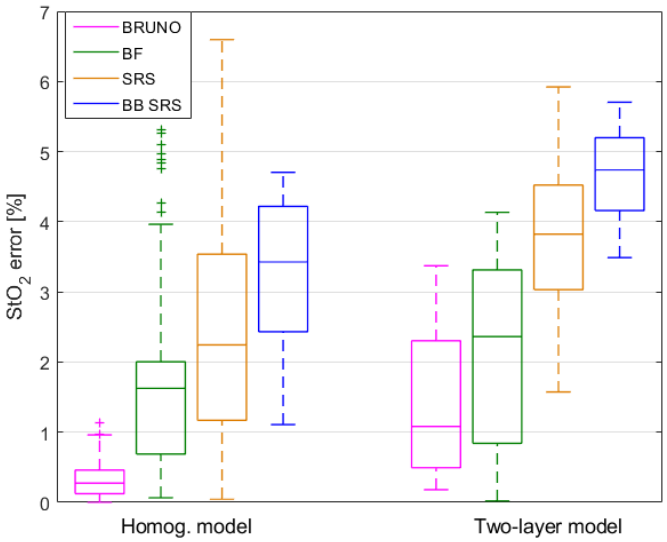

Figure 8.28: The absolute error of the recovered StO_2 with 4 different algorithms in model E, homogeneous and two-layer. The error was the absolute difference between the true brain oxygenation and the recovered StO_2.

The effect of changing oxygenation in ECT on the robustness of the brain signal was evaluated in the analysis of model F, where both brain and ECT were deoxygenated and oxygenated. The dynamic range of these changes was larger than in model E, reaching StO_2 of 10%. The result of analysing the spectra with all 4 models is in Figure 8.29.

All algorithms tracked mainly the oxygenation of brain tissue. Scatter plots were generated in Figure 8.30 and show the agreement between the recovered StO_2 and its true value. The scatter plots were generated using the MATLAB script *BlandAltman*, available online [273], which also has the functionality of plotting scatter plots and calculating correlation.

The scatter plots in Figure 8.30 show that BRUNO was following the oxygenation of brain tissue very closely, Figure 8.30, better than BB SRS, SRS and BF. As seen in Figure 8.29, the error of the estimation increased with the decrease of brain tissue oxygenation. It is interesting that during oxygenation changes of brain tissue, BB SRS, SRS and BF underestimated the oxygenation of the brain layer and recovered oxygenations lower than the true values of either layer. The difference between the true value and the BF, SRS and BB SRS StO_2 increased with the decrease of oxygenation, visible in the offset between the identity line and the regression line in Figure 8.30.

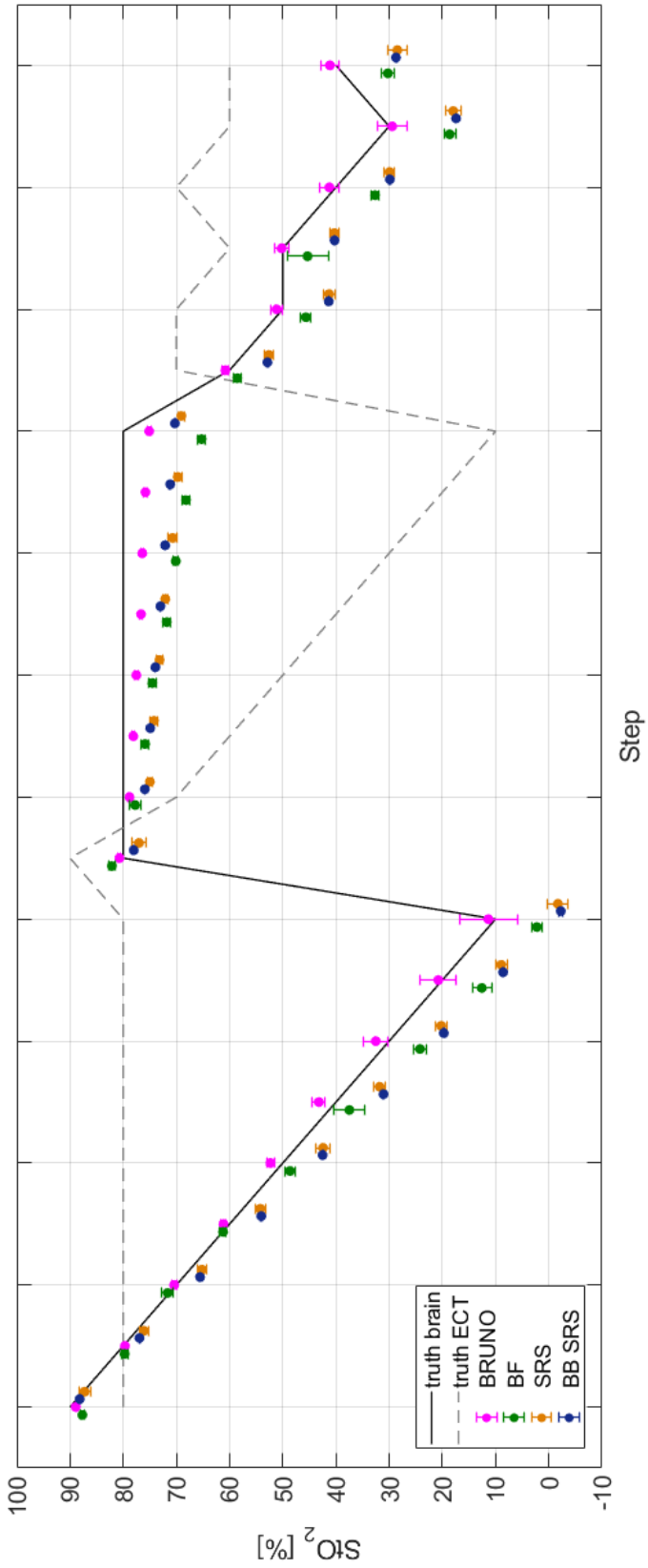

Figure 8.29: Recovering StO_2 from model F during Gm and ECT oxygenation changes. Spectra were analysed with 4 different CW algorithms: SRS with 3 wavelengths (SRS), SRS with the whole broadband spectrum of CYRIL (BB SRS), BRUNO and BF.

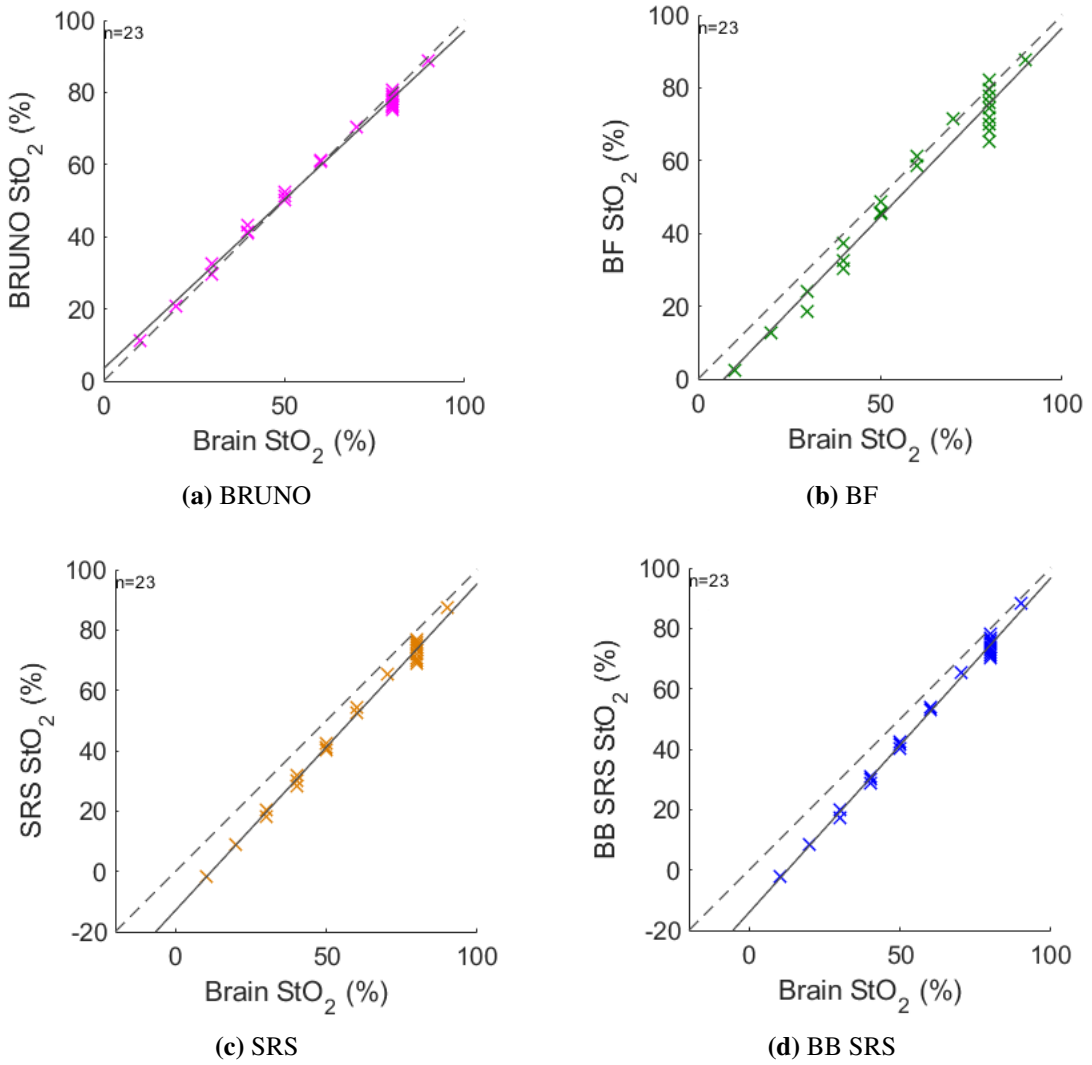

(a) BRUNO **(b)** BF

(c) SRS **(d)** BB SRS

Figure 8.30: Scatter plot of StO_2 in brain in model F compared to measured with CYRIL and analysed with BRUNO, BF, SRS and BB SRS. Multiple values of the recovered StO_2 per ground truth brain StO_2 correspond to varying ECT oxygenation. n shows the number of data pairs. The dashed line is the identity line, the full line is the regression line.

8.7.2 Phantoms

The next step in the performance assessment of BRUNO was to evaluate its performance in phantom studies, in data collected with CYRIL, and compare it to the StO_2 measured with MAESTROS. The data was analysed using the boundary conditions in Table 8.2. Figure 8.31 shows StO_2 measured with MAESTROS compared to BRUNO, SRS with discrete wavelengths, BB SRS with broadband wavelengths and BF. Note that the StO_2 traces were smoothed with a 5-step averaging filter. The agreement between MAESTROS and the individual algorithms to calculate StO_2 from CYRIL data is shown in scatter plots in Figures 8.32 and 8.33.

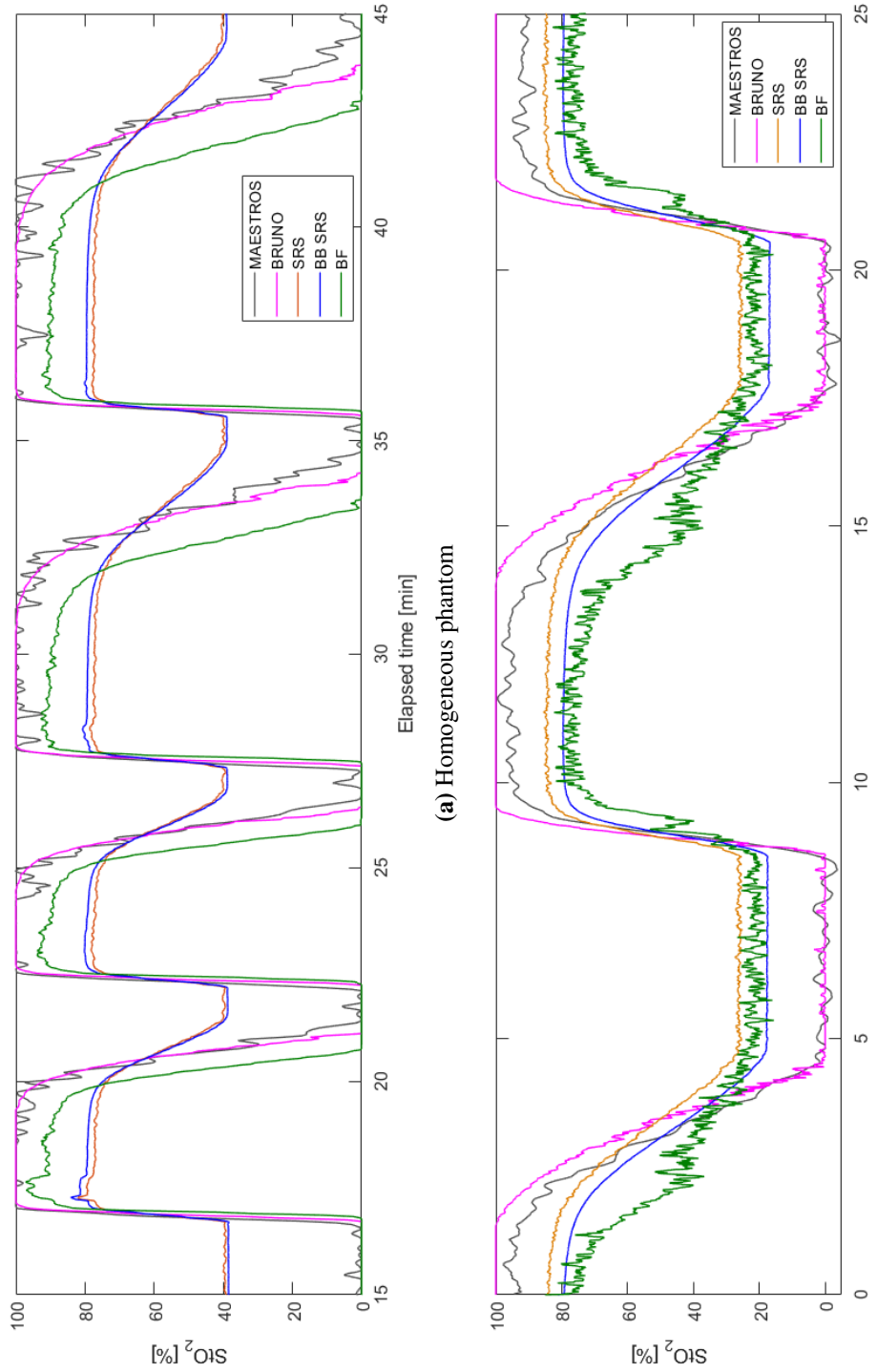

Figure 8.31: Recovering StO_2 collected in phantom measurements with 4 different CW algorithms: SRS with 3 wavelengths (SRS), SRS with the whole broadband spectrum of CYRIL (BB SRS), BRUNO and BF, compared to the MAESTROS measurement.

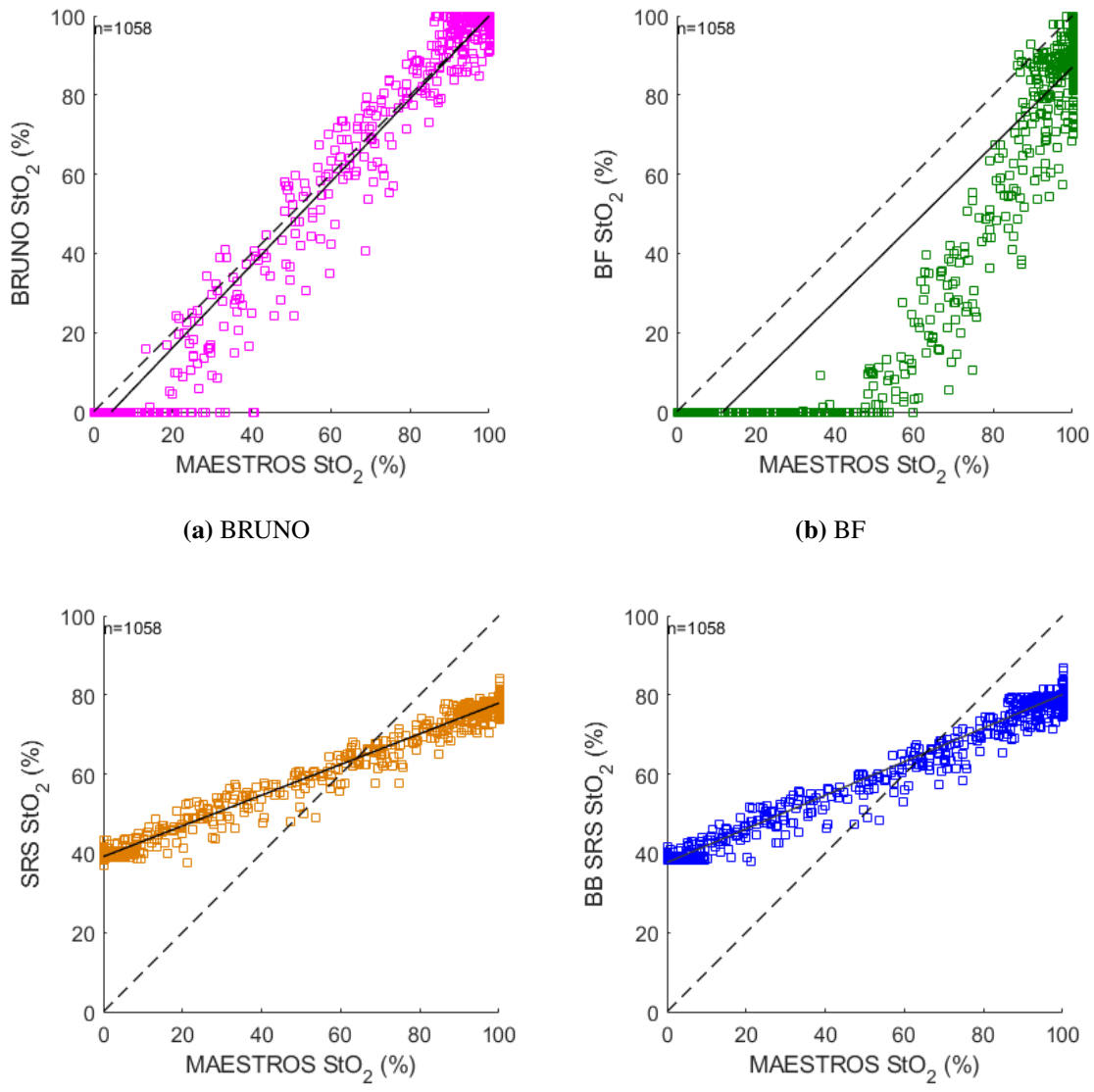

(a) BRUNO **(b)** BF

(c) SRS **(d)** BB SRS

Figure 8.32: Scatter plot of StO_2 in the homogeneous phantom measured with MAESTROS compared to measured with CYRIL and analysed with BRUNO, BF, SRS and BB SRS. n shows the number of data pairs. The dashed line is the identity line, the full line is the regression line.

Table 8.6: The duration of recovering StO_2 collected in phantom measurements with BRUNO, BF, SRS and BB SRS on a PC with a Intel(R) Core(TM) i7-8700 CPU @ 3.20, 32 GB RAM and a NVIDIA GeForce GTX 1080 Ti GPU.

	SRS	**BB SRS**	**BF**	**BRUNO**
	Analysis duration [s]			
Homogeneous	0.08	1.23	188.57	62.38
Two-layer	0.48	2.01	322.54	119.71
	Duration per spectrum [ms]			
Homogeneous	0.03	0.51	79.63	26.34
Two-layer	0.11	0.46	74.27	27.56

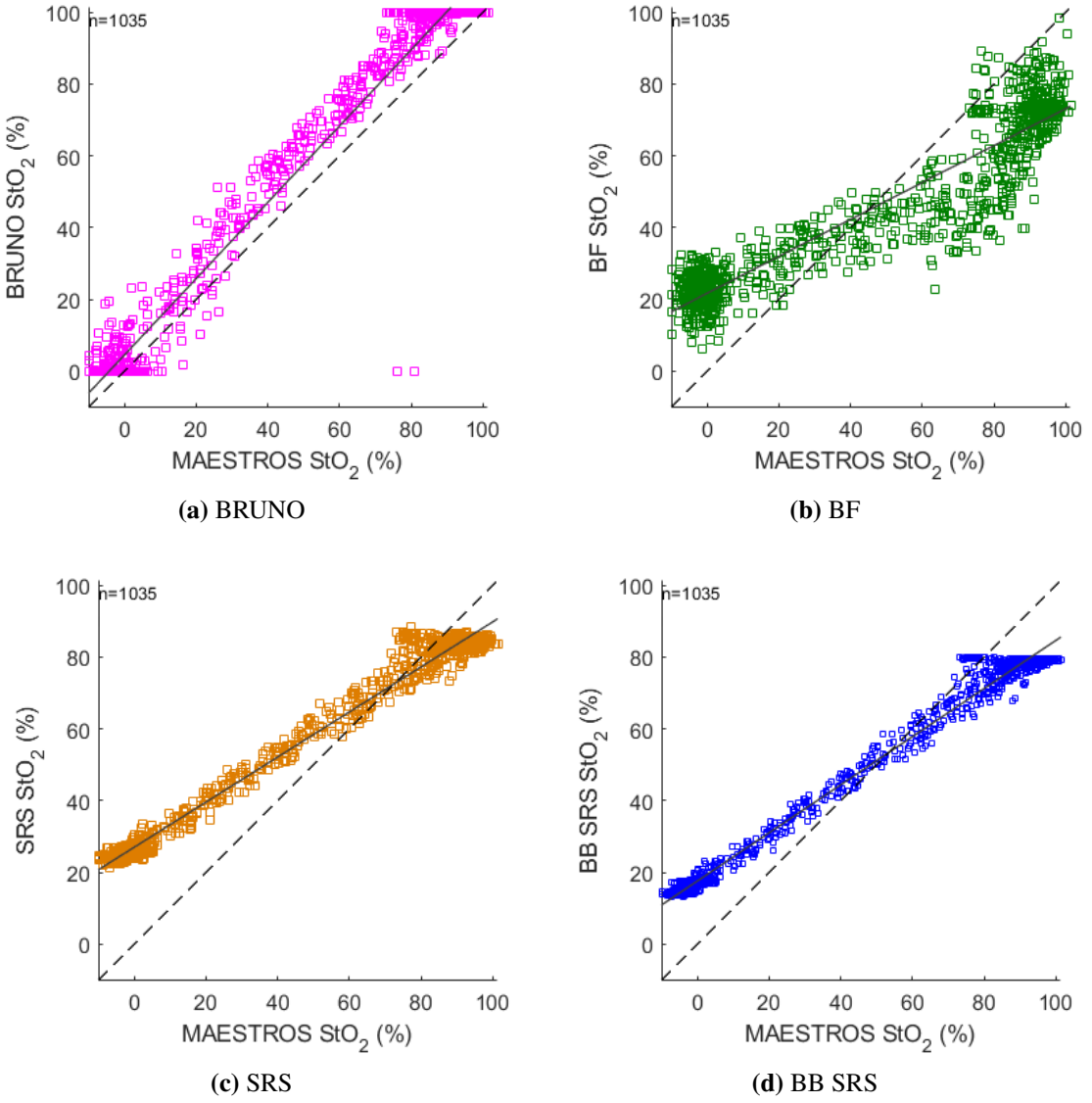

(a) BRUNO **(b)** BF

(c) SRS **(d)** BB SRS

Figure 8.33: Scatter plot of StO_2 in the two-layer phantom measured with MAESTROS compared to measured with CYRIL and analysed with BRUNO, BF, SRS and BB SRS. n shows the number of data pairs. The dashed line is the identity line, the full line is the regression line.

The BRUNO trace closely follows MAESTROS in both plots in Figure 8.31 and the regression line of BRUNO in the scatter plots is close to the line of identity, only a small offset is seen. While the disagreement between BRUNO and MASTROS was larger in the range of lower oxygenation in the homogeneous phantom, Figure 8.32a, it was larger in higher oxygenation in the two-layer phantom, Figure 8.33a.

The main difference between BF and MAESTROS was the time shift in the homogeneous phantom; BF measured deoxygenation drops sooner than MAESTROS. This is visible by the large shift from the identity line at MAESTROS StO_2 = BF StO_2 in Figure 8.32b. The temporal

sensitivity was more equal in the two-layer phantom but the dynamic range of BF was much smaller than MAESTROS, seen by the tilt of the regression line of BF StO_2 in Figure 8.33b.

A smaller dynamic range was also observed when recovering StO_2 with SRS and BB SRS. SRS and BB SRS responded to oxygenation changes at the same time as MAESTROS. However, while MAESTRO recovered changes in oxygenation from 0 to 100% in the homogeneous phantom, the dynamic range of SRS and BB SRS was only 40%. It increased to 60% in the two-layer phantom, where SRS and BB SRS measured oxygenation between 20–80%. A small constant offset between the values measured with SRS and BB SRS is visible in both measurements.

The oxygenation range between 40–90% is of main interest (physiologically relevant values), the behaviour of the algorithms in this range is shown in Figure 8.34. It highlights the agreement between BRUNO and MAESTROS in the homogeneous phantom but an offset in the two-layer phantom. BRUNO measured higher oxygenation in the oxygenation phase of the two-layer phantom and showed a delayed deoxygenation. The delay between BF and MAESTROS is evident in both cases. BF also showed a short plateau at 40% in the two-layer phantom, which was not recovered by any other algorithm. The deoxygenation measured by SRS and BB SRS was much slower than with any other algorithm.

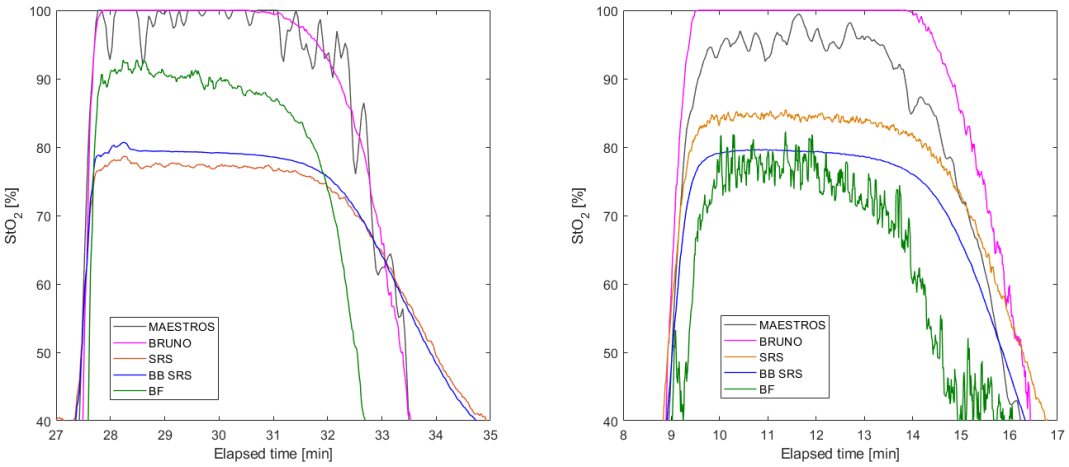

(a) Homogeneous phantom **(b)** Two-layer phantom

Figure 8.34: Recovering StO_2 in the range 40–90 % collected in phantom measurements with 4 different CW algorithms: BRUNO, BF, SRS and BB SRS, compared to the MAESTROS measurement.

The absolute errors of recovering StO_2 in both phantoms are shown in Figure 8.35; the error was calculated as the absolute difference between the MAESTROS reading and the recovered StO_2. Similarly to the simulations, BRUNO recovered StO_2 with the smallest error. BRUNO and BF recovered StO_2 with a smaller error in the homogeneous phantom than in the two-layer

phantom. The smaller dynamic range of SRS and BB SRS is shown in the width of the error distribution, the accuracy was better in the two-layer phantom.

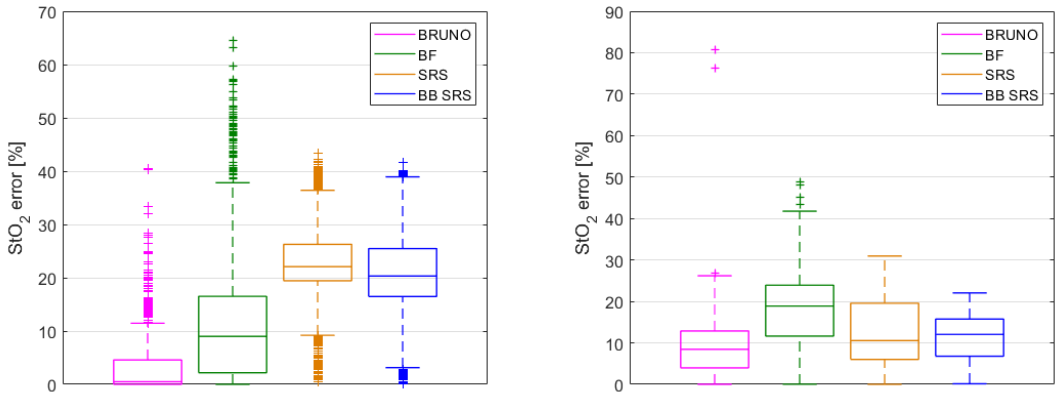

(a) Homogeneous phantom **(b)** Two-layer phantom

Figure 8.35: The error of recovering StO_2 in a homogeneous and two-layer phantom with different StO_2 recovery algorithms. The error was the absolute difference between the MAESTROS reading and the recovered StO_2.

The duration of analysis varied between all 4 algorithms; processing with SRS was the fastest and BF the slowest in both phantoms. The timings are reported in Table 8.6. The duration per spectrum was similar in the homogeneous and two-layer phantoms. All algorithms were executing fast enough for a potentially real-time application with measurements at 1 Hz.

8.8 Discussion

The development of BRUNO, a novel algorithm to measure StO_2 with broadband, multidistance CW NIRS has been described. The algorithm was designed to work in CYRIL, a broadband NIRS system. The main purpose of the system and the algorithm is to monitor neonates at the NICU.

The development of the algorithm was based on an experimental approach, where the individual aspect of the algorithm (such as model selection or wavelength selection) were tested in data obtained in NIRFAST simulations and phantoms. Such approach ensured that BRUNO is truly suited for the application in CYRIL and has optimal performance.

Most of the experimental investigation was performed on the analysis of only a few spectra from NIRFAST simulations. The generated spectra were based on the optical properties of human brain tissue. As phantom data were available for the assessment of the ability of the algorithm to recover very low StO_2 values with realistic noise levels, the use of a small data set of NIRFAST spectra was sufficient for demonstration purposes.

8.8.1 Model selection

The experimental approach to developing BRUNO has shown that sometimes, a theoretically proven advantage was in fact not an advantage when applied to CYRIL data. An example was the selection of theoretical slope models: even though the use of extrapolated boundary conditions when solving the diffusion equation is more precise, this advantage was overshadowed by the strong tendency for crosstalk between scattering and absorption and a higher sensitivity to noise in the spectra. As the computational requirements were also increased when using $\frac{\partial A_{EBC}}{\partial \rho}$, the simple model $\frac{\partial A_{ZBC}}{\partial \rho}$ was regarded as sufficient for the use of BRUNO. Other solutions to the diffusion equation with different boundary conditions were not investigated as it is expected that that would increase the computational burden of BRUNO and the results achieved with $\frac{\partial A_{ZBC}}{\partial \rho}$ were accurate when applied in NIRFAST simulations. A decrease of accuracy of BRUNO in phantoms due to the applied model is expected to be minimal compared to other sources of error, such as measurement noise.

8.8.2 Wavelength selection

The wavelength selection of BRUNO was dependent on the wavelength range of CYRIL 2, 704–911 nm. The wavelengths at the edges of the spectrum were excluded (704–709 nm and 901–911 nm) as the count rates were much lower at those wavelengths and noise was dominating the differentiated attenuation slopes. As there are no important spectral features at those wavelengths, it is not expected that including those wavelengths should give the algorithm any additional important information. The main spectral features of interest for BRUNO lie in the range from $\sim$ 715 nm to 850 nm.

The fitting of BRUNO was selected to be performed in the first spectral derivative space as differentiation removes wavelength-independent errors arising due to coupling errors affecting all detectors in the same manner and also amplifies spectral features. A fitting approach similar to BF, fitting in two steps for individual spectral features, was tested but did not bring any improvements. As fitting BRUNO across the whole spectrum at the same time gave satisfactory results, the step-wise fitting was not investigated any further.

BRUNO could be potentially improved by further optimising the used wavelengths, perhaps by expanding into wavelengths below 700 nm, as used in BF, or exploring different approaches to step-wise fitting.

8.8.3 Boundary conditions

Boundary conditions set in BRUNO affect whether the optimisation routine *fminsearchbnd* can converge and where it converges. In the case of *fminsearchbnd*, the termination depends on tolerances and stopping criteria; maximum function evaluation, maximum of iteration and termination tolerance [274]. The optimiser converges to a solution if the termination tolerance is satisfied within the maximum function evaluation and maximum iteration limits. If they are not satisfied, *fminsearchbnd* terminates without converging.

The optimisation routine in BRUNO does not have a unique global solution due to the relationship between μ_s' and μ_a in $\frac{\partial A}{\partial \rho}$ given by μ_{eff}. Boundary conditions are set to restrict the solution to the least-squares fitting problem. The minimisation function *fminsearchbnd* accepts lower and upper boundary conditions and also a start guess as input. If the termination criteria are satisfied within the allowed number of iterations and function evaluations, BRUNO finds a solution. This solution is a local solution to the problem within the range defined by the boundary conditions.

The wider the boundary conditions are, the more solutions are available, increasing the potential for crosstalk between μ_s' and μ_a. The boundary conditions set for the analysis of the phantom and the simulated data were set in a range based on expected values. It was demonstrated multiple times that even though the recovered StO_2 was correct, the accuracy of the individual fitting parameters was lower. It is hence important to set boundary conditions wide enough to allow these fluctuations and let the algorithm converge to the best solution.

The boundary conditions set in this work were guided by the expected true values. While the individual recovered fitting parameters were not reported in this chapter, it was checked whether they converged to the boundaries. No issues with either BRUNO or BF converging to the lower or upper boundaries were experienced in NIRFAST data or in optical phantom data (except for a few cases in BF analysis in models D1 and D2 due to noise, however, as the median recovered StO_2 was recovered with high accuracy, the boundary conditions were not changed).

Setting boundary conditions for human studies is challenging as the true parameter values are not known. It is recommended to use published optical properties of human tissue as a start value and set lower and upper boundary conditions accordingly. If the algorithm converges to the boundary conditions, it is worth evaluating whether the boundary conditions should be changed. The evaluation can be based on a visual assessment of the quality of the fit. Additionally, if two parameters (one relating to μ_a and one to μ_s') converge both to their boundary conditions, it is

worth trying a different set of boundary conditions.

Overall, one seeks a compromise between setting boundary conditions close to the true values but also allowing the algorithm to find different solutions which still fulfil the fitting criteria. Small measurement errors, such as the presence of noise, can change what the best solution is and hence guide the least-squares fitting to a different solution than primarily expected.

8.8.4 Fitting process

The optimisation routine used in BRUNO was not subject to scrutiny and the same solver as used in Chapter 7 was applied, *fminsearchbnd*. Currently, this minimisation algorithm is considered sufficient as it converges to the solution quickly and recovers StO_2 with high accuracy. At this point, the optimisation routine is not the main bottleneck of BRUNO - as the data fed into BRUNO is affected by noise and other measurement errors, the algorithm can lead to an incorrect solution independently of how good the fitting process is.

However, there are theoretical benefits to using a better optimisation routine: *fminsearchbnd* looks for a local minimum, and perhaps an optimisation routine that searches for the global minimum could lead to better results. Additionally, *fminsearchbnd* cannot currently be run in parallel on the CPU, increasing the computational time.

8.8.5 Noise and smoothing

BRUNO is susceptible to errors due to a low SNR as spectral features can become less distinct. Additionally, collecting spectral data with high SNR is needed as the slope calculation and spectral differentiation amplify noise.

The SNR of CYRIL for BRUNO was improved by changing the CCD data readout from CYRIL 1 to CYRIL 2, shown in Figure 8.36. The $\frac{\partial A^2}{\partial \rho \lambda}$ are from the homogeneous phantom, data was read out from the whole CCD and then binned, and the two-layer phantom, where the data was binned during readout already. The differentiation was performed on slopes normalised at 800 nm. Note that they were smoothed with a 5-step averaging filter. The CYRIL 2 setup decreased the noise as it included a noise subtraction and allowed measurements at wider bin widths without saturating the CCD.

The exposure when measuring StO_2 with CYRIL 2 was set to 1 s. Such exposure allows to collect a spectrum with a SNR suitable for BRUNO analysis, Figure 8.36, at rates compatible with real-time measurements. Increasing the exposure does increase the SNR but slows down the sampling rate of the system. If exposure is too long, the CCD gets saturated.

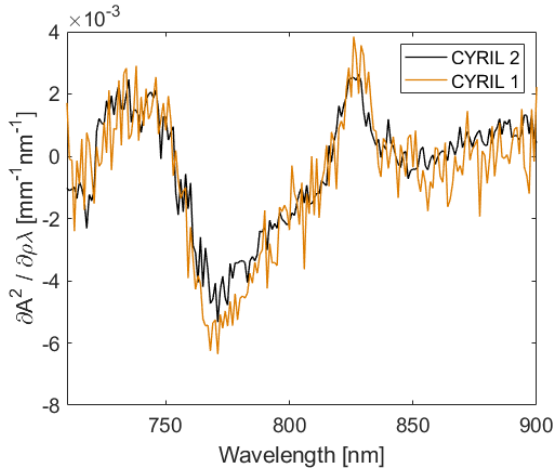

Figure 8.36: The comparison of $\frac{\partial A^2}{\partial \rho \lambda}$ collected in a CYRIL 1 and CYRIL 2 setup. The CYRIL 1 setup is shown on data collected in the two-layer phantom and the CYRIL 2 setup is shown on data collected in a homogeneous phantom. The differentiation was performed on slopes normalised at 800 nm, smoothed with a 5-step moving average filter prior to differentiation.

The quality of spectra can also be improved through smoothing. The impact of smoothing on BRUNO was not investigated in this work. The 5-step moving-average smoothing filter applied prior to differentiation was used based on literature [139, 125]. Another step that could reduce the impact of noise would be de-noising. An algorithm for the de-noising of broadband data using wavelets was published [270] but not applied in this work.

8.8.6 Recovery of absorption and scattering

Although BRUNO does lead to a recovery of both μ_s' and μ_a, only the resulting StO_2 was the target of this investigation due to the inability of the algorithm to recover μ_s' and μ_a with an accuracy comparable to the accuracy of StO_2. It is assumed that the error in μ_s' and μ_a is because of crosstalk; the dependence of $\frac{\partial A_{ZBC}}{\partial \rho}$ on μ_{eff}, which depends both on μ_s' and μ_a.

The presence of crosstalk is not a major problem for StO_2, as the application of BRUNO in this chapter has shown that StO_2 can be recovered with high accuracy even if the accuracy of μ_s' and μ_a is lower. However, attention should be paid to the values of the fitting parameters as they can converge to boundaries and prevent correct results.

Another aspect related to the correct recovery of μ_a and μ_s' is what chromophores are accounted for. In this work, the main chromophores of interest were HHb, HbO_2 and water, the strongest absorbers in the 700-900 nm range [104, 141]. Nevertheless, other chromophores contribute to light absorption, such as melanin or CCO, and not including them in the StO_2 calculation can cause inaccuracies as their contribution to attenuation is wrongly attributed to haemoglobin,

water, or scattering. The contribution of CCO to absorption was explored only briefly in this work, it was decided not to include additional chromophores in BRUNO as it would increase the computational burden and parameter crosstalk would be present. Same assumptions could be applied to melanin, as it, similarly to CCO, lacks strong spectral features in the wavelength range of interest and is only a weak absorber [141]. As no absorption by melanin or CCO was included in NIRFAST simulations or phantom measurements, the effect of these chromophores were not quantified.

8.8.7 Algorithm performance

8.8.7.1 Using MAESTROS as a reference

Before the performance of StO_2 calculation algorithms in NIRFAST simulations and phantom data will be discussed; it is necessary to point out one of the limitations of this work; the lack of a ground truth measure of oxygenation in liquid phantoms.

StO_2 was calculated in homogeneous and two-layer phantoms and compared to readings from MAESTROS. MAESTROS was not a measure of the true value of phantom oxygenation, such a measurement could be obtained with, for example, a blood gas analyser. No such device was available, and a diffuse oxygen probe was used throughout the measurements for guidance. The reading of the probe was tracked manually. The phantom was considered completely deoxygenated when the diffuse oxygen content was 0% and fully oxygenated when the probe's reading was over $\sim 120\%$.

MAESTROS is a system capable of accurate assessments of optical properties; the system's performance in the BIP and nEUROPt protocols is described in [113]. The sampling rate of the system was beneficial as it captured the fast oxygenation and deoxygenation changes in the phantom liquids.

To ensure that the MAESTROS system was measuring the same optical properties as CYRIL placed a few cm further away, the liquid was continuously stirred. It was assumed that small local inhomogeneities, such as a bubble trapped under the probe holder, should not cause significant errors.

The MAESTROS StO_2 measurement in the phantoms was in the range 0–100%, which is in agreement with the readings of the diffuse oxygen content measurement. Complete deoxygenation of the liquid was assumed due to the generous amount of yeast added, and complete oxygenation of the liquid was ensured by waiting for the amount of diffused oxygen to plateau.

While MAESTROS peaked at $StO_2 = 100\%$ in the homogeneous phantom, the maximal

oxygenation in the two-layer phantom was around 95%. As the system measures at 3 cm SDS, the influence of the thin silicone layer on the oxygenation should be minimal. Another possibility would be the presence of some artefacts, which shifted the whole StO_2 reading, as it sometimes reached negative oxygenation values as well. Studies with the same optical phantom measured reference oxygenation between 0 and 100% [165]. The stability of MAESTROS at very low and high oxygenation has not yet been thoroughly investigated and it is possible that its accuracy is decreased in those ranges. However, as such saturation values are impossible in human subjects (INVOS intervention ranges are values outside 58–82 %[204]), high accuracy of NIRS systems in those ranges is not a priority.

8.8.7.2 Performance of spatially resolved spectroscopy

SRS is a widely used algorithm to recover StO_2 at discrete wavelengths with multidistance NIRS. The implementation of the algorithm to data collected in CYRIL has already been subject to scrutiny in Chapter 6, but the recovered oxygenation was not compared to the known truth. In this chapter, the performance assessment of SRS in CYRIL is taken further. Two different versions of SRS were used, a version with discrete wavelengths (775, 810 and 850 nm) and the broadband range of CYRIL, 710–900 nm.

The impact of adding noise to the spectra had an effect on the recovery of StO_2 with SRS. In NIRFAST simulations, the interquartile range of the results remained small. Using the whole broadband spectrum decreased the deviation of the results, and, in some cases, improved the accuracy of SRS. The effect of noise was more visible in phantom measurements. When noise is applied to three wavelengths only, it can cause a significant shift of the slope value at one wavelength, however, this effect is "smoothed out" if the whole spectrum is utilised. The change of the results recovered with SRS depending on wavelength selection was already observed in Chapter 6.

In NIRFAST simulations, both versions of SRS gave a narrow distribution of results with lower accuracy than BRUNO. The results in models E and F followed a linear trend, just like the true value, but were shifted (visible in Figure 8.30). This is suggesting the presence of an offset in SRS, which could be the constant h, used in the scattering model $\mu_s' = k(1 - h\lambda)$. It has already been shown in Chapter 6 that it causes a linear offset to StO_2. To test this hypothesis, the values for h specifically for ECT and the brain in model F were calculated; $h_{ECT} = 0.00077$ mm^{-1}nm^{-1} and $h_{BR} = 0.00056$ mm^{-1}nm^{-1}. The effect on the result is shown in Figure 8.37, where the error is the absolute error defined as the difference between the true brain StO_2 in the 23 steps of model F and the estimated oxygenation. Using the h_{ECT} increased the error, while h_{BR} improved the accu-

racy for both BB SRS and SRS. This would suggest that the method is sensitive to scattering in the brain, emphasising the ability of the method to reduce the impact of extracerebral signals. It is possible to increase the accuracy of (BB) SRS by accounting for scattering flexibly. Similar decrease of SRS accuracy due to the assumptions on scattering properties has also been shown in NIRFAST simulations in adult head meshes in the work of Deepak Veesa and Dehghani, who proposed an addition to the algorithm that removes the need for prior assumptions about scattering [148].

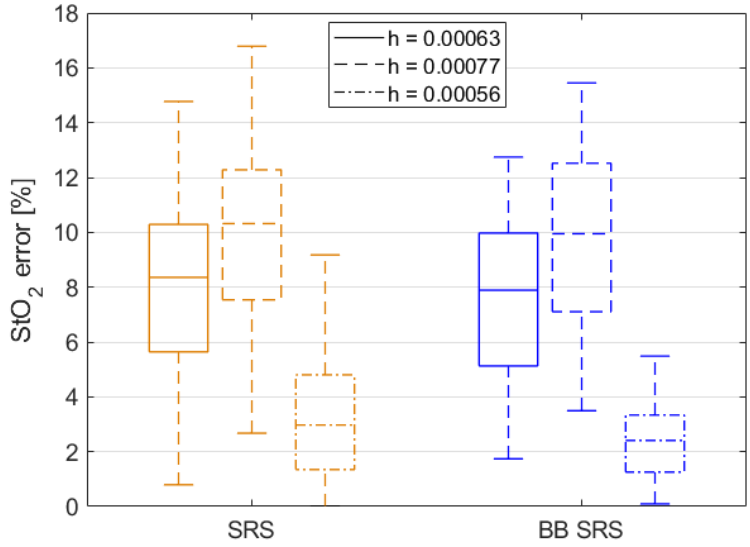

Figure 8.37: The absolute error when recovering StO_2 in model F with different scattering constant h. The typical h used in SRS is $h = 0.00063$ mm^{-1}nm^{-1}. Two other values were tested, $h_{ECT} = 0.00077$ mm^{-1}nm^{-1} and $h_{BR} = 0.00056$ mm^{-1}nm^{-1}.

The NIRFAST simulations have shown a wide dynamic range of oxygenation recovered in both BB SRS and SRS. The work in phantoms, however, has shown a reduction of this range, both in the homogeneous and the two-layer phantom. The dynamic range in the homogeneous phantom was only 40%, and 60% in the two-layer phantom. There was no temporal delay in the response of the algorithms. There are various factors which could contribute the decrease in accuracy, from the measurement itself to the content of the phantoms. One of the main differences between NIRFAST models E and F and the phantoms was the addition of water as an absorber.

Water absorption is not accounted for in SRS and BB SRS. The contribution to absorption in the wavelengths used in SRS should be minimal; there are no spectral features at those wavelengths. However, the change in StO_2 accuracy between NIRFAST models A and B, and C and D1/D2 suggest that the addition of water absorption does affect the algorithm's performance. In model A, the low accuracy of StO_2 is likely caused by h. The accuracy improved in model B, despite μ_s' being the same. It is likely that the added absorption by water was accounted for by HbO_2,

increasing StO_2. An increase of StO_2 is also found when water was added to model C, leading to models D1 and D2. This effect could have likely also lead to the increased baseline oxygenation in phantom measurements. As the water concentration was very high, SRS accounted for it by increasing the contribution of HbO_2, increasing StO_2.

The decreased dynamic range of SRS was caused by the algorithm incorrectly estimating the spectral features of HHb and HbO_2. This could lead to an overestimation of particularly HHb, the attenuation slope features mainly spectral features of HHb, HbO_2 is less visible. While BRUNO and SRS were based on the same data, the differentiation process in BRUNO amplifies these spectral features and the contribution of HbO_2 becomes more distinct. While the spectra collected in NIRFAST did not show this issue of reduced dynamic range, the noise in the CYRIL measurement, the measurement of the reference spectrum and the unequal spectral output of the light source across the whole broadband range could contribute to the decreased visibility of HbO_2.

Decreased accuracy of the SRS algorithm in NIRO devices at low oxygenations has been shown in studies in human subjects [179, 178]. A source of bias in those studies was the variations in the ratio of arterial and venous blood in the monitored area of the brain, as manufacturers include an assumption in the StO_2 measurement. No such assumption is, however, included in our calculation and the decreased accuracy at low oxygenation was not observed in the NIRFAST simulations. The effect of instrumentation on the accuracy of SRS is seen when our results are compared to results reported in [25], where a NIRO 300 was used in a homogeneous phantom and the results showed high accuracy in respect to oxygenation measured with a blood gas analyser. The concentration of water in their phantom was around 99%. The difference in the engineering of CYRIL and the NIRO device could explain the different results.

The findings of an oxygen-dependent bias of oximetry agree with a review of *in vivo* validation studies by La Cour et al. [10], who report an overestimation of blood saturation in the low ranges. A difference in oximeter dynamic range was also reported in a comparison of multiple oximeters in a two-layer phantom (same phantom as used in this work), used to find a conversion from StO_2 readings to a reference reading. For example, the reference oximeter Oxiplex TS had a hypoxic-to-hyperoxic thresholds range from 47% to 77.2%, while a NIRO 200NX with a small re-usable sensor (3 cm SDS) had a range from 62.8% to 80% [8].

It was interesting that the difference in the performance of SRS and BB SRS was minimal in this chapter, compared to the work in Chapter 6. The change in the performance of the SRS algorithm depending on wavelength is particularly visible in Figure 6.9, where the approaches

equivalent to BB SRS and SRS gave different results. It is possible that the different wavelength range used in CYRIL 2 compared to CYRIL 1 affected the performance.

In conclusion, the SRS and BB SRS algorithms show good performance in NIRFAST simulations, with the only drawback of offsets caused by scattering and potentially water absorption. The application of the algorithm to data collected in CYRIL shows a decrease of accuracy, particularly a small dynamic range, which has also been reported with SRS applied in other instruments.

8.8.7.3 Performance of broadband fitting

The precision of StO_2 measurements in NIRFAST simulations has been subject to scrutiny in Chapter 7; where the ability to recover StO_2 with high accuracy, despite issues with recovering the individual fitting parameters, has been shown.

BF recovered StO_2 with very high accuracy in Chapter 7, higher than in this chapter. The results are not comparable as previously, BF was applied across the whole broadband range suggested by the authors. Here, the wavelength range was reduced to the range of CYRIL, lowering the accuracy of BF.

Using BF in NIRFAST simulations has shown that out of the 4 algorithms, BF was most likely to be influenced by random noise. Relying on data from only one detector and the double differentiation amplifies the noise. The effect of noise is particularly visible in model D1. Although the median value was the desired StO_2, many outliers widened the distribution. While the model used in model D2 was very similar to D1, the algorithm was more stable. This difference might be only due to the effect of random noise, evident in a small sample size of spectra.

BF showed relatively high sensitivity to the brain signals in models E and F, in spite of the single-detector setup and the expectations of strong influence of ECT signal. As the ECT layer in the neonatal mesh is very thin, the majority of the signal originates in the deeper layer. However, the influence of ECT deoxygenation on BF was the strongest out of the 4 algorithms in model F; the StO_2 measurement underestimated the oxygenation of the brain layer.

Similarly to SRS, the accuracy of the algorithm decreased when implemented in CYRIL. The main drawback of BF identified in this work, the shift between the deoxygenation measured with BF and MAESTROS in the homogeneous phantom, could be due to the single-detector setup. BF responded to increases to oxygenation with a delay and detected desaturations earlier than MAESTROS, it is possible that BF was more responsive to c_{HHb} than c_{HbO_2}. This is not surprising given the more distinct spectral features of HHb, and, as BF only utilised one detector at 30 mm SDS, the SNR was lower, hiding spectral features of HbO_2. This hypothesis is proven in Figure 8.38a,

which shows StO_2 recovered with BF at 15 mm and at 30 mm. The 15 mm trace follows the MAESTROS oxygenation more closely and is almost identical to BRUNO.

The situation was different in the two-layer phantom, Figure 8.38b. The detector at 15 mm monitored a different medium than the one at 30 mm; there could have been a stronger contribution from the upper layer, decreasing the dynamic range of StO_2. A baseline offset could be due to the different noise levels at both detectors as seen in the homogeneous phantom.

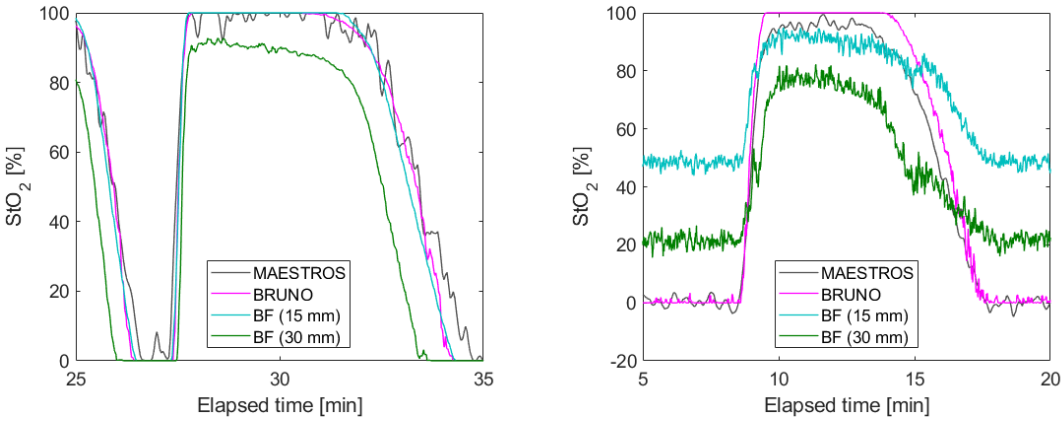

(a) Homogeneous phantom **(b)** Two-layer phantom

Figure 8.38: StO_2 in phantom measurements recovered with MAESTROS, BRUNO and BF at two different SDS, 15 and 30 mm.

Another curious finding in the BF deoxygenation is the dip mid-deoxygenation, visible both at 15 and 30 mm. No such patterns were found in the reflectance spectra. Inspecting the fit coefficients, mainly c_{HHb} and c_{HbO_2}, helped understand the behaviour of BF. While the absolute value of these coefficients was burdened by crosstalk, the trend in their changes showed why the dip in StO_2 occurred, Figure 8.39. The absolute change in c_{HbO_2} between min and max oxygenation was significantly smaller than in c_{HHb}, which mirrored the StO_2 trend. The spectral features of HHb are more distinct than those of HbO_2, giving the algorithm a more stable target and c_{HHb} was fixed in BF when c_{HbO_2} was sought. Low c_{HHb} perhaps made the accounting for absorption by HbO_2 more likely to be mistaken for scattering, increasing the noise in the recovered c_{HbO_2}. All oxygenations and deoxygenations started with a trend of c_{HbO_2} following the expected behaviour of StO_2 and then suddenly drop. There is evidently a threshold where the BF fitting optimisation did not distinguish between the spectral features sufficiently anymore, but this was not investigated any further as it is outside of the scope of this work.

Overall, it was shown that BF can track StO_2 with relatively high accuracy and is sensitive to the brain tissue signal despite using just one detector. However, the performance of the algorithm

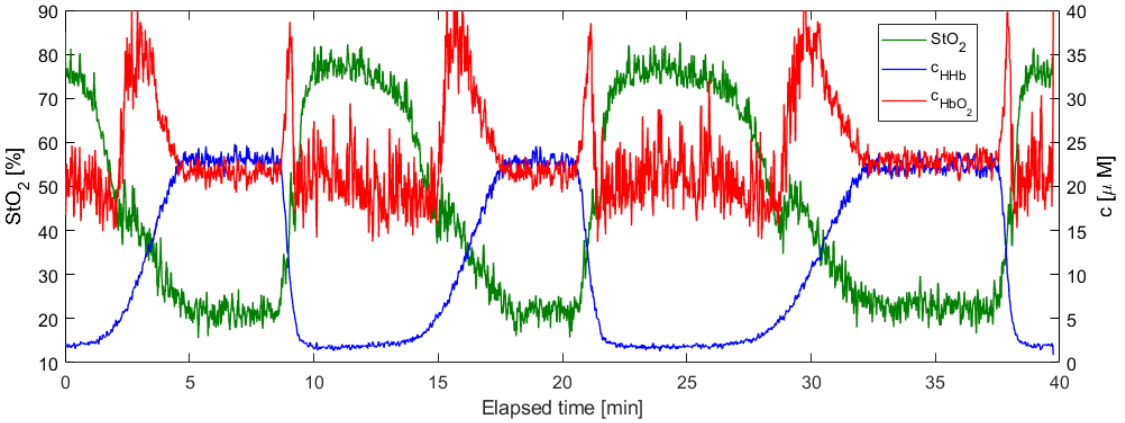

Figure 8.39: StO_2 recovered with BF in the two-layer phantom and the corresponding c_{HHb} and c_{HbO_2}.

based on accuracy and sensitivity to brain tissue signal was worse than that of BRUNO, SRS and BB SRS. The algorithm was prone to errors due to noise and additional smoothing and de-noising could improve its performance. A subject of future investigations could also be the usage of ZBC models in BF instead of EBC, as that could decrease crosstalk and computational burden similarly to the demonstrations in BRUNO.

8.8.7.4 Performance of broadband multidistance oximetry

Applying BRUNO to data simulated in NIRFAST simulations and in phantom measurements has shown that BRUNO can recover StO_2 with high accuracy. The sensitivity of the algorithm to brain tissue oxygenation changes make it a suitable candidate for the use in the neonatal intensive care to monitor haemodynamics during HIE.

Although an absolute measurement of the true oxygenation in phantom measurements was not available, BRUNO gave results closest to the reference measurement with MAESTROS. Overall, BRUNO recovered StO_2 with the highest accuracy out of all the tested algorithms, it was the most sensitive to brain tissue signal, and had the widest dynamic range.

The use of a homogeneous phantom has shown that BRUNO can track oxygenation changes with high sensitivity, covering the whole range of oxygenation, from 0% to 100%. Adding a solid, tissue simulating layer in the two-layer phantom measurement demonstrated that BRUNO can track changes of oxygenation of deeper layers, covering the whole oxygenation range, suggesting minimal impact of the solid, absorbing layer. As the sensitivity to brain tissue oxygenation was also proven in NIRFAST simulations, using BRUNO to NIRS data collected in neonates should recover StO_2 with minimal ECT signal contamination.

One issue identified in the two-layer measurements was the offset between the MAESTROS

measurement and the BRUNO StO_2 trace in the two-layer phantom, Figure 8.34b. BRUNO reached maximum oxygenation slightly earlier than MAESTROS, and also remained at maximal oxygenation for longer. It is likely that the oxygenation in the phantom was indeed 0–100%, as shown in other publications with the same phantom [8]. The small error in the MAESTROS reading could have been caused by some scaling error of the StO_2 measurement. The data without such scaling, removed by using the MATLAB function *normalize*, is shown in Figure 8.40 with StO_2 from MAESTROS, BRUNO and SRS. SRS and BRUNO followed a very similar trace as they are based on the same slope measurement. The temporal changes in BRUNO and SRS StO_2 became identical to the MAESTROS StO_2 reading, proving that the algorithms were sensitive to changes in oxygenation.

BRUNO showed that it is possible to improve the accuracy of StO_2 measurements by combining advantages of two other known StO_2 algorithms. Table 8.7 summarises the strengths of BRUNO, which make it more accurate than SRS and BF and also increase its robustness towards noise, while keeping the computational requirements relatively low.

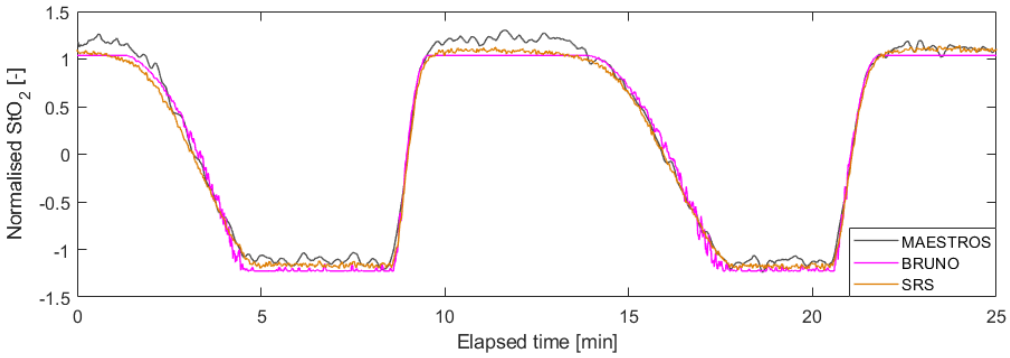

Figure 8.40: StO_2 (normalised) measured in the two-layer phantom with MAESTROS, BRUNO and SRS.

One of the main advantages of BRUNO lies in the sensitivity to brain tissue signal and not relying on prior information about scattering. However, due to the use of differentiation, BRUNO does rely on high SNR, potentially aided by appropriate smoothing if applied in CYRIL. Using NIRS instrumentation with higher SNR than CYRIL could yield better StO_2 accuracy.

The fitting over a broadband spectrum requires significantly more computational power than SRS. While the duration of the analysis was short during this work, using a less powerful PC than the one used in this analysis could make a big difference in the algorithm performance.

Another disadvantage of BRUNO is that it suffers from the crosstalk between μ_a and μ_s', similarly to BF. Overcoming this would enable a more informative description of the optical properties of the tissue. However, this is an inherent property of the attenuation models used and currently,

Table 8.7: Comparison of spatially resolved spectroscopy (SRS), broadband fitting (BF) and BRUNO. ZBC: zero boundary conditions, EBC: extrapolated boundary conditions, SD: single-distance, BB: broadband, MD: multidistance.

	SRS	**BF**	**BRUNO**
Diffusion equation boundary conditions	ZBC	EBC	ZBC
Set up	MD	SD BB	MD BB
Accounting for water absorption	×	✓	✓
Broadband spectrum	×	✓	✓
Homogeneous tissue model	✓	✓	✓
Low computational requirements	✓	×	∼
Lower noise amplification	✓	×	×
No boundary conditions needed	✓	×	×
No prior scattering assumption	×	✓	✓
Reduction of superficial layer signal contamination	✓	×	✓
Unique solution	✓	×	×
Highest StO_2 accuracy in simulations	×	×	✓
Highest sensitivity to brain tissue signal	×	×	✓
Highest StO_2 accuracy in phantoms	×	×	✓

separating the two optical properties with CW NIRS is impossible without narrow boundary conditions for the least-squares optimisation and a more thorough wavelength selection process.

Use of BRUNO in a different NIRS system

While BRUNO was designed specifically with the application in CYRIL in mind, the algorithm is publicly available to encourage implementation in different systems. An effect on the algorithms performance is expected, as some of its properties are linked to CYRIL. Firstly, the wavelength selection BRUNO was limited by the CCD calibration of CYRIL 2, 704–911 nm, with a resolution of ∼4 nm. It is expected that changing the wavelength range would influence the result as different chromophore absorption features became visible. It is also necessary that the system has sufficient resolution for the recovery of absorbing features, particularly those close to each other, such as the water feature at 730 nm and the HHb feature at 750 nm. Another important requirement for instrumentation is high SNR, as high noise content decreases the visibility of spectral features.

The SDS set up for BRUNO is not standardised. It is recommended to use more than two detectors to ensure that an attenuation slope can be measured despite potential issues with coupling with one SDS. The separation between fibre optodes in CYRIL is 5 mm but this can be changed for other systems. The MATLAB script for BRUNO's implementation supports adjusting the slope model according to the requirements of the NIRS system in use.

8.9 Conclusion

The development of BRUNO, a novel algorithm to measure StO_2 with multidistance, broadband CW NIRS data, has been described. The algorithm's design was based on the desire to improve the accuracy of StO_2 measurements. To achieve this goal, BRUNO was built on the advantages of other CW algorithms, SRS and BF; a multidistance setup and the use of broadband spectra. One of the main requirements for BRUNO was to be compatible with CYRIL, particularly its broadband wavelength range and resolution.

One of the main aims of this PhD work was to develop a novel algorithm to measure StO_2 with multidistance CW NIRS; one that would be sensitive to cerebral tissue, track oxygenation with high accuracy, sensitivity and dynamic range. High sensitivity to brain tissue oxygenation was shown both in NIRFAST simulations and in two-layer measurements, BRUNO recovered StO_2 with high accuracy in all analysed data sets, and a wide dynamic range and sensitivity to StO_2 changes was also demonstrated. The algorithm outperformed the two StO_2 algorithms on which it was based on, showing that combining the strengths of SRS and BF leads to an improved measure of StO_2.

The main purpose of the algorithm is to be used in neonatal monitoring and this impacted some of the design choices, such as the assumptions on tissue homogeneity and the models of light transport applied. The development of BRUNO was guided by applying iterations of the algorithm to data collected in NIRFAST and phantom measurements, until the version with the highest StO_2 accuracy was found. The algorithm uses a theoretical model of the attenuation slope $\frac{\partial A_{ZBC}}{\partial \rho}$ which is fitted in a least-squares minimisation procedure to the measured attenuation slope. Performing this fitting in the first spectral derivative space is beneficial as it improves the visibility of spectral features of chromophores and also decreases the impact of coupling errors. The fitting parameters are then used to calculate StO_2. While the approach is computationally more complex than SRS, the analysis was fast enough to enable real-time application.

The next step in the development of BRUNO will be applying to data collected in neonates with HIE to evaluate how well the performance in NIRFAST simulations and phantom data translates to data collected in clinical care.

Chapter 9

Measuring cerebral oxygenation in neonates with HIE

The performance of BRUNO has been investigated in NIRFAST simulations and phantom data. The task of this chapter is to show the application of the algorithm to data collected in its target subjects group - neonates in the NICU. The design of the second session of the Baby Brain study at UCLH, the data collection and the results are described.

9.1 Introduction

The development of BRUNO was guided by its performance on NIRS data collected in highly controlled environments - NIRFAST and dynamic blood phantoms. The shift towards data collected in human subjects introduces a spectrum of challenges which affect the performance of the algorithm; ranging from movement artefacts, poor tissue/probe coupling, to tissue inhomogeneities. This reduction of data quality might hinder BRUNO from being a reliable measure of StO_2 in clinical care.

Chapter 4 has shown that the measurement of StO_2 remains problematic in the neonatal intensive care, as the measured values are affected by the timing of the measurement, injury severity, lack of gold standard and even by which instrument is used for the measurement. Additionally, as summarised in section 4.1.2.5, oximetry is not yet suitable for clinical practice as a stand-alone instrument due to a lack of measurement precision. The motivation for the work in this chapter was to investigate whether BRUNO can recover StO_2 in the injured neonatal brain, to assess the repeatability of the measurement and to evaluate whether the relationship between HIE severity and StO_2 is affected by StO_2 algorithm choice.

The monitoring of infants with HIE with NIRS has been one of the main interests of the Multimodal Spectroscopy group for several years. CYRIL was already used in the NICU for

monitoring of infants within the first days of life for several years, which simplified the preparation of the study protocols for this data collection. The measurement of StO_2 has until now not been a target of the clinical studies.

The aim of this chapter is to demonstrate proof of principle that BRUNO can be applied to data collected in neonates and used for the recovery of StO_2. The data presented is from pilot studies; the clinical data collection was part of the Baby Brain Study at UCLH. CYRIL 2 was used for the collection of data in neonates during session 2 (see details in section 5.4.2) which ran from January to December 2019.

9.2 Methods

The target subject group for the Baby Brain Study session 2 were full term infants born at UCLH or transferred to the NICU at UCLH for the treatment of moderate or severe HIE. The aim was to start monitoring infants enrolled for hypothermia treatment as soon as possible after birth. It was planned to measure for as many days as possible with continuous data collection of at least one hour. The clinical team was responsible for subject recruitment and obtaining informed consent.

A secondary aim of the second session of the Baby Brain Study at UCLH was to assess the repeatability of the measurement through the performance of several short CYRIL measurements consecutively in a short time frame. The short measurement would be performed either before starting the long measurement, or afterwards, at least once in each enrolled infant.

9.2.1 Ethical approval

The measurement of StO_2 with CYRIL was part of the UCLH Baby Brain Study; approved by the NW London Research Ethics Committee 2 (Reference 13/LO/0225) and registered with the Research and Development Department of UCLH (Reference 13/0013). Dr Subhabrata Mitra was registered as a clinical co-investigator.

Parents of infants with suspected hypoxia were approached by Dr Subhabrata Mitra, who explained the aims of the study and the process of the data collection, which included a NIRS study and MRI. They were also given an information leaflet. Parents who agreed to participate were asked to sign a consent form. The consent form can be found in Appendix A. As the aim was to start the measurement as soon as possible after birth, if a parent was not present when the baby arrived at the NICU, telephone consent was an option, with a written confirmation collected after the parent's arrival.

9.2.2 Recruited infants

The treatment and monitoring of neonates with HIE diagnosis at the NICU was the same as during the first session of CYRIL measurements described in section 5.4.1. The aim was to recruit approx. one infants weekly/bi-weekly. The measurement period was later extended to increase the sample size. Over all, 3 infants were monitored with CYRIL 2 in the year 2019. Their clinical details are reported in Table 9.1. Babies A and C were monitored on two consecutive days.

Table 9.1: Clinical details of subjects monitored during the second session of the Baby Brain Study at UCLH. GA - gestational age. Measurements with a star are days when the repeatability study was also performed. Lac/NAA of 0.15, 0.17 and 0.18 suggest mild HIE.

	Baby A	**Baby B**	**Baby C**
GA [weeks + days]	39 + 5	38 + 4	40 + 5
Gender	F	M	F
Birth weight [kg]	3.3	3.2	2.3
Lac/NAA [-]	0.15	0.17	0.18
Age at measurement start [h]	42*	57*	46*
	62*		67

9.2.3 Measurement protocol

The measurement protocol was similar to the protocol in session 1 (described in section 5.4.1). The protocol was slightly changed throughout the first few studies as additional requirements were identified. The finalised study protocol for session 2 of the UCLH NICU measurements as part of the Baby Brain Study was:

1. Obtain informed consent from parents.
2. Move the CYRIL system to the cotside. Connect to the mains power supply, turn on power source and the isolation transformer.
3. Turn on the CYRIL VI on the CYRIL laptop and start cooling the CCD. Close light source shutter, turn the light power on.
4. Connect external hard drives and the Phillips Intellivue monitor to the laptop.
5. Clean and disinfect optodes and cables using anti-bacterial wipes.
6. Fill in information about the study in the "Study baby details.xlsx" file on the laptop's "Desktop" folder.
7. Check that acquisition rate is set to 1 second and that DPF is set to 4.99 in VI.

8. Once the CCD finished cooling to the required temperature, a window with the text "System ready" appears. Press "OK".

9. Place double-sided tape on the edges of the probe holder, making sure not to cover the fibres.

10. Check the light source shutter is closed.

11. Place the probe holder firmly on the subject's forehead and tuck under the EEG cap.

12. Enter file name "CYRIL(*number*)_Day(*age*)_background" on the main VI screen. Start the measurement and take a ten iterations long measurement of the background light signal.

13. Change file name to "Cyril(*number*)_Day(*age*)".

14. Open light source shutter and start measurement. Check that there are no light artefacts and the signal is good: if the CCD is saturated, a window will appear saying so and the measurement will automatically stop. In that case, reduce acquisition rate from 1 second until CCD no longer saturated. Make sure that the signal intensity is high enough: when looking at the Spectra tab in the VI, the furthest away detectors (4 5) should have at least around 22000 - 25000 counts at the peak of the spectrum. If that is not the case, make sure tissue/probe contact is good, increase acquisition rate if necessary.

15. Start ixTrend data collection.

16. Aim for at least one hour measurement.

17. Stop the data collection in the VI and ixTrend, turn off light source.

18. Remove NIRS probes from the subject's forehead.

19. Clean and disinfect optodes and cables using anti-bacterial wipes.

20. Change file name to "CYRIL(*number*)_Day(*age*)_noise". Close CCD shutter, start measurement and measure the noise for at least ten iterations. Stop measurement and close the VI.

21. Disconnect ixTrend and hard drives. Turn off the laptop, the transformer and the power supply. Disconnect the system from the main power supply.

9.2.3.1 Repeatability measurement

The aim of the repeatability study was to collect multiple consecutive short measurements in each infant. The protocol was designed with 5 measurements of 10 acquisitions at 1 s acquisition rate each in one infant. An important constraint in the design of the measurement was that it had to be quick and efficient, not to obstruct the normal work flow of the staff at the NICU. The measurements could be taken either before or after the main measurement, at least once for each infant. Physiological data was not collected during the precision study.

The measurement set-up was similar to the protocol described above, with the following differences:

- File name "CYRIL($number$)_Day(age)_resit_$number_of_repetition$".
- The probe holder was not attached with double sided tape but held in place by hand.
- Each measurement was 10 acquisitions long. The measurement was stopped, the light source shutter was closed and the probe holder was lifted and placed on the same location. The file name was changed to the subsequent repetition number.
- 5 repetitions were performed.

9.2.3.2 Reference spectra

Reference spectra were collected regularly to measure the output spectrum of the light source. The aim was to collect a reference spectrum for each subject. This was often performed in the NICU waiting area so as not to disturb the clinical team at the cotside. The process was as follows:

1. With CYRIL turned on, hard drives connected, the CCD cooled and the light source on (with shutter closed), place the light source fibre head into the slit on one end of the reference tube.
2. Place 4 detectors, either 1234 or 5678, in the probe holder on the opposite end of the reference tube.
3. Reduce acquisition rate to 0.1 s, open light source shutter.
4. Change file name to "CYRIL($number$)_Reference($detectornumbers$)".
5. Start measurement. If CCD saturated, reduce acquisition rate.
6. Collect at least 10 spectra.

7. Stop measurement. Swap detectors, change file name and take another 10 spectra.

8. Turn off the system.

9.2.4 Data analysis

The data were processed in MATLAB. A custom function was used to load the raw CCD data and sum it according to binning, the standard binning width of 20 strips per detector was used. Background CCD noise was removed by subtracting the separate noise or background light file. Attenuation and reflectance were calculated for each spectrum and a slope of attenuation against distance was calculated for the left side (LS) channel, detectors 1–4, and the right side (RS) channel, 5–8. Differentiation of the attenuation slope was performed with the MATLAB function $diff$. Reflectance spectra and the attenuation slopes were smoothed with a 5-step moving average filter prior to differentiation.

The same script applying BRUNO, SRS and BF as used in the phantom measurements was used with the baby data. The MATLAB script to run BRUNO on broadband multidistance NIRS data is available on GitHub [272].

9.2.4.1 Data quality scoring system

Previous analysis with BRUNO was performed on high quality data collected in optical phantoms, an example of a suitable fit is in Figure 9.1. The most straightforward way of inspecting the data and the BRUNO fit was to display the fit and see how well the model matches the main spectral features, in particular the water feature at 830 nm and the water/haemoglobin peak and dip around 750 nm. This was done for a few spectra. As all data from the phantom were of high quality and the fit looked very good in all instances, no data were excluded from the analysis.

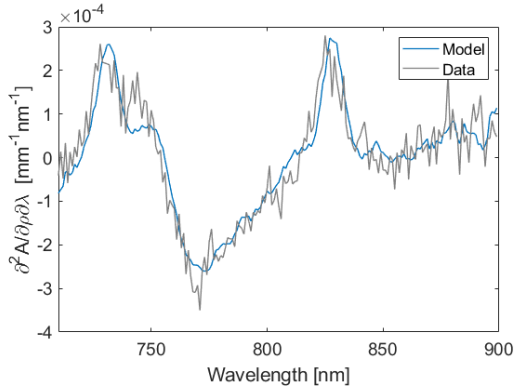

Figure 9.1: Example of a good BRUNO fit on a high-quality spectrum collected during a deoxygenation of the homogeneous phantom.

Compared to the phantom data, the baby data were more noisy with fewer distinct spectral features. Relying on visual inspection of the data is timely and not suitable for the analysis of long measurements. Instead, a scoring system was developed to evaluate BRUNO fit and data quality. A score was given to each BRUNO analysis of an individual spectrum, the aim was to have the lowest score possible.

The scoring system was developed empirically based on the assessment of BRUNO fits. This assessment was based on visual inspection of overall data quality and the closeness of the fit. A good data set had to have a clearly distinct water peak at 730 nm and at 830 nm, and a haemoglobin feature at 770 nm. The model had to closely follow the shape of the data. Examples of good and bad data and fit example are shown in Figure 9.2; the good data had distinct haemoglobin and water absorption features which are followed by the model. The bad data did have a haemoglobin absorption feature, but the water peak at 830 nm was less distinct. The model did not follow the shape of the data very well.

The scoring system was a quantification of such subjective measures of data and fit quality. The first metric included in the score calculation was the sum of squared residuals of the fit, measuring the closeness of the model to the data. As the sum of residuals depended on the value of the individual slope differential, the data were first normalised. The normalisation was performed at the maximum of the model and did not change the distribution of the residuals.

Plotting the distribution of squared residuals over the wavelength range helped identify regions where the fit performed poorly. The summed residuals of the data against wavelength are shown in Figure 9.2c and d. If the quality of the fit was poor, the highest residuals were in the region of the haemoglobin dip, 750–770 nm, and the water peak, 825–840 nm. Residuals at other wavelengths were mostly due to random noise.

The first step in calculating the score of the fit was calculating the sum of squared residuals between 750–770 nm and 825–840 nm. These two numbers were multiplied. The obtained number already gave an indication on the quality of the fit, for example, the good fit in Figure 9.2a led to the number 2.22, while the bad fit in Figure 9.2b led to the number 16.23.

Calculating this number for different data sets showed that it did not sufficiently capture the quality of the data analysis. While the quality of the fit is indeed guided by the sum of residuals, if the data were not of sufficient quality, it would lead to a good fit but not the desired StO_2. An example of poor data with low residuals is shown in Figure 9.3. The number obtained by multiplying the residuals at the haemoglobin dip and the water peak was also 2.22.

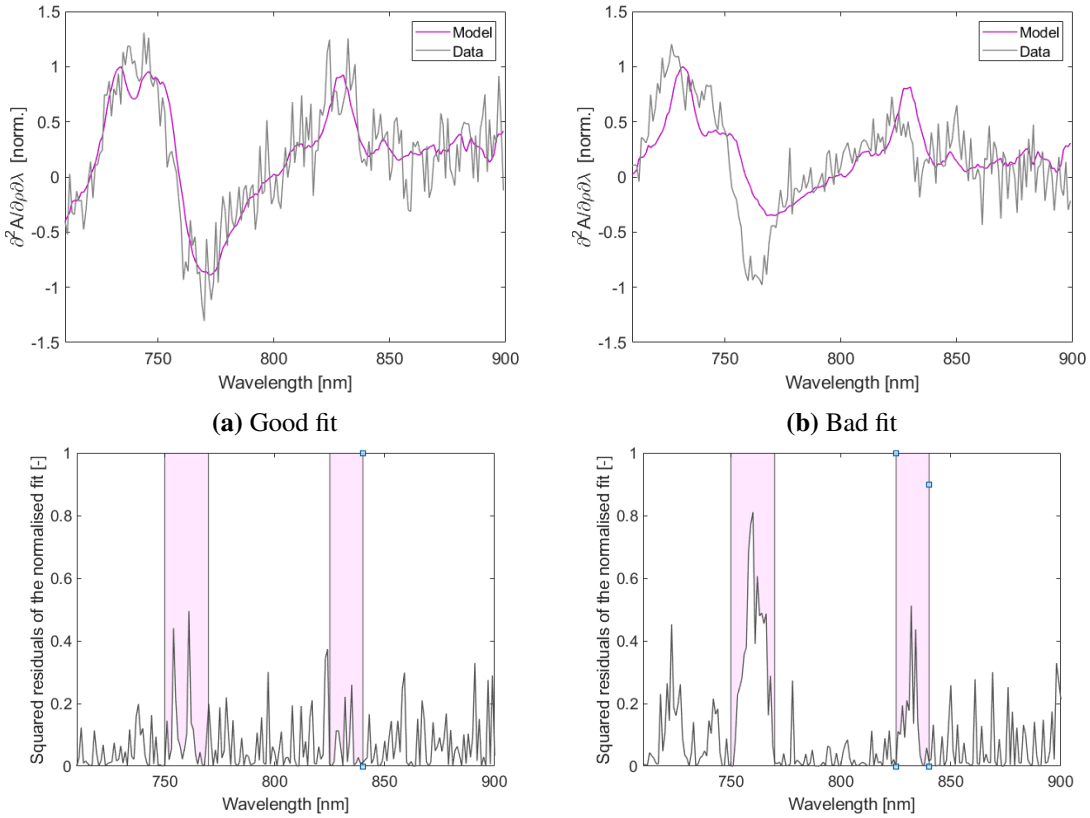

(a) Good fit

(b) Bad fit

(c) Good fit, sum of squared residuals in region of interest = 2.22.

(d) Bad fit, sum of squared residuals in region of interest = 16.23.

Figure 9.2: Example of a good and a bad BRUNO fit on data collected in baby C and the corresponding residuals of the normalised BRUNO fit. The goodness of fit was based on visual inspection of the data. The data and the model were normalised at model maximum prior to plotting. In (c) and (d), highlighted are the regions of interest where the residuals are summed for the score calculation. The data were collected in baby C with detectors 1–4, LS channel, in the good case and 5–8, RS channel, in the bad case.

The main difference between the data in Figure 9.3 and the good data in Figure 9.2a is that the spectral features are less distinct; the differentiated slope looks flatter. Therefore, the second step in the calculation of the score was to rate the quality of data based on the visibility of spectral features. If a spectrum was flat, it was penalised. The range of the slope differential was calculated as the distance between the maximal and minimal value of the fitted model. The final score was then calculated by multiplying the residual product and the reciprocal of the range. The final score of the good data example in Figure 9.2a was 1.18, the bad fit in Figure 9.2b had a score of 12.03 and the poor data fit in Figure 9.3 scored 2.55. After calculating the score and visually inspecting 40 spectra collected in multiple infants, at different time points, with different detectors, the threshold for good vs. bad fit for use in baby measurements was selected to be 2.

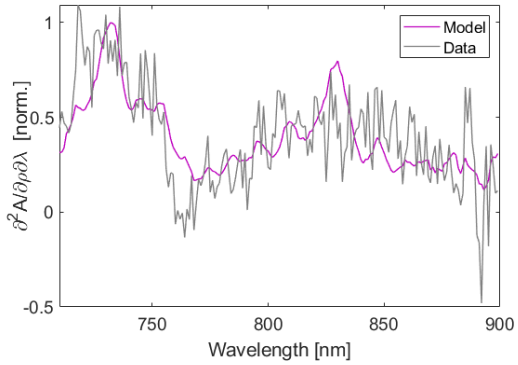

Figure 9.3: Example of a normalised BRUNO fit with small residuals but poor data quality. Data were collected in baby C with detectors 7–8.

9.2.4.2 Application to measurements

The score was calculated for each time point of the measurements. Individual spectra with a score above 2 were not immediately rejected, as noise and other random errors could penalise a fit which, upon visual inspection, looked good. Instead, the score was used for guidance. Figure 9.5a shows the scores of a whole measurement with good fit quality. The score was higher than 2 at several points, looking at Figure 9.5b suggests that it was mostly due to movement artefacts. The average score for that measurement was 1.25 so the data were used for further analysis. The flowchart in Figure 9.4 summarises the whole fit and data scoring procedure. If a data set was excluded from the analysis based on the mean score being larger than the threshold value of 2, it was not analysed using any other StO_2 algorithm. Data sets with a satisfactory score were analysed with BF, SRS and BB SRS using the same scripts as used in the analysis of phantom data. SRS, BRUNO and BB SRS was performed at 15–30 mm BF at 30 mm SDS. The boundary conditions were set based on the measurements of optical properties in neonates reported [108] and were set quite broad in order to allow for dramatic changes in optical properties during pathophysiological events occurring in the injured brain; they are listed in Table 9.2.

One StO_2 trace per algorithm was obtained for each measurement. The agreement of the four different results was assessed through pair-wise Spearman correlation, plotting of scatter plots and non-parametric Bland-Altman analysis [275] using the MATLAB add-on *Bland Altman* available online [273].

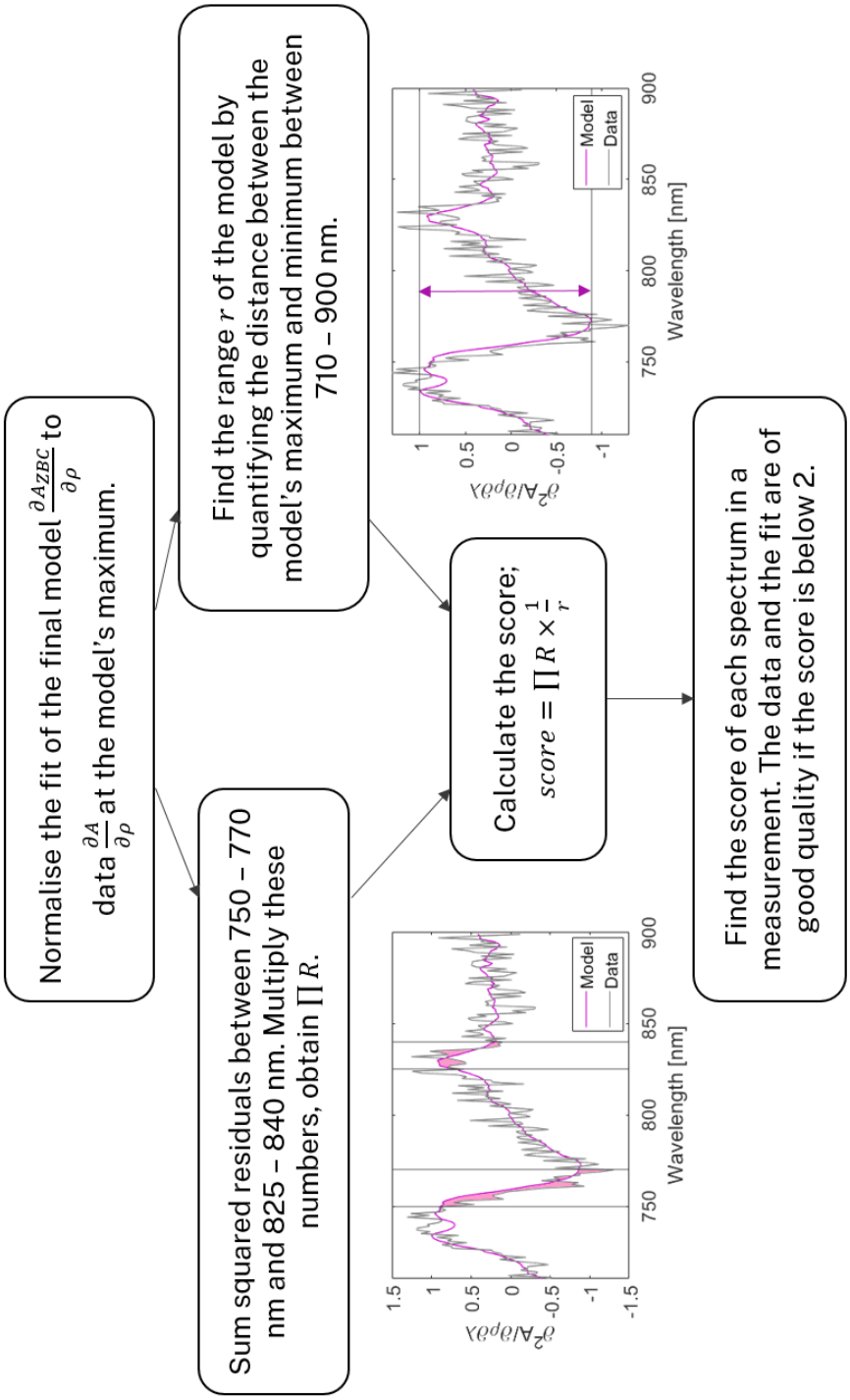

Figure 9.4: Flowchart describing the process of assessing the quality of a BRUNO fit through the calculation of a score. The threshold of 2 was guided empirically and is not exclusionary.

Table 9.2: Boundary conditions for analysing baby data with BRUNO.

	WF [%]	$\mathbf{c_{HHb}}$ [μM]	$\mathbf{c_{HbO_2}}$ [μM]	**a** [mm$^{-1}\mu$ m^{-1}]	**b [-]**
Start	80	40	100	0.5	0.5
LB	50	0	0	0.1	0.1
UB	95	70	160	2	2

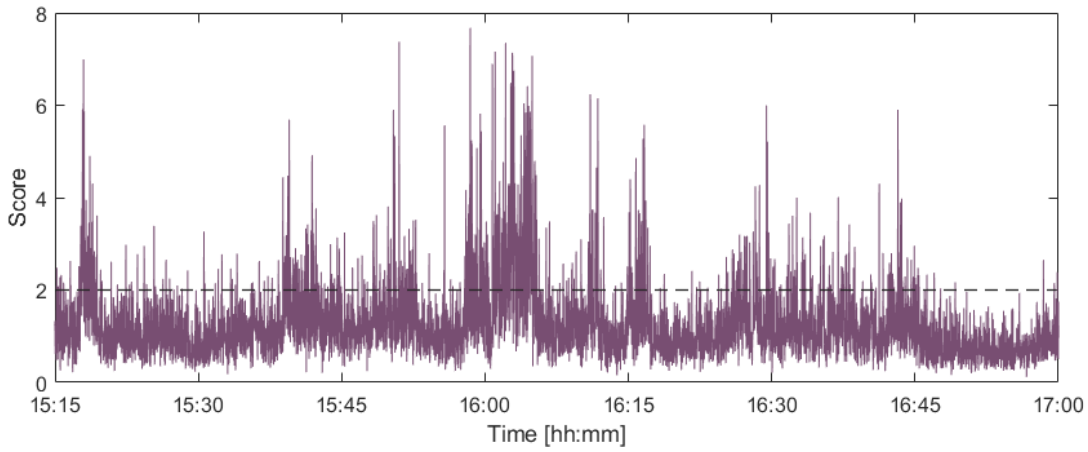

(a) The score calculated at each time point with the threshold of 2 indicated.

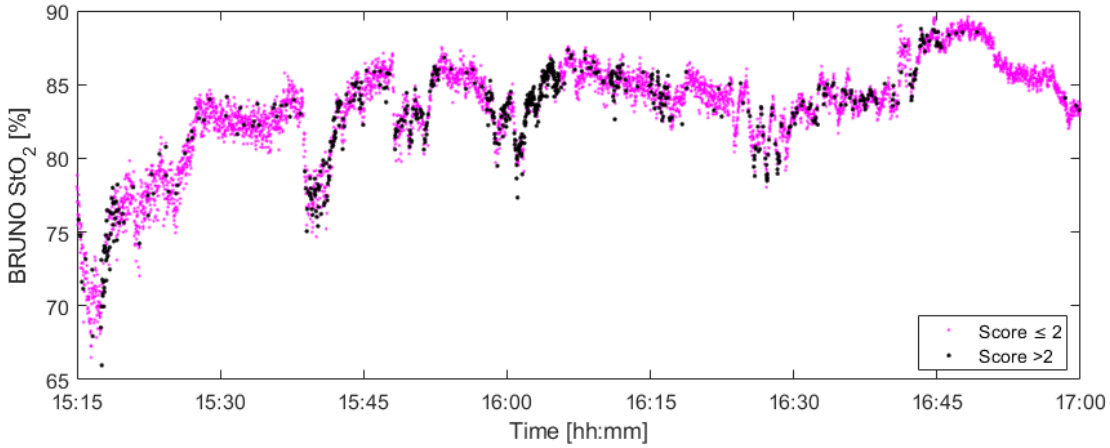

(b) StO_2 calculated with BRUNO, time points where score was above 2 are highlighted.

Figure 9.5: The score calculated for a whole measurement with the corresponding StO_2. The data were collected in Baby C with detectors 1–4.

9.2.4.3 SpO_2

The main quantity of interest collected with the monitor IntelliVue (Philips Healthcare, UK) was SpO_2 measured with pulse oximetry. Changes of SpO_2 from baseline were identified through visual inspection. As the distribution of the data was not normal, correlation with the StO_2 measurements was assessed with Spearman's rho.

9.2.4.4 Repeatability

For the repeatability measurement, to capture the different trend of algorithms within a measurement, the standard deviation σ_{block} and the mean StO_2 for each block per algorithm were calculated. According to [276], repeatability is calculated from the within-subject standard deviation σ_{subj} obtained from mean StO_2 values across all subjects. While repeatability measurements were conducted in 3 infants, 2 had to be excluded because of poor data quality. Consequently, due to the sample size of 1, repeatability could not be calculated. Instead, the change of StO_2 between blocks was measured as the variability of the StO_2 reading between-measurements σ_{intra}; calculated as the standard deviation of the 5 mean block StO_2 values per subject per algorithm.

To summarise the oxygenation differences between the algorithms, a total average StO_2 was also calculated as the mean value of the 5 block StO_2 values. The average σ_{inter} was defined as the mean of the five block measurements of σ_{inter}.

9.3 Results

In total, 5 long measurements were collected and 4 precision measurements in 3 subjects. The mean length of a long measurement was 2 hours 15 minutes, ranging from 1 h 21 min to 3 h 25 min. Mean scores were calculated for all long measurements and the precision measurement sets; results from the mean measurement are shown in Table 9.5. All data from baby A, day 3 and baby B were excluded from the analysis based on low BRUNO fit quality, the mean scores were above 2 in the long measurements and also in the short resitting measurements on both measurement channels. Data from the LS channel on baby C passed the score requirements and was included for analysis.

Table 9.3: The mean scores of long measurements in all subjects. LS channel corresponded to detectors 1–4 and RS channel to detectors 5–8.

Channel	**Baby A**		**Baby B**	**Baby C**	
	Day 2	Day 3	Day 3	Day 2	Day 3
LS	14.07	27.17	66.68	**1.25**	**1.50**
RS	14.78	93.89	145.86	10.39	25.68

9.3.1 StO_2 in baby C

Data collected on the LS in baby C were analysed with all 4 algorithms. An example of the BRUNO fit when applied to the LS data is shown in Figure 9.2a. Figure 9.7 shows the recovered oxygenation with all algorithms on both days of life.

The overall trend of oxygenation over time was similar across all algorithms, the main differ-

ence was in the dynamic range, both within-day and between-days. Multiple desaturation events were identified in the traces, Figure 9.6 shows StO_2 during two deoxygenation events measured on day 2; StO_2 was normalised to the beginning of the drop. The difference between StO_2 at the beginning of the desaturation and nadir depended on the algorithm; the speed of the response was similar. The overall agreement on the trend was assessed through correlation; scatter plots comparing BF, SRS and BB SRS to BRUNO are shown in Figure 9.8 for both days. Table 9.4 shows the correlation coefficients ρ_s for all algorithm pairs for measurements on day 2 and day 3.

Table 9.4: Spearman's rho measuring the correlation of StO_2 recovered with 4 different algorithms. ρ_s= 0 means no correlation, ρ_s = 1 indicates high correlation. Two rows are shown for each algorithm; the first row is for measurements from day 2 and the second row for measurements from day 3 in baby C.

ρ_s	**BRUNO**	**BF**	**SRS**	**BB SRS**
BRUNO	1	0.88	0.54	0.64
	1	0.59	0.81	0.84
BF		1	0.62	0.70
		1	0.75	0.80
SRS			1	0.91
			1	0.95
BB SRS				1
				1

Figure 9.8 shows that all algorithms mostly followed a similar trend to BRUNO. The behaviour is different between days 2 and 3. On day 2, BF and BRUNO StO_2 increased within the first 15 minutes, while BB SRS and SRS kept a stable baseline throughout the whole measurement. An offset between BRUNO and BF StO_2 is seen (which increases with StO_2) and high correlation. The trace of BB SRS and SRS remained relatively flat throughout the measurement.

The situation changed on day 3. Oxygenation remained relatively flat in all algorithms; SRS and BB SRS followed the same trend as BRUNO with a smaller dynamic range and a higher baseline, resulting in a higher ρ_s than on day 2. BF followed a similar baseline to BRUNO but the trend was slightly different, reflected in a decrease in ρ_s from day 2 to day 3. The decreased dynamic range of SRS, BB SRS and BF compared to BRUNO on both days is shown by the slope of the regression line in the scatter plots. The correlation between SRS and BB SRS was high on both days as the main difference between the two StO_2 traces was a baseline offset.

The agreement between the methods is further displayed in Bland-Altman plots, Figure 9.9. In Bland-Altman analysis, the methods give similar results if the distribution of the differences between the readings is close to the mean (median in the non-parametric case) of these differ-

ences. As seen in Figure 9.9, the distribution of the differences between BRUNO StO_2 and StO_2 recovered with other algorithms is skewed in all cases apart from Figure 9.9a, where BRUNO is compared to BF on day 2. BRUNO and BF gave similar results, although BF measured an StO_2 on average 5.1% lower. The agreement of BRUNO with BF on day 3 and with SRS and BB SRS was poor.

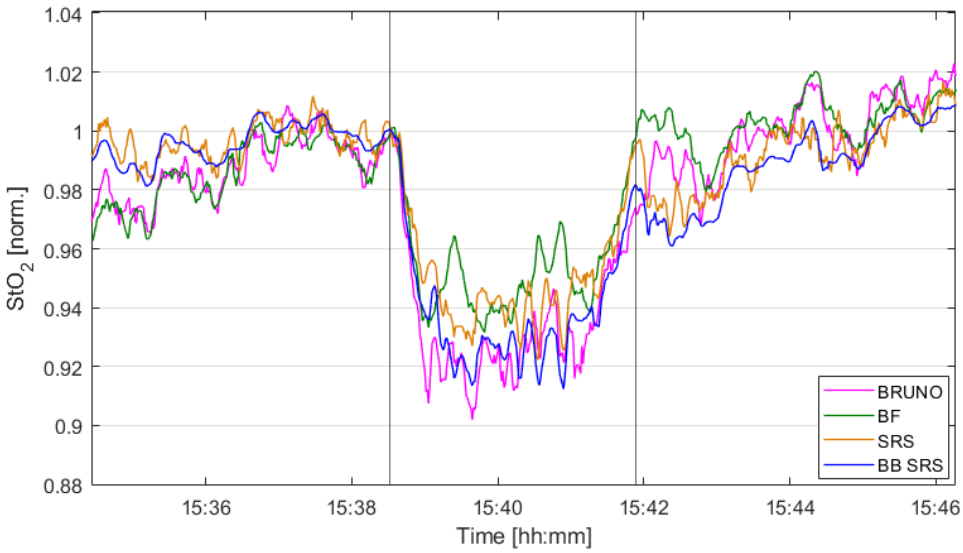

(a) Day 2

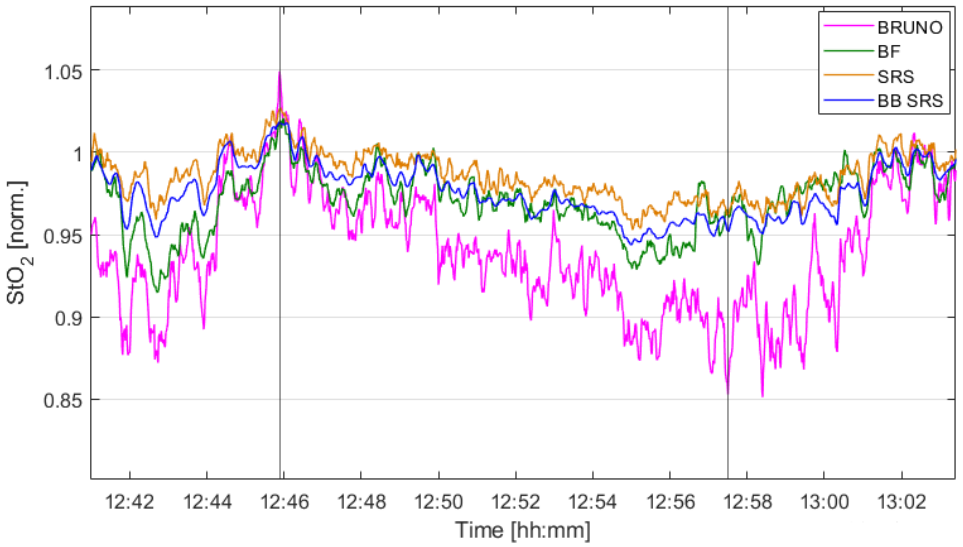

(b) Day 3

Figure 9.6: StO_2 during two selected deoxygenation events in baby C on day 2 and day 3 of life recovered with BRUNO, BF, SRS and BB SRS measured on the LS.

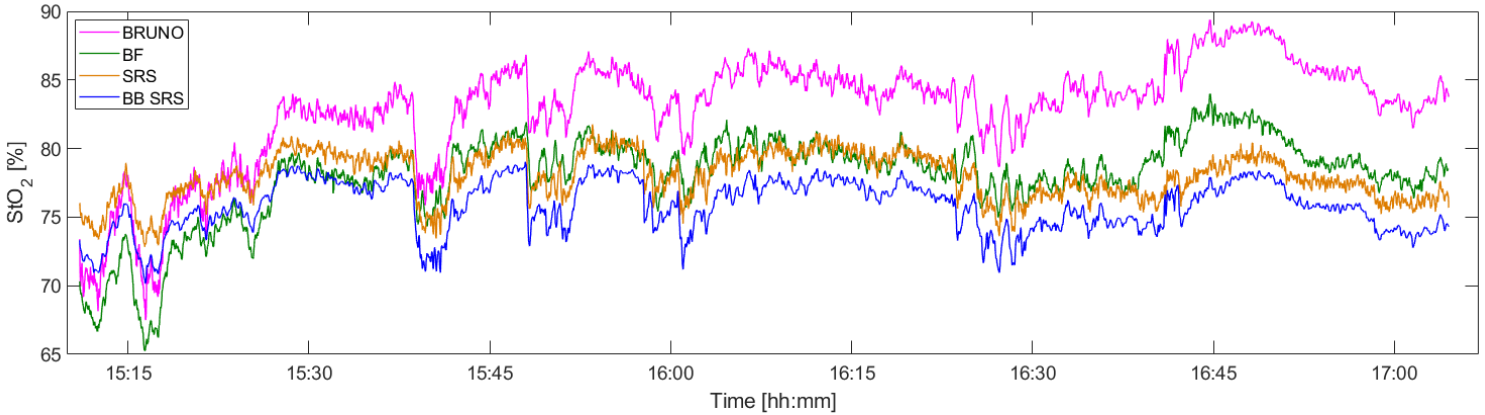

(a) Day 2

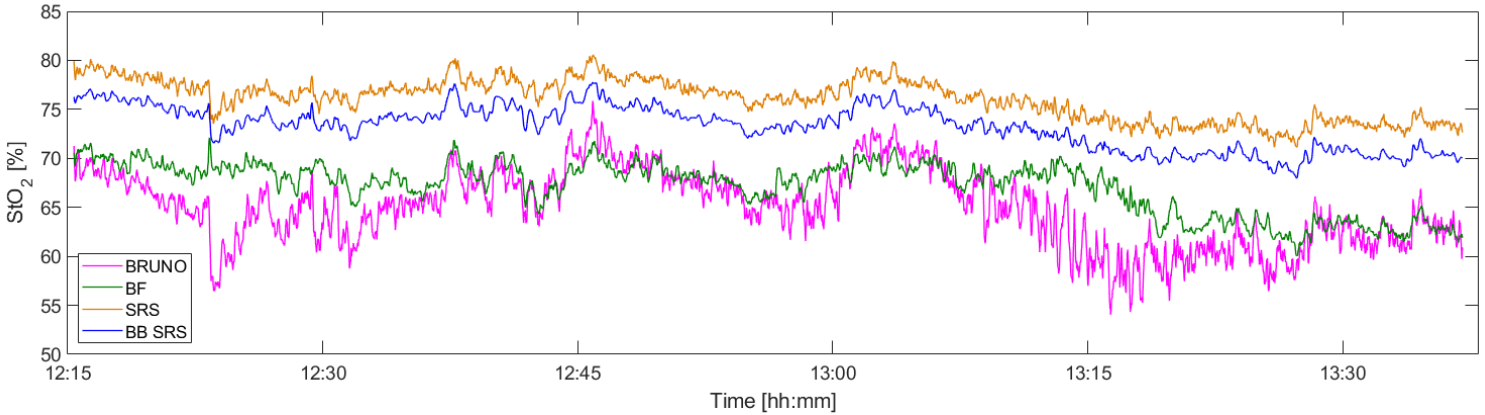

(b) Day 3

Figure 9.7: StO_2 in baby C on day 2 and day 3 of life recovered with BRUNO, BF, SRS and BB SRS measured on the LS. Data were smoothed with a 5-step averaging filter prior to plotting.

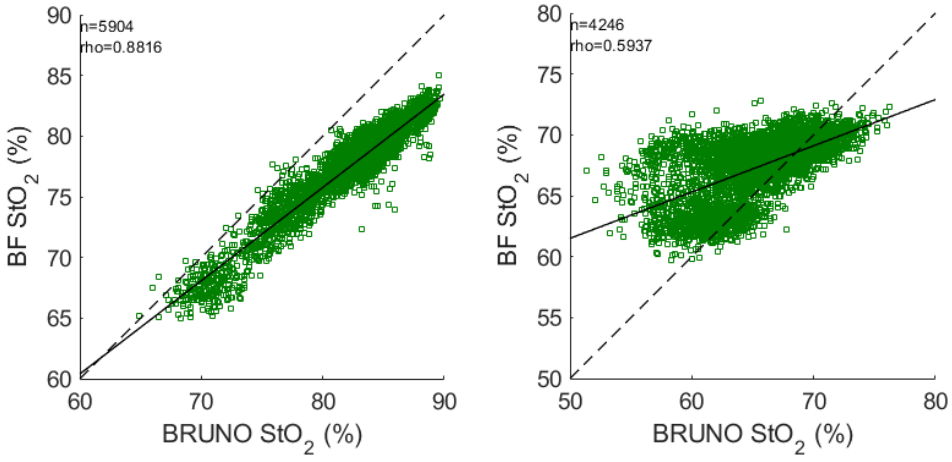

(a) Day 2: BRUNO vs. BF

(b) Day 3: BRUNO vs. BF

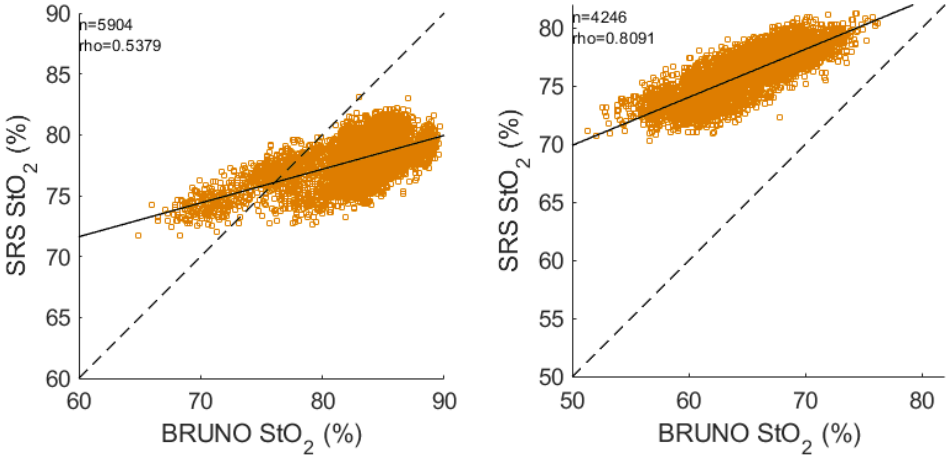

(c) Day 2: BRUNO vs. SRS

(d) Day 3: BRUNO vs. SRS

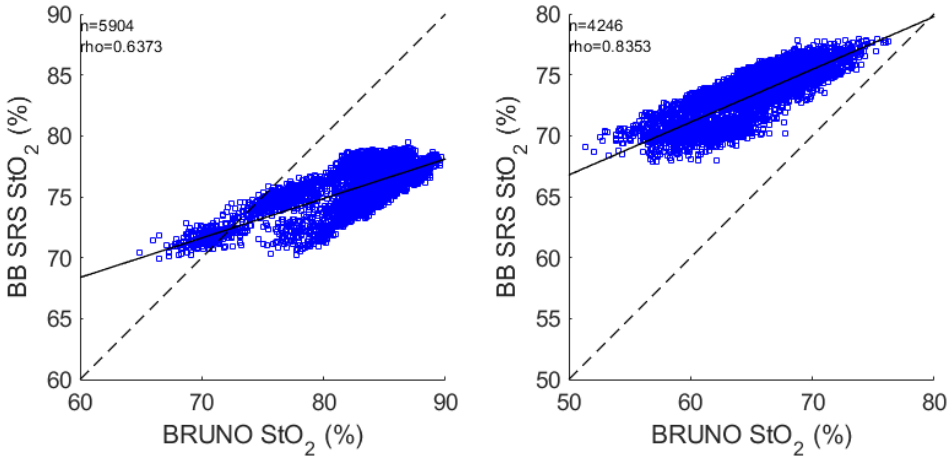

(e) Day 2: BRUNO vs. BB SRS

(f) Day 3: BRUNO vs. BB SRS

Figure 9.8: The correlation between StO_2 measured with BRUNO vs. with BF/SRS/BB SRS on day 2 and day 3 collected in baby C. rho stands for ρ_S, Spearman's correlation coefficient.

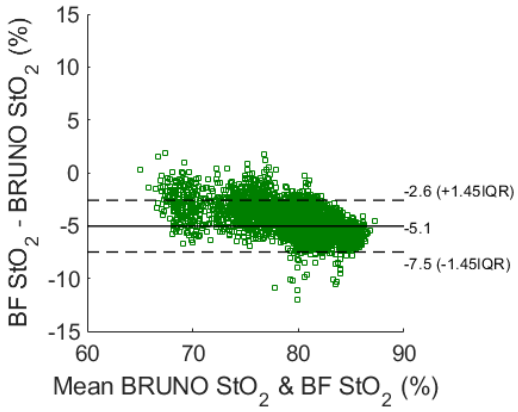

(a) Day 2: BRUNO vs. BF

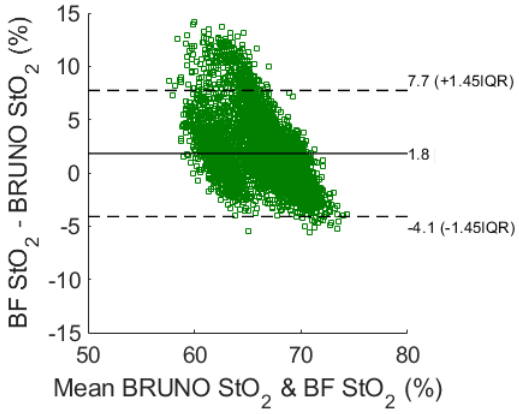

(b) Day 3: BRUNO vs. BF

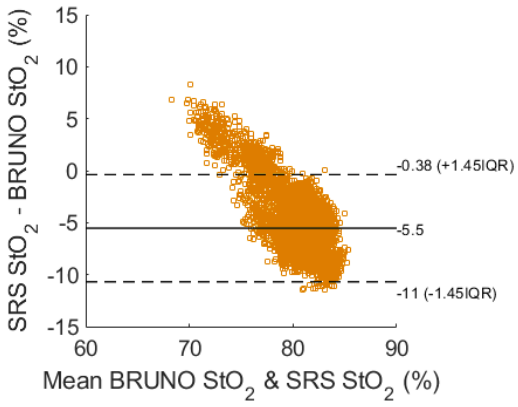

(c) Day 2: BRUNO vs. SRS

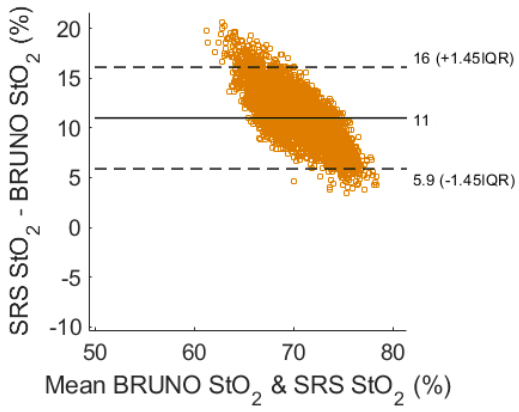

(d) Day 3: BRUNO vs. SRS

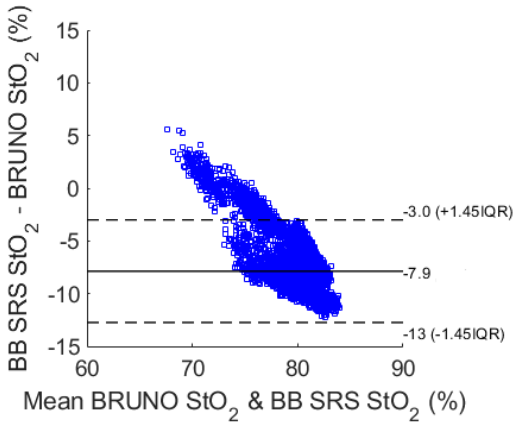

(e) Day 2: BRUNO vs. BB SRS

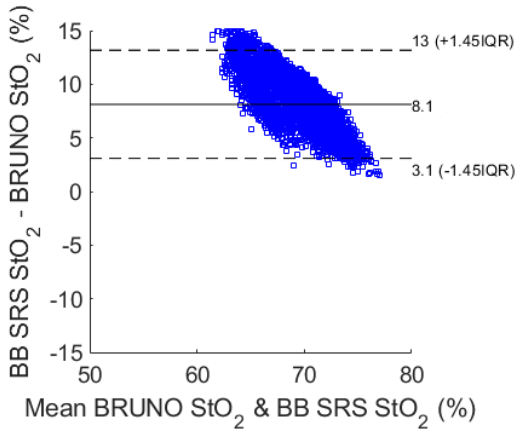

(f) Day 3: BRUNO vs. BB SRS

Figure 9.9: Bland-Altman analysis of StO_2 measured with BRUNO vs. with BF/SRS/BB SRS on day 2 and day 3 collected in baby C. The full line indicates the median difference between the two algorithm's results. IQR stands for inter-quartile range.

Table 9.5: Mean StO_2 on day 2 and day 3 in baby C measured with all algorithms. σ - standard deviation.

	Mean StO_2 (σ) [%]			
	BRUNO	BF	SRS	BB SRS
Day 2	82.9 (4.0)	78.0 (3.2)	78.0 (1.8)	75.8 (1.9)
Day 3	64.9 (4.1)	67.2 (2.6)	76.1 (2.1)	73.2 (2.2)

The mean StO_2 for each algorithm on both days are reported in Table 9.5, mean StO_2 on day 2 was highest with BRUNO, lowest with BB SRS. On day 3, mean StO_2 was the highest with SRS and lowest with BRUNO. Cerebral oxygenation decreased between day 2 and day 3 in all algorithms; the distribution of StO_2 on both days for each algorithm is shown in Figure 9.10. The difference between the median StO_2 on day 2 and on day 3 was the highest in BRUNO; a decrease from 84% to 65%, much bigger than the decrease measured with SRS, from 78% to 76%.

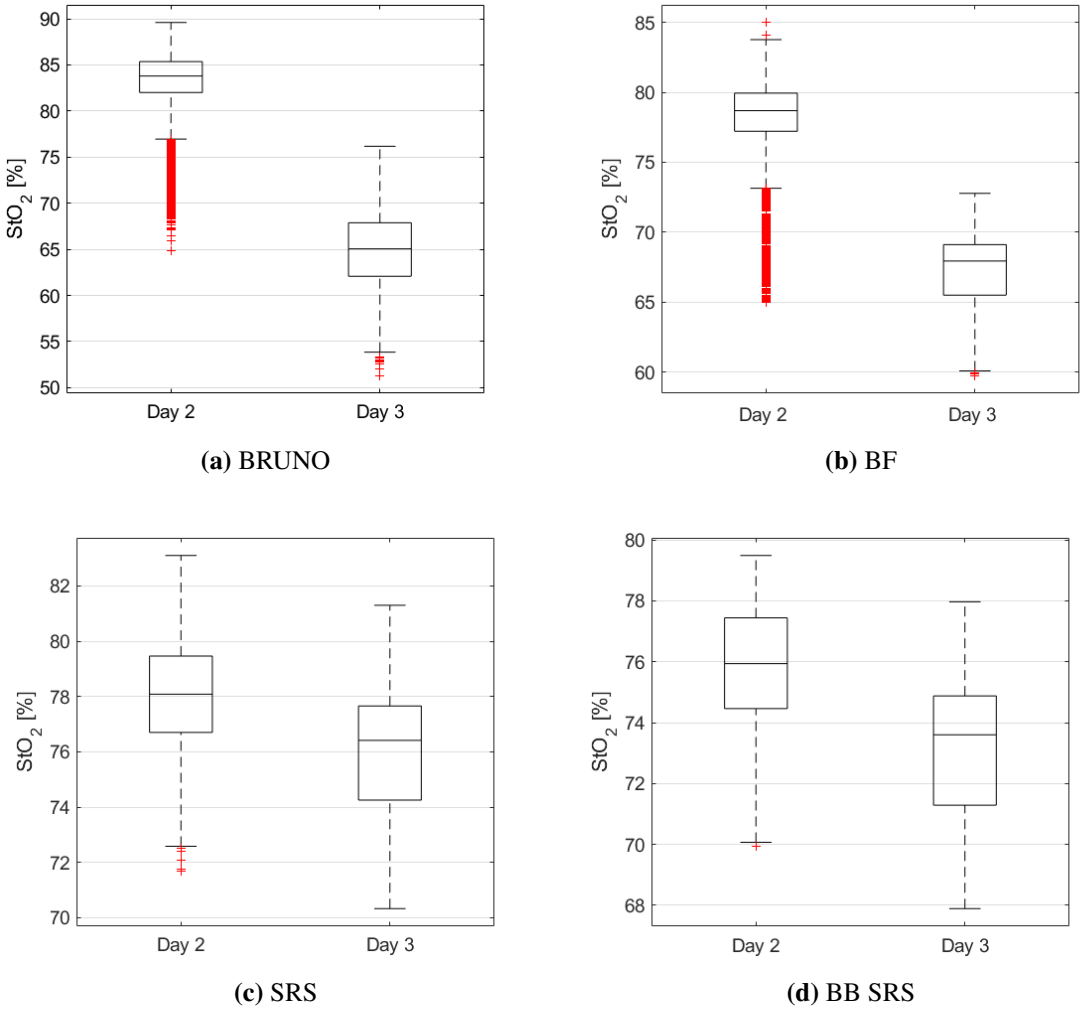

(a) BRUNO **(b)** BF

(c) SRS **(d)** BB SRS

Figure 9.10: The distribution of StO_2 grouped by day of life, recovered with BRUNO, BF, SRS and BB SRS measured on the LS.

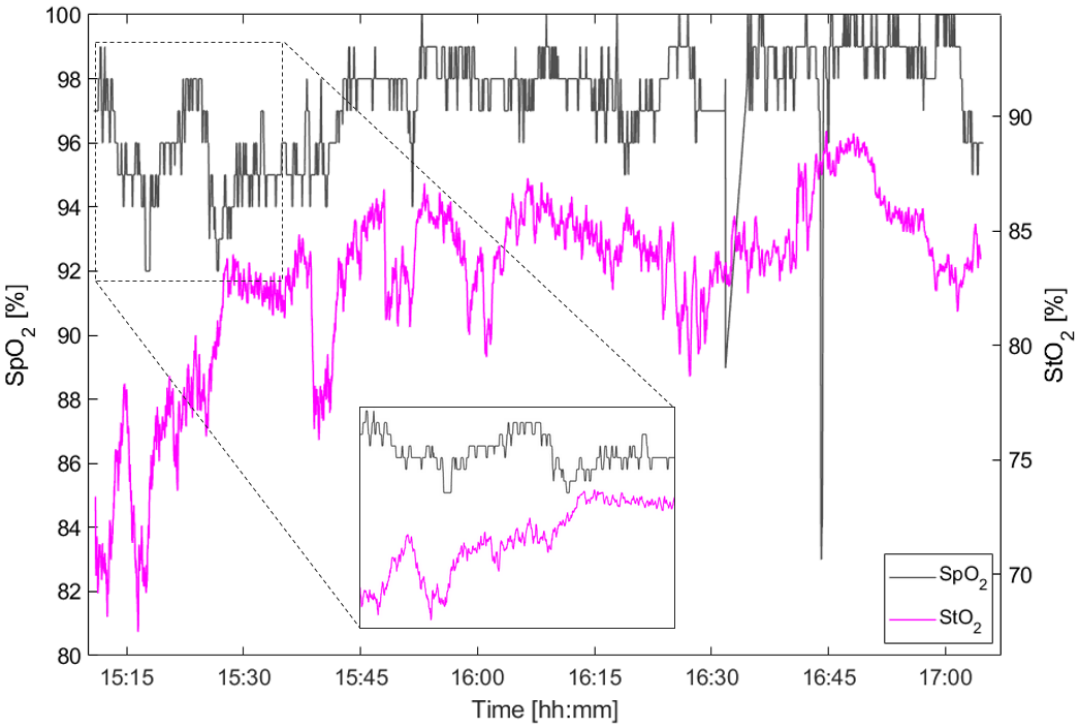

(a) Day 2

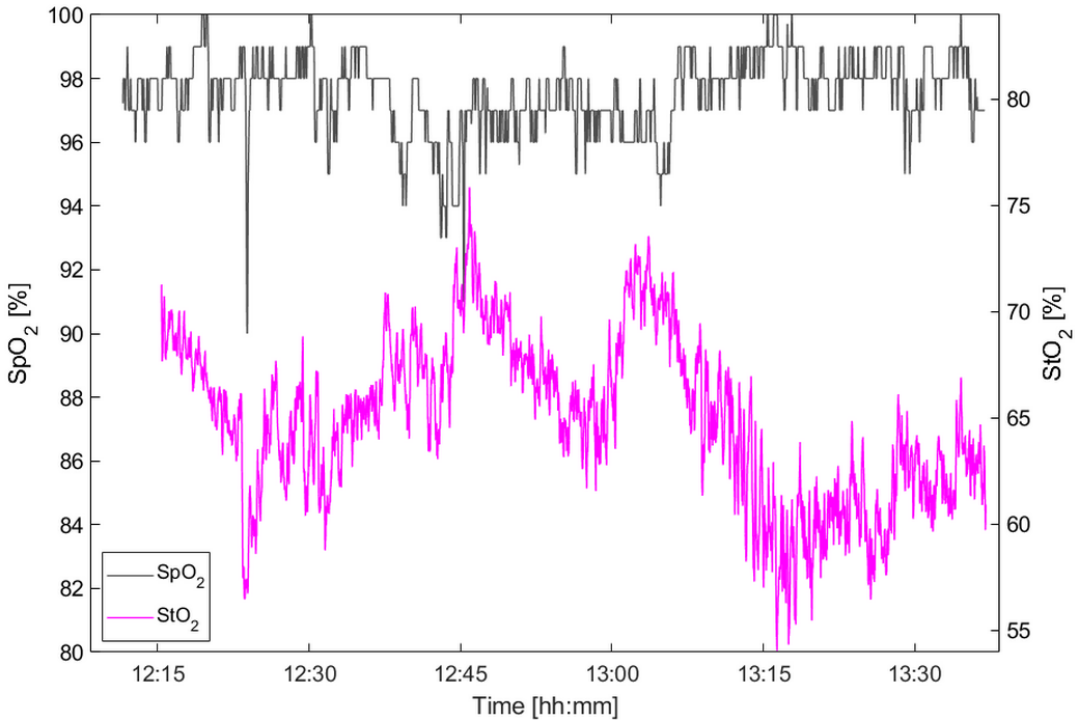

(b) Day 3

Figure 9.11: SpO_2 measured with pulse oximetry and StO_2 measured with BRUNO on days 2 and 3 in baby C, LS. The StO_2 trace was smoothed with a 5-step moving average filter prior to plotting.

9.3.2 Relationship between StO_2 and SpO_2

SpO_2 measured with pulse oximetry and StO_2 calculated with BRUNO for both days are shown in Figure 9.11. The median SpO_2 on day 2 was 98%, 25–75th percentile 96–99%. The baseline on day 3 was the same; median SpO_2 was 98%; there were fewer changes over time and the 25–75th percentile was 97–98%.

Visual inspection showed that SpO_2 remained stable and desaturation events were small in amplitude. The largest desaturation events recorded were with a 5% decrease from baseline, both on day 2 between 15:15 and 15:30. StO_2 measured on the LS with any algorithm did not follow the same trend as SpO_2 during these events and also overall, as shown by a lack of correlation. The correlation between SpO_2 and StO_2 was measured with Spearman's correlation ρ_s and the results for both days are in Table 9.6.

Table 9.6: Spearman's correlation coefficients ρ_s for SpO_2 vs. StO_2 measured with all 4 algorithms on day 2 and 3 in baby C, LS, 15–30 mm SDS.

	ρ_s			
	BRUNO	BF	SRS	BB SRS
Day 2	0.53	0.41	0.00	0.04
Day 3	-0.42	-1.16	-0.36	-0.37

9.3.3 Repeatability

The repeatability study was performed on the second day of life in baby C. Data from the LS were analysed with BRUNO, BF, SRS and BB SRS. StO_2 was measured 5 times for 10 acquisitions and the results are shown in Figure 9.12; the mean StO_2 of each measurement block is reported in Table 9.7.

The difference between the readings of the four algorithms was in the magnitude of StO_2 and its change between blocks and in the dispersion of the data points within one measurement block. The behaviour was quantified using within-measurement SD σ_{block} and between-measurement SD σ_{intra}, reported in Table 9.7. BB SRS led to StO_2 with the smallest within-measurement variability (lowest σ_{block}), but large differences between the measurement sets (high σ_{intra}), while BF led to the most consistent readings between the measurements with lowest σ_{intra}. BRUNO StO_2 had the highest σ_{intra} and also σ_{block}.

The overall StO_2 averaged across all 5 acquisitions was algorithm-dependent, BB SRS measured the lowest total mean StO_2 of 71.6% and SRS measured the highest, 76.3%.

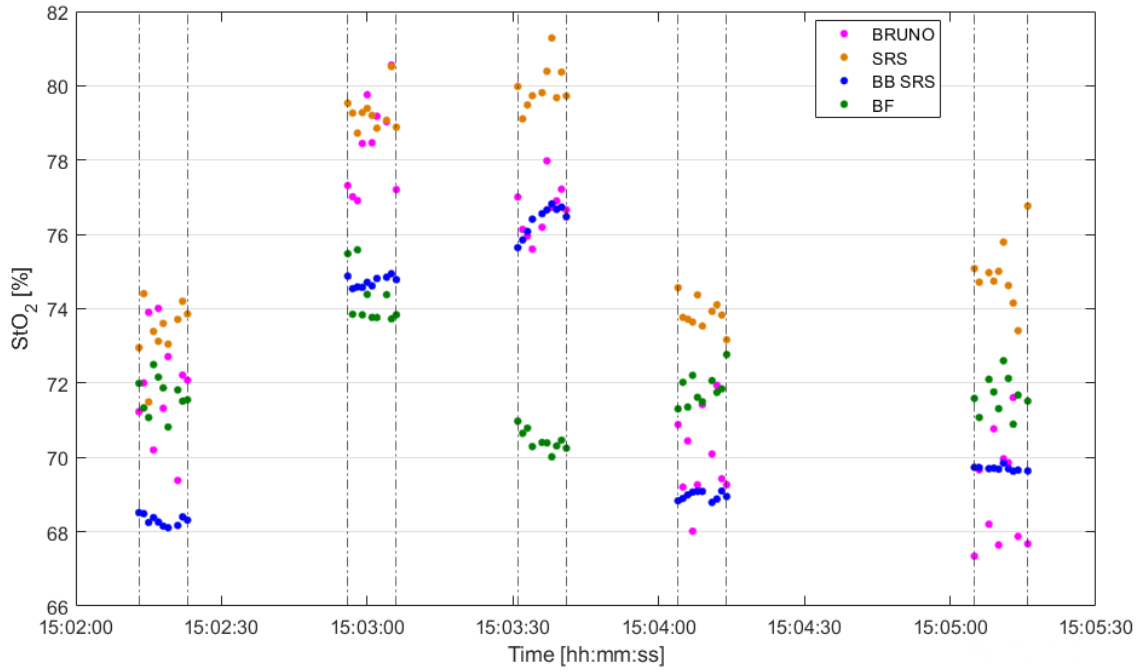

Figure 9.12: StO_2 measured with 4 different algorithms during 5 measurements during the precision study in baby C.

Table 9.7: The mean StO_2 for each block, the within-measurement standard deviation σ_{block} and between-measurement standard deviation σ_{intra} in the repeatability measurement in baby C, 15–30 mm SDS. The total StO_2 is the average of five mean StO_2 and mean σ_{block} is the average of the five σ_{block}.

Repetition	**Mean StO₂ (σ_{block}) [%]**			
	BRUNO	BF	SRS	BB SRS
1	71.9 (1.5)	71.7 (0.5)	73.4 (0.8)	68.3 (0.1)
2	78.4 (1.2)	74.3 (0.7)	79.3 (0.5)	74.7 (0.1)
3	76.6 (0.7)	70.5 (0.3)	80.0 (0.6)	76.4 (0.4)
4	70.0 (1.2)	71.8 (0.4)	73.7 (0.4)	69.0 (0.1)
5	69.1 (1.5)	71.7 (0.5)	74.9 (0.9)	69.7 (0.1)
Total StO_2	73.2	72.0	76.3	71.6
Mean σ_{block}	1.2	0.5	0.6	0.2
σ_{intra} [%]	4.1	1.4	3.1	3.7

9.3.4 Excluded data

9.3.4.1 Baby A & baby B

While data collected in baby A and baby B were excluded from the analysis, preliminary analysis of the measurements was useful for the improvement of the clinical measurements and inspired changes in the measurement protocol. These changes increased the quality of data collected in baby C.

The main source of poor data quality in the excluded measurements was poor probe-tissue contact, the quality of contact was decreasing with the increase of SDS. The effect of poor coupling was less visible on intensity spectra but became obvious when the attenuation slope was calculated and differentiated. An example of data collected with poor tissue-detector contact is shown in Figure 9.13a, Figure 9.13c and Figure 9.13e; $\frac{\partial A}{\partial \rho}$ was measured across different detector combinations to see the dependence of artefacts on SDS. The identification of the issue led to an improvement in data quality, shown in Figure 9.13b, Figure 9.13d and Figure 9.13f. The intensity spectrum with poor coupling shows a sharper dip at 760 nm, more obvious in $\frac{\partial A}{\partial \rho}$ and particularly in $\frac{\partial^2 A}{\partial \rho \partial \lambda}$. As this peak was not visible at shorter SDS and also not in the slope calculated across 15–20 and 15–25 mm, it was likely caused by external light reaching the detector at 30 mm due to peeling off the skin.

It is possible to recognise poor coupling even without external light reaching the detector. Note that while the attenuation slope in Figure 9.13c measured at 15–20 increases with wavelength, it flattens down with the increase of SDS, eventually decreasing with wavelength at 15–30 mm. The differentiated attenuation slope in Figure 9.13e also lacks most of the desired spectral features.

To overcome these issues, two changes were made to the measurement protocol. First, a new probe holder was designed with wider edges, increasing the area for tape placement and improving tissue contact. The newer probe holder is shown in Figure 5.8. Additionally, a background light measurement was performed with the CYRIL probe already attached to the head but with the light off. This was subtracted from the measured spectra instead of the CCD noise measurement, which was only used for the cleaning of the reference spectra. The improved contact and removal of external lighting significantly improved the data quality; $\frac{\partial A}{\partial \rho}$ increased with wavelength in Figure 9.13d and $\frac{\partial^2 A}{\partial \rho \partial \lambda}$ in Figure 9.13f shows the spectral features of water and HHb around 750 nm and the water peak at 830 nm.

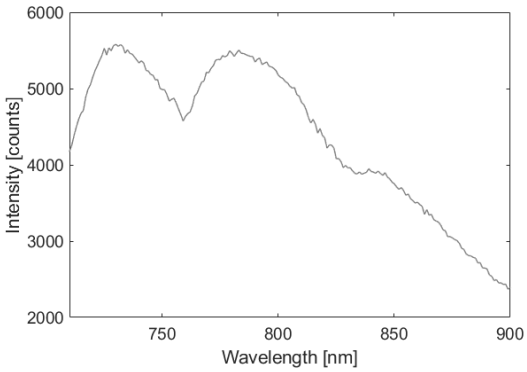

(a) Intensity spectrum, poor coupling.

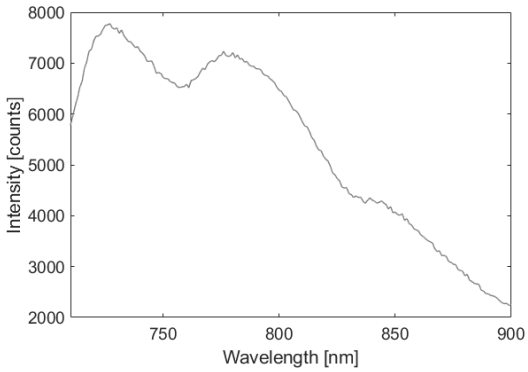

(b) Intensity spectrum, good coupling.

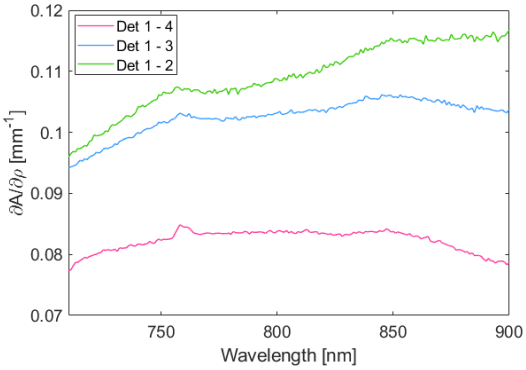

(c) Attenuation slopes, poor coupling.

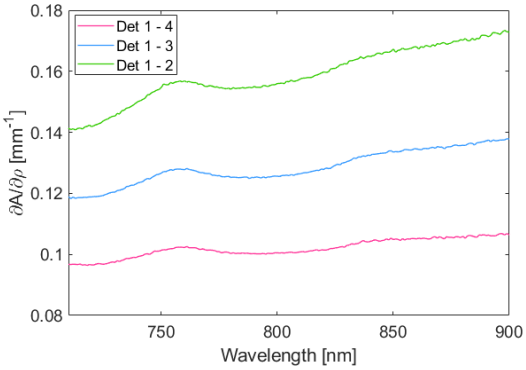

(d) Attenuation slopes, good coupling.

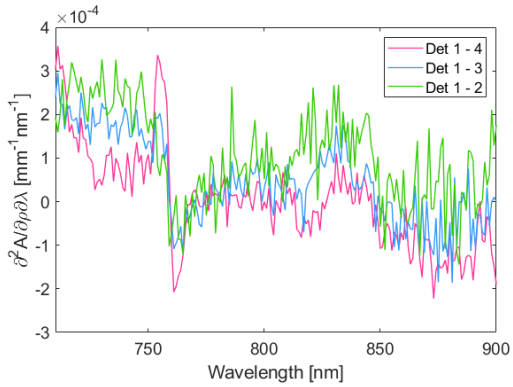

(e) Differentiated attenuation slopes, poor coupling.

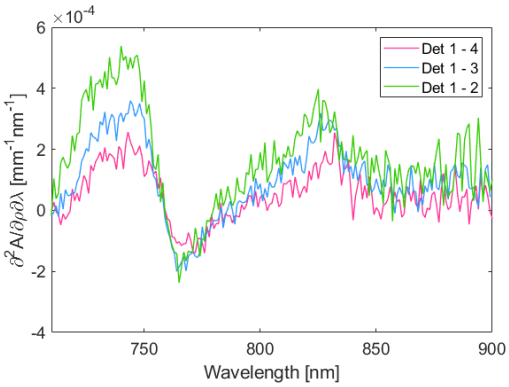

(f) Differentiated attenuation slopes, good coupling.

Figure 9.13: Examples of intensity spectra, $\frac{\partial A}{\partial \rho}$ and $\frac{\partial^2 A}{\partial \rho \partial \lambda}$ with good or poor coupling. Good examples were measured in baby C, poor examples in baby B. Intensity spectra were collected at 15–30 mm SDS (detectors 1–4), 15–25 mm (detectors 1–3) and 15–20 mm (detectors 1–2).

9.3.4.2 RS channel baby C

The implementation of changes to the data acquisition regarding tissue contact and external light artefacts improved the quality of the collected data and measurements from baby C were suitable for data analysis. However, only measurements from one channel, LS, passed the data selection criteria. The difference in the data and fit quality of the LS and RS channels is visible in Figure 9.2. The main difference between poor quality data collected on the RS $\frac{\partial^2 A}{\partial \rho \partial \lambda}$ and high quality data collected on the LS $\frac{\partial^2 A}{\partial \rho \partial \lambda}$ was the absence of the water peak at 830 nm, preventing the theoretical model from converging to the correct solution and awarding the spectrum a high score. The shown measurements were collected during the long measurement on day 2 but issues with the measurements from the RS channel were also encountered during the repeatability measurements and on day 3, shown in Figure 9.14.

Figure 9.14a shows that such problems with the spectra were not visible in $\frac{\partial A}{\partial \rho}$. The absence of the water peak in $\frac{\partial^2 A}{\partial \rho \partial \lambda}$ could have been caused by measurement errors; no artefacts were found in the reference spectra.

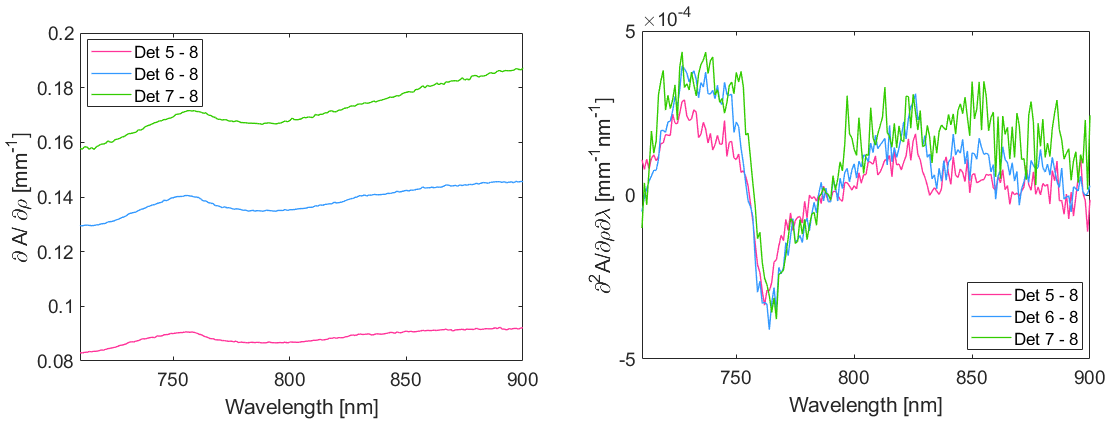

(a) $\frac{\partial A}{\partial \rho}$ **(b)** $\frac{\partial^2 A}{\partial \rho \partial \lambda}$

Figure 9.14: $\frac{\partial A}{\partial \rho}$ and $\frac{\partial^2 A}{\partial \rho \partial \lambda}$ collected on day 3 on the RS in baby C. Intensity spectra were collected at 15–30 mm SDS (detectors 5–8), 15–25 mm (detectors 6–8) and 15–20 mm (detectors 7–8).

Plotting the reflectance measured at different SDS revealed the cause of issues. In Figure 9.15, $\frac{\partial^2 R}{\partial \lambda^2}$ focused on the HHb spectral feature is shown including the locations of the centres of the peak. The measurements were collected with 4 detectors, 1, 4, 5 and 8. While detectors 4 and 5 illuminated the centre of the CCD, detectors 1 and 8 were placed on opposite edges (see Figure 5.16 for the CCD strip-detector assignment). A small shift of 2 nm is seen between detectors 1 and 4, accounted for in the calculation of the CCD resolution (around 4 nm). However, the shift between detectors 5 and 8 was larger; 5 nm. This shift caused a widening of spectral features

when $\frac{\partial^2 A}{\partial \rho \partial \lambda}$ was calculated and explains why the HHb peak collected on the RS, Figure 9.2c was wider than when collected on the LS, Figure 9.2d, and why the water peak was hidden in the noise level.

The shift was likely caused by a combination of chromatic aberration in the spectrometer (explained in section 5.1.2.2) and a misalignment of the lens relative to the CCD. The calibration of CYRIL was not checked in the hospital before the measurement and the misalignment likely occurred during the transport of the system from UCL to the NICU.

Measurements on the RS remained unsuitable for analysis even after detector 8 was removed and the slope was calculated for SDS 20–30 mm and 25–30 mm; the score was too high.

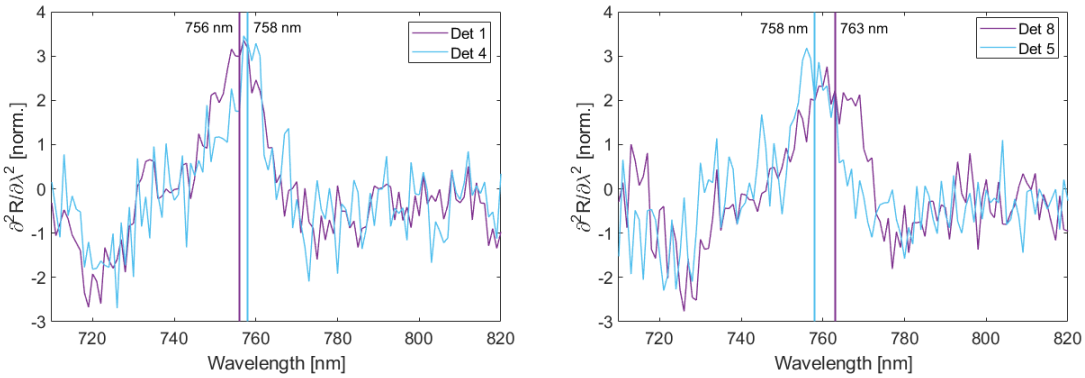

(a) LS: detectors 1 and 4.

(b) RS: detectors 5 and 8.

Figure 9.15: $\frac{\partial^2 R}{\partial \lambda^2}$ focused on the 760 nm HHb spectral feature collected on day 3 in baby C with detectors 1, 4, 5 and 8. The lines indicate the middle of each HHb peak. While the difference in the peak location collected on the LS is only 2 nm, the difference is 5 nm on the RS, larger than the resolution of the CCD.

9.4 Discussion

The work in this chapter is a preliminary demonstration of the application of BRUNO to data collected in neonates treated at the NICU with HIE. The aims were to compare StO_2 obtained with different data analysis algorithms, to measure their repeatability and to evaluate whether the information about cerebral physiology obtained from StO_2 in HIE is algorithm-dependent.

9.4.1 Data quality

Three infants were enrolled in the study, data from the first two monitored subjects had to be excluded from the analysis based on poor data quality. While the small sample size is a drawback of this work, the scarcity of measurements allowed enough time in between to perform preliminary analysis of the data and introduce changes to the measurement procedure, which led to an increase

in data quality. As a result of these improvements, data collected in the last study with the LS channel were suitable for BRUNO analysis.

The main cause of reduced data quality found was the poor tissue-detector contact. The curvature of the small neonatal head poses a challenge for probe attachment; the probe holder has to be small to fit on the forehead and not disturb any other monitors placed on the head (such as EEG probes), but also have enough surface area for the attachment of double sided tape. The use of a head band was not explored as extra pressure on the neonatal head had to be avoided. Designing an amended probe holder with wider edges has improved the results, it allowed more area for the attachment of the double-sided tape and kept the probe holder in place.

Data from the RS channel of Baby C had to be excluded because of poor resolution likely affected by the transport of the system from the lab to the hospital prior to the measurement. Currently, the means of checking the calibration of the system in the hospital are limited as a calibration light source and a dark room are needed. For future, a small black box could be built to easily test the calibration of the system *in situ*. CYRIL could also benefit from a bin-specific wavelength calibration.

One of the challenges encountered during preliminary analysis was that differentiation in BRUNO amplified the noise component of spectra and decreased the visibility of spectral features of chromophores. While the *fminsearchbnd* optimisation process can converge at a solution despite low-quality data, it is necessary to check the quality of the solution. One way of assessing the quality of the fit could be looking at the other fitting parameters, e.g. WF. WF should remain unchanged during stable periods and changes in the parameter's value between different time points could suggest instability of the fitting and low-quality data. Preliminary data analysis has shown that during the measurement on day 2 in Baby C, WF was on average around 90%. However, it did decrease up to 65% when StO_2 calculated with all algorithms increased at 16:45. This was caused by parameter crosstalk, a simultaneous change in a compensated the increase in WF. Fortunately, StO_2 is robust towards parameter crosstalk, as shown in section 8.4.4. One should not look only at the fitting parameters to assess the quality of a fit, as a sudden change in their values can be caused by alterations of optical properties.

A different approach to data quality assessment was chosen. To ensure that data were suitable for analysis, that the BRUNO algorithm could converge to the correct solution, an automated data quality assessment step was added to the pipeline. Quantifying the goodness of fit of the model to the data was used to ensure that the spectral features of HHb, HbO_2 and water were distinguishable

and BRUNO could be reliably applied.

Using a standard quantity describing goodness of fit, such as residuals, was not sufficient, as even data that evidently lacked the desired features could still have a close fit to the model. The development of the scoring system was guided empirically through visual inspection of data sets and shapes of the residual distribution. The benefit of the final scoring system is the addition of the range calculation next to the use of residuals, which is a way of capturing the expected presence of haemoglobin and water spectral features. The use of range also introduces a bias, as the HHb dip at 760 nm is going to be less distinct with high StO_2, hence decreasing the range and increasing the score. However, the water features at 730 nm and 830 nm are independent of oxygenation and should give the slope model sufficient "range". Additionally, given that the StO_2 in neonates is not expected to be above 90%, a HHb dip should always be visible. The score calculation combines the range with the residual calculation; data with a high StO_2 are not automatically rated with a high score (the score was retrospectively calculated for both phantom data sets and was ≤ 1 even at $StO_2 = 100\%$).

The threshold score of 2 used in this data selection is not meant to be used as a definite exclusion/inclusion criterion, it is to be used as guidance, combined with a visual assessment of a few data sets. Calculating the mean score of a measurement was found to be a helpful way of summarising the suitability of data for BRUNO analysis.

The data quality assessment step is included in the version of BRUNO available online [272] and will be used for real-time data scoring when BRUNO is implemented directly in the CYRIL user interface. The value of an automated data quality assessment step in the measurement of StO_2 has already been pointed out in Chapter 6, where "valid" StO_2 was calculated even from data with a slope measurement suggesting that it was likely affected by measurement errors. Highlighting BRUNO StO_2 values with a high score during real-time oxygenation measurements would point out measurement issues, such as poor coupling, which could be immediately resolved. The data quality scoring gives BRUNO another advantage compared to other algorithms, where automated data quality checks are not yet implemented.

9.4.2 Calculating StO_2 with different algorithms

Collecting data in a multidistance, broadband setup allowed for StO_2 calculation not only with BRUNO, but also the other algorithms of interest, BF, SRS and BB SRS. These were only applied to the final data selected for complete analysis. Similarly to the results obtained in phantoms and simulations, all four algorithms gave different results. The agreement of the algorithms was

assessed by correlation analysis and Bland-Altman analysis. The main differences between the measured StO_2 values observed were:

- Increase in the BF and BRUNO baseline on day 2 but not seen with SRS and BB SRS.
- Smaller dynamic range of BF, SRS and BB SRS compared to BRUNO.
- Change of correlation between BF and BRUNO from day 2 to day 3.
- Presence of offsets between the baselines of all StO_2 traces.

The disagreement of the algorithms has important implications to the clinical application of StO_2. For example, StO_2 measured by BF and BRUNO on day 2 increased between 15:15 and 15:30. This suggests the occurrence of haemodynamic changes. As fluctuations of SpO_2 were also identified during this time, it is indeed possible that some physiological events were occurring. No increase in StO_2 was, however, measured by SRS and BB SRS. The potential invisibility of a haemodynamic event links to the smaller dynamic range of the algorithms, already seen in phantom studies with CYRIL.

A difference in algorithm sensitivity to StO_2 changes is also evident in the mean StO_2 values for each day and algorithm, summarised in Figure 9.10. Oxygenation significantly increased from day 2 to day 3 measured with BRUNO, while SRS measured only a minimal decrease. The difference in the algorithm's sensitivity to StO_2 changes challenges one of the main potential appeals of oximetry - an absolute measure of tissue oxygenation. Intervention thresholds use reference ranges for physiology assessment and although the use of conversion equations to compare readings from oximeters can be used [8], they do not account for the disagreement in sensitivity. As clinical intervention guidelines are often based on StO_2 shifts from baseline, oximeters need to be able to measure changes in physiology with high sensitivity.

Another interesting observation is the decrease of correlation between BRUNO and BF from day 2 to day 3. Figure 9.7b shows that the BF trace sometimes diverges from the SRS, BB SRS and BRUNO trend. This is because BF only collects data from one SDS and monitors a slightly different region than BRUNO, SRS and BB SRS. NIRFAST simulations in Figure 8.29 have shown that BF is more likely to be influenced by changes of oxygenation in the extracerebral layer than other algorithms. This could have caused the disagreement between BF and BRUNO seen in Figure9.7b at 13:15; BRUNO showed a long, steady decrease of oxygenation from 75% to 60%, while BF measured a slightly delayed response, smaller in amplitude.

9.4.3 StO_2 as a measure of physiology in HIE

MRS in baby C indicated that the infant suffered from mild HIE injury (based on Lac/NAA reported in Table 9.1) and MRI findings were reported to be normal.

The mean SpO_2 measured on both days was in a range of SpO_2 values measured during hypothermia in infants with HIE [277]. Two desaturation events with a 5% drop from baseline were observed, a threshold value used in other studies [111, 278]. StO_2 did not follow the same trend at SpO_2 during the desaturation events and the correlation between StO_2 measured with either algorithm and SpO_2 was low throughout the whole measurements.

The lack of correlation of StO_2 and SpO_2 is expected during mild HIE with preserved autoregulation. While SpO_2 is a measure of arterial oxygen saturation SaO_2 and reflects global oxygenation, StO_2 is strongly dependent on venous saturation SvO_2 and measured localised oxygenation.

9.4.3.1 Change of StO_2 between days

All 4 algorithms measured lower StO_2 on day 3 than on day 2. A decrease of StO_2 from day 2 to day 3 indicates a change in oxygen delivery and metabolic demands of the brain during TH. HIE was in the second stage of injury progression on day 2 (see Figure 2.7 for a summary of HIE progression). This phase is characterised by mitochondrial failure and hyperperfusion. A lower StO_2 on day 3 suggests the return of normal perfusion.

While it is not possible to draw any conclusions on the prognostic value of StO_2 in HIE based on measurements in a single neonate, one can compare the results to findings in literature. Multiple studies measured StO_2 in neonates during TH and did not find an increase in oxygenation, however, the subjects were not grouped by outcome [95, 230, 242]. A stable StO_2 in neonates with favourable outcome between days 2 and 3 was reported in multiple studies [222, 225]. On the contrary, Lemmers et al. [220] measured a decrease in StO_2 between 48 h and 84 h of life in infants treated with TH and with favourable outcome, while such decrease was not found in subjects with an adverse outcome. Niezen et al. [223] monitored infants treated with TH. At 24 h, StO_2 was similar in both negative and favourable outcome. While it increased in the negative outcome groups between 24 h and 72 h, a slight decrease was reported in the favourable outcome group.

StO_2 values in baby C measured with BRUNO, BF, SRS and BB SRS are comparable to other values measured in infants with HIE; with median values between 65–85% reported in multiple publications [220, 222, 225]. Large variability in StO_2 between subjects was measured in [95],

both in the HIE and control group (approx. 60–80%). Toet et al. [84] measured a lower StO_2 on day 2 in good outcomes than other publications, below 70%. Chock et al. [279] measured StO_2 in HIE both on day 2 and 3 and reported a value of almost 85%, similar to measurements by Forman et al. [230]. The broad range of StO_2 obtained in this study is also comparable with StO_2 in healthy term neonates, summarised in section 4.2.1.

One can assume that all algorithms measured a physiologically possible value of StO_2, the question remains whether SRS and BB SRS underestimated the change of oxygenation between day 2 and 3 or whether BRUNO and BF overestimated.

Based on the better performance of BRUNO than BF, SRS and BB SRS in phantoms and NIRFAST simulations in Chapter 8, one could assume that BRUNO also performed better in the neonate. Could a drop in StO_2 of almost 20% from day 2 to day 3 be possible? Such a change indicates dramatic events in cerebral metabolism. Dehaes et al. [95] reported the progression of StO_2 over several days for each subject individually and in one subject, significant changes in StO_2 are seen: from $\approx 62\%$ on day 2 through 75% on day 3 to 65% on day 5. As other studies do not report StO_2 on individual levels, it is difficult to assess the day-to-day variations of StO_2. The small change in SRS and BB SRS agrees with the assumption of no change in StO_2 in favourable outcomes reported in other studies, but this could be the result of averaging, hiding the patterns in individual subjects. Perhaps the suggestions for the use of oximetry in HIE should not be based only on averaged measurements grouped by day and patient group, but a more individual approach should be applied. The StO_2 trace should be examined for each patient individually and the brain should be monitored at multiple regions, as the pattern of injury affects NIRS reading [231].

9.4.4 Repeatability

While the small sample size of the repeatability study prohibits the quantification of the repeatability of all four StO_2 algorithms; the measurement in baby C gives interesting insight into their behaviour.

One of the first patterns observable in Figure 9.12 is that the change in StO_2 between the blocks follows the same trend in all algorithms, captured by σ_{intra}. This suggests that one of the causes of changes in the StO_2 baseline throughout the repeatability measurement was something affecting all algorithms, particularly placement location and probe-tissue contact. As the probe holder was held in place by hand, the pressure changed throughout the measurement. BRUNO, SRS and BB SRS follow a very similar trend maintaining the same order of StO_2 - BB SRS gave the lowest reading and SRS the highest, with BRUNO StO_2 scattered in between. BF changed less

between the blocks. As it only uses data from the furthest away detector, the pressure change over time on this detector was different than the pressure applied to all 4 detectors used by BRUNO, SRS and BB SRS.

Although it visually appears that the algorithms follow the same trend, σ_{intra} is different for each. This is because it was calculated from the mean StO_2 for each block and each algorithm resulted in StO_2 with different dispersion (σ_{block}). σ_{block} varied significantly between the algorithms. It was lowest for BB SRS and it was shown already in Chapter 8 that the algorithm gave the smoothest StO_2 response in phantom studies. The trend of SRS and BB SRS was similar in the repeatability study, with SRS being more sensitive to noise.

Sensitivity to noise appears to be an issue particularly for BRUNO. BRUNO had the highest σ_{block}. Such dispersion of StO_2 was not observed in any measurements where the probe holder was attached using tape, suggesting that small fluctuations in the pressure on the probe holder can led to bigger changes in StO_2 than in other algorithms. As the spectra are differentiated twice in BRUNO, small artefacts can be significantly amplified.

Interestingly, while BF also applied a double-differentiation process, its σ_{block} was much lower than that of BRUNO. This might be because all four detectors in BRUNO are affected by slightly different pressure changes when being pressed against the forehead, changing the slope of attenuation. In BF, the pressure-induced change in intensity is removed through differentiation as long as the baseline offsets are equal across all wavelengths [138]. As σ_{block} was the second lowest and σ_{intra} the lowest for BF, it was the most robust algorithm in this repeatability study.

The calculation of σ_{intra} assumed stable haemodynamics during the measurement. A drawback of this study is that SpO_2 was not collected during the measurement, however, as no relationship between StO_2 and SpO_2 was found in this infant, measuring SpO_2 would not inform on the stability of oxygenation in the interrogated tissue. A better assessment of stable haemodynamics during a repeatability study would be the use of an additional oximeter, as used by [12]. The design of future repeatability studies would benefit from a stable attachment of the probe holder to tissue or with the incorporation of a measure of probe-tissue pressure.

9.5 Conclusion

CYRIL 2 was used to collect data in infants diagnosed with HIE treated at the NICU. All 4 data analysis algorithms, BRUNO, BF, SRS and BB SRS, were used to calculate StO_2. All recovered StO_2 values were consistent with values reported in literature, however, a disagreement in algorithm performance was also found, as already indicated by the previous analysis of NIRFAST and

phantom data.

Data from one infant were analysed. StO_2 depended on the measurement algorithm; disagreement was shown between all algorithms, with disparities found in the mean values, the StO_2 trend and sensitivity to StO_2 changes. All algorithms measured a decrease in StO_2 from day 2 to day 3, the scale of this drop depended on the StO_2 algorithm. BRUNO has measured the largest change in StO_2 over time, in agreement with the phantom studies described in Chapter 8, where the dynamic range of this algorithm was the largest. Assuming BRUNO performed better than BF, SRS and BB SRS, as shown in NIRFAST simulations and phantom studies in Chapter 8, BRUNO indicated significant haemodynamic changes in the injured brain, otherwise invisible other algorithms. Such findings could be significant in clinical care. At this point, it is impossible to compare the results to literature, as the progression of StO_2 is not reported on individual levels and large within-infant variation is expected, leading to inconsistent results. Some studies of oxygenation in HIE neonates during TH report no change in oxygenation during TH during the first days of life, a decrease from day 2 to day 3 was also reported. To further evaluate the benefits of using BRUNO in HIE compared to other algorithms, a larger cohort of infants needs to be monitored.

An automated data quality scoring system was introduced for an efficient assessment of data quality. While some data sets had to be excluded from the analysis based on poor data quality, additional steps were taken in other studies ensured sufficient data quality, such as good tissue-probe contact and the removal of external light. The addition of a data quality scoring system in the BRUNO data analysis pipeline would be beneficial for real-time measurements to ensure optimal data collection.

Chapter 10

Conclusion

The aim of this chapter is to summarise the work and the most important findings of this thesis. The investigation has, however, also opened up more questions and highlighted aspects of BRUNO and oximetry with CYRIL, which will be outlined in the second section.

10.1 Summary

The work in this thesis has presented a thorough insight into cerebral oximetry; from the theory behind continuous-wave algorithms through to the development of data analysis pipelines and finally application in neonatal care.

10.1.1 Recovering StO_2 with SRS and BF

The first step in the investigation of StO_2 recovery and the development of a novel algorithm BRUNO was the application of SRS to data collected in the NICU in neonates with HIE, Chapter 6. The results have shown that the prognostic value of StO_2 when applied to CYRIL data was influenced by multiple factors. These were investigated in applying SRS with different "approaches". StO_2 recovered with SRS was dependent on the selection of h, a constant used to account for scattering losses, highlighting the need to account for these losses flexibly when recovering StO_2. A sensitivity of the algorithm to the addition of water as a chromophore was also identified. The wavelength-dependence of the algorithm was particularly noticeable when applied to CYRIL data, as different selections of wavelengths caused significant changes to the recovered StO_2. The investigation also highlighted the benefits of using multiple detectors to measure an attenuation slope, as that increased the likelihood of a measurement less burdened by coupling errors. While the impact of instrumentation was significant in this investigation of SRS, it did emphasise patterns in the behaviour of SRS independent of instrumentation, mainly the use of the scattering constant h and lack of consistency regarding wavelength selection and accounting water

absorption.

Another important finding of the chapter was that the prognostic value of StO_2 in HIE changed with approach. For example, if SRS was used with broadband wavelengths, a significant difference in StO_2 was found between severe and moderate HIE, but not when only a selection of discrete wavelengths was used. This emphasises the need for transparency in algorithm design and the use of standardisation protocols when designing study protocols for the evaluation of the suitability of oximetry in clinical care.

The next chapter, Chapter 7, was focused on an assessment of a different StO_2 algorithm, BF. The application of the algorithm was evaluated in NIRFAST data simulated in a multilayered neonatal head mesh. The main findings were focused on the process of fitting a theoretical model of reflectance to broadband NIRS data, to minimise the crosstalk between the fitting parameters and optimise StO_2 accuracy. An important result was that StO_2 was reasonably robust towards errors caused by parameter crosstalk, suggesting that it is possible to obtain an accurate measurement of oxygenation despite incorrectly estimated concentrations of HHb and HbO_2.

The main strengths of SRS identified were the ability to reduce the influence of extracerebral layers and low computational burden. The limitations include relying on the scattering factor h and SRS was influenced by the selection of wavelengths and accounting for water absorption. BF, on the other hand, can account for scattering without relying on h and the broadband spectrum makes accounting for additional chromophore absorption easier. Some limitations are the inability to remove the contribution of extracerebral layers on the StO_2 signal and high computational burden.

10.1.2 Broadband multidistance oximetry development and performance

Identifying the strengths of SRS and BF in Chapters 6 and 7 helped design the novel StO_2 algorithm, BRUNO. The design was data-driven and each step in the implementation of BRUNO, such as light transport model or chromophore selection, were based on maximising the accuracy of StO_2 estimation from data obtained in NIRFAST simulations and phantom measurements. Such algorithm design approach was focused on the application in neonatal data collected with the instrument CYRIL.

Designing BRUNO as a combination of the the multidistance measurement setup of SRS with the spectral differentiation of broadband spectra utilised in BF led to a better estimation of StO_2 with BRUNO than achievable with either SRS or BF individually. BRUNO recovered StO_2 with higher accuracy both in NIRFAST simulations and phantom studies - e.g. in model B, the error of the median StO_2 recovered with BRUNO was only 0.2% but 2.6% with SRS, 2.3% with BB SRS

and 5.8% with BF. The BRUNO signal was also more brain-specific and suffered from least ECT signal contamination; the error of StO_2 recovered during a deoxygenation of brain tissue simulated in NIRFAST model E was 1.1% with BRUNO, 2.3% with BF, 3.8% with SRS and 4.8% with BB SRS. Measuring StO_2 in liquid phantom measurements has also shown that BRUNO had a larger dynamic range than other algorithms. No large decrease of BRUNO accuracy was observed when moving from NIRFAST simulations to phantoms, as the algorithm was specifically designed to perform well in such data.

The focus on CYRIL in the design process of BRUNO introduced some limitations, such as the wavelength selection. Using a spectrometer with a different wavelength range including wavelengths below 700 nm could improve the sensitivity of the algorithm to HbO_2 absorption. A higher SNR would also decrease the influence of noise on the analysis, which was a significant source of errors particularly when monitoring human subjects. While the computational burden of BRUNO was reduced compared to BF, it was higher than of SRS. This could be challenging when using it real-time in NIRS systems with less computational power.

Using NIRFAST data and measurements in phantoms helped identify instrumentation-dependent behaviour of StO_2 algorithms. A significant decrease of accuracy in StO_2 recovery when moving from NIRFAST spectra to phantoms was noted particularly in SRS, likely due to not accounting for water absorption. Adjusting h also increased the brain-signal specificity of the signal, suggesting that a simple mean of increasing the accuracy of SRS would be using different h values for different patient groups. Out of all algorithms, BF was most sensitive to errors due to noise, as it relies only on measurements with one SDS. Noise also affected the dynamic range of the algorithm, decreasing its ability to accurately account for absorption by HbO_2. It is likely the reduction of the wavelength range at which data was collected had an impact, as CYRIL did not cover the whole range suggested by the authors of the algorithm [26].

The advantages of BRUNO identified in the performance assessment included increased accuracy of StO_2 measurements, higher sensitivity to brain oxygenation and larger dynamic range. Out of all three algorithms, the requirements on instrumentation are the highest for BRUNO, as it requires light detectors capable of multidistance measurements and a broadband light source. The computational burden of BRUNO was much higher than that of SRS but lower than BF, shown in Table 8.6. Including an automated data quality assessment step in the analysis increases the robustness of BRUNO.

10.1.3 Measurement of StO_2 in a neonate with HIE

The algorithm-dependence of StO_2 was also observed in Chapter 9, where bNIRS data were collected with CYRIL in neonates treated at the NICU at UCLH during treatment with TH. An automated data quality scoring step was added to the data analysis pipeline to ensure that the measured attenuation slopes had sufficiently visible spectral features to be analysed by BRUNO. While, on one hand, this led to the exclusion of multiple data sets from the analysis, it helped identify aspects decreasing the quality of data, such as poor probe-tissue contact or too little signal. Additionally, the data that did pass the scoring system was more likely to lead to an accurate StO_2.

Due to the small sample size of the study, it was not possible to assess the repeatability of StO_2 measurements. The analysis of one short repeatability measurement with CYRIL probe resitting has however shown strong influence of the pressure of the CYRIL probe on the skin on the recovered StO_2, suggesting that BRUNO is particularly sensitive to artifacts caused by tissue-probe contact.

StO_2 was measured with BRUNO, SRS, BB SRS and BF in one neonate with mild HIE on day 2 and day 3 of life. Similarly to phantom measurements, the results showed poor agreement, particularly in the dynamic range. The sensitivity to changes in StO_2 was also evident in the difference in StO_2 between days, when BRUNO showed a significant decrease of almost 20% from day 2 to day 3, while SRS and BB SRS measured only a very slight decrease. A disagreement between algorithms based on the same data set could explain why other studies of oxygenation in HIE show a decrease in oxygenation between days and others show no difference.

The differences between algorithms identified in the neonate were in agreement with the findings in phantom studies. The true value of StO_2 in the neonate was not known, but as BRUNO outperformed BF, SRS and BB SRS in the analysis of both NIRFAST data and phantom studies, one could assume that its measurement of oxygenation in the neonate was a better assessment of the injured brain's oxygenation. The large drop in oxygenation between days 2 and 3 identified with BRUNO and BF was particularly interesting, as it implied significant haemodynamic changes occurring in the brain during therapeutic hypothermia. While no clinical conclusion can be drawn due to the unavailability of measurements in other patients, these promising results suggest that BRUNO could indeed lead to a more accurate measurement of StO_2 in neonatal care, more sensitive to oxygenation changes in brain tissue.

10.2 Further work

The main output of this work is the development of BRUNO, a multidistance broadband NIRS algorithm which has the potential to recover StO_2 with high accuracy. This work has demonstrated the application of the algorithm to various types of data, ranging from NIRFAST simulations to spectra collected in infants treated at the NICU. Room for improvement remains and there are various aspects of the algorithm and its application that could benefit from further work.

10.2.1 BRUNO performance

The development of BRUNO was guided empirically through the exploration of various fitting methods, diffusion theory models or wavelength combinations. Various other properties of BRUNO could be improved:

1. Fitting: the current optimisation routine follows a simple least-squares fitting procedure which find a local minimum. No space was given to the exploration of other fitting techniques as the fitting was not considered the main strength nor weakness of the algorithm. An exploration of other fitting techniques could help reduce crosstalk and improve the execution speed.

2. Wavelength selection: as already discussed in Chapter 8, the broadband range of CYRIL 2 was used for the recovery of StO_2 with BRUNO. Changing this wavelength range, perhaps to shorter wavelengths below 700 nm, could improve the accuracy of StO_2 recovery by including spectral features of HbO_2 found around 675 nm.

3. Chromophores: the selection of chromophores to detect with BRUNO is the standard selection used in NIRS; water and haemoglobin. Neither of the other algorithms used in this work, BF and SRS, accounted for other sources of background absorption. However, the use of broadband NIRS gives us the ability to capture additional chromophore, such as CCO or melanin. A short exploration of the CCO contribution to the attenuation slope model differentiated with respect to wavelength has shown that CCO could potentially be measured with BRUNO, which would also increase the accuracy of StO_2 quantification, as the extra contribution to absorption would be attributed to the correct chromophore. Another chromophore whose contribution to absorption in the 700–900 nm range is small, but not negligible, is melanin [141]. Similarly to CCO, it lacks significant spectral features, crosstalk with scattering parameters and other chromophores when recovering BRUNO fitting parameters would be expected. Additionally, as the concentration of melanin in the skin varies widely by sub-

ject [257], setting of boundary conditions could be challenging. Nevertheless, improving BRUNO's ability to account for background light absorption could lead to an improvement in the accuracy of StO_2.

4. Attenuation slope model: the ZBC model was selected for BRUNO as it allows for fast execution and gives sufficiently precise results. At this stage, the small improvement achieved through the introduction of more complex models would be overshadowed by the errors arising from noise and other measurement-related problems. If an optimisation routine is found that can accurately model the attenuation slope with more complex models of light propagation in tissue at a reasonable speed, it should be implemented in BRUNO.

5. Data de-noising: it is evident that for the best performance of BRUNO, a high SNR is desirable. Implementation of a data smoothing pipeline, perhaps based on wavelet de-noising as described by [270], could improve the measurement of StO_2 without having to carry out any hardware changes in CYRIL.

6. Recovery of μ_a and μ_s': BRUNO has been shown to measure StO_2 quickly and with high accuracy. The next step could be to try to improve the recovery of absolute optical properties, μ_a and μ_s'. Problems with crosstalk were encountered in this work, however, published work with broadband fitting [139] shows a higher accuracy of individual fitting parameters, with a smaller crosstalk burden. While the crosstalk between scattering and attenuation cannot be completely removed in CW measurements, several points could be investigated to improve the ability of BRUNO to recover μ_a and μ_s' accurately:

    - use of an optimisation routine converging to a global solution.
    - exploring other wavelengths.
    - setting some fitting parameters, for example WF, to a constant value and investigating the setting of boundary conditions. This could also enable the quantification of c_{HHb} based on the measurements by Matcher et al. [137] and use it to select boundary conditions for the optimisation routine.

10.2.2 Validation

The accuracy of BRUNO has been demonstrated in NIRFAST simulations and in phantom data. To obtain a further assessment of the algorithm's performance, it is suggested to conduct more analysis in simulated data. Firstly, the sample sizes of spectra used in this work are relatively

small (in the order of tens) and increasing the sample size at least ten-fold would improve the reliability of the results. Secondly, the NIRFAST simulations were only obtained in a neonatal mesh model; performing simulations in simple tissue slab models could help assess the suitability of the theoretical models used and working with meshes based on adult heads would quantify what depth sensitivity to expect with BRUNO.

The phantom data presented in this work consists of only two data sets, one for a homogeneous and one for a two-layer phantom. The repeatability of the homogeneous phantom is high and similar results are obtained when repeating the measurements. Regarding the two-layer phantom, only one data set collected with CYRIL 1 was available as the TR system used for reference had a fault during the time the phantom was available. It would be useful to perform additional two-layer blood phantom measurements with the updated CYRIL setup (CYRIL 2) to obtain a more confident assessment of BRUNO accuracy.

The reference measurement of StO_2 in this work was a TR system. The most suitable device for oxygenation reference measurements in liquid phantoms are blood gas analysers, which measure the oxygen content of blood samples. Unfortunately, no such device was available at the times of conducting the research; it would be useful to obtain it in future for a more reliable measure of oxygenation. Once the performance of BRUNO has been thoroughly investigated in phantoms and computational simulations, the validation process can move towards experiments in human subjects.

10.2.3 Real-time measurements

One of the main requirements for BRUNO was to recover StO_2 at times suitable for real-time application. This was achieved; the main bottleneck of the measurement was the speed of the CCD read-out, the analysis itself took much less than one second per spectrum. In total, this still allowed a measurement rate of approximately 0.95 Hz, which is suitable for real-time measurements.

Real-time use of BRUNO would require the addition of the calculation into the CYRIL 2 LabVIEW user interface. As the implementation of BRUNO in LabVIEW would be computationally demanding; a simpler solution would be to connect LabVIEW with BRUNO MATLAB scripts (such connections are possible with the use of various add-ons).

The user interface in LabVIEW should display various plots to help the user track the quality of the data collection in real-time: a plot of the attenuation at a few wavelengths against distance to allow the user to assess the linearity of the slope, the BRUNO fit with the differentiated attenuation slope and the model, and also show the data quality score. Another plot would show StO_2 over

time. The user could set a score threshold, and if an StO_2 measurement was be above the threshold, it would highlight the corresponding value in the plot.

As a reference measurement needs to be measured to obtain the attenuation, the reference measurement can be collected before the measurement and stored. The stability of the light source and the CCD needs to be assessed in order to determine the suitable frequency of updating the reference measurement. Additionally, a bin-specific wavelength calibration of the system could improve the resolution.

One of the main potential bottlenecks in the real-time application of BRUNO is the computational burden of the optimisation routine, dependent on the PC's characteristics. CYRIL is connected to a laptop computer with worse computational power than the PC used in this work and it is not expected that it could perform BRUNO at comparable speeds. This could be solved by hosting the BRUNO optimisation routine on the cloud or a powerful server.

10.2.4 Application of BRUNO in adult and muscle measurements

The work in this thesis was focused on the application in neonates but BRUNO could be further amended to be suitable for other applications, such as cerebral tissue oxygenation measurements in adults or muscle oxygenation measurements. These applications would introduce several changes to BRUNO.

The main difference between adult and neonatal head measurements is the contribution of ECT layer signal [121]. NIRFAST simulations with an adult mesh could help assess the impact of ECT signal on StO_2 recovered with BRUNO. In the case of significant contributions, two-layer light transport in tissue models should be considered, as these account for differences in optical properties between the ECT and brain layer. Thicker ECT layers in adults than in neonates also increase the attenuation of light hence it will be necessary to ensure that the collected spectra have sufficient SNR for data analysis.

Skeletal muscle oximetry could also benefit from increased tissue oxygenation measurement accuracy. The challenges facing oxygenation measurements in skeletal muscle differ from brain measurements. While the contribution of bone to light attenuation is much lower, the contribution of other absorbers than haemoglobin needs to be accounted for, particularly myoglobin, adipose tissue, water and also other background absorbers, such as intra-muscle lipids, skin melanin and CCO [280]. Another important aspect of muscle oximetry is the robustness of the algorithm to movement artefacts [280]. The addition of these absorbers to the BRUNO algorithm and the impact of movements artefacts on BRUNO StO_2 would have to be investigated.

10.2.5 Spatially resolved spectroscopy and broadband fitting

This work has identified worse StO_2 recovery performance with SRS and BF than BRUNO when applied to NIRFAST spectra and data collected with CYRIL. The algorithms offer other benefits in comparison to BRUNO: SRS requires less computational power and BF can be used with just one SDS, which is suitable for the use in miniaturised systems, e.g. miniCYRIL, a smaller version of CYRIL [281]. Further investigation of the application of these algorithms in CYRIL is encouraged. Additionally, the application of SRS in CYRIL could be improved by implementing some recently developed additions to the algorithm, such as the removal of prior scattering assumptions with h[148]. As the findings of this work are limited to the application in CYRIL, repeating the comparison of BF, SRS and BRUNO performance in a different NIRS system could offer interesting insight on the behaviour of the algorithms and aid with the design of standardisation requirements in the field of NIRS.

10.2.6 StO_2 in HIE

The sample size in the pilot neonatal study in this work was limited and it was impossible to draw any clinically valuable conclusions on the value of BRUNO in the NICU. However, the discovery of disagreement between StO_2 measured with different algorithms from data collected in the same system should be investigated. To further validate that haemodynamic changes which are otherwise invisible to other StO_2 measurement algorithms/devices are happening during TH, a larger subject cohort needs to be monitored and not only reporting an averaged StO_2 but investigating the progression of brain oxygenation over time on an individual level would further increase the understanding of the cerebral response to TH.

Increasing the reliability of StO_2 measurements is the next step towards evidence of the clinical benefits of oximetry. Nevertheless, it is not the only barrier a new oximeter would face before spreading among clinics. While the work in this thesis has shown an increase of StO_2 accuracy, clinical trials are needed to show the benefits of oximetry. Implementing a BRUNO oximeter as a clinical device would also require sufficient funding. The training requirements of an oximeter applying BRUNO would be low compared to other traditional HIE imaging technologies, such as MRI or EEG, as such oximeter would not require specialist expertise, particularly with an automated data quality assessment step included in the software. To effortlessly compare StO_2 readings with other oximetry systems, the use of linear conversion could be explored [165].

10.3 Conclusion

This thesis described the development of a novel algorithm to recover StO_2 with CW bNIRS using a multidistance approach. The motivation was based on one of the main challenges facing the field of cerebral oximetry; inconsistent agreement of results of various studies and poor comparability of StO_2 values obtained with different NIRS systems. The challenge is particularly visible in the field of oximetry in neonatal HIE, where some studies report the ability of oximetry to help with injury severity diagnosis and other studies report no such observations. While the individual physiological differences between subjects surely influence these conclusions, the hypothesis was that the algorithm to recover StO_2 also plays a role. This was shown in an investigation of SRS and BF, where small changes in the algorithm implementation could cause large shifts in StO_2. In fact, changing the SRS algorithm even affected whether there was a difference in StO_2 measured in neonates with severe or moderate HIE. These findings are important when using absolute StO_2 measurements to describe the oxygenation of tissue as they highlight the sensitivity of StO_2 to data analysis algorithm implementation. Such behaviour could be one of the causes of the lack of evidence when evaluating the prognostic value of oximetry in clinical care.

The main output of this thesis is BRUNO, a novel algorithm to calculate StO_2 with broadband, multidistance data. Advantages of the algorithm include higher StO_2 recovery accuracy, increased sensitivity to oxygenation changes in deeper tissue layers, large dynamic range of oxygenation across 0–100%, smaller computational burden than BF and the ability to check the quality of data automatically. The application of the algorithm in a pilot study focused on monitoring neonates has also suggested increased sensitivity to haemodynamic changes.

BRUNO can be implemented in any broadband multidistance CW NIRS system. However, even NIRS systems which cannot use BRUNO can benefit from the work presented in this thesis. If SRS or BF are applied, an investigation of the system's response to changes in the implementation of the algorithms and the addition of automated data quality checks can help ensure maximal StO_2 accuracy.

Measuring StO_2 with BRUNO in more neonates with HIE could reveal further insight into the complex relationship between cerebral haemodynamics and brain injury severity. The development of BRUNO shows that through transparent and data-driven algorithm design, it is possible to increase StO_2 reliability. While there are many hurdles to be overcome in the establishment of cerebral oximetry in the clinical care, the ability to obtain a reliable and accurate measure of StO_2 would benefit not only the treatment of HIE, but also seizure or stroke monitoring in the NICU.

Bibliography

[1] F. F. Jobsis, "Noninvasive, infrared monitoring of cerebral and myocardial oxygen sufficiency and circulatory parameters," *Science*, vol. 198, no. 4323, pp. 1264–1267, 1977.

[2] J. E. Brazy, D. V. Lewis, M. H. Mitnick, and F. F. Jobsis, "Noninvasive Monitoring of Cerebral Oxygenation in Preterm Infants: Preliminary Observations," *Pediatrics*, vol. 75, no. 2, 1985.

[3] A. D. Edwards, C. Richardson, M. Cope, J. S. Wyatt, D. T. Delpy, and E. O. Reynolds, "Cotside measurement of cerebral blood flow in ill newborn infants by near infrared spectroscopy," *The Lancet*, vol. 332, pp. 770–771, 10 1988.

[4] P. Bickler, J. Feiner, M. Rollins, and L. Meng, "Tissue Oximetry and Clinical Outcomes," *Anesthesia and Analgesia*, vol. 124, no. 1, pp. 72–82, 2017.

[5] A. M. Plomgaard, W. van Oeveren, T. H. Petersen, T. Alderliesten, T. Austin, F. van Bel, M. Benders, O. Claris, E. Dempsey, A. Franz, M. Fumagalli, C. Gluud, C. Hagmann, S. Hyttel-Sorensen, P. Lemmers, A. Pellicer, G. Pichler, P. Winkel, and G. Greisen, "The SafeBoosC II randomized trial: treatment guided by near-infrared spectroscopy reduces cerebral hypoxia without changing early biomarkers of brain injury.," *Pediatric research*, vol. 79, pp. 528–35, 4 2016.

[6] A. Vilke, D. Bilskiene, V. Šaferis, M. Gedminas, D. Bieliauskaite, A. Tamašauskas, and A. Macas, "Predictive value of early near-infrared spectroscopy monitoring of patients with traumatic brain injury," *Medicina (Lithuania)*, vol. 50, no. 5, pp. 263–268, 2014.

[7] C. L. Hunter, J. L. Oei, K. Suzuki, K. Lui, and T. Schindler, "Patterns of use of near-infrared spectroscopy in neonatal intensive care units: international usage survey," *Acta Paediatrica*, vol. 107, pp. 1198–1204, 7 2018.

[8] S. Kleiser, N. Nasseri, B. Andresen, G. Greisen, and M. Wolf, "Comparison of tissue oximeters on a liquid phantom with adjustable optical properties: an extension," *Biomedical Optics Express*, vol. 9, no. 1, pp. 86–101, 2018.

[9] S. N. Davie and H. P. Grocott, "Impact of Extracranial Contamination on Regional Cerebral Oxygen Saturation," *Anesthesiology*, vol. 116, pp. 834–840, 4 2012.

[10] A. la Cour, G. Greisen, and S. Hyttel-Sorensen, "In vivo validation of cerebral near-infrared spectroscopy: a review," *Neurophotonics*, vol. 5, no. 4, p. 040901, 2018.

[11] K. L. Tomlin, A.-M. Neitenbach, and U. Borg, "Detection of critical cerebral desaturation thresholds by three regional oximeters during hypoxia: a pilot study in healthy volunteers," *BMC Anesthesiology*, vol. 17, no. 6, 2017.

[12] S. Kleiser, D. Ostojic, and N. Nasseri, "In vivo precision assessment of a near-infrared spectroscopy-based tissue oximeter (OxyPrem v1.3) in neonates considering systemic hemodynamic fluctuations," *Journal of Biomedical Optics*, vol. 23, no. 6, p. 067003, 2018.

[13] J. J. Kurinczuk, M. White-Koning, and N. Badawi, "Epidemiology of neonatal encephalopathy and hypoxic–ischaemic encephalopathy," *Early Human Development*, vol. 86, pp. 329–338, 6 2010.

[14] Y. Han, N. Fu, W. Chen, J. Liang, Y. Cui, Y. Zhang, and J. Qin, "Prognostic Value of Electroencephalography in Hypothermia-Treated Neonates With Hypoxic-Ischemic Encephalopathy: A Meta-Analysis," *Pediatric Neurology*, vol. 93, pp. 3–10, 4 2019.

[15] G. Greisen, "Cerebral blood flow and oxygenation in infants after birth asphyxia. Clinically useful information?," *Early Human Development*, vol. 90, no. 10, pp. 703–705, 2014.

[16] G. Bale, S. Mitra, I. De Roever, M. Sokolska, D. Price, A. Bainbridge, R. Gunny, C. Uria-Avellanal, G. S. Kendall, J. Meek, N. J. Robertson, and I. Tachtsidis, "Oxygen dependency of mitochondrial metabolism indicates outcome of newborn brain injury," *Journal of Cerebral Blood Flow & Metabolism*, vol. 39, no. 10, 2018.

[17] L. Huang, H. Ding, X. Hou, C. Zhou, G. Wang, and F. Tian, "Assessment of the hypoxic–ischemic encephalopathy in neonates using non-invasive near-infrared spectroscopy," *Physiological Measurement*, vol. 25, pp. 749–761, 6 2004.

[18] S. V. Jain, L. Pagano, M. Gillam-Krakauer, J. C. Slaughter, S. Pruthi, and B. Engelhardt, "Cerebral regional oxygen saturation trends in infants with hypoxic-ischemic encephalopathy.," *Early human development*, vol. 113, no. July, pp. 55–61, 2017.

[19] J. K. Lee, A. Poretti, J. Perin, T. A. G. M. Huisman, C. Parkinson, R. Chavez-Valdez, M. O'Connor, M. Reyes, J. Armstrong, J. M. Jennings, M. M. Gilmore, R. C. Koehler, F. J. Northington, and A. Tekes, "Optimizing Cerebral Autoregulation May Decrease Neonatal Regional Hypoxic-Ischemic Brain Injury.," *Developmental neuroscience*, vol. 39, no. 1-4, pp. 248–256, 2017.

[20] G. Bale, S. Mitra, J. Meek, N. Robertson, and I. Tachtsidis, "A new broadband near-infrared spectroscopy system for in-vivo measurements of cerebral cytochrome-c-oxidase changes in neonatal brain injury.," *Biomedical optics express*, vol. 5, no. 10, pp. 3450–3466, 2014.

[21] Horizon 2020, "Brain injury and trauma monitoring using advanced photonics," 2019.

[22] C. Hornberger and H. Wabnitz, "Approaches for calibration and validation of near-infrared optical methods for oxygenation monitoring," *Biomed Tech*, 2018.

[23] M. Jermyn, H. Ghadyani, M. A. Mastanduno, W. Turner, S. C. Davis, H. Dehghani, and B. W. Pogue, "Fast segmentation and high-quality three-dimensional volume mesh creation from medical images for diffuse optical tomography," *Journal of Biomedical Optics*, vol. 18, p. 086007, 8 2013.

[24] H. Dehghani, M. E. Eames, P. K. Yalavarthy, S. C. Davis, S. Srinivasan, C. M. Carpenter, B. W. Pogue, and K. D. Paulsen, "Near infrared optical tomography using NIRFAST: Algorithm for numerical model and image reconstruction," *Communications in numerical methods in engineering*, vol. 25, pp. 711–732, 8 2008.

[25] S. Suzuki, S. Takasaki, T. Ozaki, and Y. Kobayashi, "A tissue oxygenation monitor using NIR spatially resolved spectroscopy," *SPIE Proceedings*, vol. 3597, pp. 582–592, 1999.

[26] H. Z. Yeganeh, V. Toronov, J. T. Elliott, M. Diop, T.-Y. Lee, and K. St. Lawrence, "Broadband continuous-wave technique to measure baseline values and changes in the tissue chromophore concentrations," *Biomedical Optics Express*, vol. 3, no. 11, pp. 2761–2770, 2012.

[27] L. S. Constanzo, "Respiratory Physiology," in *Physiology*, Philadephia, PA: Saunders, 2nd ed., 2002.

[28] P. E. Di Prampero and G. Ferretti, "The energetics of anaerobic muscle metabolism: a reappraisal of older and recent concepts," *Respiration Physiology*, vol. 118, pp. 103–115, 1999.

[29] S. Sharma and D. Rawat, "Partial Pressure Of Oxygen (PO2)," 2 2019.

[30] A. Carreau, B. El Hafny-Rahbi, A. Matejuk, C. Grillon, and C. Kieda, "Why is the partial oxygen pressure of human tissues a crucial parameter? Small molecules and hypoxia," *J. Cell. Mol. Med*, vol. 15, no. 6, pp. 1239–1253, 2011.

[31] M. M. Cloutier, "Oxygen and Carbon Dioxide Transport," in *Respiratory Physiology*, Philadephia, PA: Elsevier Inc., 2019.

[32] Mayo Clinic Staff, "Hypoxemia (low blood oxygen) - Mayo Clinic," 2018.

[33] P. Van Beest, G. Wietasch, T. Scheeren, P. Spronk, and M. Kuiper, "Clinical review: Use of venous oxygen saturations as a goal - a yet unfinished puzzle," *Critical Care*, vol. 15, 10 2011.

[34] P. Vali, M. Underwood, and S. Lakshminrusimha, "Hemoglobin oxygen saturation targets in the neonatal intensive care unit: Is there a light at the end of the tunnel?," *Can. J. Physiol. Pharmacol.*, vol. 97, pp. 174–182, 2019.

[35] P. Southwood, "File:Oxygen-Haemoglobin dissociation curves.svg - Wikimedia Commons," 2017.

[36] R. M. Leach and D. F. Treacher, "The pulmonary physician in critical care • 2: Oxygen delivery and consumption in the critically ill," *Thorax*, vol. 57, pp. 170 – 177, 2 2002.

[37] S. L. Vrancken, A. F. van Heijst, and W. P. de Boode, "Neonatal Hemodynamics: From Developmental Physiology to Comprehensive Monitoring," *Frontiers in Pediatrics*, vol. 6, p. 87, 4 2018.

[38] R. M. Leach and D. F. Treacher, "Oxygen transport-2. Tissue hypoxia.," *BMJ*, vol. 317, pp. 1370–1373, 11 1998.

[39] M. Bé Langer, I. Allaman, and P. J. Magistretti, "Brain Energy Metabolism: Focus on Astrocyte-Neuron Metabolic Cooperation," *Cell Metabolism*, vol. 14, pp. 724–738, 2011.

[40] F. A. Azevedo, L. R. Carvalho, L. T. Grinberg, J. M. Farfel, R. E. Ferretti, R. E. Leite, W. J. Filho, R. Lent, and S. Herculano-Houzel, "Equal numbers of neuronal and nonneuronal cells make the human brain an isometrically scaled-up primate brain," *The Journal of Comparative Neurology*, vol. 513, pp. 532–541, 4 2009.

[41] "Neurons and Glial Cells - General Zoology - OpenStax CNX."

[42] D. Blackburn, S. Sargsyan, P. N. Monk, and P. J. Shaw, "Astrocyte function and role in motor neuron disease: A future therapeutic target?," *Glia*, vol. 57, pp. 1251–1264, 9 2009.

[43] M. C. Diamond, A. B. Scheibel, and L. M. Elson, *The human brain coloring book*. New York: Harper Collins Publishers, 1985.

[44] H. V. Carter, "File:Lobes of the brain NL.svg - Wikimedia Commons," 1918.

[45] "The Blood Supply of the Brain and Spinal Cord," in *Neuroscience* (D. Purves, G. J. Augustine, and D. Fitzpatrick, eds.), Sunderland (MA): Sinauer Associates, 2nd ed., 2001.

[46] M. J. Cipolla, "Control of Cerebral Blood Flow," in *The Cerebral Circulation*, ch. 5, San Rafael (CA): Morgan & Claypool Life Sciences, 2009.

[47] P. Liu, C. Parkinson, D. Jiang, M. Ouyang, J. B. De Vis, F. J. Northington, A. Tekes, H. Huang, T. A. Huisman, and W. C. Golden, "Characterization of MRI techniques to assess neonatal brain oxygenation and blood flow," *NMR in Biomedicine*, vol. 32, p. e4103, 4 2019.

[48] J. Stiles and T. L. Jernigan, "The basics of brain development.," *Neuropsychology review*, vol. 20, pp. 327–48, 12 2010.

[49] O. Linderkamp, L. Janus, R. Linder, and D. B. Skoruppa, "Time Table of Normal Foetal Brain Development," *Int. J. Prenatal and Perinatal Psychology and Medicine*, vol. 21, no. 1/2, pp. 4–16, 2009.

[50] C. Lebel and C. Beaulieu, "Longitudinal Development of Human Brain Wiring Continues from Childhood into Adulthood," *The Journal of Neuroscience*, vol. 31, no. 30, 2011.

[51] A. A. Figaji, "Anatomical and Physiological Differences between Children and Adults Relevant to Traumatic Brain Injury and the Implications for Clinical Assessment and Care.," *Frontiers in neurology*, vol. 8, p. 685, 2017.

[52] Z. Li, B.-K. Park, W. Liu, J. Zhang, M. P. Reed, J. D. Rupp, C. N. Hoff, and J. Hu, "A Statistical Skull Geometry Model for Children 0-3 Years Old," 2015.

[53] J. Ruan and P. Prasad, "The Effects of Skull Thickness Variations on Human Head Dynamic Impact Responses," *SAE Technical Papers*, no. November, 2001.

[54] M. Okamoto, H. Dan, K. Sakamoto, K. Takeo, K. Shimizu, S. Kohno, I. Oda, S. Isobe, T. Suzuki, K. Kohyama, and I. Dan, "Three-dimensional probabilistic anatomical cranio-cerebral correlation via the international 10-20 system oriented for transcranial functional brain mapping," *NeuroImage*, vol. 21, no. 1, pp. 99–111, 2004.

[55] P. Liu, H. Huang, N. Rollins, L. F. Chalak, T. Jeon, C. Halovanic, and H. Lu, "Quantitative assessment of global cerebral metabolic rate of oxygen (CMRO2) in neonates using MRI," *NMR in Biomedicine*, vol. 27, pp. 332–340, 3 2014.

[56] P. J. Joris, R. P. Mensink, T. C. Adam, and T. T. Liu, "Cerebral blood flow measurements in adults: A review on the effects of dietary factors and exercise," 5 2018.

[57] P. Anslow, "Birth asphyxia," *European Journal of Radiology*, vol. 26, pp. 148–153, 1 1998.

[58] I. C. Johnstone and J. H. Smith, "Cardiovascular monitoring in neonatal intensive care," *Infant*, vol. 4, no. 2, 2008.

[59] S. Aslam, T. Strickland, and E. J. Molloy, "Neonatal Encephalopathy: Need for Recognition of Multiple Etiologies for Optimal Management," *Frontiers in Pediatrics*, vol. 7, 2019.

[60] E. Sell, F. M. Munoz, A. Soe, M. Wiznitzer, P. T. Heath, E. D. Clarke, H. Spiegel, D. Sawlwin, M. Šubelj, I. Tikhonov, K. Mohammad, and S. Kochhar, "Neonatal encephalopathy: Case definition & guidelines for data collection, analysis, and presentation of maternal immunisation safety data.," *Vaccine*, vol. 35, pp. 6501–6505, 2017.

[61] R. M. McAdams and S. E. Juul, "Neonatal encephalopathy: Update on therapeutic hypothermia and other novel therapeutics," *Clinical Perinatology*, vol. 43, no. 3, pp. 485–500, 2016.

[62] O. Dammann, D. Ferriero, and P. Gressens, "Neonatal Encephalopathy or Hypoxic-Ischemic Encephalopathy? Appropriate Terminology Matters," *Pediatric Research*, vol. 70, pp. 1–2, 7 2011.

[63] L. J. Millar, L. Shi, A. Hoerder-Suabedissen, and Z. Molnár, "Neonatal Hypoxia Ischaemia: Mechanisms, Models, and Therapeutic Challenges," *Frontiers in Cellular Neuroscience*, vol. 11, p. 78, 5 2017.

[64] K. A. Allen and D. H. Brandon, "Hypoxic Ischemic Encephalopathy: Pathophysiology and Experimental Treatments.," *Newborn and infant nursing reviews*, vol. 11, pp. 125–133, 9 2011.

[65] S. Badurdeen, C. Roberts, D. Blank, S. Miller, V. Stojanovska, P. Davis, S. Hooper, and G. Polglase, "Haemodynamic Instability and Brain Injury in Neonates Exposed to HypoxiaIschaemia.," *Brain sciences*, vol. 9, 2 2019.

[66] S. Bano, V. Chaudhary, and U. Garga, "Neonatal hypoxic-ischemic encephalopathy: A radiological review," *Journal of Pediatric Neurosciences*, vol. 12, no. 1, p. 1, 2017.

[67] K. J. Hassell, M. Ezzati, D. Alonso-Alconada, D. J. Hausenloy, and N. J. Robertson, "New horizons for newborn brain protection: enhancing endogenous neuroprotection," *Archives of Disease in Childhood - Fetal and Neonatal Edition*, vol. 100, no. 6, pp. F541–F552, 2015.

[68] J. H. Meek, C. E. Elwell, D. C. Mccormick, D. Edwards, J. P. Townsend, A. L. Stewart, and J. S. Wyatt, "Abnormal cerebral haemodynamics in perinatally asphyxiated neonates related to outcome," tech. rep.

[69] A. N. Massaro, R. B. Govindan, G. Vezina, T. Chang, N. N. Andescavage, Y. Wang, T. Al-Shargabi, M. Metzler, K. Harris, and A. J. du Plessis, "Impaired cerebral autoregulation and brain injury in newborns with hypoxic-ischemic encephalopathy treated with hypothermia," *Journal of Neurophysiology*, vol. 114, pp. 818–824, 8 2015.

[70] L. Bennet, L. Booth, and A. J. Gunn, "Potential biomarkers for hypoxic-ischemic encephalopathy," *Seminars in Fetal and Neonatal Medicine*, vol. 15, no. 5, pp. 253–260, 2010.

[71] J. Conway, B. Walsh, G. Boylan, and D. Murray, "Mild hypoxic ischaemic encephalopathy and long term neurodevelopmental outcome - A systematic review," *Early Human Development*, vol. 120, pp. 80–87, 5 2018.

[72] J. E. van de Riet, F. Vandenbussche, S. Le Cessie, and M. Keirse, "Newborn assessment and long-term adverse outcome: a systematic review.," *American journal of obstetrics and gynecology*, vol. 180, pp. 1024–9, 4 1999.

[73] N. Merchant and D. Azzopardi, "Early predictors of outcome in infants treated with hypothermia for hypoxic-ischaemic encephalopathy," *Developmental Medicine and Child Neurology*, vol. 57, no. S3, pp. 8–16, 2015.

[74] A. Gibson and P. J. Andrews, "Therapeutic hypothermia, still "too cool to be true?"," *F1000Prime Reports*, vol. 5, 7 2013.

[75] A. R. Laptook, S. Shankaran, J. E. Tyson, B. Munoz, E. F. Bell, R. N. Goldberg, N. A. Parikh, N. Ambalavanan, C. Pedroza, A. Pappas, A. Das, A. S. Chaudhary, R. A. Ehrenkranz, A. M. Hensman, K. P. V. Meurs, L. F. Chalak, S. E. G. Hamrick, G. M. Sokol, M. C. Walsh, B. B. Poindexter, R. G. Faix, K. L. Watterberg, I. D. Frantz, III, R. Guillet, U. Devaskar, W. E. Truog, V. Y. Chock, M. H. Wyckoff, E. C. McGowan, D. P. Carlton, H. M. Harmon, J. E. Brumbaugh, C. M. Cotten, P. J. Sánchez, A. M. Hibbs, R. D. Higgins, and Eunice Kennedy Shriver National Institute of Child

Health and Human Development Neonatal Research Network, "Effect of Therapeutic Hypothermia Initiated After 6 Hours of Age on Death or Disability Among Newborns With Hypoxic-Ischemic Encephalopathy: A Randomized Clinical Trial," *JAMA*, vol. 318, no. 16, pp. 1550–1560, 2017.

[76] A. Razak and A. Hussain, "Erythropoietin in perinatal hypoxic-ischemic encephalopathy: a systematic review and meta-analysis," *J. Perinat. Med*, vol. 47, no. 4, pp. 478–489, 2019.

[77] S. M. Parry and E. S. Peeples, "The impact of hypoxic-ischemic brain injury on stem cell mobilization, migration, adhesion, and proliferation," *Neural Regeneration Research*, vol. 13, no. 7, p. 1125, 2018.

[78] K. Martinello, A. R. Hart, S. Yap, S. Mitra, and N. J. Robertson, "Management and investigation of neonatal encephalopathy: 2017 update," *Archives of disease in childhood. Fetal and neonatal edition*, vol. 102, p. F346–F358, 2017.

[79] E. Briatore, F. Ferrari, G. Pomero, A. Boghi, L. Gozzoli, R. Micciolo, G. Espa, P. Gancia, and S. Calzolari, "EEG findings in cooled asphyxiated newborns and correlation with site and severity of brain damage," *Brain and Development*, vol. 35, pp. 420–426, 5 2013.

[80] T. Austin, C. Chetcuci Ganado, P. Clarke, S. O'Hare, N. Merchant, B. Vakharia, and F. Walston, "Clinical Guideline: Guidelines for Management of Infants with Suspected Hypoxic Ischaemic Encephalopathy (HIE)," tech. rep., EOE Neonatal ODN, 2016.

[81] I. Korotchikova, N. Stevenson, B. Walsh, D. Murray, and G. Boylan, "Quantitative EEG analysis in neonatal hypoxic ischaemic encephalopathy," *Clinical Neurophysiology*, vol. 122, pp. 1671–1678, 8 2011.

[82] A. Awal, M. M. Lai, G. Azemi, B. Boashash, and P. B. Colditz, "EEG background features that predict outcome in term neonates with hypoxic ischaemic encephalopathy: A structured review," *Clinical Neurophysiology*, vol. 127, no. 1, pp. 285–296, 2016.

[83] K. M. Tichauer, J. T. Elliott, J. A. Hadway, T.-Y. Lee, and K. St. Lawrence, "Cerebral metabolic rate of oxygen and amplitude-integrated electroencephalography during early reperfusion after hypoxia-ischemia in piglets," *Journal of Applied Physiology*, vol. 106, pp. 1506–1512, 5 2009.

[84] M. C. Toet, P. M. Lemmers, L. J. van Schevlven, and F. Van Bel, "Cerebral Oxygenation and Electrical Activity After Birth Asphyxia: Their Relation to Outcome," *Pediatrics*, vol. 117, no. 2, pp. 333–339, 2006.

[85] S. T. Sorokan, A. L. Jefferies, and S. P. Miller, "Imaging the term neonatal brain.," *Paediatrics & child health*, vol. 23, no. 5, pp. 322–328, 2018.

[86] S. Mitra, G. S. Kendall, A. Bainbridge, M. Sokolska, M. Dinan, C. Uria-Avellanal, D. Price, K. McKinnon, R. Gunny, A. Huertas-Ceballos, X. Golay, and N. J. Robertson, "Proton magnetic resonance

spectroscopy lactate/N-acetylaspartate within 2 weeks of birth accurately predicts 2-year motor, cognitive and language outcomes in neonatal encephalopathy after therapeutic hypothermia," *Archives of Disease in Childhood - Fetal and Neonatal Edition*, vol. 104, pp. F424–F432, 7 2019.

[87] S. Thayyil, M. Chandrasekaran, A. Taylor, A. Bainbridge, E. B. Cady, W. K. K. Chong, S. Murad, R. Z. Omar, and N. J. Robertson, "Cerebral Magnetic Resonance Biomarkers in Neonatal Encephalopathy: A Meta-analysis," *PEDIATRICS*, vol. 125, pp. e382–e395, 2 2010.

[88] B. M. Kline-Fath, P. S. Horn, W. Yuan, S. Merhar, C. Venkatesan, C. W. Thomas, and M. B. Schapiro, "Conventional MRI scan and DTI imaging show more severe brain injury in neonates with hypoxic-ischemic encephalopathy and seizures," *Early Human Development*, vol. 122, pp. 8–14, 7 2018.

[89] K. Imai, L. S. De Vries, T. Alderliesten, N. Wagenaar, N. E. Van Der Aa, M. H. Lequin, M. J. N. L. Benders, I. C. Van Haastert, and F. Groenendaal, "MRI Changes in the Thalamus and Basal Ganglia of Full-Term Neonates with Perinatal Asphyxia," *Neonatology*, vol. 114, pp. 253–260, 2018.

[90] J. Salas, A. Tekes, M. Hwang, F. J. Northington, and T. A. G. M. Huisman, "Head Ultrasound in Neonatal Hypoxic-Ischemic Injury and Its Mimickers for Clinicians: A Review of the Patterns of Injury and the Evolution of Findings Over Time," *Neonatology*, vol. 114, pp. 185–197, 2018.

[91] P. J. McLachlan, J. Kishimoto, M. Diop, D. Milej, D. S. Lee, S. De Ribaupierre, and K. S. Lawrence, "Investigating the effects of cerebrospinal fluid removal on cerebral blood flow and oxidative metabolism in infants with post-hemorrhagic ventricular dilatation," *Pediatric Research*, vol. 82, no. 4, pp. 634–641, 2017.

[92] M. Diop, J. T. Elliott, K. M. Tichauer, T. Y. Lee, and K. St. Lawrence, "A broadband continuous-wave multichannel near-infrared system for measuring regional cerebral blood flow and oxygen consumption in newborn piglets," *Review of Scientific Instruments*, vol. 80, no. 5, 2009.

[93] N. Roche-Labarbe, S. A. Carp, A. Surova, M. Patel, D. A. Boas, P. E. Grant, and M. A. Franceschini, "Noninvasive Optical Measures of CBV, StO2, CBF Index, and rCMRO2 in Human Premature Neonates' Brains in the First Six Weeks of Life," *Hum Brain Mapp*, vol. 31, no. 3, pp. 341–352, 2010.

[94] K. Verdecchia, M. Diop, T.-Y. Lee, and K. St Lawrence, "Quantifying the cerebral metabolic rate of oxygen by combining diffuse correlation spectroscopy and time-resolved near-infrared spectroscopy.," *Journal of biomedical optics*, vol. 18, p. 27007, 2 2013.

[95] M. Dehaes, A. Aggarwal, P.-Y. Lin, C. Rosa Fortuno, A. Fenoglio, N. Roche-Labarbe, J. S. Soul, M. A. Franceschini, and P. E. Grant, "Cerebral Oxygen Metabolism in Neonatal Hypoxic Ischemic Encephalopathy during and after Therapeutic Hypothermia," *Journal of Cerebral Blood Flow & Metabolism*, vol. 34, no. 1, pp. 87–94, 2014.

[96] E. M. Buckley, A. B. Parthasarathy, P. E. Grant, A. G. Yodh, and M. A. Franceschini, "Diffuse correlation spectroscopy for measurement of cerebral blood flow: future prospects.," *Neurophotonics*, vol. 1, no. 1, p. 011009, 2014.

[97] B. Massa-Buck, V. Amendola, R. McCloskey, and K. Rais-Bahrami, "Significant Correlation between Regional Tissue Oxygen Saturation and Vital Signs of Critically Ill Infants," *Frontiers in Pediatrics*, vol. 5, no. December, p. 276, 2017.

[98] C. L. Hunter, J. L. Oei, K. Lui, and T. Schindler, "Cerebral oxygenation as measured by near-infrared spectroscopy in neonatal intensive care: correlation with arterial oxygenation," *Acta Paediatrica, International Journal of Paediatrics*, vol. 106, no. 7, pp. 1073–1078, 2017.

[99] V. Iani, J. Moan, and L. W. Ma, "Measurements of light penetration into human tissues in vivo," *Photochemotherapy: Photodynamic Therapy and Other Modalities*, vol. Proc. SPIE, pp. 378–383, 1996.

[100] F. Scholkmann, S. Kleiser, A. J. Metz, R. Zimmermann, J. Mata Pavia, U. Wolf, and M. Wolf, "A review on continuous wave functional near-infrared spectroscopy and imaging instrumentation and methodology," *NeuroImage*, vol. 85, pp. 6–27, 2014.

[101] M. Cope, "The development of a near infrared spectroscopy system and its application for non invasive monitory of cerebral blood and tissue oxygenation in the newborn infants," *University of London*, 1991.

[102] G. Bale, C. E. Elwell, and I. Tachtsidis, "From Jöbsis to the present day: a review of clinical near-infrared spectroscopy measurements of cerebral cytochrome-c-oxidase," *Journal of Biomedical Optics*, vol. 21, no. 9, p. 091307, 2016.

[103] W. Weigl, D. Milej, D. Janusek, S. Wojtkiewicz, P. Sawosz, M. Kacprzak, A. Gerega, R. Maniewski, and A. Liebert, "Application of optical methods in the monitoring of traumatic brain injury: A review.," *Journal of cerebral blood flow and metabolism : official journal of the International Society of Cerebral Blood Flow and Metabolism*, vol. 36, no. 11, pp. 1825–1843, 2016.

[104] S. L. Jacques, "Optical properties of biological tissues: A review," *Physics in Medicine and Biology*, vol. 58, no. 11, 2013.

[105] C. E. Elwell, *A practical users guide to near infrared spectroscopy*. Hamatsu Photonics KK, 1995.

[106] L. V. Wang and H.-i. Wu, *Biomedical optics: principles and imaging*. Hoboken, New Jersey: John Wiley & Sons, 2007.

[107] S. J. Matcher, M. Cope, and D. T. Delpy, "In vivo measurements of the wavelength dependence of tissue-scattering coefficients between 760 and 900 nm measured with time-resolved spectroscopy.," *Applied optics*, vol. 36, no. 1, pp. 386–396, 1997.

[108] L. Spinelli, L. Zucchelli, D. Contini, M. Caffini, J. Mehler, A. Fló, A. L. Ferry, L. Filippin, F. Macagno, L. Cattarossi, and A. Torricelli, "In vivo measure of neonate brain optical properties and hemodynamic parameters by time-domain near-infrared spectroscopy," *Neurophotonics*, vol. 4, no. 04, p. 1, 2017.

[109] M. Lindkvist, G. Granåsen, and C. Grönlund, "Coherent derivation of equations for differential spectroscopy and spatially resolved spectroscopy: an undergraduate tutorial," *Spectroscopy Letters*, vol. 7010, no. January 2016, 2013.

[110] A. Duncan, J. H. Meek, M. Clemence, C. E. Elwell, L. Tyszczuk, M. Cope, and D. T. Delpy, "Optical pathlength measurements on adult head, calf and forearm and the head of the newborn infant using phase resolved optical spectroscopy.," *Physics in medicine and biology*, vol. 40, no. 2, pp. 295–304, 1995.

[111] G. Bale, *Development of Optical Instrumentation and Methods to Monitor Brain Oxygen Metabolism : Application to Neonatal Birth Asphyxia*. PhD thesis, UCL, 2016.

[112] S. Matcher, P. Kirkpatrick, K. Nahid, M. Cope, and D. T. Delpy, "Absolute quantification methods in tissue near infrared spectroscopy.," *Proc. SPIE*, vol. 2389, pp. 486–495, 1995.

[113] F. Lange, L. Dunne, L. Hale, and I. Tachtsidis, "MAESTROS: A Multiwavelength Time-Domain NIRS System to Monitor Changes in Oxygenation and Oxidation State of Cytochrome-C-Oxidase," *IEEE Journal of selected topics in quantum electronics*, vol. 25, no. 1, 2019.

[114] F. Lange and I. Tachtsidis, "Clinical Brain Monitoring with Time Domain NIRS: A Review and Future Perspectives," *Applied Sciences*, vol. 9, no. 8, p. 1612, 2019.

[115] M. Wolf, M. Ferrari, and V. Quaresima, "Progress of near-infrared spectroscopy and topography for brain and muscle clinical applications.," *Journal of biomedical optics*, vol. 12, no. 6, p. 062104, 2007.

[116] R. C. Haskell, L. O. Svaasand, T.-T. Tsay, T.-C. Feng, M. S. McAdams, and B. J. Tromberg, "Boundary conditions for the diffusion equation in radiative transfer," *J. Opt. Soc. Am. A*, vol. 11, no. 10, pp. 2727–2741, 1994.

[117] W. Jarosz, *Efficient Monte Carlo Methods for Light Transport in Scattering Media*. PhD thesis, University of California San Diego, 2008.

[118] S. L. Jacques and B. W. Pogue, "Tutorial on diffuse light transport," *Journal of Biomedical Optics*, vol. 13, no. 4, p. 041302, 2008.

[119] R. Aronson, "Boundary conditions for diffusion of light," *Journal of the Optical Society of America A*, vol. 12, no. 11, p. 2532, 1995.

[120] M. A. Franceschini, S. Fantini, L. A. Paunescu, J. S. Maier, and E. Gratton, "Influence of a superficial layer in the quantitative spectroscopic study of strongly scattering media," *Applied Optics*, vol. 37, no. 31, p. 7447, 1998.

[121] M. Dehaes, P. E. Grant, D. D. Sliva, N. Roche-Labarbe, R. Pienaar, D. A. Boas, M. A. Franceschini, and J. Selb, "Assessment of the frequency-domain multi-distance method to evaluate the brain optical properties: Monte Carlo simulations from neonate to adult," *Biomedical Optics Express*, vol. 2, no. 3, pp. 552–567, 2011.

[122] F. Martelli, S. Del Bianco, G. Zaccanti, A. Pifferi, A. Torricelli, A. Bassi, P. Taroni, and R. Cubeddu, "Phantom validation and in vivo application of an inversion procedure for retrieving the optical properties of diffusive layered media from time-resolved reflectance measurements," *Optics Letters*, vol. 29, pp. 2037–2039, 9 2004.

[123] F. Fabbri, A. Sassaroli, M. E. Henry, and S. Fantini, "Optical measurements of absorption changes in two-layered diffusive media," *Physics in Medicine and Biology*, vol. 49, no. 7, pp. 1183–1201, 2004.

[124] A. Kienle, M. S. Patterson, N. Dögnitz, R. Bays, G. Wagni*v*res, and H. van den Bergh, "Noninvasive determination of the optical properties of two-layered turbid media.," *Applied optics*, vol. 37, no. 4, pp. 779–91, 1998.

[125] O. Pucci, V. Toronov, and K. St. Lawrence, "Measurement of the optical properties of a two-layer model of the human head using broadband near-infrared spectroscopy," *Applied Optics*, vol. 49, no. 32, pp. 6324–6332, 2010.

[126] A. Pifferi, A. Torricelli, P. Taroni, and R. Cubeddu, "Reconstruction of absorber concentrations in a two-layer structure by use of multidistance time-resolved reflectance spectroscopy," *Optics Letters*, vol. 26, p. 1963, 12 2001.

[127] F. Martelli, A. Sassaroli, S. Del Bianco, and G. Zaccanti, "Solution of the time-dependent diffusion equation for a three-layer medium: application to study photon migration through a simplified adult head model," *Physics in Medicine and Biology*, vol. 52, pp. 2827–2843, 2007.

[128] J. W. Barker, A. Panigrahy, and T. J. Huppert, "Accuracy of oxygen saturation and total hemoglobin estimates in the neonatal brain using the semi-infinite slab model for FD-NIRS data analysis," *Biomedical Optics Express*, vol. 5, no. 12, p. 4300, 2014.

[129] E. Okada, M. Schweiger, S. R. Arridge, M. Firbank, and D. T. Delpy, "Experimental validation of Monte Carlo and finite-element methods for the estimation of the optical path length in inhomogeneous tissue," *Applied Optics*, vol. 35, no. 19, 1996.

[130] M. S. Patterson, S. J. Madsen, J. D. Moulton, and B. C. Wilson, "Diffusion representation of photon migration in tissue," in *IEEE Microwave Theory and Techniques Symposium Digest*, vol. BB-1, (Boston, MA), pp. 905–908, IEEE, 1991.

[131] D. Contini, F. Martelli, and G. Zaccanti, "Photon migration through a turbid slab described by a model based on diffusion approximation. I. Theory," *Appl. Opt.*, vol. 36, no. 19, pp. 4587–4599, 1997.

[132] M. S. Patterson, B. Chance, and B. C. Wilson, "Time resolved reflectance and transmittance for the non- invasive measurement of tissue optical properties," *Applied Optics*, vol. 28, no. 12, pp. 2331–2336, 1989.

[133] T. K. Biswas and T. M. Luu, "In vivo MR Measurement of Refractive Index, Relative Water Content and T2 Relaxation time of Various Brain lesions With Clinical Application to Discriminate Brain Lesions," *Internet Journal of Radiology*, vol. 13, no. 1, p. 8277, 2009.

[134] A. Kienle and M. S. Patterson, "Improved solutions of the steady-state and the time-resolved diffusion equations for reflectance from a semi-infinite turbid medium," *J. Opt. Soc. Am. A*, vol. 14, no. 1, pp. 246–254, 1997.

[135] S. J. Matcher, M. Cope, and D. T. Delpy, "Use of the water absorption spectrum to quantify tissue chromophore concentration changes in near-infrared spectroscopy," *Physics in Medicine and Biology*, vol. 39, pp. 177–196, 1 1993.

[136] S. Wray, M. Cope, D. T. Delpy, J. S. Wyatt, and E. O. R. Reynolds, "Characterization of the near infrared absorption spectra of cytochrome aa3 and haemoglobin for the non-invasive monitoring of cerebral oxygenation.," *Biochimica et biophysica acta*, vol. 933, pp. 184–192, 1988.

[137] S. J. Matcher and C. E. Cooper, "Absolute quantification of deoxyhaemoglobin concentration in tissue near infrared spectroscopy," *Phys. Med. Biol.*, vol. 39, pp. 1295–1312, 1994.

[138] H. Dehghani, F. Leblond, B. W. Pogue, and F. Chauchard, "Application of spectral derivative data in visible and near-infrared spectroscopy," *Physics in Medicine and Biology*, vol. 55, no. 12, pp. 3381–3399, 2010.

[139] M. Kewin, A. Rajaram, D. Milej, A. Abdalmalak, L. Morrison, M. Diop, and K. St Lawrence, "Evaluation of hyperspectral NIRS for quantitative measurements of tissue oxygen saturation by comparison to time-resolved NIRS," *Biomedical Optics Express*, vol. 10, no. 9, pp. 4789–4802, 2019.

[140] L. Giannoni, F. Lange, and I. Tachtsidis, "Hyperspectral imaging solutions for brain tissue metabolic and hemodynamic monitoring: Past, current and future developments," 4 2018.

[141] J. L. Sandell and T. C. Zhu, "A review of in-vivo optical properties of human tissues and its impact on PDT," *Journal of Biophotonics*, vol. 4, no. 11-12, pp. 773–787, 2011.

[142] M. Diop, J. Kishimoto, V. Toronov, D. D. S. C. Lee, and K. S. K. Lawrence, "Development of a combined broadband near-infrared and diffusion correlation system for monitoring cerebral blood flow

and oxidative metabolism in preterm infants," *Biomedical Optics Express*, vol. 6, no. 10, pp. 3907–3918, 2015.

[143] P. G. Al-Rawi, P. Smielewski, and P. J. Kirkpatrick, "Evaluation of a near-infrared spectrometer (NIRO 300) for the detection of intracranial oxygenation changes in the adult head.," *Stroke; a journal of cerebral circulation*, vol. 32, no. 11, pp. 2492–2500, 2001.

[144] H. Liu, D. A. Boas, Y. Zhang, A. G. Yodh, and B. Chance, "Determination of optical properties and blood oxygenation in tissue using continuous NIR light," tech. rep., 1995.

[145] D. M. Hueber, S. Fantini, A. E. Cerussi, and B. B. Barbieri, "New optical probe designs for absolute (self-calibrating) NIR tissue hemoglobin measurements," *Optical Tomography and Spectroscopy of Tissue III*, vol. 3597, no. July, pp. 618–631, 1999.

[146] Paul B. Benni, "Method for non-invasive spectrophotometric blood oxygenation monitoring," 2002.

[147] A. Rajaram, G. Bale, M. Kewin, L. B. Morrison, I. Tachtsidis, K. St. Lawrence, and M. Diop, "Simultaneous monitoring of cerebral perfusion and cytochrome c oxidase by combining broadband near-infrared spectroscopy and diffuse correlation spectroscopy," vol. 9, no. 6, pp. 2588–2603, 2018.

[148] J. Deepak Veesa and H. Dehghani, "Functional near infrared spectroscopy using spatially resolved data to account for tissue scattering: A numerical study and arm-cuff experiment," *Journal of Biophotonics*, vol. 12, no. e201900064, 2019.

[149] A. Moerman and S. De Hert, "Recent advances in cerebral oximetry. Assessment of cerebral autoregulation with near-infrared spectroscopy: myth or reality?," *F1000 Research*, vol. 6, p. 1615, 2017.

[150] M. Smith, "Shedding light on the adult brain: a review of the clinical applications of near-infrared spectroscopy.," *Philosophical transactions. Series A, Mathematical, physical, and engineering sciences*, vol. 369, no. 1955, pp. 4452–69, 2011.

[151] P. Le Roux, "Physiological Monitoring of the Severe Traumatic Brain Injury Patient in the Intensive Care Unit," *Curr Neurol Neurosci Rep*, vol. 13, no. 331, 2013.

[152] N. Nagdyman, T. Fleck, S. Barth, H. Abdul-Khaliq, B. Stiller, P. Ewert, M. Huebler, H. Kuppe, and P. E. Lange, "Relation of cerebral tissue oxygenation index to central venous oxygen saturation in children," *Intensive Care Medicine*, vol. 30, pp. 468–471, 3 2004.

[153] N. Nagdyman, T. Fleck, S. Schubert, P. Ewert, B. Peters, P. E. Lange, and H. Abdul-Khaliq, "Comparison between cerebral tissue oxygenation index measured by near-infrared spectroscopy and venous jugular bulb saturation in children.," *Intensive care medicine*, vol. 31, pp. 846–50, 6 2005.

[154] J. M. Lynch, E. M. Buckley, P. J. Schwab, D. R. Busch, B. D. Hanna, M. E. Putt, D. J. Licht, and A. G. Yodh, "Noninvasive Optical Quantification of Cerebral Venous Oxygen Saturation in Humans," *Academic Radiology*, vol. 21, pp. 162–167, 2 2014.

[155] L. M. L. Dix, F. van Bel, and P. M. A. Lemmers, "Monitoring Cerebral Oxygenation in Neonates: An Update," *Frontiers in Pediatrics*, vol. 5, no. March, pp. 1–9, 2017.

[156] B. G. Sood, K. McLaughlin, and J. Cortez, "Near-infrared spectroscopy: Applications in neonates," *Seminars in Fetal and Neonatal Medicine*, vol. 20, no. 3, pp. 164–172, 2015.

[157] F. Van Bel, P. Lemmers, and G. Naulaers, "Monitoring neonatal regional cerebral oxygen saturation in clinical practice: Value and pitfalls," *Neonatology*, vol. 94, no. 4, pp. 237–244, 2008.

[158] J. Choi, M. Wolf, V. Toronov, U. Wolf, C. Polzonetti, D. Hueber, L. P. Safonova, R. Gupta, A. Michalos, W. Mantulin, and E. Gratton, "Noninvasive determination of the optical properties of adult brain: near-infrared spectroscopy approach," *Journal of Biomedical Optics*, vol. 9, no. 1, p. 221, 2004.

[159] K. L. Zaleski and B. D. Kussman, "Near-Infrared Spectroscopy in Pediatric Congenital Heart Disease," *Journal of Cardiothoracic and Vascular Anesthesia*, vol. 000, pp. 1–12, 9 2019.

[160] M. Wolf, K. Von Siebenthal, M. Keel, V. Dietz, O. Baenziger, and H. U. Bucher, "Tissue oxygen saturation measured by near infrared spectrophotometry correlates with arterial oxygen saturation during induced oxygenation changes in neonates," *Physiological Measurement*, vol. 21, no. 4, pp. 481–491, 2000.

[161] S. Mölström, T. H. Nielsen, C. Andersen, C. H. Nordström, and P. Toft, "Bedside Monitoring of Cerebral Energy State During Cardiac Surgery—A Novel Approach Utilizing Intravenous Microdialysis," *Journal of Cardiothoracic and Vascular Anesthesia*, pp. 1–7, 2016.

[162] L. A. Dempsey, M. Persad, S. Powell, D. Chitnis, and J. C. Hebden, "Geometrically complex 3D-printed phantoms for diffuse optical imaging," *Biomedical Optics Express*, vol. 8, no. 3, 2017.

[163] S. Hyttel-Sorensen, S. Kleiser, M. Wolf, and G. Greisen, "Calibration of a prototype NIRS oximeter against two commercial devices on a blood-lipid phantom," *Biomedical Optics Express*, vol. 4, no. 9, pp. 1662–1672, 2013.

[164] C. D. Kurtht, H. Liuf, W. S. Thayers, and B. Chance$, "A dynamic phantom brain model for near-infrared spectroscopy," *Physics in Medicine & Biology Phys. Med. Biol. Phys. Med. Biol*, vol. 40, pp. 2079–2092, 1995.

[165] S. Kleiser, N. Nasseri, B. Andresen, G. Greisen, and M. Wolf, "Comparison of tissue oximeters on a liquid phantom with adjustable optical properties," *Biomedical Optics Express*, vol. 7, no. 8, p. 2973, 2016.

[166] A. Afshari, P. Ghassemi, J. Lin, M. Halprin, J. Wang, G. Mendoza, S. Weininger, and T. J. Pfefer, "Cerebral oximetry performance testing with a 3D-printed vascular array phantom," *Biomedical Optics Express*, vol. 10, p. 3731, 8 2019.

[167] H. Wabnitz, D. R. Taubert, M. Mazurenka, O. Steinkellner, A. Jelzow, R. Macdonald, D. Milej, P. Sawosz, M. Kacprzak, A. Liebert, R. Cooper, J. Hebden, A. Pifferi, A. Farina, I. Bargigia, D. Contini, M. Caffini, L. Zucchelli, L. Spinelli, R. Cubeddu, and A. Torricelli, "Performance assessment of time-domain optical brain imagers, part 1: basic instrumental performance protocol," *Journal of Biomedical Optics*, vol. 19, p. 086010, 8 2014.

[168] A. Pifferi, A. Torricelli, A. Bassi, P. Taroni, R. Cubeddu, H. Wabnitz, D. Grosenick, M. Möller, R. Macdonald, J. Swartling, T. Svensson, S. Andersson-Engels, R. L. P. van Veen, H. J. C. M. Sterenborg, J.-M. Tualle, H. L. Nghiem, S. Avrillier, M. Whelan, and H. Stamm, "Performance assessment of photon migration instruments: the MEDPHOT protocol.," *Applied optics*, vol. 44, pp. 2104–14, 4 2005.

[169] H. Wabnitz, A. Jelzow, M. Mazurenka, O. Steinkellner, R. Macdonald, D. Milej, N. Zolek, M. Kacprzak, P. Sawosz, R. Maniewski, A. Liebert, S. Magazov, J. Hebden, F. Martelli, P. Di Ninni, G. Zaccanti, A. Torricelli, D. Contini, R. Re, L. Zucchelli, L. Spinelli, R. Cubeddu, and A. Pifferi, "Performance assessment of time-domain optical brain imagers, part 2: nEUROPt protocol," *Journal of Biomedical Optics*, vol. 19, p. 086012, 8 2014.

[170] P. Lanka, L. Yang, D. Orive-Miguel, J. D. Veesa, S. Tagliabue, A. Sudakou, S. Samaei, M. Forcione, Z. Kovacsova, A. Behera, L. Hervé, T. Durduran, A. Liebert, P. Sawosz, A. Belli, I. Tachtsidis, A. Dalla Mora, H. Dehghani, H. Wabnitz, and A. Pifferi, "The BITMAP exercise: a multi-laboratory performance assessment campaign of diffuse optical instrumentation," in *Proc. SPIE 11074, Diffuse Optical Spectroscopy and Imaging VII* (H. Dehghani and H. Wabnitz, eds.), vol. 110741A, SPIE, 7 2019.

[171] P. B. Benni, D. MacLeod, K. Ikeda, and H. M. Lin, "A validation method for near-infrared spectroscopy based tissue oximeters for cerebral and somatic tissue oxygen saturation measurements," *Journal of Clinical Monitoring and Computing*, vol. 0, no. 0, pp. 1–16, 2017.

[172] N. Shah, N. K. Trivedi, S. L. Clack, M. Shah, P. P. Shah, and S. Barker, "Impact of hypoxemia on the performance of cerebral oximeter in volunteer subjects.," *Journal of neurosurgical anesthesiology*, vol. 12, no. 3, pp. 201–9, 2000.

[173] V. Pollard, D. S. Prough, A. E. DeMelo, D. J. Deyo, T. Uchida, and H. F. Stoddart, "Validation in volunteers of a near-infrared spectroscope for monitoring brain oxygenation in vivo.," *Anesthesia and analgesia*, vol. 82, pp. 269–77, 2 1996.

[174] L. C. Henson, C. Calalang, J. A. Temp, and D. S. Ward, "Accuracy of a cerebral oximeter in healthy volunteers under conditions of isocapnic hypoxia.," *Anesthesiology*, vol. 88, pp. 58–65, 1 1998.

[175] K. Rais-Bahrami, O. Rivera, and B. L. Short, "Validation of a noninvasive neonatal optical cerebral oximeter in veno-venous ECMO patients with a cephalad catheter.," *Journal of perinatology : official journal of the California Perinatal Association*, vol. 26, no. 10, pp. 628–35, 2006.

[176] K. Ikeda, D. B. MacLeod, H. P. Grocott, E. W. Moretti, W. Ames, and C. Vacchiano, "The Accuracy of a Near-Infrared Spectroscopy Cerebral Oximetry Device and Its Potential Value for Estimating Jugular Venous Oxygen Saturation," *Anesthesia & Analgesia*, vol. 119, pp. 1381–1392, 12 2014.

[177] D. B. MacLeod, K. Ikeda, C. Vacchiano, A. Lobbestael, J. A. Wahr, and A. D. Shaw, "Development and validation of a cerebral oximeter capable of absolute accuracy," *Journal of Cardiothoracic and Vascular Anesthesia*, vol. 26, no. 6, pp. 1007–1014, 2012.

[178] P. E. Bickler, J. R. Feiner, and M. D. Rollins, "Factors affecting the performance of 5 cerebral oximeters during hypoxia in healthy volunteers," *Anesthesia and Analgesia*, vol. 117, no. 4, pp. 813–823, 2013.

[179] T. Komiyama, V. Quaresima, H. Shigematsu, and M. Ferrari, "Comparison of two spatially resolved near-infrared photometers in the detection of tissue oxygen saturation: poor reliability at very low oxygen saturation.," *Clinical science*, vol. 101, no. 6, pp. 715–718, 2001.

[180] M. Thavasothy, M. Broadhead, C. Elwell, M. Peters, and M. Smith, "A comparison of cerebral oxygenation as measured by the NIRO 300 and the INVOS 5100 near-infrared spectrophotometers," *Anaesthesia*, vol. 57, no. 10, pp. 999–1006, 2002.

[181] A. Dullenkopf, B. Frey, O. Baenziger, A. Gerber, and M. Weiss, "Measurement of cerebral oxygenation state in anaesthetized children using the INVOS 5100 cerebral oximeter," *Paediatric Anaesthesia*, vol. 13, no. 5, pp. 384–391, 2003.

[182] L. M. L. Dix, F. Van Bel, W. Baerts, and P. M. A. Lemmers, "Comparing near-infrared spectroscopy devices and their sensors for monitoring regional cerebral oxygen saturation in the neonate," *Pediatric Research*, vol. 74, pp. 557–563, 11 2013.

[183] T. W. Hessel, S. Hyttel-Sorensen, and G. Greisen, "Cerebral oxygenation after birth - a comparison of INVOS(®) and FORE-SIGHT™ near-infrared spectroscopy oximeters," *Acta paediatrica (Oslo, Norway : 1992)*, vol. 103, no. 5, pp. 488–493, 2014.

[184] A. Schneider, B. Minnich, E. Hofstätter, C. Weisser, E. Hattinger-Jürgenssen, and M. Wald, "Comparison of four near-infrared spectroscopy devices shows that they are only suitable for monitoring cerebral oxygenation trends in preterm infants," *Acta paediatrica (Oslo, Norway : 1992)*, vol. 103, no. 9, pp. 934–938, 2014.

[185] S. Hyttel-Sorensen, L. C. Sorensen, J. Riera, and G. Greisen, "Tissue oximetry: a comparison of mean values of regional tissue saturation, reproducibility and dynamic range of four NIRS-instruments on the human forearm," *Biomedical Optics Express*, vol. 2, no. 11, pp. 3047–3057, 2011.

[186] S. Hyttel-Sorensen, T. W. Hessel, and G. Greisen, "Peripheral tissue oximetry: comparing three commercial near-infrared spectroscopy oximeters on the forearm.," *Journal of clinical monitoring and computing*, vol. 28, pp. 149–55, 4 2014.

[187] K. Steenhaut, K. Lapage, T. Bove, S. de Hert, and A. Moerman, "Evaluation of different near-infrared spectroscopy technologies for assessment of tissue oxygen saturation during a vascular occlusion test," *Journal of Clinical Monitoring and Computing*, vol. 31, no. 6, pp. 1151–1158, 2016.

[188] A. Demel, M. Wolf, C. F. Poets, and A. R. Franz, "Effect of different assumptions for brain water content on absolute measures of cerebral oxygenation determined by frequency-domain near-infrared spectroscopy in preterm infants: An observational study," *BMC Pediatrics*, vol. 14, no. 1, pp. 4–9, 2014.

[189] D. Ostojic, S. Kleiser, N. Nasseri, H. Isler, F. Scholkmann, T. Karen, and M. Wolf, "Hemoglobin spectra affect measurement of tissue oxygen saturation," *Design and Quality for Biomedical Technologies XI*, no. February, p. 28, 2018.

[190] A. J. Metz, M. Biallas, C. Jenny, T. Muehlemann, and M. Wolf, "The effect of basic assumptions on the tissue oxygen saturation value of near infrared spectroscopy," in *Oxygen Transport to Tissue*, vol. XXXIV, Springer, New York, NY, 2013.

[191] P. Farzam, E. M. Buckley, P.-Y. Lin, K. Hagan, P. E. Grant, T. E. Inder, S. A. Carp, and M. A. Franceschini, "Shedding light on the neonatal brain: probing cerebral hemodynamics by diffuse optical spectroscopic methods.," *Scientific reports*, vol. 7, p. 15786, 11 2017.

[192] B. Hallacoglu, A. Sassaroli, and S. Fantini, "Optical Characterization of Two-Layered Turbid Media for Non-Invasive, Absolute Oximetry in Cerebral and Extracerebral Tissue," *PLoS ONE*, vol. 8, no. 5, 2013.

[193] A. Liebert, H. Wabnitz, and C. Elster, "Determination of absorption changes from moments of distributions of times of flight of photons: optimization of measurement conditions for a two-layered tissue model," *Journal of Biomedical Optics*, vol. 17, no. 5, p. 057005, 2012.

[194] H. Sørensen, P. Rasmussen, C. Siebenmann, M. Zaar, M. Hvidtfeldt, S. Ogoh, K. Sato, M. Kohl-Bareis, N. H. Secher, and C. Lundby, "Extra-cerebral oxygenation influence on near-infrared-spectroscopy-determined frontal lobe oxygenation in healthy volunteers: A comparison between INVOS-4100 and NIRO-200NX," *Clinical Physiology and Functional Imaging*, vol. 35, no. 3, pp. 177–184, 2015.

[195] R. B. Saager and A. J. Berger, "Direct characterization and removal of interfering absorption trends in two-layer turbid media," *Journal of the Optical Society of America A*, vol. 22, no. 9, p. 1874, 2005.

[196] S. Brigadoi and R. J. Cooper, "How short is short? Optimum source–detector distance for short-separation channels in functional near-infrared spectroscopy," *Neurophotonics*, vol. 2, no. 2, p. 025005, 2015.

[197] G. Greisen, B. Andresen, A. M. Plomgaard, and S. Hyttel-Sørensen, "Cerebral oximetry in preterm infants: an agenda for research with a clear clinical goal," *Neurophotonics*, vol. 3, no. 3, p. 031407, 2016.

[198] L. C. Sorensen and G. Greisen, "Precision of measurement of cerebral tissue oxygenation index using near-infrared spectroscopy in preterm neonates.," *Journal of biomedical optics*, vol. 11, no. 5, p. 054005, 2006.

[199] S. J. Arri, T. Muehlemann, M. Biallas, H. U. Bucher, and M. Wolf, "Precision of cerebral oxygenation and hemoglobin concentration measurements in neonates measured by near-infrared spectroscopy," *Journal of Biomedical Optics*, vol. 16, no. 4, p. 047005, 2011.

[200] J. Menke, U. Voss, G. Möller, and G. Jorch, "Reproducibility of cerebral near infrared spectroscopy in neonates," *Biology of the Neonate*, vol. 83, no. 1, pp. 6–11, 2003.

[201] G. Pichler, C. Binder, A. Avian, E. Beckenbach, G. M. Schmölzer, and B. Urlesberger, "Reference ranges for regional cerebral tissue oxygen saturation and fractional oxygen extraction in neonates during immediate transition after birth," *Journal of Pediatrics*, vol. 163, no. 6, pp. 1558–1563, 2013.

[202] N. Baik, B. Urlesberger, B. Schwaberger, G. M. Schmölzer, L. Mileder, A. Avian, and G. Pichler, "Reference Ranges for Cerebral Tissue Oxygen Saturation Index in Term Neonates during Immediate Neonatal Transition after Birth," *Neonatology*, vol. 108, no. 4, pp. 283–286, 2015.

[203] T. Alderliesten, L. Dix, W. Baerts, A. Caicedo, S. van Huffel, G. Naulaers, F. Groenendaal, F. van Bel, and P. Lemmers, "Reference values of regional cerebral oxygen saturation during the first 3 days of life in preterm neonates," *Pediatric Research*, vol. 79, no. 1-1, pp. 55–64, 2015.

[204] Medtronic, "INVOS 7100 system," 2019.

[205] A. Pellicer, G. Greisen, M. Benders, O. Claris, E. Dempsey, M. Fumagalli, C. Gluud, C. Hagmann, L. Hellström-Westas, S. Hyttel-Sorensen, P. Lemmers, G. Naulaers, G. Pichler, C. Roll, F. Van Bel, W. Van Oeveren, M. Skoog, M. Wolf, and T. Austin, "The SafeBoosC phase II randomised clinical trial: A treatment guideline for targeted near-infrared-derived cerebral tissue oxygenation versus standard treatment in extremely preterm infants," *Neonatology*, vol. 104, no. 3, pp. 171–178, 2013.

[206] G. Greisen, "SafeBoosC-III protocol," tech. rep., Department of Neonatology 5024, Rigshospitalet, Copenhagen, 2019.

[207] S. Hyttel-Sorensen, A. Pellicer, T. Alderliesten, T. Austin, F. van Bel, M. Benders, O. Claris, E. Dempsey, A. R. Franz, M. Fumagalli, C. Gluud, B. Grevstad, C. Hagmann, P. Lemmers, W. van

Oeveren, G. Pichler, A. M. Plomgaard, J. Riera, L. Sanchez, P. Winkel, M. Wolf, and G. Greisen, "Cerebral near infrared spectroscopy oximetry in extremely preterm infants: phase II randomised clinical trial.," *BMJ (Clinical research ed.)*, vol. 350, no. January, p. g7635, 2015.

[208] Ringshospitalet, "SafeBoosC-III," 2019.

[209] E. Kratky, G. Pichler, T. Rehak, A. Avian, M. Pocivalnik, W. Müller, and B. Urlesberger, "Regional cerebral oxygen saturation in newborn infants in the first 15 min of life after vaginal delivery," *Physiological Measurement*, vol. 33, no. 1, pp. 95–102, 2012.

[210] M. Almaazmi, M. B. Schmid, S. Havers, F. Reister, W. Lindner, B. Mayer, H. D. Hummler, and H. Fuchs, "Cerebral near-infrared spectroscopy during transition of healthy term newborns," *Neonatology*, vol. 103, no. 4, pp. 246–251, 2013.

[211] B. Urlesberger, K. Grossauer, M. Pocivalnik, A. Avian, W. Müller, and G. Pichler, "Regional oxygen saturation of the brain and peripheral tissue during birth transition of term infants," *Journal of Pediatrics*, vol. 157, no. 5, pp. 740–744, 2010.

[212] P. Montaldo, C. De Leonibus, L. Giordano, M. De Vivo, and P. Giliberti, "Cerebral, renal and mesenteric regional oxygen saturation of term infants during transition," *Journal of Pediatric Surgery*, vol. 50, pp. 1273–1277, 8 2015.

[213] P. Phan, D. Highton, J. Lai, M. Smith, C. Elwell, and I. Tachtsidis, "Multi-channel multi-distance broadband near-infrared spectroscopy system to measure the spatial response of cellular oxygen metabolism and tissue oxygenation," *Biomedical Optics Express*, vol. 7, no. 11, pp. 4424–4440, 2016.

[214] E. Ziehenberger, B. Urlesberger, C. Binder-Heschl, B. Schwaberger, N. Baik-Schneditz, and G. Pichler, "Near-infrared spectroscopy monitoring during immediate transition after birth: time to obtain cerebral tissue oxygenation," *Journal of Clinical Monitoring and Computing*, vol. 32, pp. 465–469, 2018.

[215] N. P. Bernal, G. M. Hoffman, N. S. Ghanayem, and M. J. Arca, "Cerebral and somatic near-infrared spectroscopy in normal newborns," *Journal of Pediatric Surgery*, vol. 45, no. 6, pp. 1306–1310, 2010.

[216] M. A. Franceschini, S. Thaker, G. Themelis, K. K. Krishnamoorthy, H. Bortfeld, S. G. Diamond, D. A. Boas, K. Arvin, and P. E. Grant, "Assessment of infant brain development with frequency-domain near-infrared spectroscopy.," *Pediatric research*, vol. 61, pp. 546–51, 5 2007.

[217] S. M. Bailey, K. D. Hendricks-Munoz, and P. Mally, "Cerebral, renal, and splanchnic tissue oxygen saturation values in healthy term newborns," *American Journal of Perinatology*, vol. 31, no. 4, pp. 339–344, 2014.

[218] P. Zaramella, E. Saraceni, F. Freato, E. Falcon, A. Suppiej, A. Milan, A. M. Laverda, and L. Chiandetti, "Can tissue oxygenation index (TOI) and cotside neurophysiological variables predict outcome in depressed/asphyxiated newborn infants?," *Early Human Development*, vol. 83, pp. 483–489, 8 2007.

[219] G. Ancora, E. Maranella, S. Grandi, F. Sbravati, E. Coccolini, S. Savini, and G. Faldella, "Early predictors of short term neurodevelopmental outcome in asphyxiated cooled infants. A combined brain amplitude integrated electroencephalography and near infrared spectroscopy study," *Brain and Development*, vol. 35, pp. 26–31, 1 2013.

[220] P. M. Lemmers, R. J. Zwanenburg, M. J. Benders, L. S. de Vries, F. Groenendaal, F. van Bel, and M. C. Toet, "Cerebral oxygenation and brain activity after perinatal asphyxia: does hypothermia change their prognostic value?," *Pediatric Research*, vol. 74, no. 2, pp. 180–185, 2013.

[221] M. Arriaga-Redondo, J. Arnaez, I. Benavente-Fernández, S. Lubián-López, M. Hortigüela, C. Vega-del Val, and A. Garcia-Alix, "Lack of Variability in Cerebral Oximetry Tendency in Infants with Severe Hypoxic–Ischemic Encephalopathy Under Hypothermia," *Therapeutic Hypothermia and Temperature Management*, vol. 00, no. 00, pp. 1–8, 2019.

[222] S. Peng, E. Boudes, X. Tan, C. Saint-Martin, M. Shevell, and P. Wintermark, "Does Near-Infrared Spectroscopy Identify Asphyxiated Newborns at Risk of Developing Brain Injury During Hypothermia Treatment?," *Am J Perinatol*, vol. 32, pp. 555–564, 2015.

[223] C. K. Niezen, A. F. Bos, D. A. Sival, L. C. Meiners, and H. J. Ter Horst, "Amplitude-Integrated EEG and Cerebral Near-Infrared Spectroscopy in Cooled, Asphyxiated Infants," *American Journal of Perinatology*, vol. 35, pp. 904–910, 7 2018.

[224] S. Nakamura, K. Koyano, W. Jinnai, S. Hamano, S. Yasuda, Y. Konishi, T. Kuboi, K. Kanenishi, T. Nishida, and T. Kusaka, "Simultaneous measurement of cerebral hemoglobin oxygen saturation and blood volume in asphyxiated neonates by near-infrared time-resolved spectroscopy," *Brain and Development*, vol. 37, pp. 925–932, 11 2015.

[225] K. Goeral, B. Urlesberger, V. Giordano, G. Kasprian, M. Wagner, L. Schmidt, A. Berger, K. Klebermass-Schrehof, and M. Olischar, "Prediction of Outcome in Neonates with Hypoxic-Ischemic Encephalopathy II: Role of Amplitude-Integrated Electroencephalography and Cerebral Oxygen Saturation Measured by Near-Infrared Spectroscopy," *Neonatology*, vol. 112, pp. 193–202, 2017.

[226] P. Wintermark, A. Hansen, S. Warfield, D. Dukhovny, and J. Soul, "Near-Infrared Spectroscopy versus Magnetic Resonance Imaging To Study Brain Perfusion in Newborns with Hypoxic-Ischemic Encephalopathy Treated with Hypothermia," *NeuroImage*, vol. 85, no. 0 1, pp. 287–293, 2014.

[227] V. J. Burton, G. Gerner, E. Cristofalo, S.-E. Chung, J. M. Jennings, C. Parkinson, R. C. Koehler, R. Chavez-Valdez, M. V. Johnston, F. J. Northington, and J. K. Lee, "A pilot cohort study of cerebral autoregulation and 2-year neurodevelopmental outcomes in neonates with hypoxic-ischemic encephalopathy who received therapeutic hypothermia," *BMC Neurology*, vol. 15, no. 209, 2015.

[228] R. A. Shellhaas, J. S. Kushwaha, M. A. Plegue, D. T. Selewski, and J. D. E Barks, "An Evaluation of Cerebral and Systemic Predictors of 18-Month Outcomes for Neonates With Hypoxic Ischemic Encephalopathy," *Journal of Child Neurology*, vol. 30, no. 11, pp. 1526–1531, 2015.

[229] P. E. Grant, N. Roche-Labarbe, A. Surova, G. Themelis, J. Selb, E. K. Warren, K. S. Krishnamoorthy, D. A. Boas, and M. A. Franceschini, "Increased cerebral blood volume and oxygen consumption in neonatal brain injury," *J Cereb Blood Flow Metab*, vol. 29, no. 10, pp. 1704–1713, 2009.

[230] E. Forman, C. R. Breatnach, S. Ryan, J. Semberova, J. Miletin, A. Foran, and A. El-Khuffash, "Non-invasive continuous cardiac output and cerebral perfusion monitoring in term infants with neonatal encephalopathy: Assessment of feasibility and reliability," *Pediatric Research*, vol. 82, pp. 789–795, 11 2017.

[231] F. Tian, P. Sepulveda, S. Kota, Y. Liu, Y. Das, H. Liu, R. Zhang, and L. Chalak, "Regional heterogeneity of cerebral hemodynamics in mild neonatal encephalopathy measured with multichannel near-infrared spectroscopy," 2020.

[232] P. M. A. Lemmers and F. van Bel, "Left-to-Right Differences of Regional Cerebral Oxygen Saturation and Oxygen Extraction in Preterm Infants During the First Days of Life," *Pediatr Res.*, vol. 65, no. 2, pp. 226–30, 2009.

[233] S. Mitra, G. Bale, J. Meek, I. Tachtsidis, and N. J. Robertson, "Cerebral Near Infrared Spectroscopy Monitoring in Term Infants With Hypoxic Ischemic Encephalopathy—A Systematic Review," *Frontiers in Neurology*, vol. 11, 5 2020.

[234] F. Tian, H. Ding, C. Zhigang, W. Guangzhi, and Z. Fuyun, "Assessment of blood and oxygen delivery to flaps of rhesus using near infrared steady-state spectroscopy," *Chinese Science Bulletin*, vol. 47, no. 21, pp. 1797–1802, 2002.

[235] G. Ancora, E. Maranella, C. Locatelli, L. Pierantoni, and G. Faldella, "Changes in cerebral hemodynamics and amplitude integrated EEG in an asphyxiated newborn during and after cool cap treatment," *Brain and Development*, vol. 31, pp. 442–444, 6 2009.

[236] K. Gucuyener, S. Beken, E. Ergenekon, S. Soysal, I. Hirfanoglu, O. Turan, S. Unal, N. Altuntas, E. Kazanci, F. Kulali, E. Koc, C. Turkyilmaz, E. Onal, and Y. Atalay, "Use of amplitude-integrated electroencephalography (aEEG) and near infrared spectroscopy findings in neonates with asphyxia during selective head cooling," *Brain and Development*, vol. 34, pp. 280–286, 4 2012.

[237] R. A. Shellhaas, B. J. Thelen, J. R. Bapuraj, J. W. Burns, A. W. Swenson, M. K. Christensen, S. A. Wiggins, and J. D. E. Barks, "Limited short-term prognostic utility of cerebral NIRS during neonatal therapeutic hypothermia.," *Neurology*, vol. 81, pp. 249–55, 7 2013.

[238] R. A. Shellhaas, J. W. Burns, S. A. Wiggins, M. K. Christensen, J. D. E Barks, and R. D. Chervin, "Sleep-Wake Cycling and Cerebral Oxygen Metabolism Among Critically Ill Neonates," *Journal of Child Neurology*, vol. 29, no. 4, pp. 530–533, 2013.

[239] M.-H. Gagnon and P. Wintermark, "Effect of persistent pulmonary hypertension on brain oxygenation in asphyxiated term newborns treated with hypothermia," *The Journal of Maternal-Fetal & Neonatal Medicine*, vol. 29, no. 13, pp. 2049–2055, 2015.

[240] L. F. Chalak, F. Tian, T. Tarumi, and R. Zhang, "Cerebral Hemodynamics in Asphyxiated Newborns Undergoing Hypothermia Therapy: Pilot Findings Using a Multiple-Time-Scale Analysis," *Pediatr Neurol.*, vol. february, no. 55, pp. 30–36, 2016.

[241] T. Alderliesten, J. B. De Vis, P. M. Lemmers, J. Hendrikse, F. Groenendaal, F. van Bel, M. J. Benders, and E. T. Petersen, "Brain oxygen saturation assessment in neonates using T2-prepared blood imaging of oxygen saturation and near-infrared spectroscopy.," *Jcbfm*, p. 0271678X16647737, 2016.

[242] V. Y. Chock, A. Frymoyer, C. G. Yeh, and K. P. Van Meurs, "Renal Saturation and Acute Kidney Injury in Neonates with Hypoxic Ischemic Encephalopathy Undergoing Therapeutic Hypothermia," *The Journal of Pediatrics*, vol. 200, pp. 232–239, 9 2018.

[243] T. W. Wu, B. Tamrazi, S. Soleymani, I. Seri, and S. Noori, "Hemodynamic Changes During Rewarming Phase of Whole-Body Hypothermia Therapy in Neonates with Hypoxic-Ischemic Encephalopathy," *Journal of Pediatrics*, vol. 197, pp. 68–74, 6 2018.

[244] Wolfram MathWolrd, "Gaussian Function ," 2019.

[245] L. Dunne, I. Tachtsidis, and J. Hebden, "Development of a Near Infrared Multi-Wavelength, Multi-Channel, Time-Resolved Spectrometer for Measuring Brain Tissue Haemodynamics and Metabolism," *Advances in experimental medicine and biology*, vol. 812, pp. 181–186, 2014.

[246] E. W. Weisstein, "Boundary Conditions," 2019.

[247] S. Brigadoi, P. Aljabar, M. Kuklisova-Murgasova, S. R. Arridge, and R. J. Cooper, "A 4D neonatal head model for diffuse optical imaging of pre-term to term infants," *NeuroImage*, vol. 100, pp. 385–394, 2014.

[248] M. Doulgerakis, A. Eggebrecht, S. Wojtkiewicz, J. Culver, and H. Dehghani, "Toward real-time diffuse optical tomography: accelerating light propagation modeling employing parallel computing on GPU and CPU," *Journal of Biomedical Optics*, vol. 22, no. 12, p. 1, 2017.

[249] A. T. Eggebrecht, B. R. White, S. L. Ferradal, C. Chen, Y. Zhan, A. Z. Snyder, H. Dehghani, and J. P. Culver, "A quantitative spatial comparison of high-density diffuse optical tomography and fMRI cortical mapping.," *NeuroImage*, vol. 61, pp. 1120–8, 7 2012.

[250] L. Cortese, G. L. Presti, M. Pagliazzi, D. Contini, A. D. Mora, A. Pifferi, S. K. V. Sekar, L. Spinelli, P. Taroni, M. Zanoletti, U. M. Weigel, S. de Fraguier, A. Nguyen-Dihn, B. Rosinski, and T. Durduran, "Liquid phantoms for near-infrared and diffuse correlation spectroscopies with tunable optical and dynamic properties," *Biomedical Optics Express*, vol. 9, no. 5, p. 2068, 2018.

[251] F. Scholkmann, A. J. Metz, and M. Wolf, "Measuring tissue hemodynamics and oxygenation by continous-wave functional near-infrared spectroscopy - how robust are the different calculation methods against movement artifacts?," *Physiological Measurement*, vol. 35, pp. 717–734, 2014.

[252] Z. Kovacsova, G. Bale, S. Mitra, I. de Roever, J. Meek, N. Robertson, and I. Tachtsidis, "The investigation of confounding factors in measuring tissue saturations with NIRS spatially resolved spectroscopy," in *Oxygen Transport to Tissue XL*, SPIE, 2018.

[253] "NIRO-200NX Near infrared oxygenation monitor C10448 | Hamamatsu Photonics."

[254] A. Dullenkopf, A. Kolarova, G. Schulz, B. Frey, O. Baenziger, and M. Weiss, "Reproducibility of cerebral oxygenation measurement in neonates and infants in the clinical setting using the NIRO 300 oximeter.," *Pediatric critical care medicine : a journal of the Society of Critical Care Medicine and the World Federation of Pediatric Intensive and Critical Care Societies*, vol. 6, no. 3, pp. 344–347, 2005.

[255] A. Steimers, M. Vafiadou, G. Koukourakis, D. Geraskin, P. Neary, and M. Kohl-Bareis, "Muscle Oxygenation During Running Assessed by Broad Band NIRS," pp. 41–47, Springer, New York, NY, 2016.

[256] I. Tachtsidis, L. Gao, T. S. Leung, M. Kohl-Bareis, C. E. Cooper, and C. E. Elwell, "A hybrid multi-distance phase and broadband spatially resolved spectrometer and algorithm for resolving absolute concentrations of chromophores in the near-infrared light spectrum.," *Advances in experimental medicine and biology*, vol. 662, pp. 169–75, 2010.

[257] L. Couch, M. Roskosky, B. A. Freedman, and M. S. Shuler, "Effect of Skin Pigmentation on Near Infrared Spectroscopy," *American Journal of Analytical Chemistry*, vol. 6, pp. 911–916, 2015.

[258] T. S. Leung, I. Tachtsidis, M. Smith, D. T. Delpy, and C. E. Elwell, "Measurement of the absolute optical properties and cerebral blood volume of the adult human head with hybrid differential and spatially resolved spectroscopy," *Physics in Medicine & Biology*, vol. 51, pp. 703–717, 2006.

[259] D. Highton, I. Tachtsidis, A. Tucker, C. Elwell, and M. Smith, "Near Infrared Light Scattering Changes Following Acute Brain Injury," *Advances in Experimental Medicine and Biology*, vol. 876, p. 139–144, 2016.

[260] T. Kurata, S. Iwata, K. Tsuda, M. Kinoshita, M. Saikusa, N. Hara, M. Oda, E. Ohmae, Y. Araki, T. Sugioka, S. Takashima, and O. Iwata, "Physiological and pathological clinical conditions and light scattering in brain," *Scientific Reports*, vol. 6, no. 1, p. 31354, 2016.

[261] MathWorks United Kingdom, "Sign test - MA- MathWorks United Kingdom."

[262] W. Bablok and H. Passing, "Applicaton of statistical procedures in analytical instrument testing," *Journal of Automatic Chemistry*, vol. 7, no. 2, pp. 74–79, 1985.

[263] E. Whitley and J. Ball, "Statistics review 6: Nonparametric methods.," *Critical care (London, England)*, vol. 6, pp. 509–13, 12 2002.

[264] R. F. Keep, Y. Hua, and G. Xi, "Brain water content. A misunderstood measurement?," *Translational stroke research*, vol. 3, pp. 263–5, 6 2012.

[265] John D'Errico, "fminsearchbnd, fminsearchcon - File Exchange - MATLAB Central."

[266] L. Yang, P. Lanka, H. Wabnitz, R. Cubeddu, T. Gladytz, S. K. Venkata Sekar, D. Grosenick, A. Pifferi, and R. Macdonald, "Spatially-enhanced time-domain NIRS for determination of optical properties in layered structures," *Optics InfoBase Conference Papers*, vol. Part F142-, no. July 2019, 2019.

[267] N. Abayomi and M. Diop, "Improving the Accuracy of Continuous-Wave Hyperspectral Near Infrared Spectroscopy with Spatially-Resolved Measurements and Tikhonov Regularization [abstract]," in *Biophotonics Congress: Biomedical Optics 2020*, Optical Society of America, 2020.

[268] J. G. Kim and H. Liu, "Variation of haemoglobin extinction coefficients can cause errors in the determination of haemoglobin concentration measured by near-infrared spectroscopy," *Physics in Medicine and Biology*, vol. 52, no. 20, pp. 6295–6322, 2007.

[269] Y. Zhao, L. Qiu, Y. Sun, C. Huang, and T. Li, "Optimal hemoglobin extinction coefficient data set for near-infrared spectroscopy," *Biomedical Optics Express*, vol. 8, no. 11, p. 5151, 2017.

[270] M. Diop, E. Wright, V. Toronov, T.-Y. Lee, and K. St. Lawrence, "Improved light collection and wavelet de-noising enable quantification of cerebral blood flow and oxygen metabolism by a low-cost, off-the-shelf spectrometer," *Journal of Biomedical Optics*, vol. 19, no. 5, p. 057007, 2014.

[271] D. Ostojic, J. Jiang, H. Isler, S. Kleiser, T. Karen, M. Wolf, and F. Scholkmann, "Impact of Skull Thickness on Cerebral NIRS Oximetry in Neonates: An in silico Study," in *Oxygen Transport to Tissue XLI. Advances in Experimental Medicine and Biology*, pp. 33–38, Cham: Springer, 2020.

[272] Z. Kovacsova, "multimodalspectroscopy/BRoadband_mUltidistaNce_Oximetry," 2020.

[273] "Bland-Altman and Correlation Plot - File Exchange - MATLAB Central."

[274] MathWorks United Kingdom, "Find minimum of unconstrained multivariable function using derivative-free method - MATLAB fminsearch," 2020.

[275] D. G. Altman and J. M. Bland, "Measurement in Medicine: The Analysis of Method Comparison Studies," *The Statistician*, vol. 32, no. 3, p. 307, 1983.

[276] J. M. Bland and D. G. Altman, "Measurement error," *BMJ*, vol. 312, 1996.

[277] B. Afzal, P. Chandrasekharan, D. J. Tancredi, J. Russell, R. H. Steinhorn, and S. Lakshminrusimha, "Monitoring gas exchange during hypothermia for hypoxic-ischemic encephalopathy," *Pediatric Critical Care Medicine*, vol. 20, pp. 166–171, 2 2019.

[278] J. Olmo Arroyo, S. Khirani, A. Amaddeo, L. Griffon, L. De Sanctis, P. Pouard, and B. Fauroux, "A comparison of pulse oximetry and cerebral oxygenation in children with severe sleep apnea-hypopnea syndrome: a pilot study," *Journal of Sleep Research*, vol. 26, pp. 799–808, 12 2017.

[279] V. Y. Chock, G. F. T. Variane, A. Netto, and K. P. Van Meurs, "NIRS improves hemodynamic monitoring and detection of risk for cerebral injury: cases in the neonatal intensive care nursery," *The Journal of Maternal-Fetal & Neonatal Medicine*, 2018.

[280] M. Ferrari, M. Muthalib, and V. Quaresima, "The use of near-infrared spectroscopy in understanding skeletal muscle physiology: recent developments," *Trans. R. Soc. A*, vol. 369, pp. 4577–4590, 2011.

[281] P. Kaynezhad, S. Mitra, G. Bale, C. Bauer, I. Lingam, C. Meehan, A. Avdic-Belltheus, K. A. Martinello, A. Bainbridge, N. J. Robertson, and I. Tachtsidis, "Quantification of the severity of hypoxic-ischemic brain injury in a neonatal preclinical model using measurements of cytochrome-c-oxidase from a miniature broadband-near-infrared spectroscopy system," *Neurophotonics*, vol. 6, no. 4, p. 045009, 2019.

Appendix A

Baby Brain Study consent form

University College London Hospitals NHS
NHS Foundation Trust

Project ID: 13/0013
REC Ref: 13/LO/0225

Patient Identification
Number for this trial: _____

Name of Researcher: Professor Nicola J Robertson

Neonatal Services
NNU Medical Secretaries
2nd Floor, North Wing
250 Euston Road
London NW1 2PG

Telephone: 0203 456 7890
Consultants' PA: 0203 447 8094

THE UCH BABY BRAIN STUDY

FORM FOR PARENTAL CONSENT

Please initial each box

1. I confirm that I have read and understand the information sheet dated 4 September 2018 (version. 4.1) for the above study. I have had the opportunity to consider the information, ask questions and have had these answered satisfactorily. ☐
2. I understand that the participation of my baby in this study (NIRS monitoring and extra sequences during MRI/MRS) is independent from other studies and I can withdraw from any of them separately at any time. ☐
3. I understand that the participation of my baby is voluntary and that I am free to withdraw at any time without giving any reason, without the medical care or legal rights of my baby being affected. ☐
4. I understand that relevant sections of my baby's medical notes and data collected during the study may be looked at by individuals from regulatory authorities or from the NHS Trust from the sponsor's representative from UCL, where it is relevant to my baby taking part in this research. I give permission for these individuals to have access to my baby's records. ☐
5. I agree that the NIRS, MRI/MRS and other MR sequences data, video recordings and EEG tracings can be used for further research and teaching purposes; the material will always be used anonymously and my child will not be identifiable in the data used. ☐
6. I understand that I will be invited back for 3-4 assessments over the first year after my child was born and a last assessment will be performed at 2 years of age. ☐
7. I agree that my baby may take part in the above study. ☐

Name of Child:		
Name of Parent:	Date	Signature
Name of Person taking consent:	Date	Signature

3 copies: one to be retained by parent, one placed in the clinical notes and one retained by the study office.